Asteroseismic Tuning of the Magnetic Star HR 1217

Understanding magnetism and stellar structure through MOST spacebased photometry

by

Christopher J. Cameron

B. Sc., Saint Mary's University, 2001
M. Sc., University of British Columbia, 2004

A THESIS SUBMITTED IN PARTIAL FULFILLMENT OF
THE REQUIREMENTS FOR THE DEGREE OF

DOCTOR OF PHILOSOPHY

in

The Faculty of Graduate Studies

(Astronomy)

THE UNIVERSITY OF BRITISH COLUMBIA

(Vancouver)

August, 2010

Abstract

The chemically peculiar A (Ap) stars show extreme examples of astrophysical processes that have only recently been studied in detail in one other star — the Sun. These stars exhibit spectral anomalies caused by diffusion of some ionic species in a stellar atmosphere threaded by a strong ($\sim$ kG), organized magnetic field. A subset of the Ap stars rapidly oscillate (roAp) with periods ranging from 5 to 25 minutes. One of these roAp stars, HR 1217, is well studied with data from two global (ground-based) photometric campaigns that led to asteroseismic evidence of magnetically perturbed oscillation modes. This was the motivation to make HR 1217 a *MOST* space mission target.

Our analysis of the almost 30 days of near-continuous *MOST* photometry on HR 1217 reveals a number of new periodicities that show spacings of $\sim$ 15, 2.5, and 1.5 μHz. These new frequencies can be interpreted as magnetically perturbed oscillations and potentially second order spacings that could constrain the age and the magnetic interior of the star for the first time. These data are collected with a 95% duty cycle and reach a precision of 6 μmag, making this by far the best photometric data set on HR 1217.

In addition, we present a grid of almost 52,000 stellar pulsation models including a large range of magnetic dipole field strengths (1–10 kG). This

is the largest grid of stellar pulsation models of any Ap star to date and is critical to the interpretation of the *MOST* photometry. Our models can match the *MOST* observations to a fractional accuracy of about 0.05% with a mean deviation between theory and observation of a few μHz. A unique model match to the *MOST* observations could not be found. The results highlight the sensitivity to physics that has not been usually incorporated in Ap interior models, and the complex nature of the interaction of globally organized magnetic fields with stellar pulsation eigenmodes.

Table of Contents

Appendices

List of Tables

List of Figures

Acknowledgements

This thesis would not have been possible without the support of my PhD supervisor Jaymie Matthews. He has gone beyond the call of duty as a supervisor and a mentor to make sure that I was exposed to cutting edge research, and that my work was made known to other researchers in our field. I learned a lot from him. There are times in a person's life when they find out who their real friends are — Jaymie Matthews is a real friend. My sincerest thanks.

Thank you to the *MOST* science team for giving me the opportunity to work with such high quality data. I can only hope that you will be as pleased with the results as I am. Margarida Cunha, thank you for spending a significant amount of your time to teach me about your research on the roAp stars. I have benefited greatly from scientific discussions with Hideyuki Saio. He has read many versions of this thesis and has encouraged my research at every phase.

Rainer Kuschnig wasn't know as the 'fun boy' of the *MOST* lab for nothing. He is a great friend that has guided my research and patiently listened to my many rants over the years. To my other cohort in the *MOST* lab, Jason Rowe: Our science discussions have spurred many great ideas. You are one of the few people that can interpret my ramblings as I try to work

out the details of my new projects. Your friendship and honest advice are always welcome and appreciated.

I was fortunate to meet many interesting people while studying at UBC. The science discussions with other graduate students were an important part of my growth as a researcher; but, I also managed to have some fun times outside of the academic environment ... I would especially like to thank Kelsey Hoffman, Mark Huber, Jason Kalirai, Thomas Pfrommer, and Jason Rowe for all of those fun times.

My parents, Joey and Marie Cameron, and my sister, Cheryl Cameron, have continually given me support and have encouraged me in everything I have ever done. Without them I would not have been able to finish this project. I hope they are as proud of me as I am of them.

Jennifer McGillivray, my wife, has been by my side since before my graduate school days. She has moved with me from one side of Canada to the other, to Europe, and back again. Her devotion and patience mean the world to me. There would be no thesis without your loving motivation. Thank you for taking this journey with me.

Dedication

For my son, Owen.

Statement of Collaboration

The following is intended to notify the reader of publications in which work from this thesis appears. It also serves to identify people who have collaborated on various aspects of this work.

In chapter 2 (§ 2.2 and 2.3) the time-series analysis techniques and model interpretations were published in the following works: Walker et al. (2005), Saio et al. (2006), Cameron et al. (2006), King et al. (2006), Saio et al. (2007) and Cameron et al. (2008). The coauthors of those publications (see the bibliography) should be credited as collaborators on the work presented in chapter 2. My contribution to the above publications was primarily the frequency analysis, light curve analysis, some model interpretation and writing of the manuscripts. Data and models from this thesis have been presented and discussed at a number of conferences since 2004. Dr. D. B. Guenther provided the stellar pulsation and evolution software packages (JIG and YREC) used to calculate models in chapters 4 and 5. Dr. M. S. Cunha provided the software used to calculate the magnetic perturbations to the oscillation frequencies in chapters 4 and 5. I performed the model calculations and interpreted the results presented in those chapters. Dr. J. F. Rowe should be credited with the preliminary photometric reduction of the HR 1217 data.

This thesis has benefited from the revisions suggested by my PhD ex-

amining committee members: Drs. Hiromoto Shibahashi, Michael Bostock, and Jeremy Heyl. My supervisory committee, Drs. Jaymie Matthews, Neil Balmforth, Brett Gladman, and Scott Oser have helped guide and refine the final format and content of this thesis.

Chapter 1

Introduction

This thesis covers both observational (chapters 2 and 3) and theoretical (chapters 4 and 5) studies of the seismology of the pulsating, magnetic, chemically-peculiar, A-type star HR 1217. An attempt at modelling and interpreting the many physical processes that must be explored to fully describe the observed properties of HR 1217 is a daunting task. With this in mind, we compare the unique observations of the pulsations in HR 1217 obtained by the *MOST* satellite (chapter 2) to pulsation models that focus on the magnetic effects that influence the properties of the calculated, and observed, pulsation modes.

There have been many comprehensive reviews on the subject of stellar seismology, and in the past few years there has been a growing number of reviews focusing on the variable, chemically peculiar A stars as well. These will be referenced extensively as necessary sources of background information on both the theory and measured properties that detail the rapidly oscillating Ap (roAp) star phenomenon.

In this introductory chapter we briefly outline stellar seismology, the peculiar A stars, and the history of the observations of HR 1217 that are relevant to this work. Further emphasis on the details of data acquisition, reduction methods and on the modelling of stellar oscillations (in the context of HR

1217) are found in the later chapters of this thesis.

1.1 The sounding of stellar interiors

Observations of stars are typically only skin deep. Spectroscopic measurements of star light give a glimpse of a razor-thin layer of the stellar surface from which astronomers infer the chemical constitution of the star, its average surface temperature and some of its mean properties, e.g., surface gravity. Integrated light measurements (photometry) can give astronomers information about the radius of the star, assuming its distance is known and an estimate of its temperature is available.

In the early 1960s Leighton et al. (1962) noticed there were spatially incoherent, wave-like disturbances on the surface of the Sun with periods near 5 minutes. This oscillation period should be compared to the longer dynamical timescale[1] of approximately one hour that can be estimated for the Sun. Ulrich (1970) and Leibacher & Stein (1971) were the first to interpret these oscillations as sound waves produced in the solar interior that resonate in acoustic cavities defined by changes in the physical state, e.g., pressure and density, of the solar material with increasing depth. These sound waves, also known as p-modes because pressure is the restoring force, produce standing wave patterns as they propagate and provide the possibility of seismically

[1]The dynamical period of a self gravitating sphere is inversely proportional to the square-root of the mean density of the material ($\sqrt{R^3/GM}$) and represents the time it would take for a particle on the surface of the sphere to free-fall to the centre. The expression for this 'free-fall' time contains the mass M and the radius R of the sphere and the physical dimensions of the problem are scaled by the gravitational constant G.

measuring the variation of sound speed throughout the recesses of the Sun. Seismology of the Sun (helioseismology) was then possible and astronomers were at last able to lift the optically thick veil that hid the interior of a star. Since these early beginnings, millions of p-modes have been identified in the Sun and measurements of its internal rotation rate, the depth of its convective zone, constraints on element diffusion, and the run of sound speed have all been inferred. Recent reviews on helioseismology are provided by Christensen-Dalsgaard (2002) and Basu & Antia (2008).

The stellar (non-solar) equivalent of helioseismology is asteroseismology. Many stars show both photometric and spectroscopic variations that are consistent with p-modes and longer period g-modes (buoyancy waves with gravity taking the role of the restoring force). Some examples include: δ Scuti stars (oscillation periods of $P \sim 0.5$–2 h), RR Lyrae stars ($P \sim 1.5$–24 h), β Cephei stars ($P \sim 3$–6 h), variable white dwarfs ($P \sim 100$–1600 s) and supergiants (P ranges from hours to days). Cox (1980) gives a detailed description of primarily radial (spherically symmetric) stellar oscillations while the general, nonradial, case of oscillations with both horizontal and radial displacements is discussed in detail by Unno et al. (1989). An introduction to many types of variable stars and the theory of stellar oscillations can be found in Christensen-Dalsgaard (2003), and review articles by Gautschy & Saio (1995, 1996), Cunha et al. (2007), and Aerts et al. (2008) also provide general asteroseismic discussions and some recent results. Below I summarize the properties of stellar oscillations that are important for the interpretation of the rapidly oscillating Ap (roAp) stars ($P \sim 5$–30 min) — A particular type of variable star that is described in more detail in § 1.2.2. One roAp

star, HR 1217, is the focus of this research project.

1.1.1 Nonradial stellar oscillations

The properties of stellar oscillations are introduced in this section along with the asymptotic relations that connect the properties of individual oscillation modes, frequencies, and spacings to the mean properties of a star. The notation we use follows closely to that of Unno et al. (1989). Both Unno et al. (1989) and Christensen-Dalsgaard (2003) should be consulted as detailed, recent references outlining the physics of stellar oscillations. More concise reviews are provided by Gautschy & Saio (1995), Shibahashi (2005), and Basu & Antia (2008).

Stellar pulsations are described by the usual fluid equations. They are the continuity equation, the momentum equation (a.k.a. the equation of motion or the Euler equation), an energy equation that details the flow and transfer of energy in the fluid, and Poisson's equation relating the gravitational potential, Φ, of the fluid to its internal density, ρ. These equations are represented, in the order presented above, by

$$\begin{aligned} \frac{\partial \rho}{\partial t} &= -\nabla \cdot (\rho \mathbf{v}) \\ \rho \left(\frac{\partial}{\partial t} + \mathbf{v} \cdot \nabla \right) \mathbf{v} &= -\nabla p - \rho \nabla \Phi \\ \frac{\partial p}{\partial t} + \mathbf{v} \cdot \nabla p &= c_s^2 \left(\frac{\partial \rho}{\partial t} + \mathbf{v} \cdot \nabla \rho \right) \\ \nabla^2 \Phi &= 4\pi G \rho \end{aligned} \tag{1.1}$$

where the gas pressure and fluid velocity at a given time t are given by p and $\mathbf{v}$, respectively. All variables are functions of depth within the model, i.e.,

radius r, or mass shell $m(r)$. The energy equation (the third equation in the set of Eqs. 1.1) is given in the adiabatic approximation so that no heat gains or losses occur within the fluid over an oscillation cycle. In this approximation the adiabatic sound speed c_s is related to the gas pressure and density by $\sqrt{\Gamma_1 p/\rho}$, with the first adiabatic exponent defined as $\Gamma_1 = (\partial \ln p/\partial \ln \rho)_S$. The adiabatic approximation is commonly used to model stellar oscillations. In this thesis we focus on the magnetic perturbation to the acoustic oscillation spectrum of variable stars and the matching of those perturbed modes to high quality data (see chapters 4 and 5). Because we are not exploring the excitation mechanism of these magnetic oscillation modes, any non-adiabatic effects will, for simplicity, be ignored.

A non-rotating, non-magnetic star has spherical symmetry. This is also approximately true for slow rotation and if a small magnetic field is present. Assuming that oscillations about this static, symmetric, reference state have small amplitudes compared to the radius of the star, we can perform a normal mode analysis of Eqs. 1.1 by linearizing the variables, substituting them back into Eqs. 1.1, and keeping only first order terms (see, for example, Unno et al. 1989). We do this so we can describe a complex oscillation pattern on the surface of a star as the superposition of a number of small, independent, oscillations. Supposing the linearized perturbations vary with a time dependence proportional to $\exp(i\sigma t)$, with (angular) oscillation frequency σ, and that the radial and angular components are separable, the pulsation variables (for example, pressure) can be expressed as

$$f(r, \theta, \phi, t) = f_0(r) + f'(r) Y_l^m(\theta, \phi) \exp(i\sigma t) \tag{1.2}$$

The perturbation $f'(r)$ to the spherically symmetric background state $f_0(r)$

in Eq. 1.2 is evaluated at a fixed radius r. This is called an Eulerian perturbation. We can also define the Lagrangian perturbation as a perturbation calculated in a reference frame moving along with the fluid. If a fluid element moves a small distance $\xi = \delta r$ from the reference position r_0, the Lagrangian perturbation can be written as

$$\delta f(r) = f(r_0 + \xi) - f_0(r_0) \tag{1.3}$$

By expanding $f(r_0 + \xi)$ to first order about the background state, Eq. 1.3 becomes

$$\delta f(r) = f(r_0) + \xi \cdot \nabla f_0 - f_0(r_0) \tag{1.4}$$

The difference $f(r_0) - f_0(r_0)$ is just the Eulerian perturbation (f') evaluated at the radius r_0. Placing $f'(r_0)$ into Eq. 1.4, we arrive at

$$\delta f(r) = f'(r_0) + \xi \cdot \nabla f_0 \tag{1.5}$$

This expression relates the Lagrangian and Eulerian perturbations. Each of the pulsation variables can be expressed in either of the Eulerian or Lagrangian reference frames. The choice is usually one of mathematical or numerical convenience. The linearized version of Eqs. 1.1 (and a discussion on the boundary conditions needed to complete the solution set) are found in § 4.2 (see Eqs. 4.2).

The angular coordinates in Eq. 1.2 are described by spherical harmonics $Y_l^m(\theta, \phi)$. The index ℓ is commonly called the degree of the mode and divides the surface of the star into regions oscillating in opposite phase. If $\ell = 0$, the oscillation mode is radial, or more precisely, spherically symmetric. Photometric observations of pulsating stars generally show the contributions

from low-ℓ modes because the contribution from modes with $\ell \gtrsim 3$ averages out when the light from the stellar disc is summed. The index m is the azimuthal order of the mode and represents the number of longitudinal nodal lines on the stellar surface. Because the spherical harmonics are proportional to $\exp(im\phi)$, the phase velocity is

$$\left(\frac{\partial \phi}{\partial t}\right)_{phase} = -\frac{\sigma}{m} \tag{1.6}$$

The sign of m indicates the direction in which the wave travels. A standing wave pattern can be formed on the surface of the star by superimposing two waves travelling in opposite directions because the background state is, to first order, spherically symmetric.

These indices are quantized with m taking integer values from $-\ell$ to $+\ell$, where ℓ is a whole number. If $m = 0$ all nodal lines on a sphere are lines of latitude (zonal modes) and if $m = \ell$ they are all lines of longitude (sectoral modes). If m takes on values between these extremes, the modes are known as tesseral modes and of the ℓ nodal lines, $\ell - |m|$ are lines of latitude. Examples are drawn schematically in Fig. 1.1 for the cases $\ell = 3$ and $m = 0$, 1, 2, and 3. Because the modes are degenerate with respect to m, an agent such as rotation is needed to define an axis that breaks the spherical symmetry and lifts the $2\ell + 1$ degeneracy.

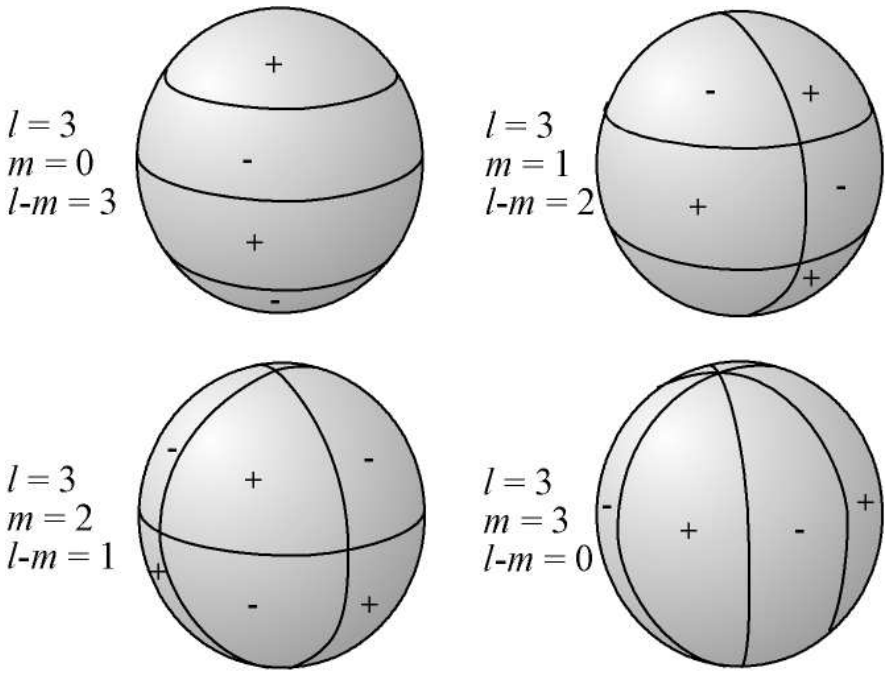

Figure 1.1: A schematic representation of different surface spherical harmonics. The upper left sphere shows harmonics having an angular degree of $\ell = 3$ and an azimuthal order of $m = 0$ while the upper right sphere illustrates $\ell = 3$ and $m = 1$. The lower left and right portions of the diagram show $\ell = 3$, $m = 2$ and $\ell = 3$, $m = 3$, respectively. The (-) and (+) represent regions (separated by nodal lines) that oscillate in opposite phase. Note there are $\ell - |m|$ lines of latitude on each sphere. (This image was taken from the wikipedia website `http://en.wikipedia.org/wiki/File:Harmoniques_spheriques_positif_negatif.png` and is available under the GNU Free Documentation License.)

Along with ℓ and m, there is another index that describes the character of an individual component of the linear analysis outlined above. The equations describing the nonradial stellar oscillations can be reduced to a fourth order

differential equation with the oscillation frequency (squared) as an eigenvalue of the system. The eigenvalues and eigenfunctions of the system are ordered into two groups (p and g-modes) that are indexed by n. Each frequency[2] has associated with it a displacement vector (or eigenfunction) with components

$$\xi_{n,\ell,m} = \left(\xi_r(r)Y_l^m, \xi_h(r)\frac{\partial Y_l^m}{\partial\theta}, \frac{\xi_h(r)}{\sin\theta}\frac{\partial Y_l^m}{\partial\phi}\right)\exp(i\sigma t) \tag{1.7}$$

The index n is the radial order of the oscillations and corresponds to the number of radial nodes (zeros) in the eigenfunction $\xi_{n,\ell,m}$. In general, p-modes (or acoustic waves) have frequencies that increase with increasing n. Their frequencies are greater than the dynamical frequency $\sqrt{GM/R^3}$. The p-modes have their largest radial displacement near the surface of a star. The g-modes (or buoyancy waves), on the other hand, have periods that increase with decreasing n and are longer than the dynamical period $\sqrt{R^3/(GM)}$. The amplitude of the radial eigenfunction is largest near the centre of a star for g-modes. This behaviour is illustrated in Fig. 1.2 for a p and g-mode calculated using a model of the Sun. The total displacement on the surface of a variable star can, in principle be described by summing Eq. 1.7 over all values of n, ℓ, and m associated with the eigenfrequencies that most closely match the observed oscillation periods of that star.

[2] A modelled frequency, or eigenvalue, may also be referred to as an eigenfrequency, eigenmode, or simply a mode.

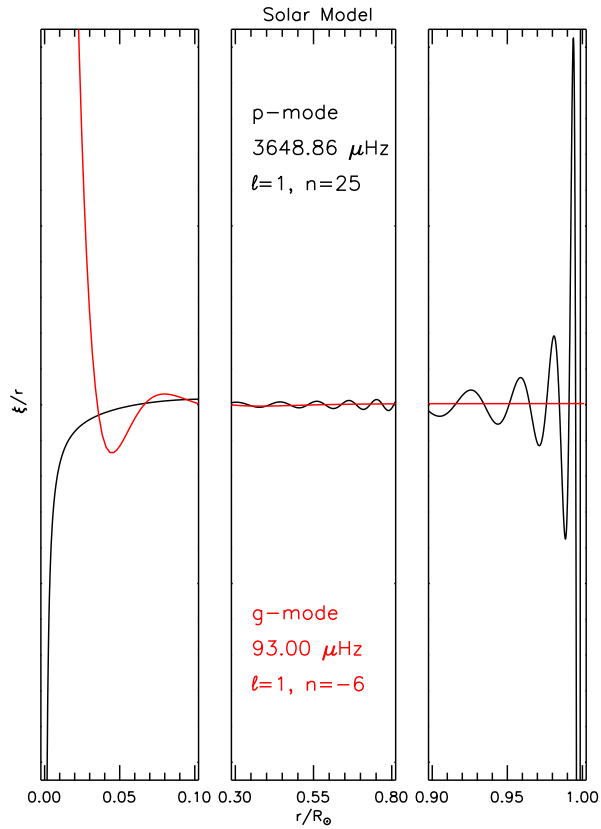

Figure 1.2: Eigenfunctions (presented here as the radial displacement ξ normalized by radius r) of a low-order g-mode (red) and a high order p-mode (black) calculated using a model of the Sun. Each mode has an angular degree of $\ell = 1$ and is axisymmetric ($m = 0$). The radial order (n) gives the number of zero crossings of the eigenfunctions. (Negative n values are used for g-modes by convention.) The g-mode has its largest amplitude near the centre of the model while the high-order p-mode has its largest amplitude near the surface.

Using the terminology defined above we will now consider the properties

of p-modes in more detail because they are important to the interpretation of the data and models presented in chapters 4 and 5.

It can be shown (see Christensen-Dalsgaard 2003) that the radial wave number, k_r, of a p-mode is approximately

$$k_r^2 = \frac{\sigma^2}{c_s^2} - \frac{\ell(\ell+1)}{r^2} \tag{1.8}$$

The second term in the above is identified as the horizontal wave number, k_h. As a wave with an oscillation frequency σ travels inward from the surface of a star toward its centre, the local sound speed increases with increasing temperature. The horizontal wavenumber begins to dominate, causing the wave front to slowly bend until the wave refracts upward again. At this turning radius, r_t, the radial wave number k_r goes to zero and the wave has only a horizontal displacement. Put another way

$$r_t^2 = \frac{c_s^2(r_t)\ell(\ell+1)}{\sigma^2} \tag{1.9}$$

Thus, for a given frequency and angular degree, a wave will bend differently from star to star (or from model to model) depending on how the sound speed changes as a function of radius within the star (or model). This is the essence of stellar seismology — A method by which the interior structure of a star can be estimated by observing oscillations having different σ and ℓ.

When studying the properties of stellar oscillations it is useful to focus on subsets of the calculated oscillation spectra that have special properties. For example, modes with a high angular degree behave differently than modes with a low angular degree. Of particular importance to this work are high-order, low-degree modes. Modes are described as being high-order (or high-overtone) when n is large. In the case of p-modes, high-order modes are

essentially radial and have vertical wave numbers of $k_r \approx \sigma/c_s$ near the stellar surface. These modes tend to have oscillation frequencies of a few mHz (a period of 5 min corresponds to a frequency of 3.3 mHz) and are consistent with oscillations observed in the Sun.

The number of nodes a given eigenfunction has between the centre and surface of a star can be estimated by adding up the number of nodes per wavelength there are in that radius range (see Hansen & Kawaler 1994). That is,

$$n \propto \int_0^R 2dr/\lambda \approx \int_0^R k_r dr \tag{1.10}$$

This relation gives a hint that the frequency of a given mode is related to the number of nodes the eigenfunction has because $k_r \propto \sigma$. A careful asymptotic analysis of high-overtone, low-degree, p-modes by Tassoul (1980, 1990) gives

$$\nu_{n,\ell} \cong \left(n + \frac{\ell}{2} + \beta\right)\Delta\nu - \left[A(\ell + 1/2)^2 - \epsilon\right]\frac{\Delta\nu^2}{\nu_{n,\ell}} \tag{1.11}$$

with

$$\Delta\nu = \left(2\int_0^R \frac{dr}{c_s(r)}\right)^{-1} \tag{1.12}$$

and

$$A = \frac{1}{4\pi^2\Delta\nu}\left(\kappa - \int_0^R \frac{dc_s}{dr} d\ln r\right) \tag{1.13}$$

where we now make the transition between angular frequency σ and the observed oscillation frequencies $\nu = \sigma/2\pi$. In this asymptotic form (see also Christensen-Dalsgaard 2003) constants β, ϵ, and κ are small and depend on the surface structure of the star. Equation 1.11 is valid for adiabatic oscillations about a spherically symmetric star and for p-modes with $n \gg \ell$. This asymptotic relation holds when $n/\ell \sim 10$ or greater.

Equation 1.11 tells us that frequencies of the same degree and with orders that differ by one are approximately equally spaced by $\Delta\nu$ ($= \nu_{n+1,\ell} - \nu_{n,\ell}$). The quantity $\Delta\nu$ is known as the large spacing and it will be used extensively in this thesis. If the modes have orders that differ from each other by one and ℓ values that alternate between even *and* odd values, Eq. 1.11 provides a frequency spacing of $\Delta\nu/2$. If, however, consecutive ℓ values are either all even *or* odd, the frequencies are spaced by about $\Delta\nu$. Another spacing that has diagnostic importance is the second-order, or small spacing, $\delta\nu$. Modes with ℓ values differing by two and n values differing by one ($\nu_{n,\ell} - \nu_{n-1,\ell+2}$) have nearly the same frequency.

Both the large and small spacings are illustrated schematically in Fig. 1.3, where a picket fence pattern of frequencies similar to that observed, for example, in the Sun is shown. (For completeness, a solar model yields values of $\Delta\nu \sim 135$ μHz and $\delta\nu \sim 10$ μHz.) Frequencies generally increase in value as n and ℓ increase. Figure 1.3 presents both large and small spacings, shown between consecutive overtones, depending on the degree difference between adjacent modes. It is important to note that both the large and small spacings are functions of both frequency and degree and are not strictly constant over a large frequency range for a given star or model.

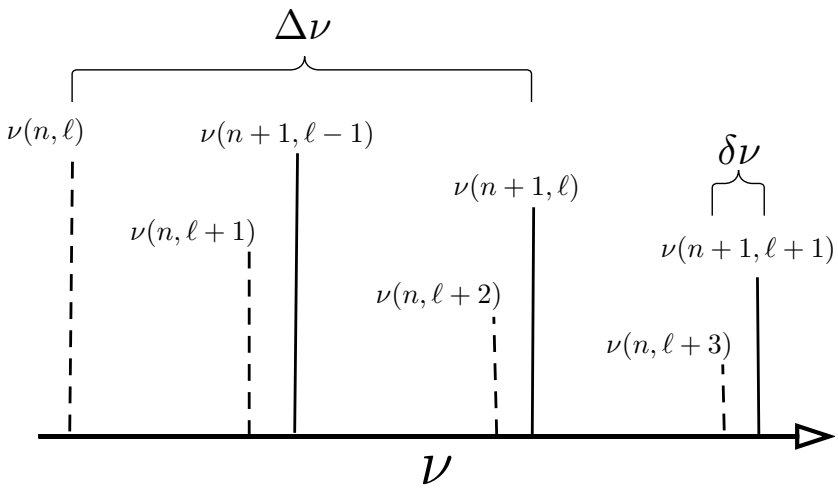

Figure 1.3: A schematic showing frequency spacings. Frequencies increase to the right in this diagram. Modes with common radial overtone n are shown as either solid or dashed vertical lines. Both the large and small spacings ($\Delta\nu = \nu_{n+1,\ell} - \nu_{n,\ell}$ and $\delta\nu = \nu_{n,\ell} - \nu_{n-1,\ell+2}$, respectively) are shown. In general, increasing either n or ℓ causes an increase in frequency and the larger the degree of the mode, the lower its observed amplitude.

The spacing parameters can easily be isolated in a calculated oscillation spectra by noting the radial overtones and the degrees of the modes. More important is the physical interpretation of these parameters and what the spacing between observed oscillation periods can tell us about the star.

Physically the large spacing $\Delta\nu$ is the inverse of the time it takes sound to cross the diameter of the star. The sound speed can be approximated as $\sqrt{p/\rho}$ and is dimensionally the same as $\sqrt{GM/R}$. Placing this into Eq. 1.12 shows the large spacing is on the same order as the inverse of the free-fall (or dynamical) timescale and is related to the mean density (M/R^3) of the star. Gabriel et al. (1985) showed from a grid of stellar evolution models that the

large spacing is approximately

$$\Delta\nu = (0.205 \pm 0.011)\left(\frac{GM}{R^3}\right)^{1/2} \text{ Hz} \tag{1.14}$$

with G, M, and R given in SI units. Matthews et al. (1999) rewrote the large spacing in terms of a star's effective temperature T_{eff} and luminosity L to give

$$\Delta\nu = (6.64 \pm 0.36) \times 10^{-16} M^{1/2} T_{\text{eff}}^3 L^{-3/4} \text{ Hz} \tag{1.15}$$

In this form L and M are in solar units and T_{eff} in degrees Kelvin. If a regular frequency spacing is observed in an oscillating star it can be used to determine the star's luminosity independent of other distance determination methods like trigonometric parallax. This method of asteroseismically determining a star's luminosity assumes there is some constraint on the star's mass and a measurement its effective temperature is available.

The wavenumber (Eq. 1.8) of a high-overtone, low-degree mode has essentially no contributions from ℓ near the stellar surface. The potential to probe the deep stellar interior, while at the same time cancelling out the small contributions of ℓ near the stellar surface, motivates the isolation of the small spacing. Computing the frequency difference $\nu_{n,\ell} - \nu_{n-1,\ell+2}$ in Eq. 1.11 shows

$$\delta\nu \propto \int_0^R \frac{1}{r}\frac{dc_s}{dr}dr \tag{1.16}$$

Close to the centre of a star, the leading contribution to the small spacing comes from the $1/r$ factor in the integrand of Eq. 1.16. As a star evolves, its interior composition changes through nuclear burning (increasing the amount of He in the core) and the sound speed gradient, weighted by this $1/r$ term, is sensitive to this evolutionary change. As a star ages, the mean molecular

weight in its core increases causing a decrease in both the local sound speed and in the small spacing. Therefore, the small spacing can be exploited as a diagnostic of stellar age (e.g., Provost 1984, Gough 1987, Christensen-Dalsgaard 1988, and Guenther & Demarque 1997).

Observations of the large and small spacings allow the unique determination of a star's evolutionary status and position on the HR diagram.

1.2 The chemically peculiar A stars

We next discuss a subset of A-type stars that have a number of distinguishing characteristics that strongly influence their pulsation spectra.

The Ap stars are spectroscopically (chemically) peculiar A-type stars. Also known as CP2 stars (Preston, 1974), the class actually ranges from late B to early F spectral type with a temperature range of about $7,000\ \mathrm{K} \lesssim T_{\mathrm{eff}} \lesssim 14,000\ \mathrm{K}$. The peculiarities in these stars are observed as spectral line strength anomalies that are significantly different from the majority of other stars and are interpreted as abundance enhancements or depletions on the stellar surface. The peculiar line strengths correspond to photospheric overabundances up to 10^5 times the corresponding solar value and under abundances down to 10^{-2} times the solar value.

Near the main sequence there are a number of chemically peculiar stars, with the Ap stars making up less than about 10 percent of the bright stars on the main sequence (North et al., 2008). Each group is defined by a specific temperature range, magnetic field strength, spectral line anomalies, and their pulsational properties. As an example, the hotter Ap stars, with tem-

peratures ranging from about 10,000–14,000 K, can exhibit either Si or Hg and Mn peculiarities in their spectra. The Ap Si stars have a detectable magnetic field while the Ap HgMn stars generally do not. The cooler stars with $T_{\rm eff} \lesssim 10,000$ K are classified as Ap SrCrEu stars and show very strong line strengths for the rare earth elements (La to Er) Sr, Cr, and Eu. Both hot and cool Ap stars seem to have weak He lines, if they are present at all. An overview of the Ap class of stars is provided by Wolff (1983) and Kurtz & Martinez (2000).

1.2.1 Magnetic fields, diffusion, & Ap stars

The Ap stars show magnetic fields that appear to be global, predominately dipolar, and have strengths ranging from about 0.3 kG to 30 kG (Landstreet, 1992a). These magnetic fields seem to be connected to the chemical peculiarities and the variability of these stars, both of which will be discussed below. A general discussion of magnetic fields in stars is given by Mathys (1989), Landstreet (1992a; 1992b and 1993), and more recently by Wade (2006).

In the presence of a magnetic field, spectral lines having a wavelength, λ, can show splitting caused by the Zeeman effect. For magnetic field strengths up to a few tens of kG, the separation between the split spectral line components is $\propto \lambda^2 B$ (Landstreet, 1992b). Competing effects like thermal and Doppler broadening of spectral lines means that only a small subset of stars with $B \gtrsim 10$ kG and small projected (rotational) velocities $v \sin(i) \lesssim 10$ km s^{-1} show significant broadening from the Zeeman effect (Landstreet, 1992b). Examples of this average magnetic field modulus determination are given by Mathys et al. (1997).

When Zeeman components are not resolved it is possible to exploit the polarization properties of the magnetically perturbed lines. If a spectral line is observed in both left and right-circularly polarized (LCP and RCP respectively) light, the contribution to the spectral line from each of the unresolved, split components is different. The difference in the position of the mean wavelength of the line in RCP and LCP light provides a measurement of the line-of-sight component of the magnetic field averaged over the stellar disc. This measurement is known as the mean longitudinal field strength and is represented by B_l. For most Ap stars, B_l, and its variation with rotation of the star, are the only magnetic observations available because they are relatively easy to obtain (Landstreet, 1993)—The measurement is most sensitive to modest fields with simple structures and no *a priori* information about the line profile is needed.

B_l varies periodically through rotation phase ϕ as

$$B_l(\phi) \propto B_p \left(\cos\beta \cos i + \sin\beta \sin i \cos\phi\right) \tag{1.17}$$

Here B_p is the polar field strength, assumed to be a centred dipole, i is the angle between the rotation axis and the line of sight, and β is the angle between the rotation and magnetic axis. The zero point of the rotation phase ($\phi = 0$) is defined at the time of magnetic maximum. The geometry of this model, known as the oblique rotator model (Stibbs, 1950), is shown in Fig. 1.4. As the star rotates, the angle from the magnetic pole to the line-of-sight changes, leading to a modulation of B_l with the rotation of the star.

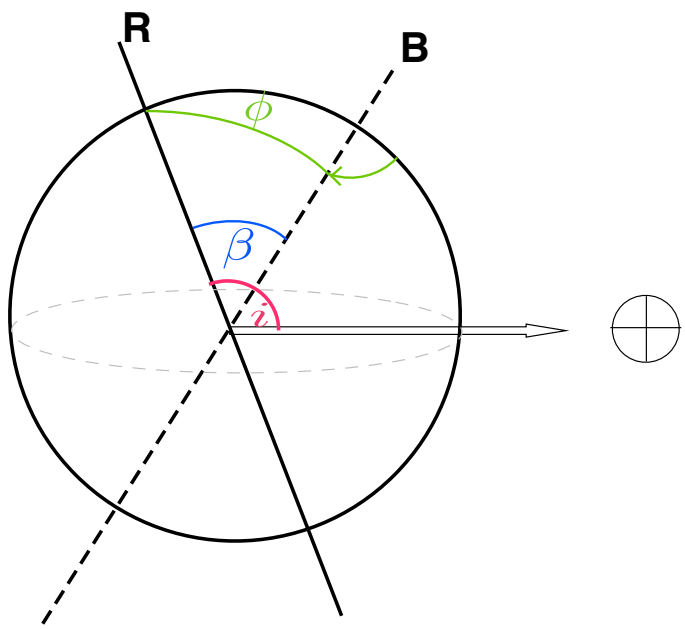

Figure 1.4: A schematic diagram showing the oblique rotator model geometry. The rotation axis and dipole magnetic axis are labelled R and B, respectively. As the star rotates through a phase angle ϕ (the zero point of the phase is at the time of magnetic maximum) an observer (located to the right in the diagram) sees the magnetic field vary in strength. The aspect of the magnetic axis varies because it is inclined to the star's rotation axis by an angle β and to the observer's line-of-sight by an angle i. See the discussion in § 1.2.1 for more details.

If there is a strong field ($\gtrsim$ 1 kG) we may also obtain information about its geometry from the transverse field component. In this case, the central, unsplit, spectral line component will saturate before the split components and the integrated line profile will have a net linear polarization (e.g., Leroy et al., 1993). From this net linear polarization one can, in some cases, obtain

unique values for i, β and B_p defined in Eq. 1.17. The technique that exploits this characteristic of the Zeeman components is known as broadband linear polarization.

The separation of elements through gravitational settling and radiative lifting of some ionic species was used to explain the observed abundance patches of Ap stars as early as the late 1960s and early 1970s (e.g., Michaud, 1970). In principle, any element that is heavier than the surrounding (mainly Hydrogen) mixture will sink under the influence of gravity. Exceptions occur for elements that have absorption lines at the wavelengths near the local flux maximum. In these cases, the elements may be levitated upward toward the stellar surface if the radiative forces are greater than the gravitational force. Once the elements reach an equilibrium position between the gravitational and radiative forces they may accumulate in sufficient amounts, resulting in abundance anomalies at these locations. General reviews of diffusion theory may be found in Vauclair & Vauclair (1982), Michaud & Proffitt (1993) and more recently in Turcotte (2003; 2005).

The element segregation described above depends on a fragile equilibrium. If there are turbulent or convective velocities in the upper atmospheres of these stars that exceed the diffusion velocities of a few cm s^{-1} the abundance anomalies will simply be mixed away (Michaud, 1976). While the main sequence A stars do not have large convective envelopes, the A giants do. This explains why the A-type giants lose their abundance peculiarities. For the diffusion mechanism in these stars to be efficient there must be a stabilizing mechanism against turbulence. It is believed that the magnetic field provides this stabilizing mechanism (e.g., Gough & Tayler 1966 and Balmforth et al.

2001). A magnetic field also influences the distribution of elements, causing horizontally distributed abundances on the stellar surface near regions of horizontal magnetic field lines (Michaud et al., 1981). The effect of a magnetic field on element diffusion is described in Babel & Michaud (1991) and Michaud (1996). For a recent discussion on the spectroscopic determination of abundance variations with depth in Ap star atmospheres see Ryabchikova (2008).

1.2.2 Stellar seismology & Ap stars

Before the late 1970s observations of variable stars did not show p-modes with periodicities and frequency spacings like those observed in the Sun. This changed when Kurtz (1978, 1982) discovered the rapidly oscillating Ap (roAp) stars. These stars are variable both photometrically and spectroscopically, have long term variability (with periods on the order of the stellar rotation period; ranging from days to years), and also show rapid oscillations with periods ranging from about 5 to 30 minutes. The amplitudes of the oscillations are generally small, with semi-amplitudes being less than about 10 mmag when seen through a Johnson B filter (Johnson & Morgan, 1953). The roAp stars tend to be the coolest members of the Ap class (usually showing enhancements in one or all of Sr, Cr, and Eu) and have masses of less than about 3.0 $M_{\odot}$. The approximate position of the roAp stars on the Hertzsprung-Russell (HR) diagram is shown in Fig. 1.5. Some of these stars are multi-periodic and exhibit asymptotic (see § 1.1.1) spacings indicative of the large spacing. While some oscillate with periods that seem to be stable over many years, other members of the class may pulsate with only

one periodicity or have frequencies that vary over a timescale as short as a few days. To date there are about 40 known roAp stars. Some detailed reviews of roAp stars are provided by Kurtz (1990), Matthews (1991), Kurtz & Martinez (2000) and Kochukhov (2008).

As Ap stars rotate they show both photometric and magnetic field strength variations. The magnetic fields of the Ap stars seem to play a critical role in both the micro- and macroscopic physics that influences these unique stellar structures. In the outer layers of the Ap stars the strong magnetic field produces pressures that are greater than the local gas pressure and it is expected that this results in an observable effect on the rapid oscillations of the roAp stars (see, e.g., Cunha 2007). In fact, the magnetic field influences the observed oscillation spectrum of these stars in a number of ways. One of which is a 'point-of-view' effect where the observed frequencies are split into multiple components (akin to the Zeeman splitting of spectral lines) spaced by the rotation period of the star. Another is a physical perturbation to the displacements of the rapidly oscillating medium, producing frequency shifts (and spacings) that cannot be predicted by models that do not include magnetic fields. These two examples are discussed below, with more details on the latter of these effects being provided in chapter 4.

It was noted in § 1.2 and 1.2.1 that the magnetic field and the accumulated patches of certain elements on the surface of an Ap star were linked. As an Ap star rotates, the magnetic field strength varies as the magnetic pole comes in-and-out of an observer's field-of-view. The spotty abundance patches on the star's surface tend to lower the stellar flux, causing a decrease in the light an observer sees, while the spot (or a portion of it) is in view. Interestingly,

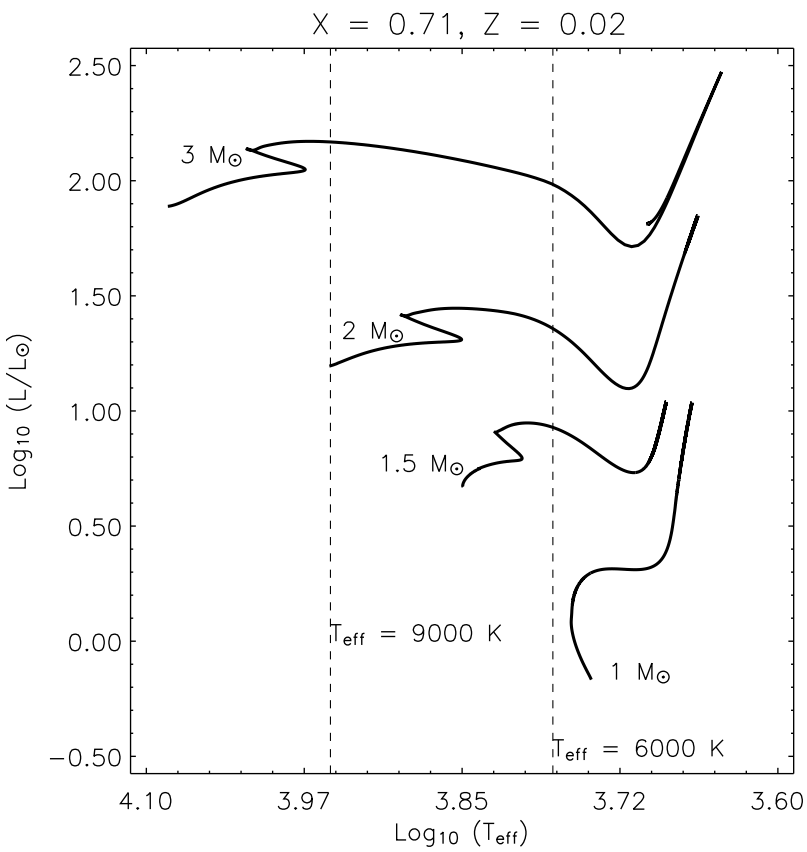

Figure 1.5: A theoretical HR diagram showing the approximate location of the roAp stars. Solid lines are stellar evolution tracks calculated with the Yale Rotating Evolution Code (YREC) described in § 4.1. Vertical dashed lines show the upper and lower bounds of effective temperature ($6,000$ K $\lesssim T_{\rm eff} \lesssim 9,000$ K) where the roAp phenomenon occurs. The roAp stars are main-sequence (stars that burn Hydrogen in their cores) variables and have a mass range of 1.3 $M_\odot \lesssim M \lesssim 3.0$ $M_\odot$.

the amplitude of the rapid stellar oscillations of the roAp stars is generally at maximum during this minimum of the mean light of the star. Each of the long-term variability (or mean light variations), the rapid variability, and the magnetic field strength are related to each other, and are functions of rotation phase. Figure 1.6 compares the variation in the amplitude of the rapid pulsation ($\sim$ 6 minute period) to that of the magnetic field strength as a function of rotation phase (referenced to a rotation period of about 12.5 days) for the roAp HR 1217. The pulsation amplitude of HR 1217 is in phase with the magnetic field. (Later, in Fig. 3.6 of § 3.3, we show that the mean light amplitude; associated with the spotty abundance patches, and the pulsation amplitudes vary in anti-phase as HR 1217 rotates.) The modulation of the magnetic field strength is described well by the oblique *rotator* model of Stibbs (1950, see § 1.2.1). Following this model, Kurtz (1982) suggested that the amplitudes of the rapid variations may be modulated in a similar way, through what is now called the oblique *pulsator* model.

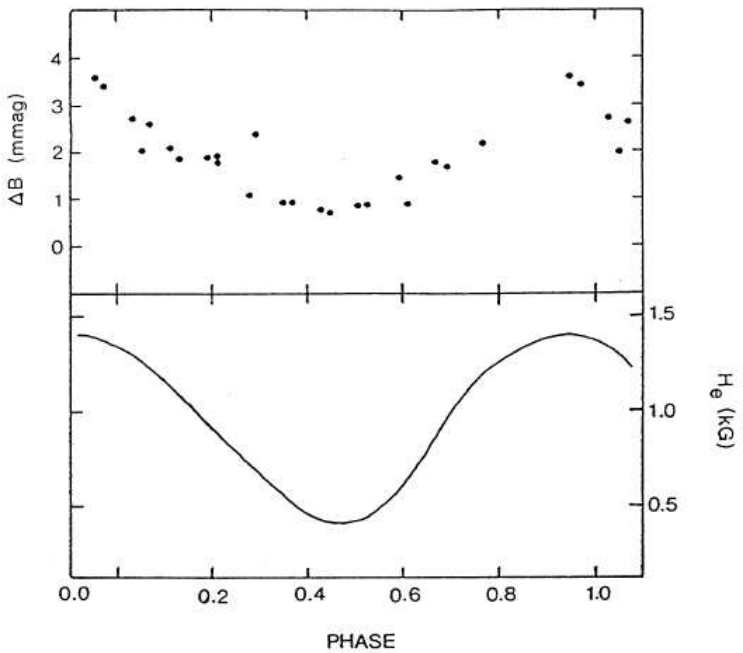

Figure 1.6: (Upper panel) The variation in the pulsation amplitude of HR 1217 (through a B filter) as a function of the rotation phase (referenced to a rotation period of about 12.5 days) of the star. The magnetic field variation defined by B_l (shown as H $_e$ in the figure) in § 1.2.1 as a function of rotation phase is presented in the lower panel. The pulsations ($\sim$ 6 minute period) have amplitudes that vary synchronously with the magnetic field strength. Pulsation data and magnetic field data were taken from Kurtz (1982) and Preston (1972) respectively. This figure was obtained with permission from Matthews (1991).

In this model, the pulsation axis of the star is aligned with the magnetic axis and both are inclined to the rotation axis. As the star rotates the aspect of the pulsation and magnetic axis varies, modulating the pulsation amplitudes. The geometry is the same as that shown in Fig. 1.4 with the magnetic and pulsation axis being the same. Consider an axisymmetric (m

$= 0$) pulsation mode oscillating with frequency ν. Kurtz (1982) showed the luminosity varies with rotation like

$$\frac{\Delta L}{L} \propto P_\ell^m(\cos\alpha)\ \cos\left[\nu t + \varphi_p\right] \tag{1.18}$$

where P_ℓ^m is the associated Legendre polynomial, φ_p is an arbitrary oscillation phase, and α is the rotation phase angle zeroed at the time of pulsation or magnetic maximum. For a dipole pulsation mode $\ell = 1$ and the Legendre polynomial is equal to $\cos\alpha$. Equation 1.18 may be expanded as

$$\frac{\Delta L}{L} \approx A_0 \cos\left(\nu t + \varphi_p\right) + A_1 \left[\cos\left(\{\nu + \Omega\}t + \varphi_p\right) + \cos\left(\{\nu - \Omega\}t + \varphi_p\right)\right] \tag{1.19}$$

where α was replaced by the product of the rotation rate and time, Ωt, and the two amplitude functions are defined as $A_0 = \cos i \cos\beta$ and $A_1 = (\sin i \sin\beta)/2$. This model predicts that a single dipole mode is split into a triplet exactly spaced by the rotation period of the star. Generally, a mode with degree ℓ is split into $2\ell + 1$ frequencies. The roAp stars do show this fine structure in their oscillation spectra (see, e.g., chapter 3). The shortcoming of this simple model put forth by Kurtz (1982) is that it does not explain the amplitude asymmetry between the split frequency components observed in some roAp stars. Equation 1.19 shows us that the split frequencies should have the same amplitude A_1. The equal amplitudes of the rotationally split components is not observed in the Ap stars' oscillation spectra. This is resolved if the effects of both rotation and the magnetic field on the eigenfunctions (through the Coriolis and Lorentz forces) are taken into account. The most recent contribution to the oblique pulsator model comes from Bigot & Dziembowski (2002). They used a non-perturbative approach

to show that the centrifugal force is important in determining the frequency splitting while the Coriolis force is dominant in determining the amplitude asymmetries. Those authors also show that the pulsation, rotation, and magnetic axes are all inclined to each other, i.e., the magnetic and pulsation axis are not necessarily aligned. The geometry of roAp oscillations is reviewed by Cunha (2005).

The effects of the strong magnetic field on the rapidly varying normal modes (i.e., those eigenfrequencies calculated in the case of no magnetic field or rotation) will be discussed in chapter 4. Recent theoretical reviews discussing the interaction between the magnetic field and the pulsation frequencies are given by Cunha (2007), Saio (2008) and Shibahashi (2008). In the interior of Ap stars, the gas pressure dominates the magnetic pressures. It is only in a small surface layer ($\gtrsim 0.95$ r/R) where perturbations become significant enough to strongly modify the motions of the local plasma. With this in mind, a number of authors have attempted to model the effect of a strong magnetic field on high overtone stellar pulsations that have their largest amplitudes near the stellar surface. Roberts & Soward (1983) described an analytic matching procedure used to link the surface effects to those of pulsations in the stellar interior where the magnetic field can be neglected. Numerical experiments by Campbell & Papaloizou (1986) expanded upon the work of Roberts & Soward (1983) and paved the way for the modern numerical simulations of Dziembowski & Goode (1996), Cunha & Gough (2000), Saio & Gautschy (2004), and Saio (2005). In general, the magnetic field modifies the surface of an Ap star to such a high degree that a single spherical harmonic cannot describe the displacement, which has a significant

horizontal component. Each of the investigations above recognize that in the deep interior of the star, the magnetic and acoustic components of the displacement decouple and the magnetic component dissipates as it propagates inward, draining energy from the pulsation. The above studies conclude that there is a significant observable effect on the oscillation spectrum of an Ap star; however, there are some differences in the details. Cunha & Gough (2000) and Saio & Gautschy (2004), for example, notice a cyclic variation (or shift) to some frequencies in the calculated eigenspectrum. They differ mainly in the amplitude of that shift, with the method of Cunha & Gough (2000) giving larger shifts in frequency over the method used by Saio & Gautschy (2004) by about 30%. In this study, we use the method of Cunha & Gough (2000) to calculate the perturbations to the acoustic modes caused by the presence of a magnetic field. The method is described in § 4.3 and has been successfully tested against observations of HR 1217 (discussed in the following section).

Finally, it should be noted that a number of authors have attempted to modify stellar evolution models in such a way as to excite the frequencies that are observed in roAp stars. Recent efforts include modifications to the atmospheric temperature stratification (Gautschy et al., 1998) to reflect pulsation modes, the inclusion of helium gradients and convective suppression of the stellar envelope (Balmforth et al., 2001), a magnetic and radiative damping (non-adiabatic) study of oscillations Saio (2005), and the inclusion of the effects of stellar winds and metal gradients in the stellar envelope (Théado et al. 2005,2009). While there have been some successes in exciting the high overtone modes in Ap stars, none of the studies is able to provide

a globally applicable excitation mechanism for these stars. In this study we focus solely on adiabatic results; i.e, we ignore excitation, so that we can, for the first time, attempt to constrain the physical parameters of a roAp star using a large grid of magnetically perturbed pulsation models.

1.3 The roAp star HR 1217

This thesis focuses on observations and models of the roAp star HR 1217 (a.k.a HD 24712; DO Eri; B = 6.3 mag; δ = -12° 5′ 56.″78; α = 03 hr 55 min 16.^{s}128). This was one of the first Ap stars to be identified as a roAp star by Kurtz (1982) and has since become one of the most studied. Recently, high-quality data has provided information about the abundance, magnetic and photometric characteristics of HR 1217. The most recent photometric data is analyzed in this thesis and is, in many ways, an unrivalled photometric data set on HR 1217 (chapter 3). A review of the other recent observations of HR 1217 is presented below.

The magnetic field of HR 1217 was measured by Bagnulo et al. (1995). They were able to model the magnetic field geometry for HR 1217 and give values of 137°, 150°, and 3.9 kG for i, β and B_p respectively. Estimated uncertainties on the above angular measurements are $\approx$ 2–3° and the uncertainly of the polar field strength is about 5%. The mean longitudinal field, B_l, for HR 1217 varies between $\sim$ 0.5 and 1.5 kG (Preston, 1972), and is illustrated in the lower panel of Fig. 1.6. Kochukhov & Wade (2007) discuss current magnetic and rotation properties of HR 1217. The most recent magnetic field measurements are given by Lüftinger et al. (2008). They measure

a magnetic field variation of 2.2 to 4.4 kG (no uncertainty given) based on a Doppler imaging analysis.

The first thorough abundance analysis of HR 1217 was performed by Ryabchikova et al. (1997). Their results are consistent with the idea that the abundance enhancements on the surfaces of these stars are patchy. In particular they find the mean chemical abundances vary with the magnetic and rotational phase of the star. When compared to solar values, the rare earth elements are the most overabundant and show the largest variation over the rotation of the star. The iron peak elements, on the other hand, tend to be under abundant. An estimate of the metal content of HR 1217 based on the work of Ryabchikova et al. (1997) is presented in § 4.1.1.

The first global photometric campaign to observe HR 1217 was headed by Don Kurtz and Jaymie Matthews (Kurtz et al., 1989). The goal of those observations was to achieve as much continuous coverage of the star as possible so that gaps in their data would not affect their frequency analysis. They achieved a 29% duty cycle (compare this to the 95% duty cycle obtained in this work; see chapter 3) with 325 hrs of data spanning a 46-day period. The results of the campaign are shown schematically in the top panel of Fig. 1.7. There exists an ambiguity in identifying $\Delta\nu$ from the observed frequency spacing (§ 1.1.1). If the modes are alternating between even and odd ℓ values we would expect to see a $\Delta\nu \sim 68$ μHz. In fact, the alternating spacing of 33 and 34 μHz is consistent with models having alternating even and odd modes (e.g., chapter 4). If the modes were all even or odd, we would expect that the spacing between adjacent modes would remain the same. Each of the frequencies in Fig. 1.7 are actually multiplets having fre-

quencies spaced by approximately 0.9 μHz (the rotational frequency of the star). The unexpected frequency spacing ($\sim$ 50 μHz) between the last two frequencies (between $\sim$ 2750–2800 μHz) is not consistent with asymptotic theory and the observed large spacings. The gap in the frequency spectrum of HR 1217 observed by Kurtz et al. (1989) is usually said to be a "missing mode".

Almost a decade after Kurtz et al. (1989) released their results the true large spacing value of $\sim$ 68 μHz was unambiguously determined. Using Eq. 1.15, Matthews et al. (1999) were able to calculate a parallax for HR 1217 based on an inferred large spacing of 68 μHz. Their predicted parallax of $\pi = 19.23 \pm 0.54$ mas was shown to be consistent with the recent Hipparcos parallax (Perryman et al., 1997) of $\pi = 20.41 \pm 0.84$ mas (§ 4.1.1).

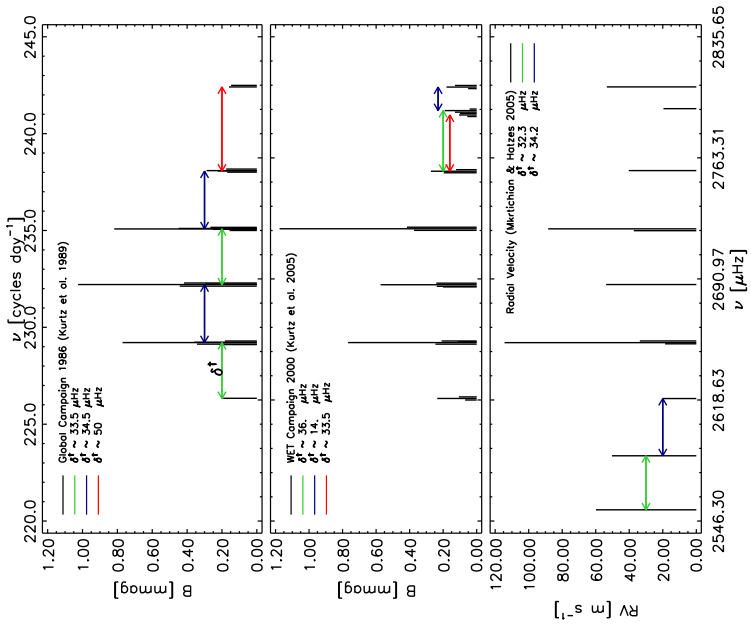

Figure 1.7: Schematic amplitude spectra of HR 1217 oscillations from previous observations. The upper panel shows the frequencies identified in the 1986 global observation campaign of HR 1217 (Kurtz et al., 1989). Frequencies are regularly spaced (see discussion on asymptotic spacing in § 1.1), alternating between ~ 33.5 (green) and 34.5 (blue) μHz. The exception to the regular spacing is a spacing of ~ 50 μHz represented by a red line in the top panel. The middle panel gives the frequencies found in the more recent 2000 global campaign (Kurtz et al., 2005). This campaign uncovered a "missing" frequency near 2800 μHz that fit with the previously identified asymptotic spacing of ~ 33.5 μHz (represented by the red line in the middle panel). In addition to this discovery, Kurtz et al. (2005) discovered a frequency spacing of ~ 2.5 μHz (the difference between the red and green lines) that is consistent with a second order asymptotic spacing for a main sequence A star. The furthest frequency spacing (blue line) of ~ 14 μHz is inconsistent with the observed asymptotic spacings and may be explained by magnetic perturbations (see Cunha 2001 and § 4.3). The lower panel shows the results from recent spectroscopic observations of Mkrtichian & Hatzes (2005). Those authors recovered the previously observed periodicities of HR 1217 and suggested new frequencies with spacings of ~ 34 (blue line) and 32 (green line) μHz may exist at the low frequency end of the oscillation spectrum.

A success in the interpretation of the frequency spacings of HR 1217 was provided by Cunha (2001). She predicted that magnetic damping could be the cause of the missing frequency in the 1986 data set. She also showed that some frequencies may be shifted by approximately 10–20 μHz because of magnetic field effects (Cunha & Gough 2000, and Cunha 2001; further discussion is provided in § 4.3). In 2000, HR 1217 was selected to be observed in another global campaign (organized by the Whole Earth Telescope, WET; see Kleinman et al. 1996 and Kurtz & Martinez 2000) and a preliminary data reduction for this data set did find the missing frequency at $\sim$ 2795 μHz (Kurtz et al., 2002). Although it was long suspected, this was the first time it was shown that the influence of the magnetic field along with stellar rotation and surface chemical gradients plays a critical role in the pulsation characteristics of the roAp stars. These unique properties of the roAp stars could allow us the opportunity to model the *magneto-acoustic* pulsation modes and study in detail an environment that is significantly different to that found in other stars, including the Sun.

The full analysis of the global WET campaign data (collected in 2000) is given in Kurtz et al. (2005). Their results are drawn schematically in the middle panel of Fig. 1.7. They collected at total of 35 days of data with a duty cycle of 36% and reached an amplitude precision of 14 μmag (one of the most precise ground based photometric studies to date). Along with the discovery of the missing mode, they also discovered a closely spaced frequency grouping of about 2.5 μHz that could not be explained by the oblique pulsator model. This "small" spacing is on the order of magnitude that one would expect for a second order asymptotic spacing discussed in § 1.1.1 for a main

sequence A star. This could be the first time such a small spacing was observed in a star other than the Sun. That being said, the diagnostic power of the small separation may be limited because the magnetic perturbations to the frequencies may be of the same order, or larger than, the small spacing (Dziembowski & Goode, 1996). This is further illustrated in § 4.3.

A recent radial velocity study by Mkrtichian & Hatzes (2005) has also uncovered some new frequencies (shown in the lower panel of Fig. 1.7). Those observations covered about a month of time (from 22 Dec, 1997 to 30 Jan 1998 with two additional days in early Feb 1998) giving about 5 hours of observations per night for 9 nights over the month. They find new frequencies at ~ 2553 and 2585 μHz. These frequencies were only identified in a subset of the authors' data and are, admittedly, of low significance and of low frequency resolution.

1.4 Thesis goals

Progress in the study of the Ap and roAp stars has been steadily increasing over the past few years with the development of new observational and theoretical tools. In this thesis we attempt to tie together the most recent photometric observations (chapter 3) on the roAp star HR 1217 (obtained by the *MOST* satellite, which is described in chapter 2) to theoretical stellar evolution and pulsation models that include the effects of a magnetic field (chapter 4).

The data collected by the *MOST* mission has obtained both ultra-high precision and time sampling that has never been achieved before, on this

target (HR 1217), and for a vast majority of asteroseimic targets. With this data in hand, we have the following observational goals and questions:

1. It has been known since the early 1980s that HR 1217 is a multiperiodic variable with near equally spaced modes, alternating between $\sim$ 33.5 and 34.5 μHz. The most recent confirmation of this was the analysis of Whole Earth Telescope data by Kurtz et al. (2005), who achieved a duty cycle of 36% and reached an unprecedented precision of 14 μmag for a ground-based photometric study. We will be able to unambiguously identify the spacings in the *MOST* data because of its near continuous coverage and ultra-high precision. Are the already identified periodicities constant over time for all observations on HR 1217, or do they vary over time, pointing to a selective mode damping mechanism or some nonlinear interaction?

2. The strange, apparently non-asymptotic, spacing that was observed between the highest two frequencies in HR 1217 remained a mystery until the recent results of Kurtz et al. (2005, 2002). Those authors identified a previously unidentified frequency near 2790 μHz that could only be explained as a magnetic perturbation Cunha (2001). Explaining that frequency (or lack of that frequency) has driven the theory of roAp star oscillations for more than two decades. Is this frequency identified in the *MOST* data on HR 1217 and is it stable since the last observations of Kurtz et al. (2005)?

3. We expect to observe a number of new periodicities in the data because of the high level of photometric precision and the near contiguous data

sampling of the *MOST* satellite. Can new periodicities be identified and, if so, can they be used to constrain the physics of this magnetic pulsator?

4. A recent spectroscopic study on HR 1217 by Mkrtichian & Hatzes (2005) identified new frequencies at $\sim$ 2553 and 2585 μHz. These frequencies are interesting because they approximately match the alternating $\sim$ 33.5 and 34.5 μHz pattern previously observed in HR 1217, but were not identified in the photometry of Kurtz et al. (2005). Does the *MOST* data uncover those potentially new periodicities?

5. In order to determine the reliability and uniqueness of the periodicities in a multiperiodic variable, we need to develop tools that can test the precision and resolution of our data set. Techniques we have developed for other *MOST* targets will be applied to the HR 1217 data. The resolution of our data set and the assertion that closely spaced frequencies are spaced by the rotation rate of the star will be tested.

A massive grid of A star evolution and pulsation models (chapter 4) has been constructed for this research project. The magnetically perturbed pulsation modes are calculated and are matched to the observed frequencies of HR 1217 (chapter 5) for the first time. The scope of this model grid eclipses any previous attempts to constrain the properties of HR 1217, or any other roAp star. The following theoretical questions will be answered in this thesis:

1. For the first time, a realistic stellar model grid, covering a vast swath of parameter space appropriate for matching the observable character-

istics of HR 1217, is constructed that includes the magnetic perturbations to the calculated normal modes of the models. Is the magnetic perturbation a necessary ingredient for the matching of a model to the observations?

2. Are the spacings observed by the *MOST* mission reproducible with the physics used to construct our model grid?

3. How are models matched to the observations and what are the sensitivities of those matching procedures?

4. Is there a preference as to what angular degree ℓ is matched to an observed frequency?

5. We test the calculations of the pulsation modes in our grid by using a new method developed by Kobayashi (2007) for the calculation of normal modes in a geophysical context.

The methodology and the results of the observational and theoretical analysis of the HR 1217 observations from the *MOST* mission are outlined and discussed throughout the following chapters. The results are summarized in chapter 6 of this thesis.

Chapter 2

The *MOST* mission: Data reduction techniques

The HR 1217 data presented in chapter 3 of this thesis was collected by the *MOST* satellite and analyzed using techniques developed over a period of about 5 years by the *MOST* team and its collaborators; including the author of this thesis. In this chapter we give an overview of the *MOST* mission, the photometric and time-series methods that are relevant to the HR 1217 data reduction, and finish with some examples of other *MOST* results that used the described data analysis methods.

2.1 An overview of the *MOST* mission

The Microvariability & Oscillations of STars (*MOST*) mission is Canada's first space telescope[3]. Launched into a sun-synchronous orbit at an altitude of $\sim$ 820 km (orbital period = 101.413 min) on 30 June 2003, the micro-satellite (weighing about 54 kg with dimensions similar to that of a typical suitcase) functions as an ultra-precise light meter, that routinely obtains near

[3]Being a Canadian space mission it is also appropriate that the acronym *MOST* works equally well in French ... Microvariabilité et Oscillations STellaire

continuous[4], micro-magnitude, photometric measurements of oscillating stars and extrasolar planets.

The instrument is a 15/17.3 cm Rumak-Maksutov telescope that directs light through a custom broadband filter, covering a wavelength range of 350–700 nm,[5] to two CCDs: One used for tracking and the other for scientific measurements. The experiment is outlined in Matthews et al. (2000), with more technical details provided by Walker et al. (2003).

Originally, *MOST* produced scientific data in Fabry and direct imaging modes. In the Fabry mode, an image of the telescope entrance pupil (illuminated by starlight) is projected onto the science CCD, spreading light over ~ 1500 pixels so as to limit tracking jitter and the effect of individual pixel variations (caused, for example, by radiation). The direct imaging mode provides in-focus photometry of fainter ($\gtrsim 6$ mag) stars on the science CCD. The satellite, through software updates, was eventually (after about a year of operation) able to achieve sub-arcsecond pointing, allowing scientific data to be gathered on guide stars from the tracking CCD, greatly increasing the scientific output of the mission. *MOST* functioned in this way until early 2006, when the tracking CCD suddenly failed. It is suspected that a particle hit damaged the CCD. Since that time, both science and tracking are performed on the science CCD.

The first science results from *MOST* were published by Matthews et al.

[4] *MOST* has a Continuous Viewing Zone that ranges in declination from $+36° \geq \delta \geq -18°$. Stars in this declination range can, at most, be viewed continuously for up to 60 days.

[5] A Johnson B filter (Johnson & Morgan, 1953) is centred at about 445 nm with a full width at half maximum of ~ 94 nm (see Binney & Merrifield 1998)

(2004) and recent reviews of the mission results are given by Matthews (2007) and Walker (2008). They clearly illustrate the breadth of the scientific accomplishments of the *MOST* instrument to date. Data on binary stars, rapidly rotating stars, stars with spots, magnetic stars, exoplanets, and even stable stars are providing new insights into exotic and, in many cases, otherwise untestable physical scenarios. With more than 1000 stars observed—about a quarter of which show detectable light variations — the scientific discoveries are on-going.

2.2 Photometry & time-series analysis

Reducing *MOST* photometry is a challenging task because of stray-light contamination caused by Earth shine illuminating the CCDs. This parasitic addition to the stellar signal depends on the orbital phase and orientation of the satellite and varies with season. From one orbital period ($\sim$ 101 min) to another, this contaminant changes its character, making it very difficult to model.

The result is a superposition of orbital components ($\sim$ 14 cycles day^{-1}), along with their harmonics and aliases, and the stellar signal in the Fourier amplitude spectra (discussed below) of a target's light curve. Methods have evolved since the launch of *MOST* to combat the stray-light effect. These are discussed in detail in Rowe et al. (2006b, 2006c), Reegen et al. (2006), and Rowe (2008). Typical photometric data techniques such as sky background removal (estimated from the dimmest $\sim$ 200 pixels), flat-fielding, and PSF modelling (using $\sim$ 150 of the brightest pixels) are also discussed in those

papers. Photometric errors are estimated from Poisson statistics and are described, for example, in Everett & Howell (2001).

The asteroseismic results are determined from relative amplitude fluctuations in the star's light curve. Absolute magnitude determinations are not necessary, so limiting the stray-light contribution to the data is more important than applying mean corrections to the counts. In the work presented in this thesis the stray-light was suppressed by subtracting a smoothed profile created by phasing the data over a number of satellite orbits (see, e.g., Rucinski et al. 2004 and Rowe et al. 2006b). The larger the number of orbital bins used to find the correction, the less aggressive is the reduction of the orbital signal and its harmonics. This is because the mean stray-light contribution may not well represent the contribution from one orbit to another. By finding the correction to data phased over a small number of satellite orbital periods, we remove orbital signal averaged over shorter timescales, essentially over-smoothing the orbital component. The main advantage of this method is that no prior information about the structure of the orbital contamination is assumed. Any remaining long term trends can be removed by either subtracting a low-order polynomial or a spline fit to binned data. The application of this method is further discussed in § 3.1 (see Fig. 3.1 for an example of the stray-light contamination to the HR 1217 light curve).

The frequency analysis of the reduced time-series is carried out using CAPER[6](Cameron et al., 2006). CAPER is a collection of Fortran driver routines that use a Discrete Fourier Transform (DFT) as a frequency and amplitude estimation tool and nonlinear least squares fitting to refine the

[6]Controlled or Automated Period Estimation and Refinement

identified parameters. The software package has been used in a number of recent publications (Walker et al. 2005, Saio et al. 2006, Cameron et al. 2006, King et al. 2006, Saio et al. 2007 and Cameron et al. 2008) and follows the same reduction philosophy as the popular, and time-tested, time-series analysis packages Period98 (Sperl, 1998) and Period04 (Lenz & Breger, 2005).

For a time-series of length T, the amplitude spectrum (calculated from the DFT) is defined by

$$\mathbb{A}_n(\nu) = \frac{2}{T}\sqrt{a_n^2 + b_n^2} \tag{2.1}$$

where a_n and b_n are the imaginary and real parts of the Fourier transform and are calculated from

$$a_n = \sum_{j=1}^{T} f(t_j)\sin(2\pi\nu t_j) \text{ and } b_n = \sum_{j=1}^{T} f(t_j)\cos(2\pi\nu t_j) \tag{2.2}$$

In these expressions $f(t_j)$ is the magnitude (or flux value) at time t_j and ν is the current frequency of interest. The amplitude spectrum is calculated efficiently over a range of ν values using the algorithm proposed by Kurtz (1985). This algorithm is a modified version of the Deeming algorithm for computing the DFT of data with sampling gaps (Deeming 1975; also see Matthews & Wehlau 1985). Once the largest peak in the amplitude spectrum is identified, its phase can be calculated as $\phi = \arctan(a_n/b_n)$.

The set of parameters (ν, A, ϕ) obtained from the DFT are next refined by nonlinear least squares fitting using the Levenberg-Marquardt method (Press et al., 1992)[7] which minimizes χ^2 between a fitting function and the data. A sinusoidal fitting function of the form

$$F_{fit}(t) = A\sin(2\pi\nu t + \phi) \tag{2.3}$$

[7]The name of the Numerical Recipes routine used by CAPER is mrqmin

is used by CAPER.

Once F_{fit} is optimized, it is subtracted from the original data set. A Fourier spectrum of the residuals is calculated and a new parameter set is identified. These new parameters, in conjunction with the previous set(s), are re-fitted to the original time-series and the process is iterated to a predefined stopping criterion, usually set as a signal-to-noise (S/N) threshold. The fit is improved at each step based on the original data until there are no longer any meaningful changes in the residuals from the fit.

A S/N threshold of ~ 3.5 is commonly used in the asteroseismic community as a lower limit to the significance of a detectable peak in the DFT. Peaks in the DFT with a S/N greater than this represent a detection $\gtrsim 2.5\sigma$ (Breger et al. 1993 and Kuschnig et al. 1997). This is adopted as a lower limit to the significance of the extracted periodicities in this work. The S/N for each recovered signal component is calculated (before prewhitening[8] that component) as the mean amplitude in a box around the identified peak, sigma clipped until the mean converges. The clipping is done so that additional high amplitude peaks near the identified frequency do not skew the local mean amplitude (noise) value. This method of calculating the S/N has two potential sources of uncertainty: 1. The width of the box used to average the amplitude spectrum (the noise) and 2. Uncertainties in the fitted amplitude. The uncertainty in the noise calculation is estimated by varying the width of the averaging box in small steps and then calculating an average of each noise value along with a standard error on that average noise. Once

[8]Prewhitening is a term used to describe the subtraction of a sinusoidal function from the data.

amplitude uncertainties are assessed from a bootstrap analysis (described below), we combine both to arrive at the final uncertainty in S/N.

The uncertainties we calculate for time-series parameters derived from nonlinear least-squares methods depend on the noise of the data (which may be a combination of instrumental and random processes) and on the time sampling. It is also known that fitted phase and frequency parameters are correlated, leading to underestimated uncertainties in these parameters when calculated from a covariance matrix (see, e.g., Montgomery & O'Donoghue 1999). A bootstrap analysis is an ideal way to assess the uncertainties in fitted parameters. The procedure has recently been used in a number of *MOST* applications (Walker et al. 2005, Saio et al. 2006, Cameron et al. 2006, Rowe et al. 2006a, Gruberbauer et al. 2007, Saio et al. 2007, Cameron et al. 2008, Rowe 2008, Rowe et al. 2008a, and Rowe et al. 2008b) and was used by Clement et al. (1992) to estimate the uncertainties in Fourier parameters they derived for RR Lyrae stars.

The bootstrap (see Wall & Jenkins 2003) produces a distribution for each calculated parameter by constructing a large number of light curves (usually $> 10,000$) from the original data. No assumptions need to be made about noise properties of the data and individual photometric errors are not needed. Each new light curve is assembled by randomly selecting N points from the original light curve (also containing N points) with the possibility of replacement. In this way, the new synthetic light curves preserve the noise properties of the original data. The fit procedure is repeated for each new light curve, eventually building distributions in each of the fit parameters.

Recently, Breger (2007) discussed the difference between frequency resolu-

tion and the precision of fit parameters to time-series data. Traditionally one assigns a frequency resolution as T^{-1}, also known as the Rayleigh criterion, where T is the length of the observing run. Loumos & Deeming (1978) suggests an upper limit of 1.5 T^{-1} be used when extracting peaks directly from the amplitude spectrum. This roughly corresponds to the spacing between the main peak of the window function[9] and the peak of its first sidelobe. Lower, and arguably more realistic, estimates are used by Kurtz (1981), who estimates frequency resolution as 0.5 T^{-1} (approximately the half-width at half-maximum of a peak in the amplitude spectrum), and by Kallinger et al. (2008b), who suggest $\sim$ 0.25 T^{-1} can be used based on a large number of simulated data sets. Ultimately, the resolution of frequencies in Fourier space is a function of S/N (or significance) of each individual peak; see, for example, Kallinger et al. (2008b), and the above criteria are only estimates used as an average frequency resolution for all frequencies of a given data set. The precision of fitted parameters, on the other hand, can be estimated by refitting identified parameters to a large number of data sets created by sampling the fitted function in the same way as the data and adding random, normally distributed noise. This Monte Carlo procedure is used, for example, in Period04 (Lenz & Breger, 2005).

A bootstrap analysis differs from such a Monte Carlo procedure in that there are no assumptions made about the noise of our re-sampled data sets (we only use the data) and that the frequency resolution of our data sets can be estimated because the windowing (determined from the temporal sampling

[9]The window function of the data is estimated as the DFT of a noise free sinusoid, sampled in the same way as the data, and varying at a period of interest.

of the data) of each of the re-sampled data sets is randomly changed. Thus, the uncertainties on each of the fitted parameters take into account both the inherent noise of the data and the sampling of the data as well. Put another way, the robustness of our fit parameters to the variations in the data (due to any source) is estimated.

2.3 Applications of CAPER to other *MOST* science

The following sections review a number of published examples of *MOST* observations that use the reduction methods described above, and that were used for the reduction of the HR 1217 observations collected by *MOST*. (In particular, each subsection outlines the results of a Fourier analysis using the CAPER software and a combined bootstrapping error analysis.) The results for the roAp star HD 134214 and the B supergiant HD 163899 are summarized and a more detailed frequency analysis of the slowly pulsating Be (SPBe) stars HD 127756 and HD 217543 is presented. Background information and a more thorough physical interpretation of these results are found in the references provided. Although the following analyses are common to those undertaken in this thesis, the results are independent of this work and reader may wish to proceed to the analysis of the HR 1217 data in chapter 3.

2.3.1 The roAp star HD 134214

The roAp star HD 134214 was observed by *MOST* as a trial Direct Imaging target on 1 May 2006 and the results were published by Cameron et al. (2006). The star was in one of two target fields observed during each *MOST* satellite orbit (period = 101.413 min), so data were collected $\sim 47\%$ of the observing time. In total there were 505 measurements spanning a 10.27 hrs base-line. HD 134214 was shown to be monoperiodic and oscillating at a frequency of $2948.97 \pm 0.55\ \mu$Hz. This is consistent with earlier ground based photometric campaigns (e.g. Kreidl et al. 1994).

Recent results by Kurtz et al. (2006) suggest that HD 134214 is oscillating spectroscopically in up to 6 modes. Our observations can rule out additional photometric oscillations at a 2σ detection level of 0.36 mmag, based on S/N estimations described in § 2.2. Our estimated DFT noise level of ~ 0.12 mmag for 10 hours of observations with *MOST* is comparable to that obtained by Kreidl et al. (1994) based on about 56 hours of photometry from four observatories over about 4 months. The excitation and selection of pulsation modes in roAp stars is an open question. In the case of HD 134214, there are several avenues to be explored with respect to the additional modes seen spectroscopically: 1. Is it a case of radial velocities of certain elements and ionization stages being more sensitive to degrees of higher ℓ? 2. If the sensitivity of the photometry can be improved sufficiently, will these modes also appear? 3. Is the broadband photometry just averaging over too wide an extent of the pulsating atmosphere? or 4. Might there be new physics in the upper atmospheres of (some) roAp stars to account for the differences observed?

Kurtz et al. (2007) presented new photometric measurements on HD 134214 and confirm some of the frequencies seen spectroscopically by Kurtz et al. (2006). The authors suggest that the additional frequencies may be below the detection limit of the short *MOST* run. As a result, *MOST* has re-observed HD 134214, surpassing the 10.27 hrs of data presented in Cameron et al. (2006) with over a month of data. The results are currently being analyzed and will hopefully shed new light on the questions raised by these works.

2.3.2 The B supergiant HD 163899

The *MOST* satellite observed the B supergiant HD 163899 (B2 Ib/II) as a guide star and detected 48 frequencies $\lesssim 2.8$ cycles day^{-1} with amplitudes of a few mmag and less (Saio et al., 2006). HD 163899 was observed as one of 20 guide stars used during the photometry measurements of WR 103 (HD 164270). Observations were made from 2005 June 14 to July 21 for a total of 36.6 days. Because the WR 103 field is outside the *MOST* Continuous Viewing Zone, the duty cycle was limited to about 50% of the 101 min orbit.

The frequency range suggests g- and p-mode pulsations. It was generally thought that no g-modes are excited in less luminous B supergiants because strong radiative damping is expected in the core. Theoretical models calculated by Saio and Gautschy (Saio et al., 2006) show that such g-modes are excited in massive post-main-sequence stars. Excitation by the Fe-bump in opacity is possible because g-modes can be partially reflected at a convective zone associated with the hydrogen-burning shell, which significantly reduces radiative damping in the core. The *MOST* light curve on HD 163899 shows

that such a reflection of g-modes actually occurs, and reveals the existence of a previously unrecognized type of variable, slowly pulsating B supergiants (SPBsg). Such g-modes have great potential for asteroseismology. HD 163899 is the first member of the SPBsg family, showing both g-modes and hybrid β Cephei-type (p-mode) behaviour.

2.3.3 The SPBe stars HD 127756 & HD 217543

MOST discovered SPBe (Slowly Pulsating Be) oscillations in the stars HD 127756 (B1/B2 Vne) and HD 217543 (B3 Vpe). The results are published in Cameron et al. (2008). HD 127756 and HD 217543 join the stars HD 163868 (Walker et al., 2005) and β CMi (Saio et al., 2007) as SPBe stars discovered by *MOST*. High radial order g-modes with pulsation frequencies in the co-rotating frame that are much smaller than the rotation frequency appear in groups that depend on the azimuthal order m in a DFT. Theoretical models (see, for example, models calculated by Saio in Cameron et al. 2008) indicate that, in rapidly rotating stars, high-order g-modes are excited near the Fe opacity bump as in SPB stars. One difference from slowly rotating SPB stars is the fact that among the high-order g-modes, prograde modes are predominantly excited. These modes have frequencies of $\sim |m|\Omega$ in the observer's frame with Ω being the rotation frequency of the star. For $m = -1$ and -2, expected frequencies are grouped at Ω and 2Ω consistent with observed frequencies previously discovered in HD 163868 (Walker et al., 2005). The analysis of HD 127756 and HD 217543 also shows this behaviour, opening up the possibility of determining the rotation rates of the stars by matching the observed frequency groups to models of rapidly rotating stars.

HD 127756 was observed for a total of 30.7 days by *MOST* . The target field was outside the *MOST* CVZ so there is a gap during part of each 101.4 min satellite orbit resulting in a duty cycle of 30.7% (Note that our data sampling ($\sim$ 20 s), even with gaps every orbit, thoroughly covers the time scale of the intrinsic variations ($\sim$ 1 day period) of HD 127756, giving us an effective duty cycle of near 100%). The light curve is presented in Fig. 2.1 and shows clear variations with periods near 1 day and 0.5 day. Table A.1 lists the frequencies, amplitudes, phases, the 1 and 3σ uncertainties from the bootstrap analysis (using 100,000 realizations), and the S/N of the 30 most significant periodicities. The 1 and 3σ uncertainties are estimated for each parameter as the width of the region, centred on the parameter in question, that contains 68 and 99% of the bootstrap realizations, respectively. The fit is shown superimposed over two zoomed sections of the light curve labelled A and B in the lower panels of Fig. 2.1.

The amplitude spectrum of the data along with the fitted points and the residuals from the fit are shown in the top panel of Fig. 2.2. Most of the frequencies gather into three groups; $\sim$ 0 cycles day^{-1}, $\sim$ 1 cycles day^{-1}, and $\sim$ 2 cycles day^{-1}. This property is similar to the frequency groupings of the SPBe star HD 163868 (Walker et al., 2005). The lower panel of Fig. 2.2 plots the S/N for each of the identified periodicities and the window function of the data. Among the frequencies listed in Tab. A.1, $\nu_1 = 0.0335$ cycles day^{-1} and $\nu_2 = 0.0739$ cycles day^{-1} have the fewest observed cycles (close to the length of the run at $1/30.7 = 0.0326$ cycles day^{-1}) and are included to reduce the scatter in the residuals from our fit. They may not be genuine stellar oscillation frequencies but it should be noted that observational artifacts

associated with the baselines of other *MOST* observations, especially with such a relatively large amplitude of 7 mmag as in the case of ν_1 here, have not been observed.

A comparison of the closely spaced frequencies near ~ 1 cycles day^{-1} to the window function and to our fit is given in Fig. 2.3. Notice that the peak with the largest amplitude has an asymmetric component that is wider than the window function. When that frequency (ν_{14}) is prewhitened, significant power remains near that asymmetry and is fitted as ν_{13} (shown as the data point with the smallest amplitude in Fig. 2.3). These frequencies are spaced by ~ 0.04 cycles day^{-1} which is greater than the Rayleigh criterion for our data (~ 0.03 cycles day^{-1}). The points are clearly separated in frequency within their respective 3σ errorbars. The peak labelled as $\mathrm{A_X}$ (ν_{15} in Table A.1) is spaced from ν_{14} at nearly the resolution limit suggested by Loumos & Deeming (1978) (~ 0.06 cycles day^{-1}). This peak is clearly resolved from ν_{14} and has an amplitude that is ~ 4 times that of the first side lobe of the window function (labelled as $\mathrm{A_Y}$). Although the amplitude of this peak may be influenced by windowing of the data, the evidence suggests the frequencies are resolved. Frequencies ν_{18} and ν_{19} (shown circled in Fig. 2.3) have the smallest frequency separation and are barely resolved within their 3σ errorbars with a separation of ~ 0.004 cycles day^{-1}. The bootstrap distributions for these frequencies are plotted in Fig. 2.4 and shows the parameters are normally distributed and the frequency distributions of ν_{18} and ν_{19} nearly overlap.

We suggest, based on our bootstrap distributions, that frequencies spaced by less than $0.5\ T^{-1} \sim 0.0163$ cycles day^{-1} (within their 3σ errorbars) are at

the resolution limit of our data set. Using this resolution criterion, frequency pairs ν_6 and ν_7; ν_{18} and ν_{19}; and ν_{23} and ν_{24} may not be resolved frequencies. Cameron et al. (2008) show that the resolution of these frequencies doesn't affect the physical interpretation of the data.

MOST observed HD 217543 as a guide star for a total of 26.1 days with a duty cycle of $\sim$ 33% (like HD 127756 the effective duty cycle is closer to 100%). Figure 2.5 shows the light curve with clear periods of $\sim$ 0.5 and $\sim$ 0.25 days with modulations characteristic of more complex multi-periodicity. The fit to the 40 most significant frequencies (see Tab. A.2) is shown in zoomed regions labelled A and B in the lower panels of the plot. Note that in Tab. A.2 there are 6 frequencies with S/N ranging from 3.09 to 3.38. These are below the S/N $\sim$ 3.5 limit described above and represent $\gtrsim$ 2σ detections (Kuschnig et al., 1997). They are included to illustrate that within the S/N errors plotted in the lower panel of Fig. 2.6 all identified frequencies reach the S/N $\sim$ 3.5 limit. These periodicities do not adversely influence the fit and do not change the physical interpretations of Cameron et al. (2008).

Figure 2.6 shows an amplitude spectrum of HD 217543 in the top panel and the S/N of the identified frequencies and the window function of the data in the lower panel. As with HD 127756, most frequencies are grouped around three ranges; $\sim$ 0 cycles day^{-1}, $\sim$ 2 cycles day^{-1}, $\sim$ 4 cycles day^{-1}. The second and the third frequency range is higher by a factor of $\sim$ 2 than the corresponding ones of HD 127756. Frequencies $\nu_1 = 0.0269$ cycles day^{-1}

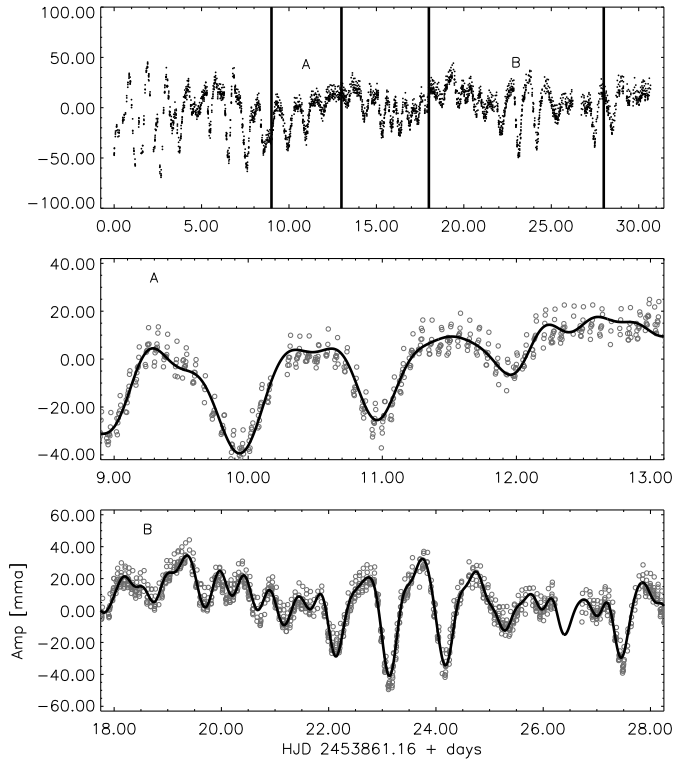

Figure 2.1: *MOST* light curve of HD 127756. The top panel shows the entire light curve spanning a total of 30.7 days. The middle and the bottom panels are expanded light curves for the portions A and B, respectively, indicated in the top panel. Solid lines indicate the fit of the 30 significant frequencies (Tab. A.1) from the frequency analysis of the full light curve. The short-term variability seen in the middle panel is a consequence of stray Earth shine modulated with the *MOST* satellite orbital period of ~ 101.4 min.

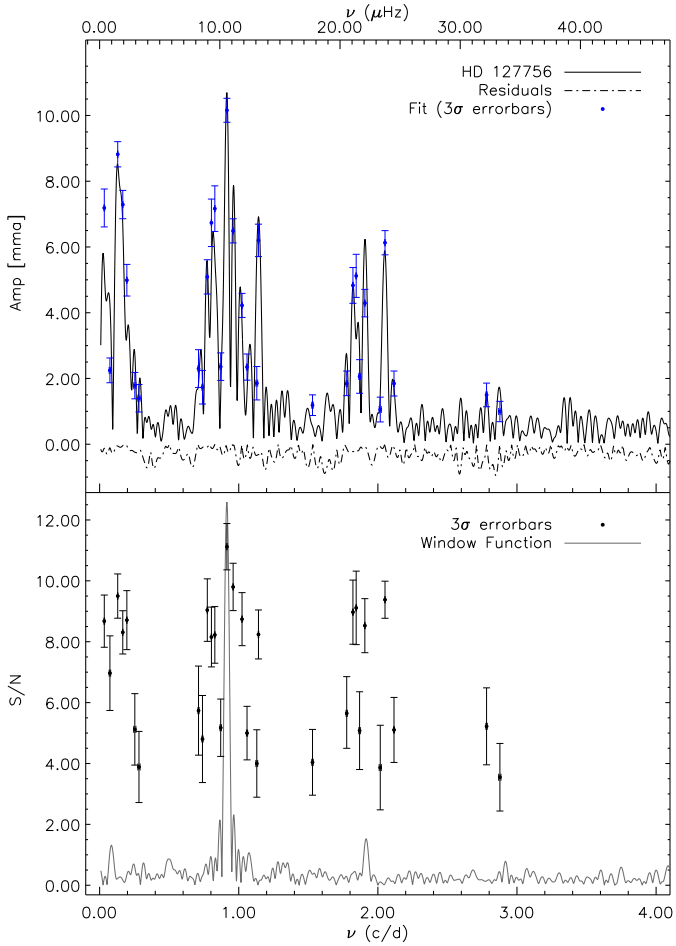

Figure 2.2: (Top panel) The Fourier amplitude spectrum of the light curve of HD 127756. Filled (blue) circles with 3σ error bars are the fitted parameters (see Tab. A.1). The inverted dash–dot line is the residual amplitude spectrum obtained after the fit was subtracted from the light curve. (Lower panel) The S/N of the identified periodicities with 3σ uncertainties estimated from both the fitted amplitudes and frequencies and the mean of the amplitude spectrum (see § 2.2 for details). The light grey line represents the window function of the data centred on the frequency with the largest amplitude and scaled to the maximum S/N for clarity.

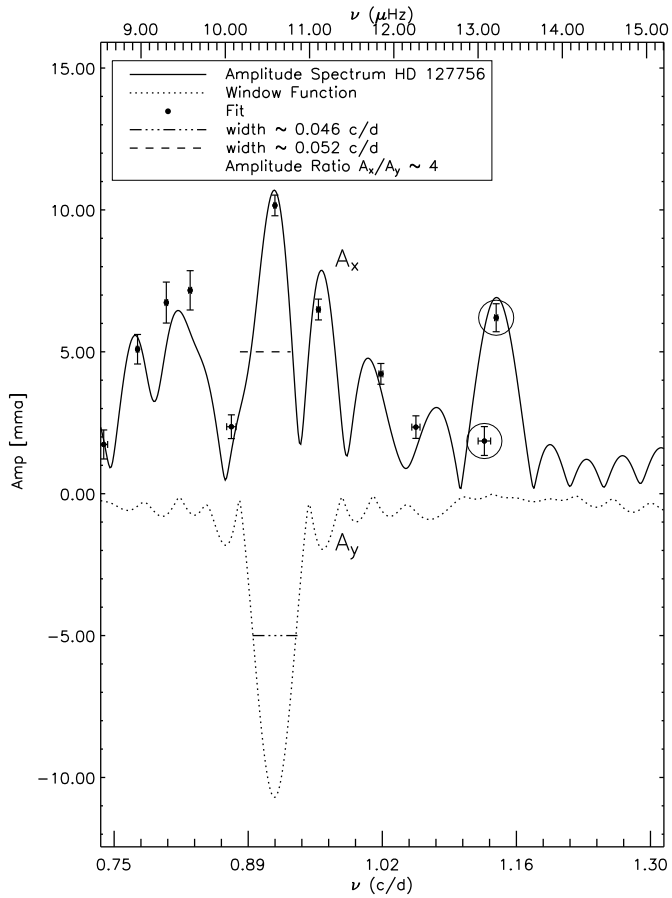

Figure 2.3: The zoomed region around the largest peak in the amplitude spectrum of HD 127756. The window function is shown as the inverted, dotted line and the fit is shown as points with 3σ errorbars. The asymmetry of the largest peak in the amplitude spectrum (width ~ 0.052 cycles day^{-1} [dashed line]) is compared to the width of the window function (~ 0.048 cycles day^{-1} [dash dot line]). The amplitude of the first sidelobe of the window function (labelled $\mathrm{A_y}$) is ~ 4 times smaller than the second largest peak in the amplitude spectrum at $\mathrm{A_X}$. The resolution of frequencies ν_{18} and ν_{19} (both circled) is discussed in section 2.2.

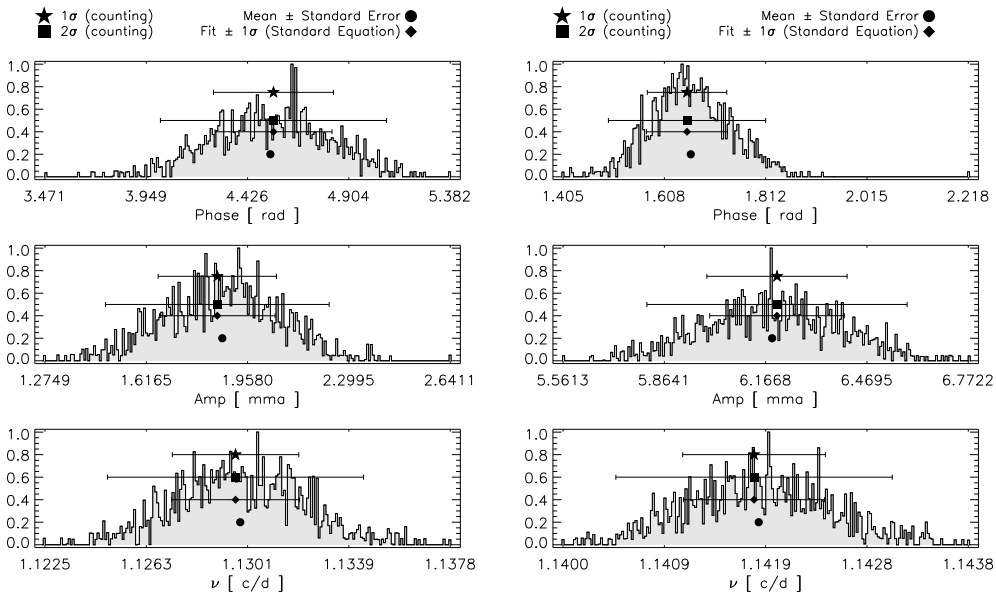

Figure 2.4: A comparison of bootstrap distributions for parameter sets (ν_{18}, A_{18}, ϕ_{18}) and (ν_{19}, A_{19}, ϕ_{19}) [see Tab. A.1] for 100,000 realizations of the HD 127756 light curve. The top panels are distributions for the fitted phase (ϕ) while the middle and lower panels show distributions for the amplitude (A) and frequency (ν) parameters, respectively. In each panel symbols are shown (from top to bottom) for the 1σ (★) and 2σ (■) error intervals containing 68 and 95 % of the realizations (note that Tab. A.1 lists the 3σ, or 99%, error interval) centred on the fitted parameter. Below those symbols in each panel are the 1σ (♦) errorbars obtained from the formula definition of standard deviation and the mean (•) of the distribution with the standard error on the mean. These distributions are shown because the frequencies are the closest to each other.

and $\nu_2 = 0.0806$ cycles day^{-1} are close to the length of run ($1/26.1 = 0.0383$ cycles day^{-1}) but were included to reduce the residuals in the light curve. They may not be intrinsic stellar pulsations.

Frequencies ν_6 and ν_7 of Table A.2 overlap within their 3σ uncertainties. The bootstrap distributions are given in Fig. 2.7 and show all parameters are normally distributed like those in Fig. 2.4 for HD 127756. However, the long tails on the frequency distributions suggest that these frequencies are not fully resolved. If we adopt the same resolution criterion as for HD 127756, frequencies spaced less than 0.5 $T^{-1} \sim 0.0192$ cycles day^{-1} (within their 3σ errorbars) are at (or below) the resolution limit of our data set. This means frequency sets ν_6 and ν_7; ν_{19} and ν_{20}; and ν_{34} and ν_{35} may not be fully resolved.

The SPBe stars provide an opportunity to determine the rotation frequency without referring to $v \sin i$ (Cameron et al., 2008). It now seems possible to determine the rotation rates of these stars by matching the observed frequency groups to models of rapidly rotating stars. This is only a possibility now because of the high quality of the *MOST* data. Cameron et al. (2008) provide a detailed modelling effort for the SPBe stars already published by *MOST* team. However, even without presenting detailed models here, we can say that HD 217543 rotates about twice as fast as HD 127756 based solely on the spacings between the frequency groups observed in Figs. 2.2 and 2.6. Unfortunately, detailed g-mode asteroseismolgy is not possible at this time because of the complexities involved in modelling these rapidly rotating stars and the long observation runs needed to resolve the

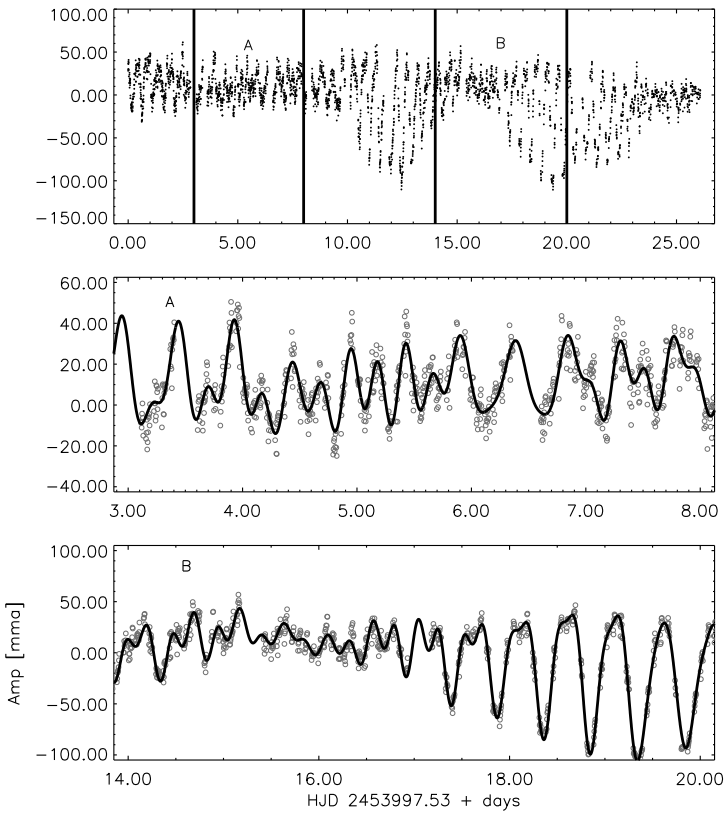

Figure 2.5: *MOST* light curve of HD 217543. (Top panel) The full light curve for a total of 26.1 days. The middle and the bottom panels show expanded light curves for the portions A and B (respectively) indicated in the top panel. Solid lines indicate the fit of the 40 most significant frequencies from the frequency analysis of the full light curve (see Tab. A.2).

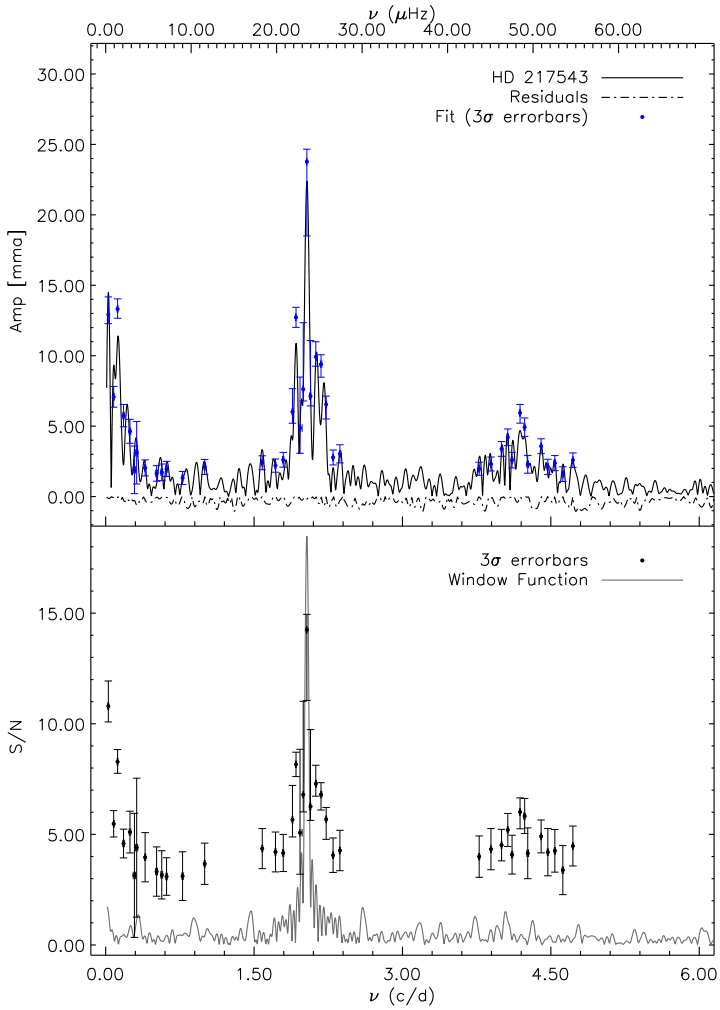

Figure 2.6: Fourier amplitude spectrum of the light curve of HD 217543 and the identified frequency parameters from Table A.2. The panels and the meaning of the symbols are described in Fig. 2.2.

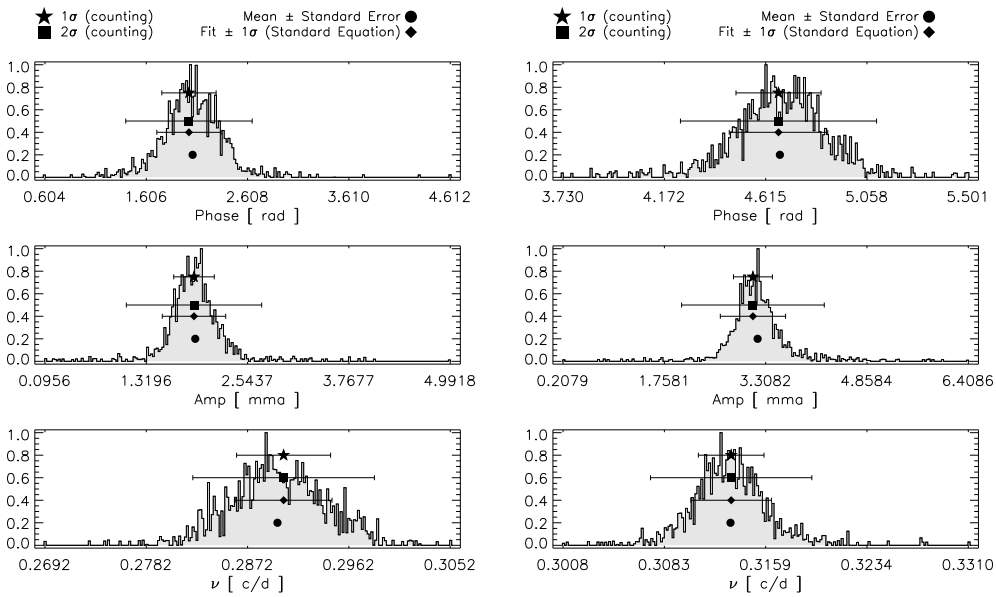

Figure 2.7: A comparison of bootstrap distributions for parameter sets (ν_6, A_6, ϕ_6) and (ν_7, A_7, ϕ_7) [see Tab. A.2] for 100,000 realizations of the HD 217543 light curve. Symbols are the same as those in Fig. 2.4. These distributions are shown because the fitted frequencies are the closest to each other. In this case, the long tails on the frequency distributions suggest that these frequencies are not fully resolved.

many g-modes excited in these stars.

Chapter 3

MOST & HR 1217

The data analysis methods discussed in chapter 2 are applied to the HR 1217 photometry collected by the *MOST* satellite. This chapter begins with an outline of the photometric reduction, followed by a discussion on the determination of the rotation period of HR 1217, and then finishes with a detailed frequency analysis of the photometric time-series. The results from this chapter will be interpreted, for the first time, using a dense grid of stellar models outlined in the following chapters.

3.1 The light curve reduction

MOST observed HR 1217 near continuously as a Fabry target (§ 2.1) from Nov. 5 to Dec. 4, 2004. Integration times for the target were 30 sec and more than 72,000 data points were collected. The preliminary light curve reduction was performed (by Dr. Jason Rowe) using methods described in § 2.2. Stray-light was removed by binning the data at 35 orbital periods ($\sim$ 2.5 days), then folding the binned light curve at the orbital period and removing the running mean trend from data (e.g.,Rucinski et al. 2004). Residual trends in the data were removed by subtracting a mean value, determined by splining 0.005 day bins, while at the same time, making sure that no periodicities were introduced or subtracted near the periods of interest. The interesting

frequency range is the range where oscillations were previously identified (§ 1.3) in HR 1217, and approximately covers 2500 to 2800 μHz. Extreme outliers were clipped from the data, leaving a total of 68,095 data points, spanning a time of 29.02 days. These reduction steps are further described below, and are presented in Fig. 3.1. There are two $\sim$ 0.2 day gaps in the data caused by a particle hit on the CCD and a satellite software upgrade during the observations. The resulting duty cycle of the data, based on those gaps, is 95%. If the duty cycle is calculated as the total number of potential data points that could have been taken every 30 sec over 29 days, the result would be closer to 82%. Because the oscillation periods HR 1217 are about 6 minutes, our time sampling and coverage warrant the use of the 95% effective duty cycle.

Along with stray-light, the long-term, rotational modulation — with a period near 12.5 days (§ 1.2.2, 1.3) — is removed from the light curve. Figure 3.1 (left panels) shows the reduction steps used to arrive at the final light curve for HR 1217 plotted in Fig. 3.2. There are three steps in the light curve reduction. The first step, shown in the top panel (labelled A), shows the light curve with only a first sigma clip performed to remove the outliers. The light curve clearly shows repeating spikes in brightness that are superimposed over the 12.5 day, near sinusoidal, stellar rotation trend in the data. These light spikes are the result of stray Earth shine illuminating the CCD during satellite observations and occur every $\sim$ 101 minutes. The second reduction step is the removal of those light spikes (stray-light) from the data. The folding of the light curve in 35 orbital bins, and the subtraction of the mean trend at each orbital phase, results in a light curve

shown in the middle left panel (labelled B). At this step, the light curve only shows the rotational modulation in the HR 1217 data. There are a total of three mean-light maximums and two minimums covered over the 29 days of observations. The third, and final, reduction step is the removal of this long-term, or rotational, trend (with peak-to-peak amplitude of about 4 mmag) from the data. As stated above, this was done be removing a running mean (determined by splining binned data) from the light curve. The amplitude of the light variations that remain in the data; i.e., the light variations caused by the rapid, $\sim$ 6 min, oscillations (§ 1.2.2, 1.3), are less than 1 mmag. The final light curve is shown in the lower, left panel (labelled C), and illustrates what looks like a beat pattern in the data. During mean light minimum, the rapid oscillations reach their maximum amplitude. This will be shown, and discussed, later in this chapter.

We next check that only the stray-light and rotation trends are removed from the data. In the right panels of Fig. 3.1, the DFTs of the corresponding light curves in the left panels are plotted. In order to show the reduction of the stray-light amplitude over a large range in frequency space, we have phased the DFT to the orbital frequency ($\sim$ 14 cycles day^{-1}) for each of these reduction steps and showed only a window in phase space that is $\pm$ 6 cycles day^{-1} wide and centred on the Nth orbital harmonic. (The value of N is indicated by the colour bar below the right panels in the figure.) The frequency range where pulsations occur in HR 1217 is inverted in those panels. The stray-light components, and their associated aliases, are dramatically reduced in amplitude by the final reduction step. Because of the phase window used in the right panels of Fig. 3.1, the frequency peak associated with

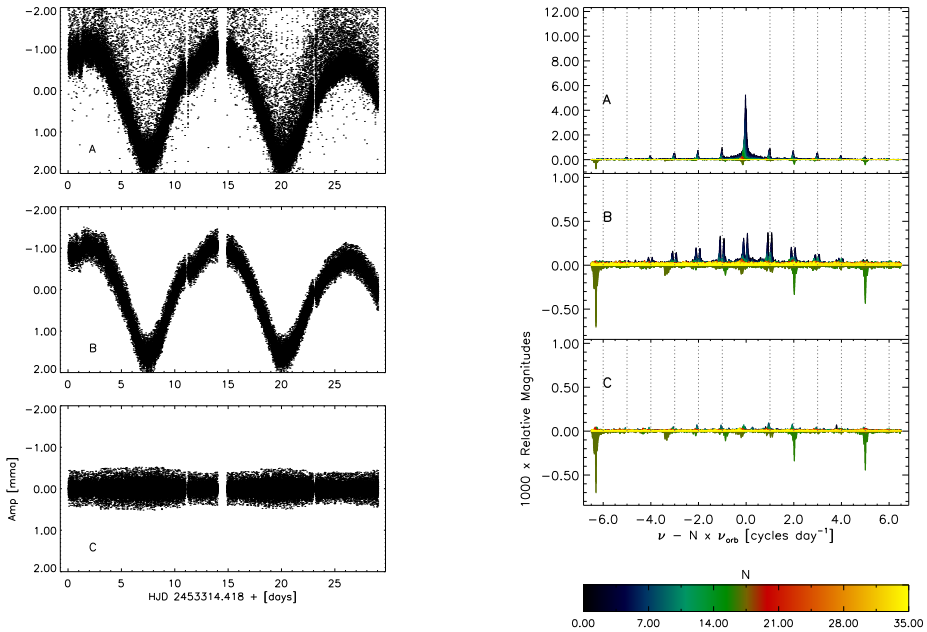

Figure 3.1: Photometric reduction steps using the *MOST* data of HR 1217. The left panels show the light curves of HR 1217 in three separate reductions phases described in § 3.1. The first light curve (labelled A) shows only a preliminary sigma clipping of the data. The middle panel (labelled B) shows the removal of the stray-light component. The final, lower panel, (labelled C) shows the light curve with both stray-light and the long-term, rotation modulation removed. The rotation modulation occurs over a period of about 12.5 days. The right panels show the phased DFTs for each of the reduction steps, folded at the orbital frequency of the satellite ($\sim$ 14 cycles day^{-1}). Each panel shows a phase window $\pm$ 6 cycles day^{-1} wide centred on the Nth orbital harmonic. The Nth harmonics are colour coded, with the colour legend below the lowest panel. The amplitude of the top right panel is set to the amplitude of the peak in the DFT that is associated with the rotation of HR 1217. The DFTs are inverted for frequencies in the range of 220 to 250 cycles day^{-1}, where the known oscillation frequencies of HR 1217 are observed. Note the reduction of the orbital components and the daily aliases (vertical dotted lines) from panels A to C.

the rotation period of HR 1217 is not shown. (It is approximately 14 cycles day^{-1} away from the first stray-light peak.) The amplitude of the first, upper right, panel is scaled to the amplitude of the peak associated with rotation (at about 0.08 cycles day^{-1}) in the DFT. Its amplitude is much larger than the stray-light and pulsation amplitudes.

The final, zoomed, version of the time-series is presented in Fig. 3.2. The top panel shows the light curve with an apparent beat pattern having a period of about 12.5 days (§ 3.2) and the lower panels are zoomed portions (about 0.6 hr) of the data. Over-layed on those zoomed panels is the fitted sinusoidal function (parameters are found in Tab. 3.1) obtained using the CAPER software (§ 2.2). The errorbars on the photometric data are estimated from Poisson statistics and are about 0.1 mmag. The fit is discussed in more detail below.

3.2 On the rotation period of HR 1217

The oscillations observed in roAp stars are described well by the oblique pulsator model (§ 1.2.2). As a result, the DFTs of most roAp star light curves show a number of periodicities that are spaced from each other by the stars' rotation frequencies. (This is illustrated later in this chapter, in Fig. 3.8, for HR 1217.) The rotation period of HR 1217 has been measured by a number of authors. Kurtz & Marang (1987) determine a rotation period of 12.4572 ± 0.0003 days from photometric data collected from a variety of sources. A slightly longer period of 12.4610 days (no uncertainty given) was determined by Mathys (1991) based on the variation of magnetic field

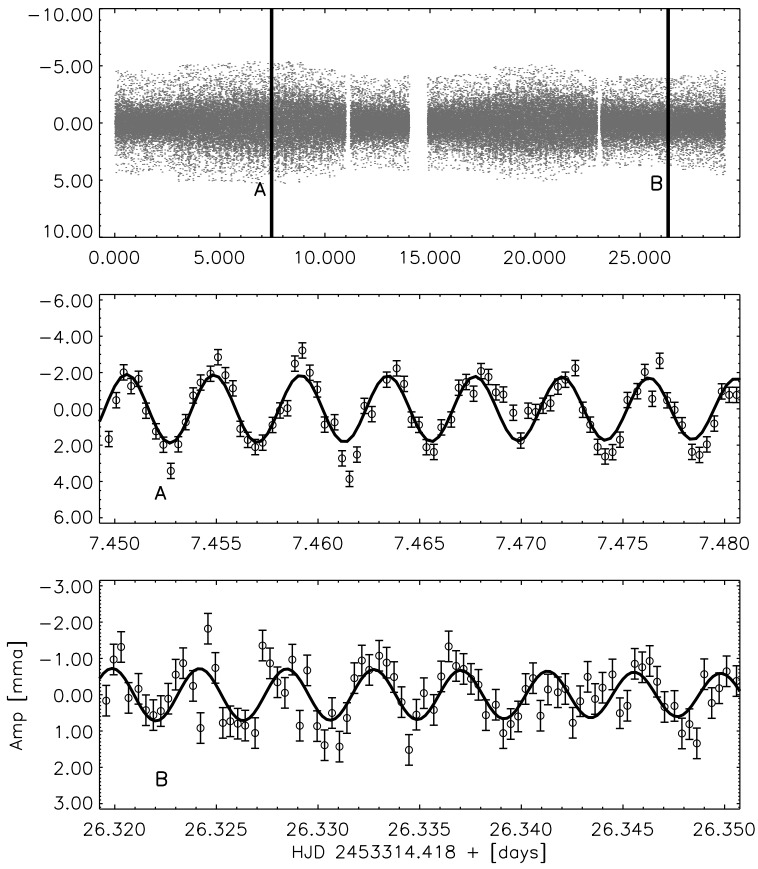

Figure 3.2: The reduced HR 1217 light curve. The entire ($\sim$ 29 day) time-series is shown in the top panel after being reduced using procedures outlined in § 3.1. The lower two panels are expanded views of sections labelled A and B in the top panel, respectively, and each cover approximately 0.6 hr of data. The nonlinear least squares fit using a multi-sinusoid function (with parameters listed in Tab. 3.1) is over-plotted on the data points for sections A and B. Those fit parameters are described in § 3.3. Errorbars represent Poisson errors and are about 0.1 mmag. The duty cycle for the entire light curve is about 95%.

strength over time. More recent measurements by Leone & Catanzaro (2004) and Ryabchikova et al. (2005) arrive at values of 12.4582 ± 0.0006 days and 12.45877 ± 0.00016 days, respectively. Assuming that the magnetic field and photometric variations should yield the same rotation period; i.e., there are no zero-point shifts that have to be taken into account, these rotation period determinations seem to be statistically inconsistent. The *MOST* data on HR 1217 covers about 29 days, corresponding to $\sim$ 2.3 rotation periods. Over that baseline there are three photometric maximums and two minimums (see Fig 3.1). Although the coverage of the *MOST* light curve is near 100%; something that has never been achieved before, the small number of rotation periods observed does not allow us to determine the rotation period of HR 1217 to the level of precision quoted in the above works. As a comparison between the completeness of the coverage of the *MOST* observations to the coverage of the data used in the works cited above, we note that Ryabchikova et al. (2005) – having the most precise period determination – arrive at a rotation period using 39 data points collected over about 50 years of magnetic field measurements.

A single sinusoid is the simplest model that gives information about amplitude, frequency, and phase. This model was used to estimate the rotation period of HR 1217 in the studies described above. A fit to a single sinusoid function using the *MOST* data, with the unbinned light curve ($\sim$ 70,000 data points), and without the rotation trend removed (middle panel of Fig. 3.1), yields the following fit parameters: 1. Amplitude, $A_{\rm m} = 1.1634\times10^{-2}$ mag, 2. Rotation frequency, $\nu_{\rm m} = 0.0807$ cycles day^{-1} (period = 12.3916 days), and 3. Phase, $\phi_{\rm m} = 3.9481$ rad. (The phase is referenced to the time of

the first data point of the observations = HJD 2451545.00 + 1769.42 days.) These are the minimum χ^2 parameters calculated by CAPER (§ 2.2). The fit of a single sinusoid can reproduce most of the variation in the light curve (see Fig. 3.3) and results in a reasonable estimate of the rotation period of the star given that there are only a few cycles observed. However, with a reduced $\chi^2 \sim 17.5$ the quality of the single sinusoid fit is not satisfactory. The residuals of the fit have a standard deviation of 2.7 mmag compared to the individual point uncertainties of about 1 mmag. The sharpness of the minimums is illustrated through the unprecedented time coverage of the HR 1217 photometry. Introducing additional Fourier components to our fit will improve the overall quality of the fitted parameters but our single frequency fit is precise enough to determine which variations are associated with the rotation of the star, given that only a few cycles are observed.

The rotation period determined from our fit is shorter than the values measured by the sources listed above. We illustrate the difference between the *MOST* rotation period and previously determined rotation periods by looking at the likelihood of the fits. The top panel of Fig. 3.3 shows the HR 1217 light curve with the single sinusoid fit plotted over the data (green line). (It should be noted again that the peaks at the light minimums are much sharper than those predicted from a single sinusoidal model but this simple model gives us a rotation period that can be used to identify the effects of rotation in our oscillation spectrum.) By fixing the amplitude of our fit at $A_{\rm m} = 1.1634\times10^{-2}$ mag and then varying frequency and phase parameters, we can see how changing those quantities (frequency and phase) affects the likelihood of the model fit. For each ($A_{\rm m}$, ν, ϕ) parameter set we construct

a χ^2 measure from

$$\chi^2(d; A_{\rm m}, \nu, \phi, \sigma) = \sum_{i=1}^{N} \frac{(A_{\rm m} \sin[2\pi\nu t_i + \phi] - d(t_i))^2}{2\sigma^2} \tag{3.1}$$

where each of the $i = 1 \ldots N$ photometric points, measured at time t_i, are represented by d. A similar χ^2 measure can be constructed for the single, best-fit, set of parameters ($A_{\rm m}$, $\nu_{\rm m}$, $\phi_{\rm m}$). Labelling this $\chi^2_{\rm m}$, we construct a likelihood ratio as

$$L/L_0 = \exp\left(-\Delta\chi^2\right) \tag{3.2}$$

where $\Delta\chi^2 = \chi^2 - \chi^2_{\rm m}$. The individual photometric errors (σ in Eq. 3.1) are taken to be unity so we can explore the variation of parameters per unit error. This is done for clarity of presentation. Individual point uncertainties ($\sigma \sim 1$ mmag) can be used and result is a very sharply peaked likelihood function near our best fitted parameters. Figure 3.3 (lower panel) shows the results of this analysis. The *MOST* fit and the previously determine values are represented by white dots in the centre of the contour plot. They are consistent with each other for this ideal case of unit residual error. The larger the $\Delta\chi^2$ value is, the further the fit solution is from the minimum $\chi^2_{\rm m}$ value. As discussed in § 2.2, the uncertainty in the rotation frequency can range from about $0.25/\Delta T = 0.009$ cycles day^{-1} to $1.5/\Delta T = 0.05$ cycles day^{-1}. Using our best fit value of $\nu_{\rm m} = 0.0807$ cycles day^{-1}, and those estimates of frequency uncertainty, the *MOST* measurement of the rotation period is 12.4 $\pm$ 1.4 days, or, 12.4 $\pm$ 7.6 days. Clearly we do not reach the level of precision on the measured rotation period of HR 1217 (using the *MOST* data) that the previous studies achieve (four decimal places).

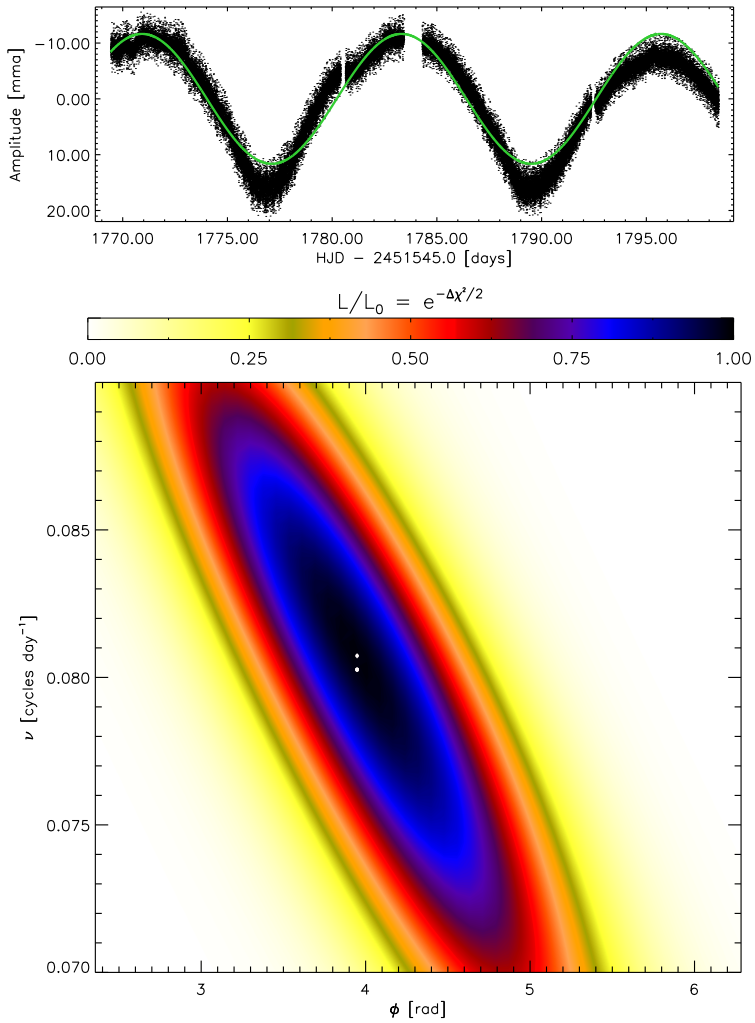

Figure 3.3: Likelihood ratio for the rotation period of HR 1217. The top panel shows the time-series with the fit of a single sinusoid over-plotted in green. The parameters of the fitted sinusoid represent the minimum χ^2 solution using CAPER. The lower panel presents the contours for the likelihood ratio in frequency-phase (ν-ϕ) space. The likelihood ratio is defined by Eqs. 3.1 and 3.2. The white dots near the centre of contour plot show the separation between the *MOST* determination of the rotation frequency (0.0807 cycles day^{-1}) compared to the previous measurements discussed in this in this section ($\sim$ 0.0803 cycles day^{-1}).

The simplest explanation for the difference in the measured precision from all sources is that each data set spans a different length of time. For example, the magnetic data used by Ryabchikova et al. (2005) covers a period of about 50 yrs while the *MOST* data covers about 30 days. But why is the fitted rotation period so inconsistent given that we all fit a similar model to our data sets?

Each group used observations that were spread (unevenly) over time. As a result, the sharp (non-sinusoidal) amplitude minimums seen in the *MOST* data (Fig. 3.3) were essentially smoothed out in their observations. To explore what affect the time sampling has on the fitted rotation period from the *MOST* data, we bin the data in different bin sizes (0 bins, 25 bins, and 100 bins), refit the parameters, and perform a bootstrap analysis using 25,000 realizations. By binning we increase the time between individual observations and essentially smooth the sharp minimums observed in the light curve. Figure 3.4 gives the results of this experiment. The lower panel of Fig. 3.4 shows the the rotation frequency for all of the binned data. The previously determined values of the rotation frequency are over-plotted (with errors smaller than the point sizes), as is the approximate resolution (§ 2.2) of $0.25/\Delta T = 0.009$ cycles day^{-1} (shown as the horizontal dashed line). In the first, 0 data bin case, the fit is determined to be 0.08073 ± 0.00008 cycles day^{-1}. The 100 data bin case yields a rotation frequency of 0.081 ± 0.002 cycles day^{-1} and the 25 data bin case results in a rotation period of 0.081 ± 0.007 cycles day^{-1}.

The more the data is binned, the more consistent our rotation period determination is with those that were previously determined. This experi-

ment is not used to improve agreement between our observations and those previously determined values. The precisions quoted in each study are simply a function of the length of the observations. The inconsistencies in the calculated values comes primarily from the differences in the completeness of the time sampling between the various data sets. Binning the data gives a quick illustration of the sensitivity of rotation period determination to the sampling of the data. The high precision obtained for the fit using all of the *MOST* data reflects the fact that the fit parameters are insensitive to small variations in the data. This can be thought of as a standard error on a mean determination — the more data you have, the smaller the error you measure for that mean. However, in our case, a single sinusoid does not properly model the sharp minimums of the light curve and overstating the precision of the measurement without acknowledging the pitfalls of the model could be misleading.

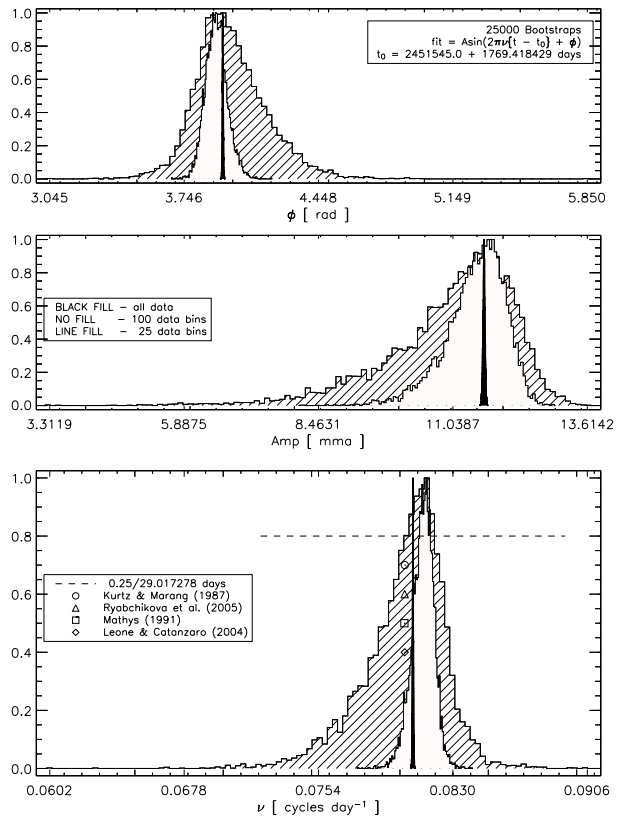

Figure 3.4: Bootstrap distributions of the rotation frequency of HR 1217. The panels show (from top to bottom) the bootstrap (using 25,000 realizations) distributions for the phase ϕ, amplitude A, and frequency ν parameters of the single sinusoid fit (shown in the legend of the top panel). The filled, dashed distributions represent the light curve of HR 1217 (Fig. 3.2) binned into 25 segments. The distributions with no fill are for the light curve with 100 equal bins and the black filled distributions is the fit using all of the data. Symbols in the lower panel are for previously determined rotation frequency values (see discussion in § 3.2). Note that the frequency resolution estimated from the length of our data set (given by $\sim 0.25/\Delta T$) is shown as the dashed horizontal line in the lower panel and is much larger than the errors obtained for any of the rotation frequencies presented.

We will show in the next section that determining the rotation frequency of HR 1217 to better than 10^{-3} μHz (9×10^{-5} cycles day^{-1}) does not influence our asteroseismic analysis because our pulsation frequencies are not determined to better than that level of precision.

3.3 The frequency analysis

The identification and refinement of the rapid variations in the HR 1217 data is done using the CAPER software that was described in chapter 2. The largest peaks in the DFT are sequentially identified, are used to determine an appropriate set of amplitude, frequency and phase parameters. A set of sinusoids characterized by those parameters is then subtracted from the light curve. Parameters are refined as they are identified by nonlinear least squares fitting to the original time-series until the identified parameters have a signal-to-noise (S/N) of less than about 3.5. This corresponds to a detection limit of $\gtrsim 2.5\sigma$ (Breger et al. 1993, Kuschnig et al. 1997).

An analysis of the *MOST* photometry of HR 1217 yields a series of 29 periodicities that are listed in Tab. 3.1 and are shown plotted over a DFT in Fig 3.5. (Note that appendix B has all tables presented in this section with frequencies listed in cycles day^{-1} rather than in μHz.) Uncertainties for the identified parameters are determined from 100,000 bootstrap samples (see § 2.2). Appendix C shows all of the bootstrap distributions for the fitted parameters. In all cases the distributions are normal (Gaussian) in nature and all of the fitted amplitudes have a S/N > 3.5 within the determined uncertainties. The uncertainties we calculate for time-series parameters using

nonlinear least-squares methods depends on the noise of the data, correlations between parameters, and on the time sampling. For example, it is known that fitted phase and frequency parameters are correlated, leading to underestimated uncertainties in these parameters when calculated from a covariance matrix (see, e.g., Montgomery & O'Donoghue 1999). Typically the uncertainties obtained by using only the diagonal elements of the covariance matrix are underestimated by a factor of 2 or more. The uncertainties determined for the parameters identified in the WET (Whole Earth Telescope) observations of HR 1217 (Kurtz et al., 2005) were determined from the diagonal elements of the covariance matrix and have an average value of 0.017 μHz. The frequencies extracted from the *MOST* data have an average (1σ) uncertainty of 0.032 μHz. We have checked that the uncertainties of the parameters calculated using the *MOST* data are about the same as those from the parameters identified from the WET data if the covariance matrix is used to calculate the uncertainties. Therefore, we are confident that our bootstrap analysis gives realistic error estimates that take into account correlations between our frequency and phase parameters. The 1σ frequency uncertainties are listed in all data tables along with the 3σ values. As discussed in § 2.2, the uncertainty (commonly calculated as the frequency resolution of the data) on extracted periodicities from a time-series can range from $0.25/\Delta T$ to $1.5/\Delta T$, depending on the preference of the investigators. The bootstrap analysis gives a measure of the precision of the fitted parameters and gives an indication of the frequency resolution of our data. To be conservative we will generally make reference to our 3σ bootstrap uncertainties when discussing the fitted frequency parameters found in this thesis.

The *MOST* mission has uncovered the following new frequencies in the spectrum of HR 1217 (Tab. 3.1): $\nu_1 = 2603.832$ μHz, $\nu_8 = 2684.832$ μHz, $\nu_9 = 2685.659$ μHz, $\nu_{13} = 2718.984$ μHz, $\nu_{17} = 2723.469$ μHz, $\nu_{20} = 2756.035$ μHz, and $\nu_{21} = 2756.925$ μHz. The average difference between the frequencies observed by Kurtz et al. (2005) for HR 1217 and the *MOST* results is 0.08 μHz. The average 3σ error on that difference is $\pm$ 0.09 μHz. This indicates that all frequencies identified by both the ground-based and space-based campaigns are consistent with each other and shows that those periods common to each of the data sets are stable since the initial ground-based collaboration of Kurtz et al. (1989). In addition, the frequencies near $\sim$ 2790 μHz (see Fig. 1.7) that were present in the WET data of Kurtz et al. (2005), but were not found in the Kurtz et al. (1989) data, are identified in the *MOST* data. (ν_{22} through ν_{27} in Tab. 3.1) This suggests that those frequencies are stable over a baseline of at least 4 years.

A direct comparison between the photometric amplitudes observed by *MOST* and Kurtz et al. (2005) is not possible because the data sets were measured using different photometric filters that average over different parts of the visible spectrum. However, the *MOST* data shows the frequency ($\sim$ 2720 μHz) having the largest corresponding amplitude ($\sim$ 760 μmag) is still the dominant peak in the DFT of the *MOST* and the WET's 2000 data. This is a change from the 1986 global campaign data (Kurtz et al., 1989) where the largest amplitude of 1.069 $\pm$ 0.018 mmag occurred at a frequency of 2687.60 $\pm$ 0.06 μHz. Although amplitude differences have been shown between the campaigns of Kurtz et al. (1989) and Kurtz et al. (2005), the net power (sum of the square amplitudes) is conserved. The precision of

the amplitude determinations from the WET data was 14 μmag. The most precise amplitude determined from the *MOST* data is 6 μmag; a value that is less than half of the quoted precision of the WET data, even without taking into account the differences in the precision calculations.

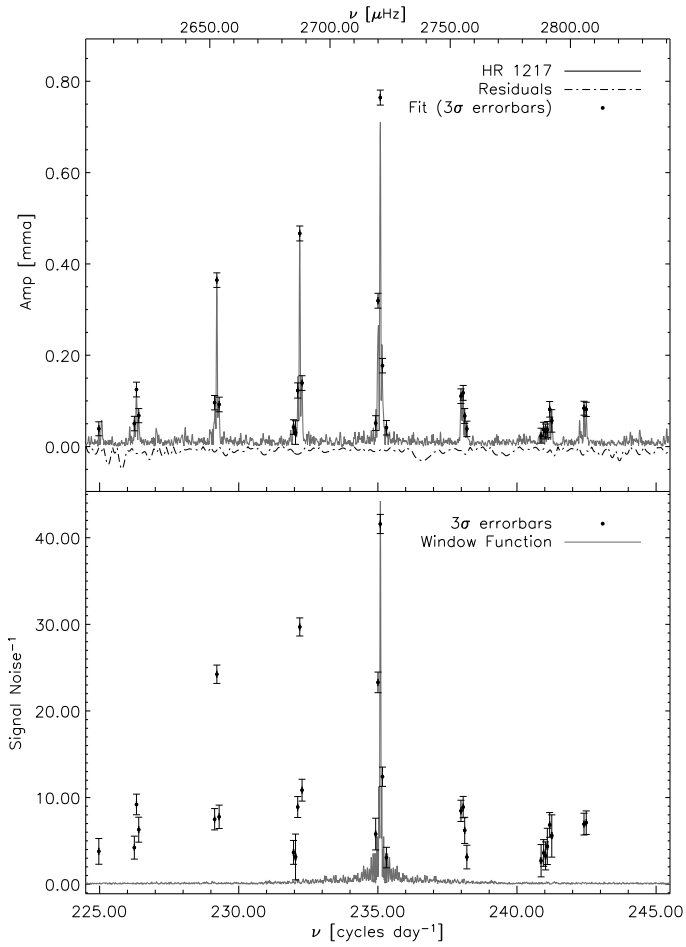

Figure 3.5: (Top Panel) The Fourier amplitude spectrum of the HR 1217 light curve. Filled circles with 3σ error bars are the fitted parameters (see Tab. 3.1). The inverted dash–dot line is the residual amplitude spectrum obtained after the fit was subtracted from the light curve. (Lower Panel) The signal–to–noise (S/N) of the identified periodicities with 3σ uncertainties estimated from both the fitted amplitudes and the mean of the amplitude spectrum. The light grey line represents the window function of the data centred on the frequency with the largest amplitude and scaled to the maximum S/N for clarity.

Table 3.1: Frequency model parameters identified using the *MOST* data. Both 1 and 3σ uncertainties on the fitted parameters are estimated from 100,000 bootstrap realizations. The phases are referenced to the time of the first observations of HR 1217 (= HJD 2451545.00 + 1769.42 days). See appendix B for frequencies in units of cycles day^{-1}.

#	ν [μHz]	A [μmag]	ϕ [rad]	$\sim$ S/N	σ_ν	$3\sigma_\nu$	σ_A	$3\sigma_A$	σ_ϕ	$3\sigma_\phi$
1	2603.832	39	2.22	3.8	$\pm$ 0.028	0.080	6	15	0.34	0.93
2	2618.600	50	3.29	4.2	$\pm$ 0.024	0.066	6	16	0.27	0.72
3	2619.495	125	5.70	9.2	$\pm$ 0.015	0.039	6	16	0.11	0.29
4	2620.440	68	1.68	6.3	$\pm$ 0.028	0.074	6	16	0.28	0.74
5	2651.998	96	3.36	7.5	$\pm$ 0.017	0.045	6	16	0.14	0.35
6	2652.924	365	5.56	24.2	$\pm$ 0.004	0.011	6	16	0.04	0.10
7	2653.883	92	2.07	7.8	$\pm$ 0.012	0.033	6	16	0.10	0.27
8	2684.832	43	2.02	3.7	$\pm$ 0.054	0.145	6	16	0.38	1.10
9	2685.659	31	2.83	3.1	$\pm$ 0.091	0.241	9	26	0.55	2.18
10	2686.560	123	1.26	8.9	$\pm$ 0.011	0.029	7	17	0.10	0.26
11	2687.420	467	4.46	29.7	$\pm$ 0.004	0.009	6	16	0.03	0.08
12	2688.364	139	1.13	10.9	$\pm$ 0.009	0.023	6	16	0.07	0.18
13	2718.984	51	4.50	5.8	$\pm$ 0.051	0.137	6	16	0.25	0.68
14	2719.957	319	6.04	23.3	$\pm$ 0.006	0.014	6	16	0.05	0.13

continued on next page

Table 3.1: *continued*

#	ν [μHz]	A [μmag]	ϕ [rad]	$\sim$ S/N	σ_ν	$3\sigma_\nu$	σ_A	$3\sigma_A$	σ_ϕ	$3\sigma_\phi$
15	2720.914	764	1.83	41.6	$\pm$ 0.002	0.005	6	16	0.02	0.05
16	2721.822	177	4.59	12.4	$\pm$ 0.011	0.027	6	16	0.10	0.26
17	2723.469	41	2.08	3.1	$\pm$ 0.034	0.097	6	16	0.39	1.10
18	2754.470	110	1.81	8.5	$\pm$ 0.016	0.043	6	16	0.17	0.45
19	2755.393	118	3.45	8.9	$\pm$ 0.015	0.039	6	16	0.17	0.45
20	2756.035	67	2.75	6.2	$\pm$ 0.038	0.107	6	16	0.36	1.05
21	2756.925	39	5.14	3.1	$\pm$ 0.045	0.159	6	17	0.53	1.67
22	2787.799	24	4.72	2.7	$\pm$ 0.127	0.317	6	16	0.90	2.59
23	2788.872	37	0.24	3.6	$\pm$ 0.034	0.096	6	16	0.29	0.80
24	2789.673	33	5.56	3.3	$\pm$ 0.047	0.157	7	16	0.38	1.16
25	2790.406	37	2.85	4.4	$\pm$ 0.073	0.196	7	18	0.45	1.24
26	2791.384	82	5.00	6.8	$\pm$ 0.033	0.085	7	17	0.29	0.74
27	2792.249	57	1.47	5.6	$+$ 0.054	0.206	9	24	0.35	1.06
.....	2792.249	57	1.47	5.6	$-$ 0.054	0.178	9	25	0.35	1.06
28	2805.650	84	1.10	6.9	$\pm$ 0.015	0.038	6	15	0.15	0.37

continued on next page

Table 3.1: *continued*

#	ν [μHz]	A [μmag]	ϕ [rad]	$\sim$ S/N	σ_ν	$3\sigma_\nu$	σ_A	$3\sigma_A$	σ_ϕ	$3\sigma_\phi$
29	2806.592	81	2.09	7.1	$\pm$ 0.018	0.048	6	16	0.16	0.44

Table 3.2 lists the calculated differences between the various frequencies identified in the *MOST* data. We adopt the symbol $\delta^{\dagger}$ as a general spacing between two frequencies. There are 19 potential frequency spacings having a value of $\delta^{\dagger} \sim 0.9$ μHz. In the previous section (§ 3.2) we identify the rotation period of HR 1217 to be ~ 12.5 days, corresponding to a rotation frequency of 0.08 cycles day^{-1} or 0.93 μHz. The average of those 19 potentially rotationally split frequencies is 0.924 ± 0.047 μHz, and is consistent with the observed rotation rate of HR 1217. As stated at the end of § 3.2, the rotationally split frequencies measured in the *MOST* data do not reach the same level of precision ($\lesssim 10^{-3}$ μHz) as that on the rotation rate quoted by other authors (see § 3.2). Using one author's value for the rotation rate over another's does not change the frequencies determined from the *MOST* data.

Frequency spacings $\delta_1^{\dagger}$ through $\delta_5^{\dagger}$, $\delta_8^{\dagger}$ and $\delta_{26}^{\dagger}$ of Tab. 3.2 show alternating values of ~ 33.5 and ~ 34.5 μHz. These spacings were also identified in previous studies of HR 1217 (e.g.,Kurtz et al. 2005) and are interpreted as half of the large separation, $\Delta\nu$. In chapter 1 (§ 1.1.1) we state that the large spacing is related to the mean density of the star by Eq. 1.14. Because of this, Matthews et al. (1999) was able estimate the asteroseismic parallax of HR 1217 and showed that it was consistent with the measured Hipparcos parallax (§ 1.3). These consistent measurements on the position of HR 1217 in the HR diagram will be used to define the relevant model parameter space in § 4.1.1. The alternating values of ~ 33.5 and ~ 34.5 μHz suggests that the observed modes are alternating between even and odd angular degree.

Another set of recurring frequency spacings are ~ 1.5 and ~ 2.5 μHz ($\delta_{19}^{\dagger}$ through $\delta_{23}^{\dagger}$). Main sequence models of A-type stars (e.g., § 4.2) have small

spacings (§ 1.1.1) that are about 3 μHz and higher. This small spacing can potentially constrain the age of the star because its value is most sensitive to changes in the composition of the stellar core as the star evolves.

Are these observed spacings actually rotational splittings? Consider the average rotation frequency derived from all of the (near rotationally split) frequency spacings in Tab. 3.2. Its value is 0.924 ± 0.047 μHz and multiplying it by 2 and 3 yields 1.848 ± 0.094 μHz and 2.772 ± 0.141 μHz, respectively. This suggests that $\delta^{\dagger}_{19}$ and $\delta^{\dagger}_{23}$ are potentially rotational components in the set of frequencies ν_8 through ν_{12} (Tab. 3.1). However, the frequency spacing between ν_{10} and ν_{11} ($\delta^{\dagger}_{15}$) is not consistent with a rotational spacing, even using 3σ uncertainties. Likewise, the frequency spacing between ν_{19} and ν_{20} ($\delta^{\dagger}_{29}$) is the most inconsistent with a rotational splitting in Tab. 3.2. So if these are related to rotation there are other anomalies between adjacent frequencies that need to be explained. That, coupled with observations of Kurtz et al. 2005, who also see $\delta^{\dagger}_{23} \sim 2.5$ μHz, leads us to believe that these additional spacings cannot be explained away as rotational components in the oscillation spectrum. Because of the low amplitudes associated with those potential small separations, including them in our nonlinear fitting routine does not influence the other parameters in the fit. It should also be noted that interpreting these spacings as small separations may not be appropriate in strongly magnetic stars (e.g., § 1.3 and 4.3).

Kurtz et al. (2005) discovered a frequency spacing of ~ 14 μHz that was explained by Cunha (2001) as a potentially magnetically perturbed mode. This spacing has also been identified in the *MOST* photometry along with another possible magnetic spacing of 15.663 μHz ($\delta^{\dagger}_{6}$) at the opposite end

of the spectrum. These modes spacings do not conform to the alternating asymptotic pattern that is observed between the other periodicities in the *MOST* data and will be modelled in the following chapters of this thesis.

Table 3.2: The frequency separations $\delta^\dagger$ of the frequencies identified in the *MOST* data. Columns with headers ν_i - ν_j use i and j to denote the frequency number from Tab. 3.1. The average rotation separation (spacings 9 ... 18 & 27 ... 35) is 0.924 $\pm$ 0.047 μHz ($3\sigma = 0.130$ μHz). See appendix B for frequencies in units of cycles day^{-1}.

#	ν_i - ν_j	$\delta^\dagger$ [μHz]	$\sigma_{\delta^\dagger}$	$3\sigma_{\delta^\dagger}$	#	ν_i - ν_j	$\delta^\dagger$ [μHz]	$\sigma_{\delta^\dagger}$	$3\sigma_{\delta^\dagger}$
1	6 - 3	33.429	0.015	0.041	19	11 - 8	2.588	0.054	0.145
2	11 - 6	34.495	0.006	0.014	20	11 - 9	1.761	0.091	0.242
3	15 - 11	33.494	0.004	0.010	21	17 - 15	2.555	0.034	0.097
4	19 - 15	34.479	0.015	0.040	22	21 - 19	1.532	0.047	0.164
5	23 - 19	33.479	0.037	0.104	23	26 - 23	2.512	0.047	0.128
6	3 - 1	15.663	0.032	0.089	24	28 - 26	14.266	0.036	0.093
7	17 - 8	38.637	0.064	0.174	25	17 - 9	37.811	0.097	0.260
8	21 -17	33.456	0.056	0.187	26	26 - 21	34.459	0.056	0.181
9	3 - 2	0.895	0.029	0.077	27	16 - 15	0.908	0.011	0.028
10	4 - 3	0.945	0.032	0.084	28	19 - 18	0.923	0.022	0.058
11	6 - 5	0.926	0.018	0.046	29	20 - 19	0.642	0.041	0.114
12	7 - 6	0.958	0.013	0.035	30	21 - 20	0.890	0.059	0.192
13	9 - 8	0.827	0.106	0.281	31	23 - 22	1.072	0.131	0.332

continued on next page

Table 3.2: *continued*

#	ν_i - ν_j	$\delta^\dagger$ [μHz]	$\sigma_{\delta^\dagger}$	$3\sigma_{\delta^\dagger}$	#	ν_i - ν_j	$\delta^\dagger$ [μHz]	$\sigma_{\delta^\dagger}$	$3\sigma_{\delta^\dagger}$
14	10 - 9	0.901	0.091	0.243	32	24 - 23	0.802	0.058	0.184
15	11 - 10	0.860	0.012	0.030	33	26 - 25	0.978	0.080	0.213
16	12 - 11	0.945	0.010	0.025	34	27 - 26	0.866	0.063	0.197
17	14 - 13	0.973	0.051	0.138	35	29 - 28	0.942	0.023	0.061
18	15 - 14	0.957	0.006	0.015					

In § 1.2.2 it was noted that the roAp stars show amplitude modulation that is a direct result of modes being excited preferentially near a magnetic pole that is inclined to both the rotation axis of the star and to the line-of-sight of the observer. The amplitude modulation of the sinusoidal components identified in the *MOST* data is shown in Fig. 3.6. The time-series is divided into 30 segments and the amplitudes and phases are refitted at a fixed frequency for the modes identified in Tab. 3.1. Rotation modulation is clearly seen for the periodicities with the three largest amplitudes but the other frequencies have corresponding amplitudes that are too small to properly see the variation. In general, all modes follow the apparent "beat" period of ~ 12.5 days in the data and show maximum amplitudes at minimum brightness (maximum magnitude) of the light curve. This is also confirmed by a time-frequency analysis presented in Fig. 3.7. In that figure, the DFT is calculated for a 4 day segment of the data and then a moving average DFT is made by advancing the data segment by 0.1 days and then recalculating the DFT. There is clear substructure surrounding the highest amplitude frequency. Because the time coverage of the *MOST* data is near 100%, we can see the amplitude modulations in the light curve of HR 1217 in an unprecedented way.

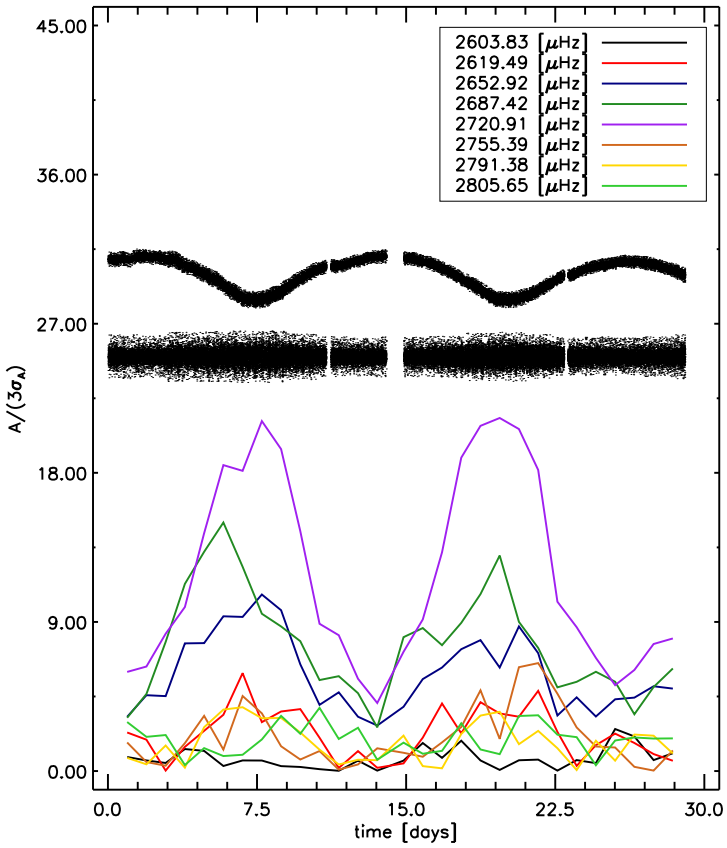

Figure 3.6: Normalized pulsation frequency amplitudes as a function of time. The HR 1217 time-series is broken into 30 segments and the amplitudes of the frequencies listed in the figure are then refitted for each data segment. Plotted are the fitted amplitudes per 3σ error. The light curves of the HR 1217 data with and without the rotational modulation removed are shown above the computed amplitudes using an arbitrary scaling. Note that the amplitude maxima correspond to the maximum magnitudes (minimum brightness) of the light curve with the rotation modulation and also to the maximum "beat" amplitude of the light curve with the rotation modulation removed.

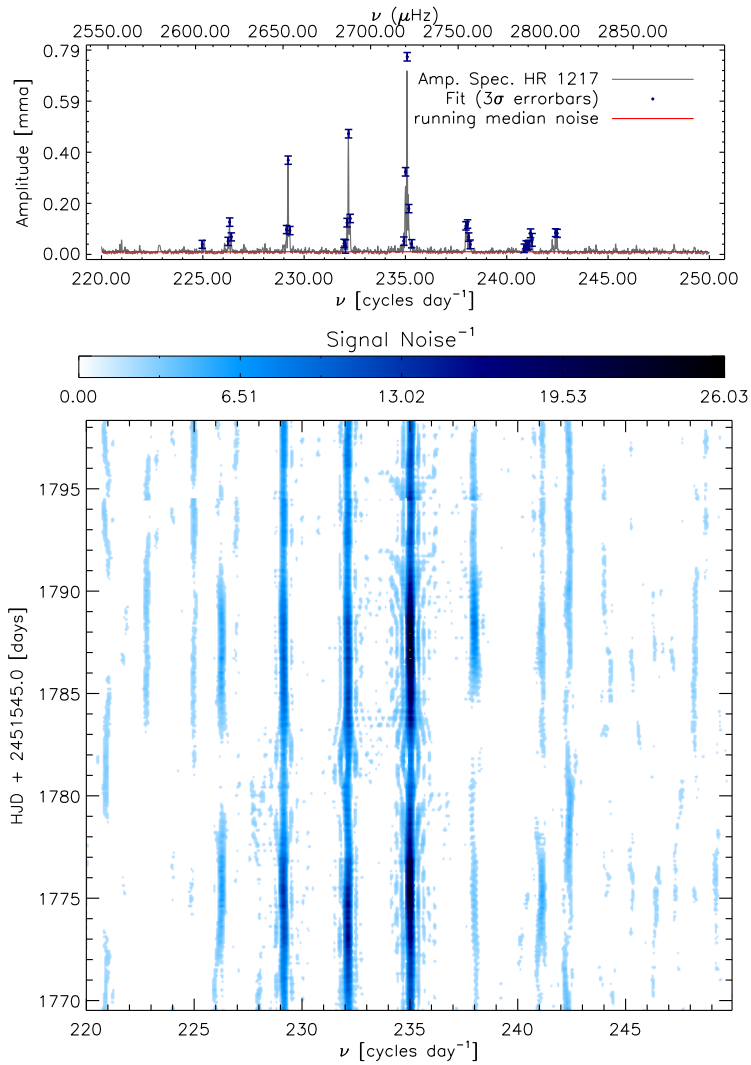

Figure 3.7: Time-frequency plot of the HR 1217 data. The top panel is the DFT of the HR 1217 data with the red line representing the median noise in the DFT over the data range presented above. The lower plot is a moving box average DFT of the data. The box width is 4 days and it is moved at 0.1 day intervals. The contours represent S/N of the moving box.

Finally, we discuss the resolution of the observed periodicities in the *MOST* data and the potential for the identification of other, closely spaced frequencies. During the frequency analysis there were a number of frequencies identified that were spaced from their neighbour frequencies by about one half of the rotation frequency of HR 1217. To assess the resolution of these frequencies we perform a bootstrap analysis (using 100,000 realizations) on the data but keep these frequencies as part of the fitted solution. In order to converge the fit with these additional frequencies we had to lower the convergence criteria on the χ^2 fitting routine in CAPER by 2 orders of magnitude, allowing the fit to relax to its final solution using a lower tolerance. The fit with all of the components is given in Tab. 3.3 (frequencies having numbers greater than 30 are the unresolved components). The results for the top 5 most prominent (largest amplitude) frequency groups is shown in Fig. 3.8 with the fits using both the resolved and unresolved frequencies over-plotted on the DFT. The addition of the extra, unresolved frequencies causes the fit to become unstable and the new frequencies clearly interact with the previously identified, resolved, parameters of Tab. 3.1.

The identifications of the unresolved frequencies that are about half of the rotation period of the star are highly suspect given the resolution of the data set. While there may be independent frequencies still to be discovered in the data, at this time these are more likely a convolution of closely spaced modes (spaced by the rotation period of the star) that are amplitude modulated. This interpretation is in line with that of Kurtz et al. (2005).

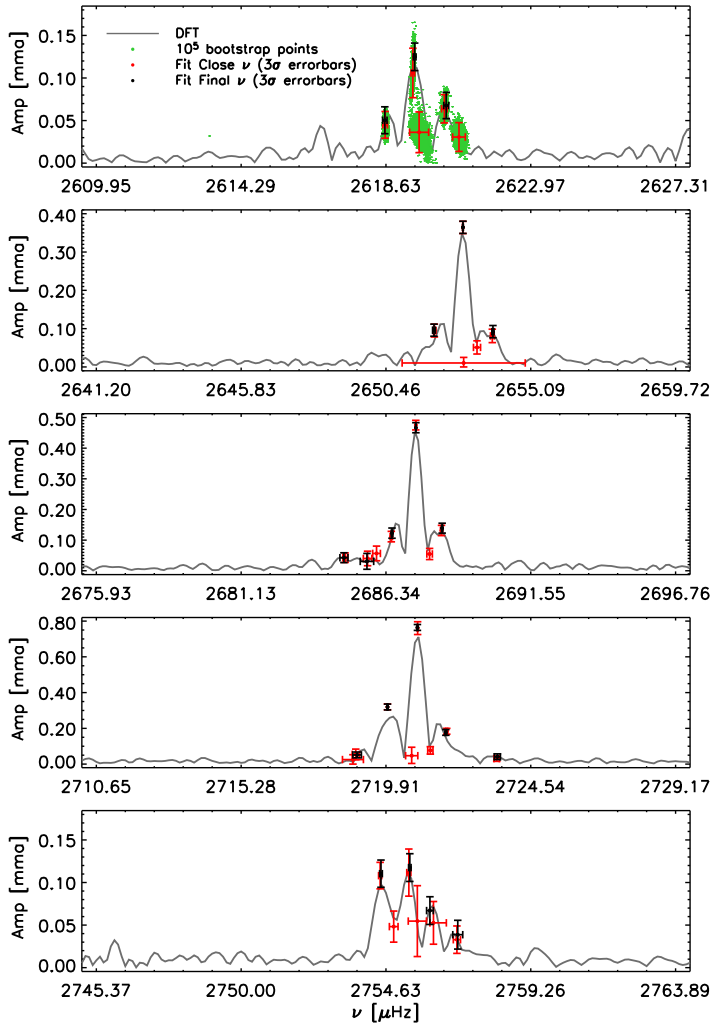

Figure 3.8: Comparison between resolved and unresolved frequencies. A bootstrap analysis using 100,000 realizations is shown for the five largest amplitude components in the HR 1217 data. Black points are for the final frequency solution (Tab. 3.1) and the red points are the unresolved frequency components found in the data (Tab. 3.3). Green dots in the top panel show the bootstrap points. Note that the frequencies common to both Tabs. 3.1 and 3.3 agree within the uncertainties while the additional frequencies tend to adversely affect the fit, and in some cases overlap each other.

Table 3.3: Unresolved frequency model parameters identified using the *MOST* data. Both 1 and 3σ uncertainties on the fitted parameters are estimated from 100,000 bootstrap realizations. Frequencies with numbers greater than 30 are the unresolved components. The phases are referenced to the time of the first observations of HR 1217 (= HJD 2451545.00 + 1769.42 days). See appendix B for frequencies in units of cycles day^{-1}.

#	ν [μHz]	A [μmag]	ϕ [rad]	σ_ν	σ_A	σ_ϕ	$3\sigma_\nu$	$3\sigma_A$	$3\sigma_\phi$
1	2603.831	38	2.22	± 0.027	5	0.26	0.077	16	0.11
2	2618.611	45	3.25	± 0.023	5	0.21	0.070	17	0.50
3	2619.440	106	5.96	± 0.025	12	0.20	0.055	15	0.75
4	2620.384	64	2.07	± 0.042	5	0.34	0.083	24	1.42
5	2652.012	95	3.20	± 0.014	5	0.16	0.049	17	0.36
6	2652.923	364	5.59	± 0.004	5	0.04	0.013	16	0.08
7	2653.863	81	2.13	± 0.020	9	0.14	0.060	17	0.31
8	2684.876	43	1.67	± 0.044	5	0.35	0.084	30	0.95
9	2685.682	40	3.02	± 0.049	10	0.44	0.153	16	0.11
10	2686.536	111	1.37	± 0.020	10	0.10	0.042	36	0.12
11	2687.416	475	4.50	± 0.004	9	0.05	0.009	16	0.23
12	2688.340	131	1.30	± 0.018	8	0.17	0.036	16	0.88
13	2718.943	54	5.18	± 0.042	8	0.52	0.115	16	0.50

continued on next page

Table 3.3: *continued*

#	ν [μHz]	A [μmag]	ϕ [rad]	σ_ν	σ_A	σ_ϕ	$3\sigma_\nu$	$3\sigma_A$	$3\sigma_\phi$
14	2719.956	320	6.11	$\pm$ 0.004	5	0.06	0.012	28	0.58
15	2720.920	761	1.81	+ 0.005	8	0.02	0.014	36	0.12
.....	2720.920	761	1.81	− 0.005	8	0.02	0.013	36	0.12
16	2721.852	184	4.45	$\pm$ 0.014	6	0.13	0.030	16	0.23
17	2723.448	31	2.33	$\pm$ 0.028	9	0.27	0.085	16	0.88
18	2754.444	108	1.99	+ 0.022	5	0.18	0.049	16	0.50
.....	2754.444	108	1.99	− 0.022	5	0.18	0.049	16	0.45
19	2755.361	112	4.02	$\pm$ 0.028	6	0.22	0.066	28	0.58
20	2756.149	53	1.75	+ 0.044	12	0.40	0.412	25	1.29
.....	2756.149	53	1.75	− 0.044	12	0.40	0.114	25	1.29
21	2756.898	33	5.35	$\pm$ 0.031	6	0.29	0.115	16	1.24
22	2787.801	24	4.73	$\pm$ 0.047	5	0.44	0.143	15	1.37
23	2788.871	36	0.19	$\pm$ 0.030	5	0.28	0.089	15	0.84
24	2789.676	34	5.48	$\pm$ 0.036	5	0.31	0.107	15	0.95
25	2790.395	35	3.02	$\pm$ 0.034	5	0.30	0.100	16	0.87
26	2791.377	82	5.04	$\pm$ 0.015	5	0.14	0.045	16	0.41

continued on next page

Table 3.3: *continued*

#	ν [μHz]	A [μmag]	ϕ [rad]	σ_ν	σ_A	σ_ϕ	$3\sigma_\nu$	$3\sigma_A$	$3\sigma_\phi$
27	2792.243	58	1.50	± 0.025	5	0.22	0.078	16	0.69
28	2805.651	84	1.10	± 0.013	5	0.12	0.038	15	0.36
29	2806.593	82	2.09	± 0.013	5	0.13	0.039	15	0.37
30	2619.628	36	4.63	+ 0.157	12	0.72	0.286	24	1.65
.....	2619.628	36	4.63	− 0.157	12	0.72	0.286	24	4.38
31	2620.823	31	5.19	± 0.099	6	0.54	0.190	17	1.50
32	2652.948	10	2.08	+ 1.073	8	2.00	1.968	15	4.13
.....	2652.948	10	2.08	− 1.073	8	2.00	1.968	10	2.08
33	2653.374	51	3.47	± 0.034	5	0.31	0.113	17	0.99
34	2686.004	57	2.84	± 0.033	8	0.27	0.139	24	1.20
35	2687.912	55	2.10	± 0.042	7	0.47	0.100	18	0.92
36	2718.852	25	3.63	+ 0.112	8	1.22	0.335	27	2.63
.....	2718.852	25	3.63	− 0.112	8	1.22	0.335	25	2.73
37	2720.730	47	2.06	+ 0.065	16	0.51	0.195	47	1.68
.....	2720.730	47	2.06	− 0.065	16	0.51	0.195	44	1.68
38	2721.327	77	3.06	± 0.035	10	0.20	0.084	21	0.76

continued on next page

Table 3.3: *continued*

#	ν [μHz]	A [μmag]	ϕ [rad]	σ_ν	σ_A	σ_ϕ	$3\sigma_\nu$	$3\sigma_A$	$3\sigma_\phi$
39	2754.877	48	3.48	$\pm$ 0.059	6	0.49	0.138	18	1.28
40	2755.633	55	6.07	+ 0.086	17	0.49	0.291	42	1.76
.....	2755.633	55	6.07	− 0.086	17	0.49	0.291	42	2.57
41	2792.612	28	0.19	$\pm$ 0.049	5	0.46	0.148	15	1.39

The frequencies identified in the *MOST* data on HR 1217 are consistent with those previously discovered in two earlier ground-based campaigns. However, because of the unprecedented precision of the *MOST* data, we were able to identify a number of additional frequencies that need to be interpreted in the context of models of magnetic stars. The following two chapters describe the modelling procedure used in this work and the efforts put forth to theoretically match and interpret the *MOST* observations. Like the *MOST* data, the parameter space appropriate to the oscillations of HR 1217 is explored in an unequalled, and unique, way.

Chapter 4

Modelling stellar oscillations

In this chapter a grid of evolution and pulsation models of A-type stars is calculated exploring a variety of parameters, constrained by the observed properties of HR 1217. The effect of a magnetic field on the resulting pulsation frequencies is estimated, for the first time, using an extensive grid of stellar models. The matching of models to the observed periodicities of HR 1217 is described in chapter 5.

4.1 Stellar evolution models

Stellar models are calculated using the Yale Rotating Evolution Code (YREC) in its non-rotating configuration. YREC solves the mechanical, conservation, and energy transport equations of stellar structure using the Henyey relaxation scheme (Henyey et al. 1959; also see Larson & Demarque 1964 and Kippenhahn & Weigert 1994). These equations are standard and may found in a number of texts on stellar structure (e.g, Kippenhahn & Weigert 1994). The nuclear cross sections, element diffusion, the equation of state and opacities available to YREC were discussed recently by Demarque et al. (2008). The code is flexible enough to allow automatic computation of a number of stellar evolutionary tracks with the convective treatment or atmospheric parameters of one's choice. For example, Fig. 1.5 shows a number of evolution

tracks on an HR diagram that were computed using YREC. Tracks of stellar models with parameters suited to those observed in HR 1217 are shown in Fig. 4.1 and are discussed in § 4.1.1.

The density of a stellar model is related to the other material functions (temperature and pressure) that are calculated from the stellar structure equations using a tabulated equation of state (EOS). YREC interpolates between OPAL EOS tables (Rogers1986, and Rogers, Swenson, & Iglesias 1996) with scaled solar composition (Grevesse & Noels, 1993) in order to obtain the appropriate densities for a particular model. These EOS tables mentioned above are commonly used, but other tables are also available. Guzik & Swenson (1997) discuss the effects that different EOS tables have on the calculated solar pulsation frequencies. They find the effect is less than about 1 μHz. This type of detailed comparison between oscillation frequencies and different input physics is most fruitful for helioseismic investigations because the global parameters of the Sun are well known. In asteroseismic investigations we make the assumption that the physics included and tested in helioseismic investigations are valid for other stars.

The energy transport equations of stellar structure require information about the opacity of the stellar plasma. These are interpolated from two separate tables depending on the local temperature in the model. If the temperature of a mass shell in a given model is greater than $\log T = 4.1$, the OPAL opacities (Iglesias & Rogers, 1996) are used. The low-temperature (molecular) opacity tables of Alexander & Ferguson (1994) are used to obtain the opacity for temperatures less than $\log T = 4.1$. Linear interpolation is used to smoothly transition between the two tables.

The models calculated in this work are evolved from the zero age main sequence (ZAMS) to a point near the end of the main sequence. Each model generated has ~ 3000 shells evenly distributed over the interior, envelope and the atmosphere. The model interior represents approximately the inner 99% of the model by mass while the envelope makes up the other 1%. The overlying atmosphere is calculated assuming the Eddington grey approximation, which is a frequency independent temperature-optical depth (T-τ) relation.

YREC is used in its non-rotating configuration even though real stars do rotate. Because the roAp stars are generally moderate rotators, and because the observed pulsation modes are high-order, rotation has little affect on the frequencies. Shibahashi & Saio (1985) estimate the effect of rotation on the calculated pulsation modes to be $< 10^{-3}$ (frequency units) so the additional complexity of adding rotation to the calculations would not yield useful information.

4.1.1 Defining the parameter space

Stellar models are calculated for a given mass, luminosity, effective temperature and element composition (specified as a mass average). In most cases spectroscopic observations give information about the effective temperature and the heavy metal (elements with atomic numbers > 2) content of a star. The luminosity can be estimated for stars using parallax measurements and the mass is only tightly constrained if the star belongs to a binary from which an orbital solution can be derived. There is also the potential to use asteroseismic observations to further constrain the evolutionary status of a star through parameters like the large spacing $\Delta\nu$ described in chapter 1 (see

Matthews et al. 1999). Even with information on all observable quantities, the standard treatment of convective energy transport (mixing length theory of Böhm-Vitense 1958) adds a free parameter known as the mixing length parameter α. This parameter sets the number of pressure scale-heights a convective element rises before releasing its heat to the surrounding plasma. Traditionally, α is calibrated by calculating a solar model, having the same input physics as the model grid that is being calculated, that reproduces the solar radius and luminosity. For example, a value of $\alpha = 1.6$ is appropriate for a solar model without element diffusion or overshoot (Guenther, 2002).

Cunha et al. (2003) examined a set of stellar models for HR 1217 in hopes of determining its evolutionary status. Their results are complementary to those of this thesis and there is an overlap in the choice of model parameters presented below. The model physics described above was also chosen to be similar to their choices for an easier comparison. This study explores the magnetic effects on the pulsation frequencies for models of HR 1217 for the first time and significantly extends the number of models and the breadth of the parameter space explored when compared to earlier asteroseismic studies on HR 1217.

The mass of HR 1217 was estimated previously by a number of authors using a variety of assumptions. Shibahashi & Saio (1985) estimated a mass of 2.0 ± 0.5 $M_\odot$. (This mass was also adopted by Matthews et al. 1999.) Wade (1997) gives a tighter constraint of 1.8 ± 0.3 $M_\odot$ assuming that HR 1217 is a rigid rotator and the recent results of Kochukhov & Bagnulo (2006) find 1.55 ± 0.03 $M_\odot$ based on a statistical analysis of a sample of Ap stars. Each of these mass determinations are based on stellar evolution models that

come close to the observed luminosity and effective temperature of HR 1217. The models calculated in this study have masses of 1.3 to 1.8 $M_\odot$ in 0.05 $M_\odot$ steps.

The effective temperature of HR 1217 is estimated from two sources. Ryabchikova et al. (1997) use their spectral synthesis code to estimate an effective temperature of $T_{\rm eff} = 7250$ K (with no uncertainty provided). The other estimate comes from the Strömgren photometry of Moon & Dworetsky (1985). Matthews et al. (1999) used those measurements to estimate an effective temperature of 7400 $\pm$ 100 K. We adopt a value of $T_{\rm eff} = 7400^{+100}_{-200}$ K to cover the span in temperature determined in those earlier works. This is identical to the effective temperature estimate used by Cunha et al. (2003) and is consistent with a more recent estimate of $T_{\rm eff} = 7350$ K (Lüftinger et al., 2008) using the same methods as Ryabchikova et al. (1997).

The luminosity of HR 1217 is determined from its Hipparcos (Perryman et al., 1997) parallax. Matthews et al. (1999) derive a luminosity of 7.8 $\pm$ 0.7 $L_\odot$ from a parallax of 20.41 $\pm$ 0.84 mas (milli-arc seconds). An asteroseismic parallax can also be estimated from Eq. 1.15. Using the above estimates on $T_{\rm eff}$ and mass, and assuming a large spacing of $\sim$ 68 μHz we arrive at a luminosity of $8.2^{+1.6}_{-1.5}$ $L_\odot$. If half the large spacing ($\sim$ 34 μHz) is used, the asteroseismic luminosity is $20.7^{+4.0}_{-3.8}$ $L_\odot$. The latter value is inconsistent with the more accurate Hipparcos value. All physical parameters used in our model grid are also consistent with those determined by Kochukhov & Bagnulo (2006).

A difficulty arises when determining the metallicity for the Ap stars because the metal content estimated from spectroscopic observations can dra-

matically change over the magnetic (rotation) phase of the star. There is also no reason to believe that the interior metal content of an Ap star is reflected by the observed, patchy, surface values. The spectroscopy of Ryabchikova et al. (1997) indicates [Fe/H] $\approx 0.32 \pm 16\%$ (an average of Fe I and II lines at both B_{max} and B_{min}). Assuming Fe is a tracer of the interior metal content of a star, a heavy metal mass fraction of Z = 0.008 is calculated. If it is (naively) assumed that the average of all of the metal abundances from Ryabchikova et al. (1997) for each of the magnetic maximum and minimum phases represent the interior heavy metal content of HR 1217, we estimate a value of Z $\sim$ 0.022. Thus, the inferred interior Z for HR 1217 can vary over a large range depending on how the surface metallicity is used. For completeness we use Z = 0.008 to 0.022 in steps of 0.002 in our evolutionary models and adopt a hydrogen mass fraction of X = 0.700 to 0.740 in steps of 0.020. The large extent of our parameter space in composition encompasses the uncertainties from the observed [Fe/H] above.

Finally, mixing length parameters of $\alpha = 1.4,\ 1.6$, and 1.8 are used in the model grid. If a star possesses a convective envelope, α may be used to set the adiabatic temperature gradient at the base of the convective zone. Luminosity is a function of temperature and radius so varying α will slightly change the radius of the model because it changes the temperature at the base of the convective zone (Guenther et al., 1992). Because the envelopes of A stars are essentially radiative, any structural changes from the different values of α are small when compared to the effects introduced by varying the other model parameters.

All models are plotted on the theoretical Hertzsprung-Russell (HR) di-

agram in Fig. 4.1. The Hipparcos luminosity and the effective temperature determination discussed above constrain the location of HR 1217 in the HR diagram. The error box outlining that area in the HR diagram is shown as a black box in Fig. 4.1. There were approximately 10^5 stellar models generated in the model grid. Detailed models (containing information necessary for the pulsation analysis; see § 4.2) were output in age steps of 0.05 Gyr from the ZAMS, decreasing the number of models by an order of magnitude. Of those models, a total of 569 fall within the HR 1217 error box. Those 569 models are used in the pulsation and magnetic perturbation (§ 4.3) calculations.

Figure 4.2 shows histograms of the mass, radius, and composition (Z/X) of the models. The mass is nearly evenly distributed, with slightly more models at 1.65 $M_\odot$. Composition is also nearly uniform in its distribution. For comparison, in the Grevesse & Noels (1993) mixture $(Z/X)_\odot = 0.0245$ and the metallicity is $Z_\odot = 0.0175$. The lower panel of Fig. 4.2 plots the mean sound speed of the models, offset by the mixing length parameter α, as a function of Z/X. All models are split evenly for each of the mixing length values used in the calculations (α = 1.4, 1.6, and 1.8). The large spacing of the models ($\Delta\nu \sim (M/R^3)^{1/2}$) ranges from $\sim$ 57–81 μHz. Some physical characteristics of the models that are closest to the four corners of the errorbox, along with the model that is closest to the centre of the box, are listed in Tab. 4.1. Those models show a range of physical parameters and will be used in the following sections as examples illustrating the properties of the oscillation spectra and magnetic perturbations to those model spectra.

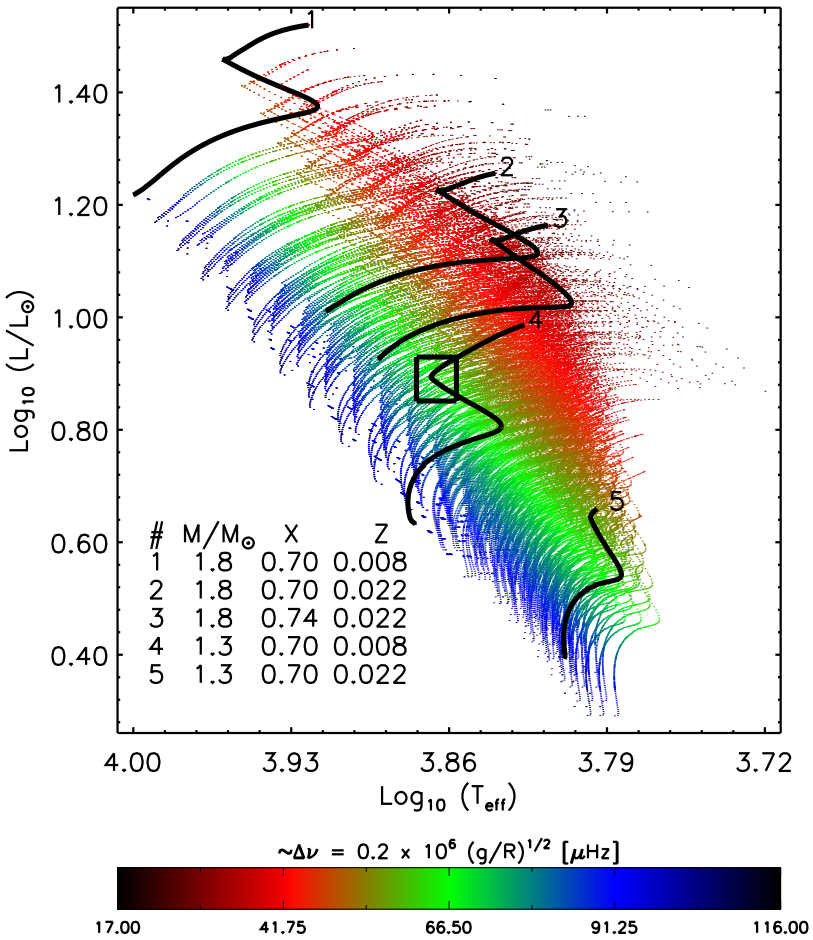

Figure 4.1: A theoretical HR diagram showing the extremes of the explored parameter space. The black error box represents the Hipparcos luminosity and the effective temperature appropriate for HR 1217 (see § 4.1.1 for details). Contours show lines of constant $\Delta\nu$ and five evolutionary tracks are selected showing how position on the HR diagram is affected by changing composition and mass. The metallicity has the greatest effect on the evolutionary status of the stellar model. A track shifts toward the lower right of the HR diagram (making the stars cooler and less luminous) by increasing Z.

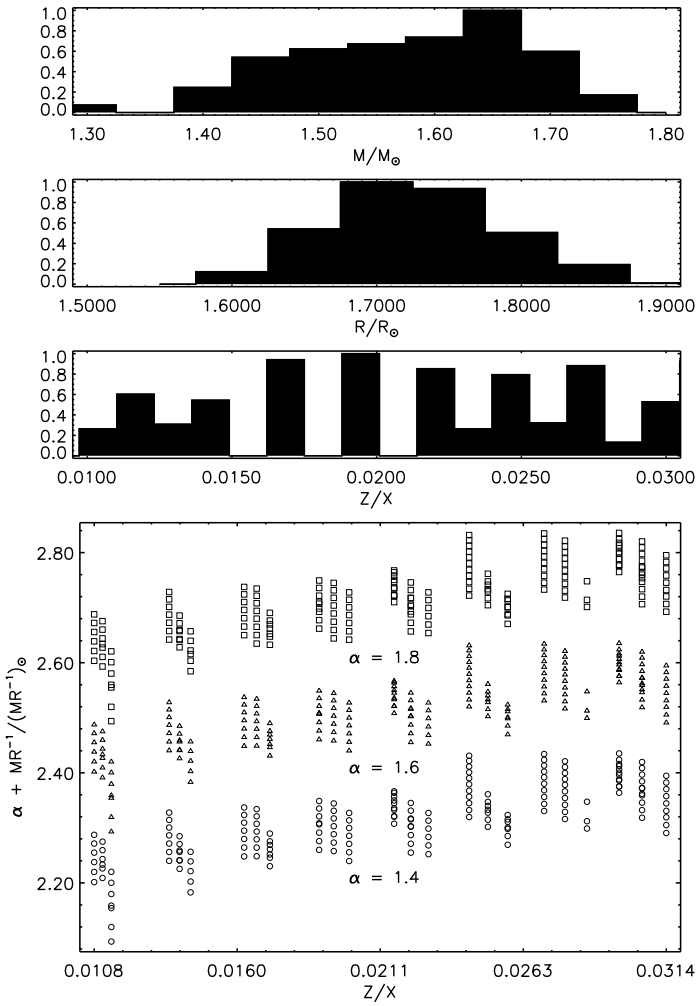

Figure 4.2: Histograms of model properties. The three smaller panels at the top of the figure show how mass (solar units), radius (solar units) and composition (Z/X) are distributed within the Hipparcos error box (see Fig. 4.1). The lower panel plots mixing length α plus the ratio of the average dynamical speed squared to that of the sun as a function of composition. That quantity is plotted to illustrate that the models are nearly equally split in mixing length values ($\alpha = 1.4$, 1.6 and 1.8).

Table 4.1: Some properties of selected models. Models A and B have luminosities and effective temperatures that are the closest to the upper left and right corners (respectively) of the error box shown in Fig. 4.1. Model C is the closest to the centre of the error box while models D and E are nearest to the lower left and right corners, respectively.

#	$M/M_\odot$	X	Z	Age (Gyr)	α	$M_{conv.core}/M_\star$
	$M_{conv.env.}/M_\star$	$\log_{10}(T_{\rm eff})$	$\log_{10}(L/L_\odot)$	$\log_{10}(R/R_\odot)$	$\Delta\nu$ (μHz)	Acoustic cut-off (μHz)
A	1.30	0.700	0.008	2.15	1.8	0.000
	0.0	3.8577	0.9284	0.2727	57.60	1393.52
B	1.45	0.720	0.008	1.35	1.8	0.118
	0.0	3.8740	0.9289	0.2403	66.96	1703.88
C	1.55	0.740	0.012	1.10	1.8	0.142
	0.0	3.8691	0.8912	0.2312	71.53	1908.77
D	1.40	0.700	0.010	1.40	1.8	0.119
	0.0	3.8576	0.8518	0.2346	67.80	1790.08
E	1.65	0.740	0.018	0.45	1.8	0.148
	0.0	3.8730	0.8523	0.2039	80.76	2280.42

Convection can influence both the evolutionary status and pulsation properties of a star, and a near-surface convective zone has implications for the surface chemical inhomogeneities of Ap stars. Models with higher Z/X tend to have convective cores that last longer than those with a smaller Z/X ratio. Models with a lower Z value tend to be the oldest models in the sample. This is also true for higher X, but the relation is not as strong. The mass of the convective envelope is insignificant in our models. Only a small fraction of the models exhibit convection over a large fraction of the stellar envelope ($\sim$ 1% of the model mass). These models should be more efficient at mixing away patches of chemical inhomogeneities, and as such, we may (potentially) rule out low mass, evolved, and high Z models as candidates Ap stars.

Of the models shown in Fig. 4.1, those with a $\Delta\nu \sim 34$ μHz are higher mass models and have Z values greater than the solar value. The change in the heavy metal content of the models produces the largest change on the position of a model on the HR diagram. Many of the models in the errorbox have a mid-range mass of about 1.6 $M_\odot$ and a metallicity ranging from Z $\sim$ 0.014–0.020. Models that seem to best reproduce the observed large spacing are those with a mass $\gtrsim$ 1.5 $M_\odot$ and a near solar composition of Z/X $\sim$ 0.024.

4.2 Pulsation models

The pulsation calculations are carried out using the nonadiabatic pulsation package of David Guenther (JIG, Guenther 1994). JIG solves the six linearized, nonadiabatic equations of nonradial stellar oscillations using the

Henyey relaxation method (Henyey et al., 1959). These six complex partial differential equations describe the radial dependence of the vertical and horizontal displacement vectors, the Lagrangian perturbations to the entropy and the radiative luminosity, as well as the Eulerian perturbations to the gravitational potential and its radial derivative. The time dependence of the perturbed quantities is periodic through the function $\exp(i\sigma t)$, where the σ is the complex eigenfrequency. A complete introduction to both the adiabatic and nonadiabatic, nonradial oscillation equations can be found in Unno et al. (1989) or Christensen-Dalsgaard (2003). (See chapter 1 for a short introduction to the subject of non-radial oscillations.)

In this thesis we avoid the complications associated with modelling the stability of calculated eigenmodes. As such, we only make use of the adiabatic frequencies calculated by the JIG code. In the adiabatic approximation perturbations to the energy equation (luminosity) are ignored and the sound speed is given by

$$c_s^2 = \frac{dp}{d\rho} = \Gamma_1 \frac{p}{\rho} \tag{4.1}$$

$\Gamma_1 = (\partial \ln p / \partial \ln \rho)_S$ is the first adiabatic exponent. The linear, adiabatic, nonradial stellar pulsation equations represent a fourth-order system of equations with two boundary conditions at the centre of the model and two conditions at the models surface. (See § 1.1.1 for the pulsation equations.) The presence of an eigenvalue makes the system nonlinear and a normalization of one of the eigenfunctions (radial displacement ξ) at the surface is used to close the system. We present an alternative method of calculating normal modes of stellar models in § 4.2.1 so, for completeness, we list the adiabatic

equations as given in Unno et al. (1989). Namely,

$$\begin{aligned}
\frac{1}{r^2}\frac{d}{dr}(r^2\xi) &= \frac{g\xi}{c_s^2} - \left(1 - \frac{\ell(\ell+1)c_s^2}{r^2\sigma^2}\right)\frac{p'}{\rho c_s^2} + \frac{\ell(\ell+1)}{r^2\sigma^2}\Phi' \\
\frac{1}{\rho}\frac{dp'}{dr} &= -(N^2-\sigma^2)\xi - \frac{g}{\rho c_s^2}p' - \frac{d\Phi'}{dr} \\
\frac{1}{r^2}\frac{d}{dr}(r^2\frac{d\Phi'}{dr}) &= \frac{\ell(\ell+1)}{r^2}\Phi' + 4\pi G\rho\left(\frac{p'}{\rho c_s^2} + \frac{N^2\xi}{g}\right)
\end{aligned} \tag{4.2}$$

In the above equations primed (´) quantities are Eulerian perturbations (see § 1.1.1), $\mathrm{N}^2 = g\left(\Gamma_1^{-1} d\ln p/dr - d\ln\rho/dr\right)$ is the Brunt-Väisälä (or bouncy) frequency, and Φ is the gravitational potential. Other symbols have their usual meaning. JIG calculates eigenfunctions defined by the variables first used by Dziembowski (1971)

$$y_1 = \xi_r/r,\ y_2 = \frac{1}{gr}\left(p'/\rho + \Phi'\right),\ y_3 = \frac{1}{gr}\Phi',\ \text{and } y_4 = \frac{1}{g}\frac{d\Phi'}{dr} \tag{4.3}$$

Using these definitions we arrive at the final form of the adiabatic oscillation equations used in this thesis:

$$\begin{aligned}
r\frac{dy_1}{dr} &= (V_g - 3)\,y_1 + \left(\frac{\ell(\ell+1)}{c_1\bar{\sigma}^2} - V_g\right)y_2 + V_g y_3 \\
r\frac{dy_2}{dr} &= \left(c_1\bar{\sigma}^2 + A^*\right)y_1 + (1 - U - A^*)\,y_2 + A^* y_3 \\
r\frac{dy_3}{dr} &= (1-U)y_3 + y_4 \\
r\frac{dy_4}{dr} &= -UA^* y_1 + UV_g y_2 + (\ell(\ell+1) - UV_g)\,y_3 - Uy_4
\end{aligned} \tag{4.4}$$

In the above, the homology relations $U = 4\pi\rho r^3/M_r$ and $V_g \equiv V/\Gamma_1$ (with $V = GM_r\rho/rp$) are introduced. The measure of the local density to the mean density of the star is given as U and V is the ratio of gravitational energy to the internal energy of the stellar material. A^* and c_1 are defined as

$A^* \equiv rA = -rN^2/g$ and $c_1 = (r/R)^3/(M_r/M)$. The dimensionless frequency $\bar{\sigma} = \sigma\sqrt{R^3/(GM)}$ is used.

The boundary conditions are described in Saio & Cox (1980) and in the books by Unno et al. (1989) and Cox (1980). The outer mechanical boundary condition assumes a finite pressure at the stellar surface. A potential condition matches the perturbed gravitational potential and its derivative at the stellar surface. The two inner boundary conditions require regular solutions of the pulsation variables as the stellar radius goes to 0. Written in terms of the Dziembowski variables, the outer boundary conditions are

$$\left(1 - \frac{4 + c_1\bar{\sigma}^2}{V}\right) y_1 + \left(\frac{\ell(\ell+1)}{c_1\bar{\sigma}^2 V} - 1\right) y_2 + \left(1 - \frac{\ell+1}{V}\right) y_3 = 0 \tag{4.5}$$

and

$$U y_1 + (\ell+1) y_3 + y_4 = 0 \tag{4.6}$$

The inner boundary conditions are

$$\frac{c_1\bar{\sigma}^2}{\ell} y_1 - y_2 = 0 \tag{4.7}$$

and

$$\ell y_3 - y_4 = 0 \tag{4.8}$$

We calculate frequencies for models of HR 1217 using angular degrees ranging from $\ell = 0$–4 in the frequency range 1900–3100 μHz. This encompasses the observed oscillations of HR 1217 (see chapter 3). In all there are about 50,000 individual modes (oscillation frequencies) calculated. Example spectra, including magnetic effects, will be discussed in § 4.3 and in chapter 5. (See also Fig. 4.4 for example spectra.) Because there are so many modes calculated in a grid of models, we first explore (qualitatively) matches

between quantities like the large and small spacing (Eqs. 1.12 and 1.16). By design our grid of models shows large spacing values appropriate for HR 1217 ($\sim 68\ \mu$Hz). The grid, plotted in Fig. 4.1, shows that increasing Z shifts the models to the lower right of the HR diagram and decreasing Z shifts the models to the upper left. The lowest mass models in our grid that enter our defined error box (highlighting the position of HR 1217 in the HR diagram) have the lowest Z values in our grid. Likewise, the models with the largest mass in our grid that fall in the same error box have the highest Z values as well. Generally, the more luminous the model is, the lower its large spacing is because it tends to be less dense (because of its larger radius).

The models with a small spacing of $\sim 2.5\ \mu$Hz may be important for the interpretation of the frequency analysis of § 3.3. Figure 4.3 shows the small spacing for the models outlined in Tab. 4.1 with the angular degree differences of $\ell = 2$ - $\ell = 0$, $\ell = 3$ - $\ell = 1$, and $\ell = 4$ - $\ell = 2$. The models with the second order spacing of $\lesssim 3\ \mu$Hz are either older (compared to other models listed in Tab. 4.1), or have a mass less than $\approx 1.5\ M_{\odot}$. The metallicity Z of these models also tends to be lower than a solar metallicity. This is in agreement with Cunha et al. (2003) who show the best qualitative model match has a Z value that is less than solar. It is also interesting to note that the second order separations between $\ell = 4$ - $\ell = 2$ are much larger ($\gtrsim 4\times$) than the observed value of about 2.5 μHz. This suggests that if the observed differences are indeed small spacings, they are separations defined by differences between the lowest degree modes. We will show in § 4.3 that including the magnetic field can dramatically alter the spacings of the models, casting doubt on whether or not we really observe a small

spacing as defined by asymptotic theory.

4.2.1 A new search method for eigenmodes

There are a number of numerical methods that have been used to solve the set of Eqs. 4.4. A general discussion of these methods may be found in the lecture notes of Christensen-Dalsgaard (2003). Recently, a number of researchers have compared their software and outline the reduction procedures used to calculate the normal modes of a stellar model (see Moya et al. 2008 and references therein). The most popular methods for calculating oscillation spectra of models are the shooting method and variants of the relaxation (Newton) method (e.g., the Henyey relaxation).

In the case of the shooting method, the solution is integrated both inward and outward from the surface and central boundary conditions and then matched at a suitable fitting point for a given eigenfrequency σ^2. If the difference between the inward and outward solutions at the fitting point is zero (to some numerical accuracy) then σ^2 is an eigenvalue of the problem. Thus, a number of σ^2 can be scanned to find the eigenvalue to a prescribed numerical accuracy. The drawback of this method is in the choice of fitting point. This is highly dependent on the mode being investigated and may be placed either in the upper atmosphere of the model or in the deep interior. Experience is required to find a fitting point that yields an accurate and stable numerical solution.

Relaxation methods also exist in which all of the eigenfunctions and the eigenvalue are iteratively refined at each mesh point in the model. Examples

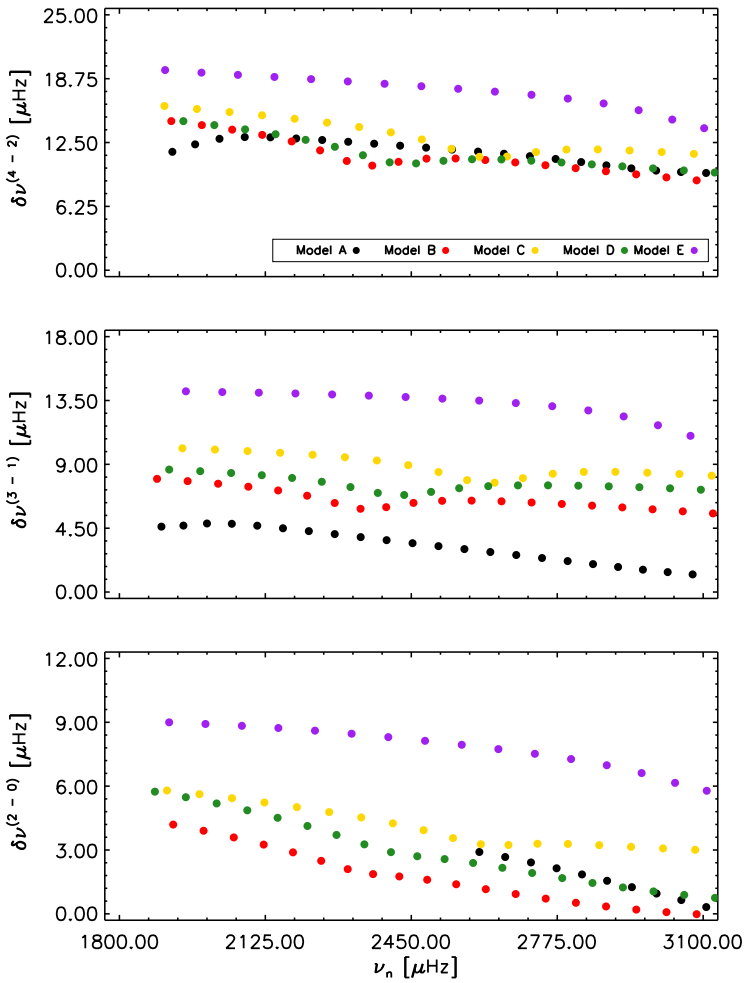

Figure 4.3: Small spacings for the models listed in Tab. 4.1 (see legend for colour codes) as a function of mode frequency. The top panel gives the frequency differences of modes with degrees between $\ell = 4$ and 2, the middle panel for degrees between $\ell = 3$ and 1, and the lower panel for degrees between $\ell = 2$ and 0. The potential small spacing (§ 1.1.1, and Eq. 1.16) observed in the *MOST* data is $\lesssim$ 3 μHz (see Tab. 3.2) and is best reproduced by models with lower Z and for small separation between the lowest angular degrees ($\ell =$ 0 and 2).

of this method are found, for example, in Unno et al. (1989) and Henyey et al. (1964). The JIG code described above uses a relaxation method to find the eigenvalues of a model. This method requires an initial guess that is close to the eigenvalue in order have fast convergence. In addition, the initial setup of this method tends to be complicated.

A direct solution to the eigenvalue problem using matrix methods also exists but they tend to be the least efficient (in time and memory) of all the methods (see Christensen-Dalsgaard 2003).

A new method of calculating and scanning for eigenmodes was developed by Kobayashi (2007). This method efficiently integrates the set of adiabatic equations using a matrix method and was developed to study normal modes in the Earth's atmosphere. This method is, in some sense, a cross between a relaxation method and a direct integration. We show the results for two selected models as a consistency check with the modes calculated using JIG.

Equations 4.4 are written in matrix form as

$$\frac{dy_j^i}{dr_j} = B_j y_j^i, \; i = 1, \ldots, 4 \text{ and } j = 1, \ldots, \aleph \tag{4.9}$$

where B is a 4x4 matrix, defined at the jth shell, with entries filled as the terms on the right hand side of Eqs. 4.4. The model is comprised of $\aleph$ shells with the first shell ($j = 1$) located at the centre of the model. Equation 4.9 may be rewritten in a finite difference form, relating variables between shells in the model as

$$C_n y_n + D_{n+1} y_{n+1} = 0 \tag{4.10}$$

with $C_n = \mathbf{I} + \Delta r B_n/2$, $D_{n+1} = -\mathbf{I} + \Delta r B_{n+1}/2$, and $\Delta r = r_{n+1} - r_n$.

A Henyey-type banded matrix is formed from the system of Eqs. 4.10 with the following definitions:

$$P_n \equiv [C_n^L \ \mathbf{0}]^T \ n = 2, \ldots, \aleph$$

$$S_n \equiv [D_n^L \ C_n^U]^T \ n = 2, \ldots, \aleph - 1$$

and

$$Q_n \equiv [\mathbf{0} \ D_{n+1}^U]^T \ n = 1, \ldots, \aleph - 1$$

The upper indices L and U refer to (respectively) the lower and upper halves of matrices C or D. S_1 is a special case which has its upper half as the inner boundary conditions and its lower entries as the upper entries of C_1. Likewise, $S_\aleph$ is composed of the lower half of $D_\aleph$ and the outer boundary conditions.

In this banded form, and for a given σ^2, the system of equations may be integrated recursively from the centre of the model to its surface using

$$y_n = R_n y_{n+1}$$

where

$$R_n = -X_n^{-1} Q_n,$$
$$X_n = P_n R_{n-1} + S_n$$

and starting from $R_1 = -S_1^{-1} Q_1$.

At the surface of the model $X_\aleph y_\aleph = 0$ and σ^2 is an eigenvalue only if $\det X = 0$. Integrating the equations in this manner is accomplished in order

$\aleph$ time and with order $\aleph$ memory because storage is only needed for the $\aleph$ R values (required to calculate the eigenfunctions).

Along with the speed of this integration method there is also an advantage in the form of the eigenvalue search. Kobayashi (2007) showed that if we expand $X_\aleph y_\aleph = 0$ about a perturbation in the eigenvalue $\delta\sigma^2$, we arrive at a small (4 x 4 matrix in the adiabatic case) generalized eigenvalue problem at the surface of the model

$$\left(X_\aleph + \delta\sigma^2 \frac{\partial X_\aleph}{\partial \sigma^2}\right) y_\aleph = 0 \tag{4.11}$$

where the partial derivatives of X are also found through the recursion relations used to integrate the system. Given a guess value of σ^2 the solution relaxes to the correct eigenvalue by replacing σ^2 with $\sigma^2 + \delta\sigma^2$ until some predefined stopping criteria is satisfied.

We calculate the eigenfrequencies for models A and E of Tab. 4.1 using the method outlined above. Following Roxburgh (2008), we first define the functions

$$\Xi = \frac{d\Phi'}{dr} + 4\pi G\rho\xi \tag{4.12}$$

and

$$r\sigma^2\zeta = \delta p/\rho + \xi g + \Phi' \tag{4.13}$$

where ζ is identified as the horizontal component of the displacement vector. We normalize the stellar structure variables using

$$\begin{gathered} r = Rx, \quad \rho = \frac{M}{4\pi R^3}\bar{\rho}, \quad g = \frac{GM}{R^2}\bar{g}, \\ c^2 = \frac{GM}{R}\bar{c}^2, \quad p = \frac{GM^2}{4\pi R^4}\bar{p}, \quad \sigma^2 = \frac{GM}{R^3}\bar{\sigma}^2 \end{gathered} \tag{4.14}$$

and recast Eqs. 4.2 in the following form:

$$\begin{aligned}
\frac{dy_1}{dx} &= \frac{\ell(\ell+1)}{x}y_0 - \frac{2}{x}y_1 - \frac{1}{x}y_2 \\
\frac{dy_2}{dx} &= -\frac{\ell(\ell+1)\bar{\rho}\bar{g}}{x\bar{p}}y_0 + \left(\frac{\bar{\sigma}^2\bar{\rho}}{\bar{p}} + \frac{4\bar{g}\bar{\rho}}{x\bar{p}}\right)y_1 + \frac{\bar{g}\bar{\rho}}{\bar{p}}y_2 - \frac{\bar{\rho}}{\bar{p}}y_4 \\
\frac{dy_3}{dx} &= -\bar{\rho}y_1 + y_4 \\
\frac{dy_4}{dx} &= \frac{\ell(\ell+1)\bar{\rho}}{x}y_0 + \frac{\ell(\ell+1)}{x^2}y_3 - \frac{2}{x}y_4
\end{aligned} \tag{4.15}$$

The eigenfunctions of the system are defined by

$$\begin{gathered}
y_0 = \zeta/R, \quad y_1 = \xi/R, \quad y_2 = \frac{\delta p}{p}, \\
y_3 = \frac{R}{GM}\Phi', \quad \text{and} \quad y_4 = \frac{R^2}{GM}\Xi
\end{gathered} \tag{4.16}$$

Note that in Eqs. 4.15 we use the Lagrangian variation of the pressure δp. The result is that the Brunt-Väisälä (N^2) frequency disappears from the linearized pulsation equations.

Figure 4.4 shows the comparison between the frequencies calculated using this method and those calculated using JIG for models A and E of Tab. 4.1. The plot shows the (non-dimensional) eigenvalue correction $\delta\sigma^2$ as a function of frequency ν (the guess for the eigenvalue of the system) for ℓ values from 0 to 4. If the correction is positive, our guess eigenvalue is too low and the correction leads us forward (toward the true eigenvalue) by increasing our guess by the increment $\delta\sigma^2$. When the correction goes to zero for a given guess frequency, we have found an eigenvalue. Note that not all of the zeroes of the function $\delta\sigma^2(\nu)$ shown in Fig. 4.4 correspond to pulsation eigenvalues for the models A and E. Consider the behaviour of the correction near a zero where the function $\delta\sigma^2(\nu)$ has a positive slope. A positive $\delta\sigma^2$ near that zero

will move our guess further away from the zero. A negative $\delta\sigma^2$ will also move us away from the x-intercept if the local slope is positive. If the local slope of $\delta\sigma^2(\nu)$ is negative, $\delta\sigma^2$ can be either positive or negative, and the correction will guide our guess towards the zero (or eigenvalue). Therefore, values of the $\delta\sigma^2(\nu)$ function that approach zero with a negative slope (suggesting a decreasing correction) are eigenvalues of the system. The normal modes calculated from JIG are shown as red points distributed along the line $\delta\sigma^2 = 0$. The agreement is exact to the precision output by JIG (5 decimal places) and no eigenmodes were missed during the calculation of frequencies used for this thesis.

Although only tested in the adiabatic case, this method was originally designed to work for a complex set of non-adiabatic equations used in a geophysical context (Kobayashi, 2007). Traditionally an adiabatic solution is required as an initial guess for both the eigenvalues and the eigenfunctions of the non-adiabatic solution to the stellar pulsation equations. This method offers an efficient alternative to that approach.

4.3 The magnetic effects

The effects of the magnetic field on both the oscillation frequencies and the eigenfunctions have been described by a number of authors (see recent reviews by Cunha 2007, Saio 2008 and Shibahashi 2008). The kG strength magnetic fields in roAp stars complicate the interpretation of the observed eigenmodes by introducing deviations from the expected (near asymptotically spaced) frequency spectrum. In the outer layers of the roAp stars

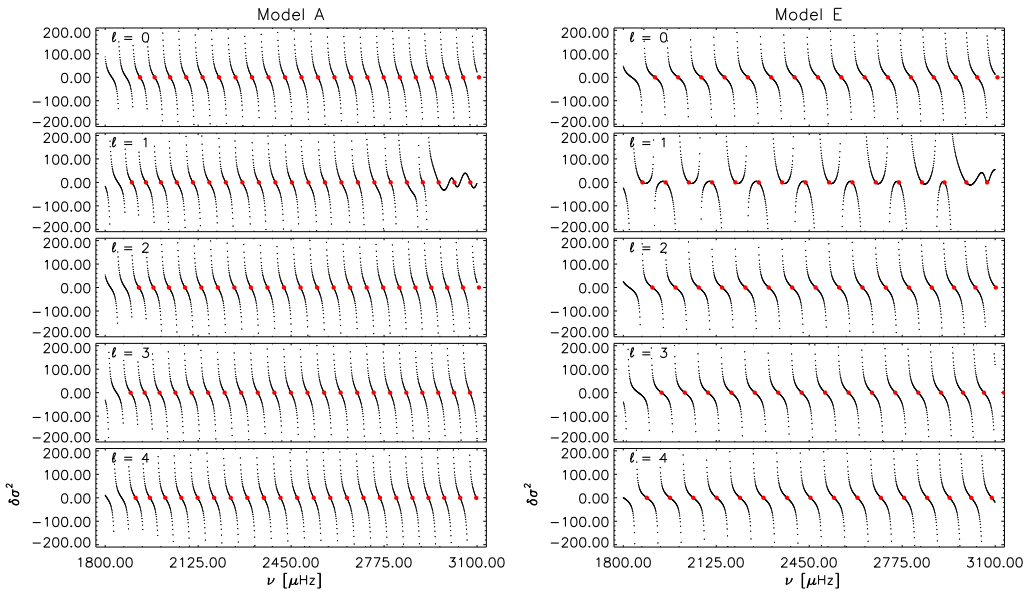

Figure 4.4: A comparison of eigenfrequencies determined by two different methods. The left panels show the non-dimensional eigenfrequency correction $\delta\sigma^2$ (normalized by GM/R^3) as a function of frequency ν, for ℓ values of 0 to 4 (from top to bottom panels), for model A of Tab. 4.1. The black dots represent the eigenfrequency corrections described in § 4.2.1 and the red circles are the eigenfrequencies calculated for this thesis with JIG (§ 4.2, and Eqs. 4.4). The right panels are the same as those on the left but use model E of Tab. 4.1. A value of $\delta\sigma^2 = 0$ is an eigenvalue of the system of Eqs. 4.15. Modes calculated with JIG agree with those determined using the new method developed by Kobayashi (2007).

($\lesssim 3\%$ of the total stellar mass) the Alfvén speed ($\propto \sqrt{B^2/\rho}$) is comparable to, or greater than, the local sound speed ($\propto \sqrt{p/\rho}$). The eigenmodes are no longer purely acoustic and are better described as magnetoacoustic waves. As the stellar density increases inward and the sound speed becomes larger than the Alfvén speed, these magnetoacoustic waves decouple into acoustic and magnetic components. The resultant magnetic slow waves act as an energy sink as they dissipate in the dense stellar interior. It is this loss of energy that results in the shifting of some frequencies and the deviations from the regular asymptotic spacing. There has been recent success in the interpretation of roAp oscillations (e.g., Cunha 2001).

Cunha & Gough (2000) (see also Cunha 2006) estimate the magnetic perturbation to the eigenmodes of nonmagnetic stellar models using a variational principle. The method matches a numerical solution of the ideal magneto-hydrodynamic equations in a boundary layer located in the upper envelope and atmosphere of the model to an asymptotic expression for the eigenfunctions of high-overtone, acoustic oscillations in the stellar interior. The phase difference between the numerical and asymptotic expressions for the eigenfunctions is used to estimate the corresponding frequency shifts as a result of magneto-acoustic interactions. A determination of the perturbed eigenmodes using a variational principle, calculated from an estimate of the perturbed eigenfunctions (obtained using a background stellar model that does not include magnetic fields), is an attractive alternative to a perturbation analysis or a full scale MHD calculation of magneto-acoustic modes. This method, developed by Cunha & Gough (2000), follows the earlier work of Campbell & Papaloizou (1986).

To start the modelling procedure, Cunha & Gough (2000) divide the star into a thin outer boundary layer and the interior. In the boundary layer, the Lorentz forces are comparable to, or larger than, the gas pressure, while in the interior the field is essentially force free. Because the magnetic boundary layer is thin, a plane-parallel approximation may be used. It is also assumed that the effects of the magnetic field can be calculated locally at each latitude. For this geometry the field only varies in the vertical direction and has components $\mathbf{B} = (B_x, 0, B_z)$. The magneto-acoustic waves are described using a horizontal wavenumber $\mathbf{k} = (k_x, k_y, 0)$. Using this information, the adiabatic, magnetically non-diffusive, pulsation equations may then be written as (Campbell & Papaloizou 1986, Cunha & Gough 2000 and Cunha 2006)

$$-\sigma^2 \rho u = i|\mathbf{k}|\mathrm{W} + (\mathbf{B}\cdot\nabla)^{\mathbf{2}} \frac{\mathrm{u}}{\mu_{\mathbf{0}}} - \frac{\mathrm{k_x B_x}}{\mu_{\mathbf{0}}|\mathbf{k}|} (\mathbf{B}\cdot\nabla)(\nabla\cdot\xi) \tag{4.17}$$

$$-\sigma^2 \rho v = (\mathbf{B}\cdot\nabla)^2 \frac{v}{\mu_0} + \frac{\mathrm{k}_y \mathrm{B}_x}{\mu_0|\mathbf{k}|} (\mathbf{B}\cdot\nabla)(\nabla\cdot\xi) \tag{4.18}$$

$$-\sigma^2 \rho \xi_z = \frac{\partial W}{\partial z} - g\nabla\cdot(\rho\xi) - \frac{\mathrm{B}_z}{\mu_0}\left[(\mathbf{B}\cdot\nabla)(\nabla\cdot\xi)\right] + (\mathbf{B}\cdot\nabla)^2 \frac{\xi_z}{\mu_0} \tag{4.19}$$

where

$$W = \xi\cdot\nabla p + \left(\gamma p + \frac{\mathrm{B}^2}{\mu 0}\right)(\nabla\cdot\xi) - \frac{(\mathbf{B}\cdot\nabla)(\mathbf{B}\cdot\xi)}{\mu_0} \tag{4.20}$$

and

$$g = \frac{1}{\rho}\frac{dp}{dz} \tag{4.21}$$

In these equations the displacement vector ξ is decomposed into a vertical component $\xi_z = \xi\cdot\mathbf{e_z}$, a component that is perpendicular to the wavenumber $v = \xi\cdot(e_z \times \mathbf{k})/|\mathbf{k}|$, and a component that is parallel to the wavenumber $u = (\xi\cdot\mathbf{k})/|\mathbf{k}|$. The local gravitational acceleration is denoted by g and the first adiabatic exponent is γ. All other symbols have their usual meanings.

In the deep interior a magneto-acoustic mode completely decouples into a pure Alfvénic mode and a pure acoustic mode. This was verified analytically by Roberts & Soward (1983) and numerically by Campbell & Papaloizou (1986). The JWKB approximation is used to describe the magnetic modes in the interior. This approximation to the eigenfunctions takes the functional form (Cunha & Gough 2000; see also Gough 2007)

$$(v_{mz}, u_{mz}) \backsim \rho^{-1/4}(C, D) \exp\left[i \int_0^z \left(\frac{\mu_0 \rho \sigma^2}{B_z^2}\right)^2 dz - i\frac{k_x B_x z}{B_z}\right] + \rho^{-1/4}(C_+, D_+) \exp\left[-i \int_0^z \left(\frac{\mu_0 \rho \sigma^2}{B_z^2}\right)^2 dz - i\frac{k_x B_x z}{B_z}\right] \quad (4.22)$$

where C, D, C_+, and D_+ are complex constants. The inward propagating Alfvén waves are expected to dissipate before they are reflected back toward the surface of the star (Roberts & Soward, 1983). With this in mind, the constants C_+ and D_+ in Eq. 4.22 may then be set to zero to guarantee that no outwardly propagating magnetic waves occur in the interior.

In the interior, the vertical component of the uncoupled modes is essentially acoustic. The amplitude of this vertical mode may be represented asymptotically by (Cunha & Gough 2000)

$$\xi_z \backsim \frac{A\varkappa^{1/2}}{\rho^{1/2}} \cos\left(\int_z^{z^*} \varkappa dz + \delta_p\right) \quad (4.23)$$

were δ_p is a phase and $\varkappa$ is the vertical acoustic wavenumber. The coordinates z and z^* represent the depth in the boundary layer and the position of the base of the boundary layer, respectively.

To integrate Eqs. 4.17–4.19 there need to be five boundary conditions (Cunha & Gough, 2000) to match the components of the displacement and

the magnetic field variations. We use a fully reflective mechanical outer boundary condition of the form

$$p\nabla \cdot \xi = 0 \tag{4.24}$$

The other outer boundary condition requires that the magnetic field be matched continuously onto a vacuum field. This may be written as

$$(B \cdot \nabla)\xi - B\nabla \cdot \xi = \nabla\phi_m \tag{4.25}$$

where ϕ_m is an exponentially decreasing plane wave solution of the Laplace equation. The boundary condition 4.25 can be separated into two conditions: one condition relating the vertical displacement and the variable u (defined above), and the other involving the variable v (defined above; also see Cunha & Gough 2000). The numerical solutions of the system of Eqs. 4.17 to 4.19 are matched to the asymptotic relations 4.22. This provides the two interior boundary conditions.

The vertical component of the solution is then matched to Eq. 4.23 at each latitude to obtain values for the magnetic phases δ_p. The purely acoustic (numerical) solution; i.e, $\mathbf{B} = 0$ in Eqs. 4.17 to 4.19, is also matched to Eq. 4.23 to obtain the unperturbed phases δ_{p0}. Phase shifts $\Delta\delta_p$ are calculated from the difference between these two phases at each latitude. The matching procedure is outlined in Cunha & Gough (2000) and Cunha (2006).

The variational method of Cunha & Gough (2000) is used to estimate the first-order frequency shifts of the eigenmodes caused by a magnetic field. The frequency shifts are calculated from

$$\frac{\delta\sigma_M}{\sigma_0} \backsimeq -\frac{\overline{\Delta\delta_p}}{\sigma_0^2 \int_{r_1}^{R^*} c_s^{-2} \varkappa_0^{-1} dr} \tag{4.26}$$

where the average of the phase shifts $\Delta\delta_p$ over a sphere is

$$\overline{\Delta\delta_p} = \frac{\int_0^\pi \Delta\delta_p (Y_\ell^m)^2 \sin\theta d\theta}{\int_0^\pi (Y_\ell^m)^2 \sin\theta d\theta} \tag{4.27}$$

The quantities with a subscript of zero are non-perturbed values. A complete description of the numerical procedure used to calculate the frequency shifts is outlined in the appendices of Cunha & Gough (2000) and Cunha (2006).

Examples of the magnetic shifts are presented below. There are sudden drops in the frequency corresponding to a maximum of energy loss of that particular mode. These sharp jumps are cyclic and depend on the magnetic field strength, the frequency range explored, and on the mode/magnetic field geometry. It is important to fully explore all relevant frequency ranges, mode geometries and magnetic field strengths if we hope to successfully match a calculated frequency spectrum to observations of roAp stars. For each of the modes calculated from the models presented in § 4.2, a magnetic perturbation is estimated for a dipolar magnetic field with polar strengths running from 1 to 10 kG in steps of 0.1 kG. In total there are 51,795 magnetic models calculated using physical parameters appropriate to the properties of HR 1217. This is the largest grid of magnetic models calculated for the seismic study of any roAp star.

The cyclic nature of the magnetic perturbations is shown in Fig. 4.5. Both real and imaginary parts of the magnetic shifts occur regularly as a power-law function ($\nu \times B^{\mathrm{n}}$). The index n in the power law is dependant on the structure of the outer layers of the background model. The models in Tab. 4.1 are used in this calculation. A value of n = 0.75 does a good job of phasing together the frequency shifts. This behaviour is discussed in Saio 2008 and references therein. It is important to notice the frequency shifts

between modes of degrees that differ by two are at least of the same order as the second-order, small spacing (Eq. 1.16). This may hamper efforts to use an observed small spacing as a diagnostic of stellar structure (Dziembowski & Goode, 1996).

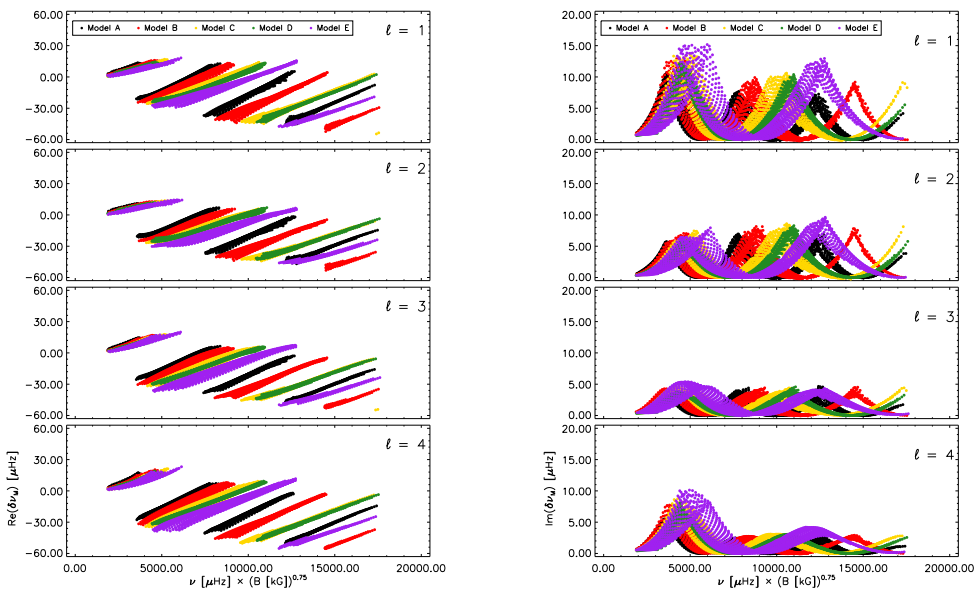

Figure 4.5: The cyclic behaviour of the real and imaginary magneto-acoustic shifts. The real part of the shifts calculated for models in Tab. 4.1 are presented in the left panels and the imaginary parts are given in the right panels. From top to bottom are the degrees of the modes (from $\ell = 1$ down to $\ell = 4$) and all magnetic fields (B = 1–10 kG) are shown. The position of the shifts is cyclic and can approximately be phased as $\nu \times \mathrm{B}^{0.75}$. The exponent on B is sensitive to the outer layers of the model. Note that a maximum in the imaginary part corresponds to a sudden jump in the real frequency shift.

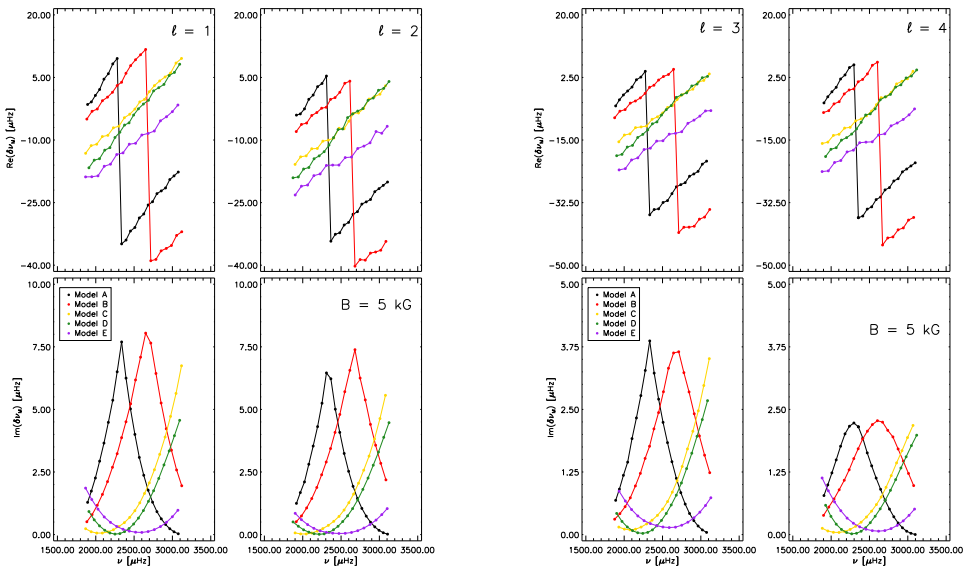

Figure 4.6: The magnetic perturbations for a 5 kG magnetic field using models from Tab. 4.1. The left plot set (consisting of four plots) are for degrees of $\ell = 1$ and 2 and the right plot set is for degrees of 3 and 4. The upper panels show the real frequency shifts as a function of frequency while the lower portions of the figure give the imaginary shifts. Models with frequency shifts of ~ -15 μHz around 2800 μHz could explain the anomalous frequency (or "missing mode", see § 1.3) identified by Kurtz et al. (2002). Note that the difference between the magnetic shifts of degrees that differ by 2 can be as large as, or greater than, the small spacing for a main sequence, A-type star (~ 10 μHz; see Fig. 4.3).

The magnetic perturbations to frequencies from 1500 to 3500 μHz are shown in Fig. 4.6 assuming a dipolar magnetic field with a polar strength of 5.0 kG and using the models of Tab. 4.1. This frequency range is consistent with measurements of HR 1217 (§ 3.3) and shows the real and the imaginary

frequency shifts for modes having degrees of $\ell = 1$ through 4. Note that the difference between real frequency shifts for modes of different degree amounts to a few μHz. The imaginary part of the even $\ell = 2$ and 4 modes are lower than the odd ℓ counterparts. This was also shown for the case of a polytrope stellar model of Cunha & Gough (2000).

In general, if the imaginary part of the frequency is positive, the magneto-acoustic mode loses energy. The smaller amplitude of the imaginary part for the $\ell = 2$ modes, for example, suggest that they are less susceptible to damping from the magnetic field. This effect depends on the geometry of the mode and the magnetic field. Cunha & Gough (2000) and Cunha (2006) show that the maximum energy loss of a magneto-acoustic mode occurs approximately at the latitude where $B_z B_x$ is a maximum. This occurs at 45° for a dipolar magnetic field. Modes of higher degree ℓ decrease in amplitude as they approach the equator more quickly than modes of lower degree. When the phase shifts are averaged over a sphere, the net effect is a smaller imaginary frequency shift for modes of larger ℓ. These modes have smaller amplitudes near the latitude where the maximum of energy loss occurs.

A typical first step for pulsation modelling of a roAp star is to look at a small number of non-magnetic pulsation models and compare the calculated spacings to those observed in the spectrum of the star. Cunha et al. (2003) did this for HR 1217. They found that models with a sub-solar metallicity (Z $\lesssim$ 0.018) provided a better (qualitative) match to the observed (approximately asymptotic) spacing of HR 1217 ($\sim$ 68 μHz). We extend their analysis by looking at the spacings of models A–E in Tab. 4.1. The large spacings listed in Tab. 4.1 show that models B ($\Delta\nu = 66.96$ μHz), C

($\Delta\nu = 71.53$ μHz), and D ($\Delta\nu = 67.80$ μHz) come close to the large spacing of HR 1217. These models have metallicities of Z = 0.008, 0.012, and 0.010, respectively. Each of those metallicities is sub-solar. That being said, only one model (E) in Tab. 4.1 has a near solar metallicity of Z = 0.018. We can not say that only models with a smaller than solar Z value best match the properties of HR 1217. We can only say that the (small number of) models in Tab. 4.1 are in agreement with Cunha et al. (2003). Models with a Z $\lesssim$ 0.018 can reproduce the large spacing of HR 1217; but, models with a larger Z can also show such a match (see chapter 5).

Perhaps the more important question is: How does the introduction of a magnetic field affect the large spacing of the models? Figure 4.7 shows the large spacing calculated from the model pulsation frequencies ($\Delta\nu = \nu_{n+1,\ell} - \nu_{n,\ell}$), as a function of frequency, for the models in Tab. 4.1. The left panel of Fig. 4.7 shows models with B = 0 kG and the right panel shows pulsation models having B = 5 kG. Comparing the models between the two sets of panels shows the large spacing (on average) is not affected by the introduction of a magnetic field. A major exception to this rule occurs when one of the frequencies suddenly jumps in value. At that point (e.g. model A (black line) and B (red line) of Fig. 4.7), the large spacing shows a sharp decrease in value. This decrease can be a large fraction of the value of the large spacing itself. While $\Delta\nu$ varies slowly as a function of frequency even in the non-magnetic case, the magnetic field perturbation causes an abrupt decreases in $\Delta\nu$ over one spacing between modes. The inclusion of a magnetic field in the pulsation calculations seems to be the most reasonable way of producing such a sharp, and localized, feature in the

stellar oscillation spectrum. For HR 1217, the frequencies alternate between ~ 33.5 and 34.5 μHz over a frequencies ranging from about 2600 to 2800 μHz. That alternating pattern is suddenly cut by about half near the beginning and the end of the observed frequency range (see § 3.3). The introduction of a 5 kG magnetic field to the models in Tab. 4.1 does not show multiple jumps over the range of observed frequencies in the HR 1217 spectrum. The size of the decrease of $\Delta\nu$ shown in Fig. 4.7 is also too large by a factor of more than two compared to what is observed. In Fig. 4.8 we show the large spacing as a function of magnetic field for the same background models. Each of these background models exhibits a sudden jump in $\Delta\nu$ for some values of magnetic field. Interestingly, jumps in $\Delta\nu$ of less than about 20 μHz occur (for some models) at magnetic fields $\lesssim 5$ kG. This is similar behaviour to what is observed in HR 1217. Models with larger magnetic fields tend to show larger jumps for all ℓ values.

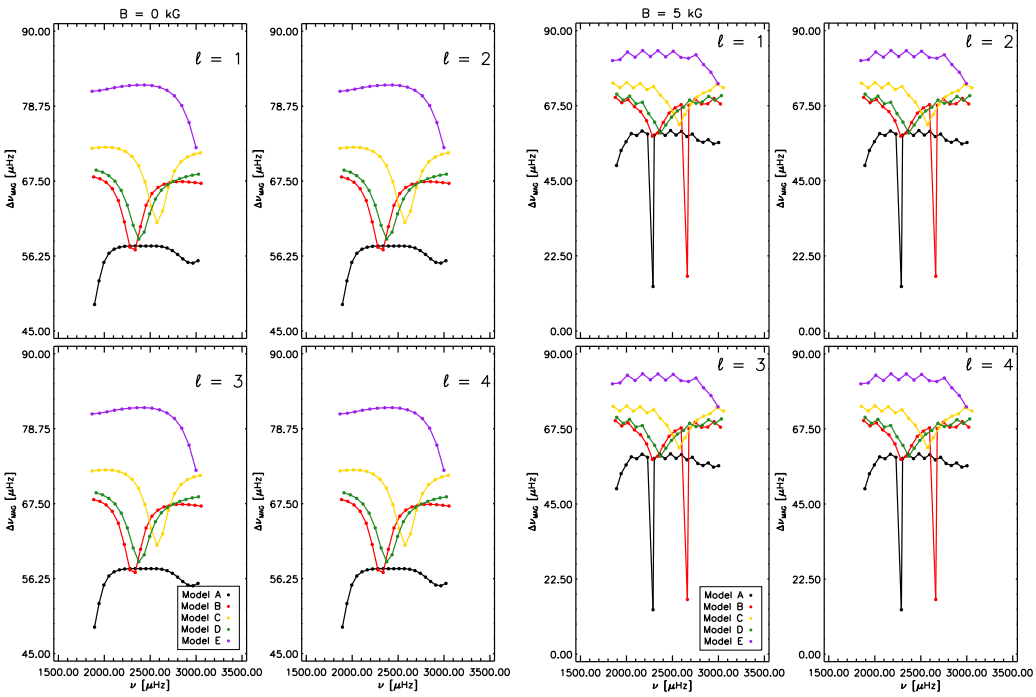

Figure 4.7: The magnetic perturbations to $\Delta\nu$ for a 0 and 5 kG magnetic field using models from Tab. 4.1. The left set of four plots show the large spacing $\Delta\nu = \nu_{n+1,\ell} - \nu_{n,\ell}$ as a function of frequency $\nu_{n,\ell}$ for angular degrees $\ell = 0$ through 4. The right set of plots show that perturbation to the large spacing caused by a 5 kG magnetic field. The inclusion of a magnetic field causes a sharp decrease in $\Delta\nu$ when there is a jump in frequency (see Fig. 4.6).

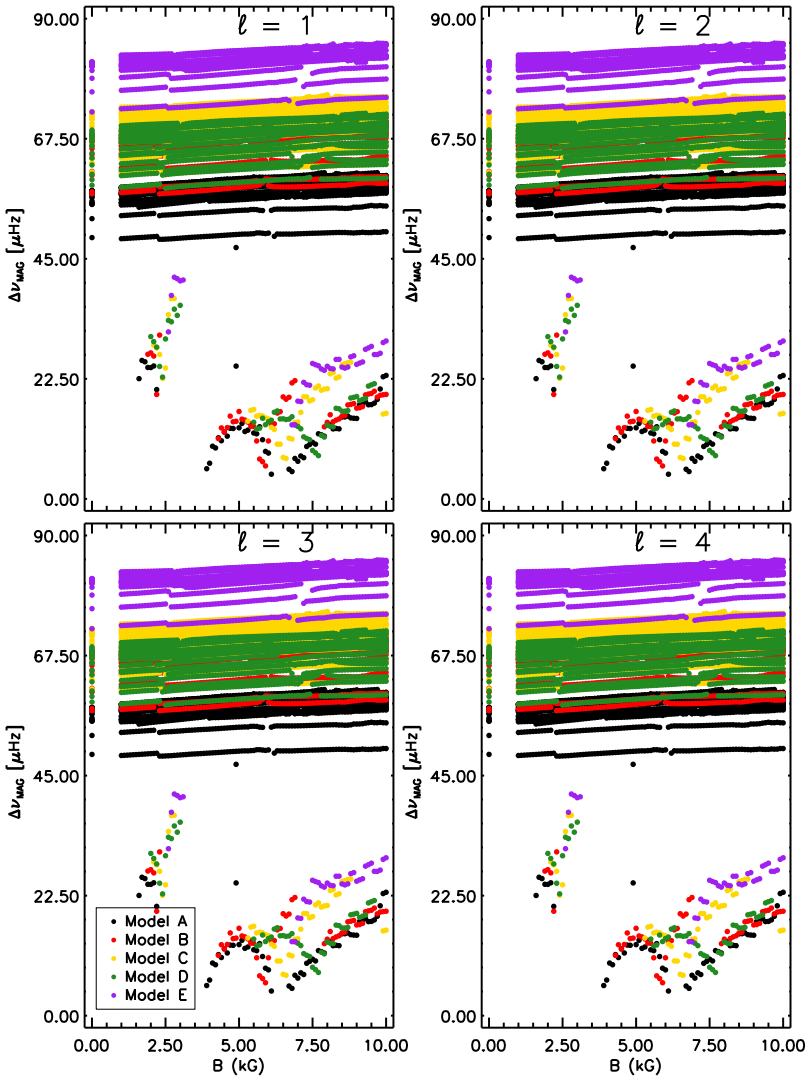

Figure 4.8: The magnetic perturbations to $\Delta\nu$ for all calculated magnetic field strengths using models from Tab. 4.1. The plots show the large spacing $\Delta\nu = \nu_{n+1,\ell} - \nu_{n,\ell}$ as a function of magnetic field strength for ℓ values identified at the top of each panel. The inclusion of a magnetic field causes a sharp decrease in $\Delta\nu$ when there is a jump in frequency (see Fig. 4.6). This jump occurs cyclically for varying magnetic field strengths.

In § 3.3 we observed for the first time a number periodicities with spacings that were between $\sim$ 1 and 3 μHz (Tab. 3.2; spacings 19 through 23). Those spacings are close to what we expect for a second order (small) spacing of a main-sequence A-type star. The small spacings for the non-magnetic pulsation models given in Tab. 4.1 are plotted in Fig. 4.3. The properties of the non-magnetic models were previously discussed in § 4.2. If we observed small spacings in the *MOST* data then, based on models A through E, the adjacent modes are most likely even, low-order, $\ell = 0$ and 2 modes. (Once again we note that assessment is based only on the models presented in Tab. 4.1.) Figure 4.9 gives the small spacing for the same models as in Fig. 4.3 with a magnetic perturbation (B = 5 kG) included. The perturbation to the small spacing is large and is more reminiscent of what happens to individual frequencies than what happens with the magnetic perturbation to the large spacing. The spacings show a slow increase in value before a sudden decrease ($\sim$ 5–10 μHz). This introduces significant difficulties in distinguishing the magnetic effects from the asymptotic spacings (Dziembowski & Goode, 1996). The small spacings calculated as $\nu_{n,\ell} - \nu_{n-1,\ell+2}$ can even be negative. The mode having order n has a greater frequency value than the adjacent mode with order n - 1 in the non-magnetic case. The introduction of a magnetic field can cause this pattern to be reversed so that a frequency labelled n - 1 in the non-magnetic model now has a larger frequency than the mode having order n in the non-magnetic model. In general n is not an observable, but the frequency shifts caused by a magnetic field introduce a large enough perturbation to significantly complicate the analysis of our theoretical spectra. The small spacing perturbations (with an offset added

for clarity) are given in Fig. 4.10 as a function of magnetic field. The perturbation is cyclic and shows the large variation in the magnitude of the second order separations caused by the addition of a magnetic field to the pulsation calculations.

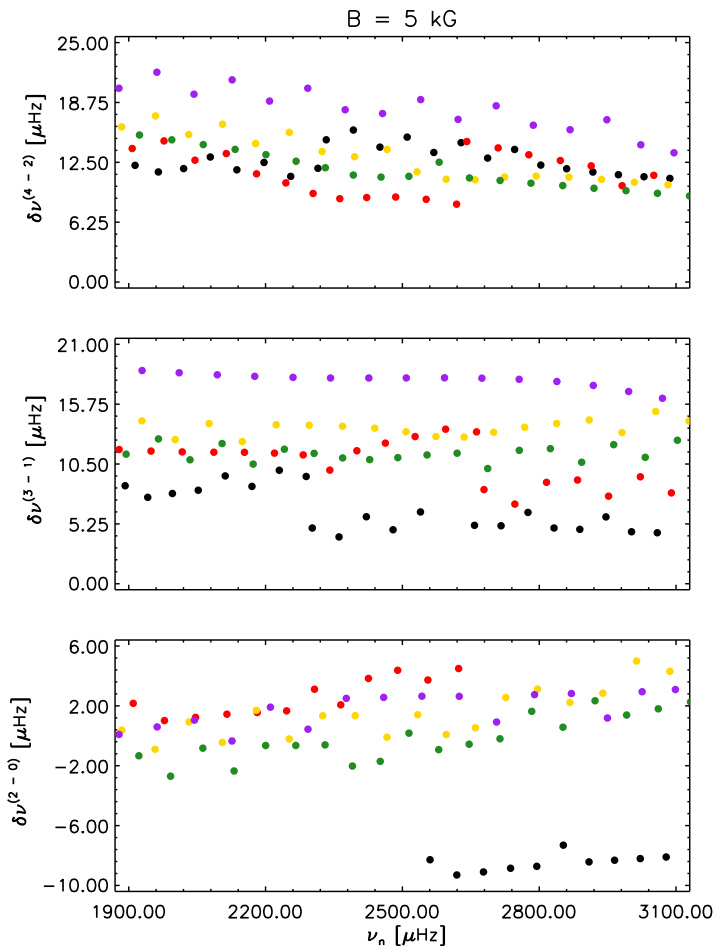

Figure 4.9: The magnetic perturbations to $\delta\nu$ for a 5 kG magnetic field using models from Tab. 4.1. The plots show the small spacing $\delta\nu = \nu_{n,\ell} - \nu_{n-1,\ell+2}$ as a function of frequency $\nu_{n,\ell}$. The figure labels are the same as the labels in Fig. 4.3 – the small spacings neglecting a magnetic field. Compared to the nonmagnetic case the small spacing can increase or decrease depending on the angular separations. The magnetic perturbation can even cause a frequency (labelled n) with angular degree $\ell + 2$ to have a larger value than the frequency (labelled n - 1) with degree ℓ, resulting in a negative small spacing. This means close (adjacent) frequency pairs (see Fig. 1.3) can appear in the reverse order.

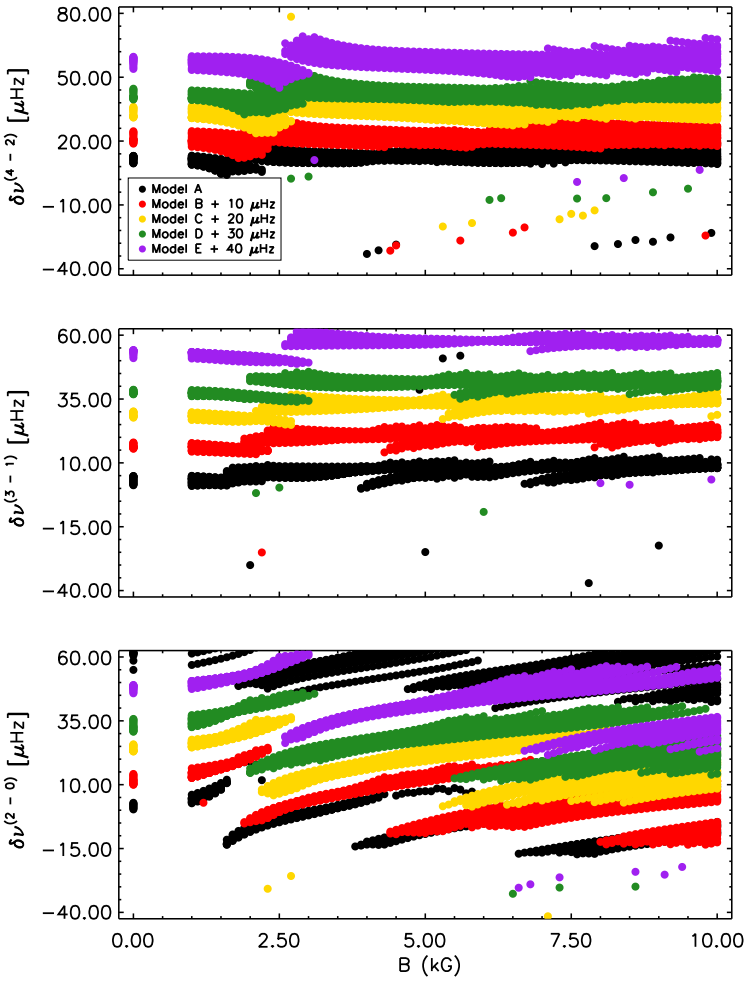

Figure 4.10: The magnetic perturbations to $\delta\nu$ for all calculated magnetic field strengths using models from Tab. 4.1. The panels are labelled with the same ordinates as Fig. 4.3. For clarity, the small spacings for some models are offset by a constant value shown in the legend found in the top panel. The small spacing is highly sensitive to magnetic field strength and the angular degrees of the modes.

A close inspection of Figs. 4.7 and 4.9 shows a rapid variation in the magnitude of the magnetically perturbed spacings. This rapid variation has an amplitude of a few (~ 5) μHz over a baseline of about 100 μHz. The small spacings (~ 3 μHz) observed by *MOST* seem to vary by about 1 μHz over a similar baseline (see Tab. 3.2). This similarity between the theory and observations is noted with caution. We are unsure if this rapid variation in the spacings is a physical phenomenon or a numerical artifact in our models. A comparison to frequency spacings calculated using another method (e.g., the models of Saio & Gautschy 2004) is necessary to substantiate the reality of this variation.

The models for HR 1217 presented in this chapter represents the first time a large grid of realistic stellar models has been calculated for this star that includes the magnetic perturbations to the eigenfrequencies. The general characteristics of the models was discussed. The following chapter will expand upon this analysis by attempting to find the closest matched model frequencies to the observed *MOST* periodicities (chapter 3).

Chapter 5

Best matched models

In the previous chapter we discussed the calculation of a large grid of stellar models of HR 1217 that, for the first time, included the effects of magnetic perturbations to the oscillation modes. The general properties of those models were discussed but a quantitative match to the frequencies extracted from the *MOST* photometry (chapter 3) was not performed. This chapter outlines a procedure to match the observed periodicities to the calculated magneto-acoustic modes. The properties of models from our grid that best match the observations are described.

5.1 The matching procedure

To begin we ask ourselves a simple question: Can models of roAp stars be used to constrain the properties of a roAp star?

Mkrtichian et al. (2008) recently studied HD 101065; a roAp star commonly referred to as Przybylski's star, and uncovered between 15 and 20 periodicities from their radial velocity data. The authors explored theoretical models with masses ranging from 1.5 to 1.7 $M_\odot$ in steps of 0.05 $M_\odot$ and with chemical compositions of (X, Z) = (0.7, 0.02) and (0.695, 0.025). Mkrtichian et al. (2008) included magnetic effects in their pulsation models using the method of Saio (2005) and calculated the magnetic perturbation (for two

or three models in the evolutionary sequences at each mass) for fields with strengths between 2 and 10 kG in steps of 0.2 kG. Their use of a few hundred magnetic models (= 2–3 selected models × 5 available model masses × 40 magnetic field strengths) should be compared to the almost 52,000 models used in this study. They were able to find a mean deviation between the observed oscillations and the theoretical pulsation modes of ~ 1.3 μHz. (In determining the mean the authors used the logarithm of the radial velocity amplitudes as a weight.) Individual deviations between their best matched modelled modes and their observed frequencies ranged from about 3.3 μHz in the worst match to about 0.1 μHz in the best case. (The observed frequency uncertainties from their study range from 0.004 to 0.47 μHz.) From their matched models they give constraints of $M/M_{\odot} = 1.525 \pm 0.025$, Age = 1.5 $\pm$ 0.1 Gyr, $\log T_{eff} = 3.821 \pm 0.006$, $\log L/L_{\odot} = 0.797 \pm 0.026$, $\log g = 4.06$ $\pm$ 0.04, and B = 8.7 $\pm$ 0.3 kG on the physical parameters of HD 101065. Mkrtichian et al. (2008) give impressive constraints on the properties of HD 101065 and show the potential for roAp asteroseismology.

For HR 1217, Cunha et al. (2003) obtained a qualitative agreement between models and observations. Their conclusions were based on a small number of models that did not include the effects of a magnetic field. These non-magnetic models could not explain deviations from the asymptotic spacing that were observed, for example, by Kurtz et al. (2005). Cunha (2001) suggested that the magnetic field was an essential ingredient in the pulsation calculations used to explain the roAp phenomenon and the observed frequency shifts. In this work, the largest grid of magnetically perturbed oscillation frequencies was calculated using the methods outlined in chapter

4. We illustrated in § 4.3 that the addition of the magnetic perturbation to the pulsation calculations causes large shifts in frequency of certain eigenmodes. The shifts are on the order of what is observed in HR 1217 ($\sim$ 15–20 μHz) and they occur cyclically as a function of magnetic field strength. We also showed that the asymptotic spacings (both large and small) are altered by the magnetic field, with the small spacing showing the largest deviations from the standard, non-magnetic, case. We must now find the model(s) in our grid that best reproduce the observed photometric variations presented in Tab. 3.1.

5.1.1 Seismic observations & models of the Sun

Before continuing with the asteroseismic matching of the HR 1217 data to our model grid it is instructive to compare the quality of the frequency matches obtained for a well known star — the Sun. In the introduction chapter (§ 1.1) we alluded to the successes of helioseismology at constraining the physics that makes up a standard solar model (SSM). Detailed reviews of the physics included in the SSM and helioseismic inferences are provided by Christensen-Dalsgaard (2002) and Basu & Antia (2008).

We know the mass, radius, composition and age of the Sun from a number of different sources (see Basu & Antia 2008). When we construct a SSM we must meet the constraints provided by those measurements. Typically we calculate the radius and luminosity of the Sun to within 1 part in 10^5 and match the value of Z/X $\simeq$ 0.0244 to within about 1 part in 10^4. The mixing length parameter is used as a scalable parameter that is adjusted to match the SSM radius to the observed solar radius. The best combinations

of constituent physics and scalable parameters arrive at an age estimate of the Sun from solar models of $\sim$ 4.57 Gyr, in agreement with meteoritic data (Bahcall et al., 1995). Seismic models of the Sun are constructed to constrain the input physics of the SSM (EOS, opacities, diffusion physics, convection physics, composition ...) with the strict requirement that the other observables mentioned above are also matched.

An illustration of the quality of the frequency matches from a SSM and the observations of the Birmingham Solar Oscillations Network (BiSON; Chaplin et al. 1999) is shown in Fig. 5.1. The SSM was calculated with YREC. The EOS and opacity tables used in the construction of this SSM are updated versions of the same tables used in our HR 1217 models and the model atmosphere is constructed using a Krishna Swamy T-τ relation (Krishna Swamy, 1966). Diffusion was not included in this calculation. The relative difference between the adiabatic frequencies calculated with this SSM and the BiSON data is plotted as a function of the BiSON frequencies (Fig. 5.1). The model deviates from the observations by $\sim$ 10 μHz for the highest overtone (= highest frequency) modes. The calculated solar model frequencies are systematically offset from the observed frequencies.Guenther et al. (1993), for example, discussed the role of diffusion on calculated SSM eigenmodes and showed the inclusion of He diffusion in the SSM model calculation improve the agreement between the model and the observed periodicities by about 1–5 μHz. The additions of heavy element diffusion, a non-adiabatic frequency calculation, and turbulent pressure corrections from 3D simulations improve the agreement between theory and observation even further. (We again point to the review of Basu & Antia 2008.) Currently, the most accurate solar

models still show frequency differences of about 0.3%, or a few μHz. Even this impressive agreement of a fraction of a percent at high frequencies is still statistically poor given that the individual frequency deviations are many times the frequency uncertainties.

The mass, age, radius and composition of the Sun can be matched reasonably well by only considering the agreement between model frequencies and observations, even with the systematic offset between the observations and theory at high frequencies.Guenther & Brown (2004) used a χ^2 matching procedure that calculates the average, weighted square deviation from a set of model frequencies to those observed in the Sun. They found that by matching the frequencies only (they did not take any other measured constraint into account), they could arrive at a mass of 0.99 $M_\odot$ for a model that favoured diffusion and had a composition of Z/X = 0.028 at an age of 4.7 Gyr. Metcalfe et al. (2009) used a genetic algorithm to explore the parameter space for the closest match between the calculated and observed solar modes. Their results are similar to those obtained by Guenther & Brown (2004).

A more thorough helioseismic investigation would also include the disc resolved information about the solar oscillations that provides us with measurements of millions of modes with identifiable angular degrees starting from $\ell = 0$ and ranging into the thousands. All of the observed solar modes coupled with the external constraints on the bulk properties of the Sun allow us to very accurately calculate the internal state of the Sun using inversion methods. In asteroseismology we do not usually have a large number of observed oscillation frequencies or a direct measure of the angular degree of those observed light variations. If the matching of the normal modes from

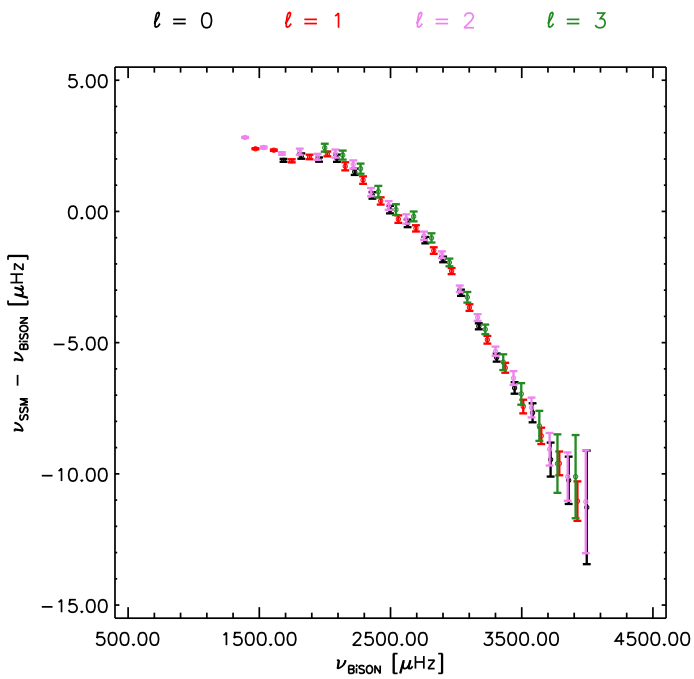

Figure 5.1: Standard Solar model (SSM) frequencies compared to the Birmingham Solar Oscillations Network (BiSON) observations. Shown is the relative difference between the adiabatic frequencies calculated from a SSM (without element diffusion) and those measured from BiSON data as a function of the BiSON frequencies. The model deviates from the observations by ~ 10 μHz for the highest overtone modes. The addition of Helium and heavy element diffusion in the model, a non-adiabatic frequency calculation, and turbulent pressure corrections from 3D simulations improve the agreement between theory and observation. At this time, the most accurate solar models; including the aforementioned additions, still show frequency differences of about 0.3% (a few μHz). This is still many times the uncertainty of the individual frequency measurements.

a SSM to helioseismic data using the procedures outlined by Guenther & Brown (2004) and Metcalfe et al. (2009) is applicable to other stars, then we expect that accurate frequencies (precise to about 1 μHz or better), will (in the best case) give physical parameters that are accurate to within a few percent. Matching a SSM to the low-ℓ helioseismic observations gives us a rough estimate on the accuracy of the physical parameters we can hope to extract from matching asteroseismic data to models.

5.1.2 Seismic observations & models of HR 1217

Matching observed oscillation frequencies to large grids of modelled pulsation modes is a relatively new extension to the forward problem in asteroseismology. The observations are now of sufficiently high photometric quality (thanks to missions like *MOST*) to uncover low amplitude oscillations. The extended, continuous, coverage of the observations over long periods of time also gives unprecedented frequency resolution in a Fourier transform that is free of aliasing artifacts. On the theoretical side, the increase in computing speed and memory facilitates the calculation of the large grids of models needed to uncover the parameter combinations that can best reproduce the observations.

The models calculated in this thesis will be matched to the *MOST* observations using a probability model. The matching procedure is similar to that used by Kallinger et al. (2008a). For each model in our grid, the calculated modes are compared to each of the observed frequencies listed in Tab. 3.1. Under the assumption that the residuals between a best-matching model mode and the corresponding observed frequency are normally distributed,

the Gaussian probability for a one frequency match is

$$P_i = f(\sigma_\nu) \exp\left(-\frac{(\nu_{\rm mod} - \nu_{\rm obs})^2}{2\sigma_\nu^2}\right) \tag{5.1}$$

where $f(\sigma_\nu) = 1/\sqrt{2\pi\sigma_\nu^2}$, σ_ν^2 is the observed frequency (ν_{obs}) uncertainty (Tab. 3.1), and ν_{mod} is the model frequency that is the closest match to the observed frequency. The exponentiated function is essentially a χ^2 measure. A probability is calculated for each of the $N_{\rm M}$ observed frequencies and the total probability for the model is

$$\ln P = \ln \prod_{i=1}^{N_{\rm M}} P_i = \sum_i^{N_{\rm M}} \left(\ln f(\sigma_\nu) - \frac{(\nu_{\rm mod} - \nu_{\rm obs})^2}{2\sigma_\nu^2}\right)_i \tag{5.2}$$

Once a probability is assigned to each of the models in the grid, Eq. 5.2 is normalized by assuming the total grid probability is equal to unity; i.e, each model probability is divided by $\sum P$, with the sum taken over all model probabilities within the grid. This method has an immediate advantage over a χ^2 matching because it gives a simple way to statistically compare models within the grid and, by adjusting the normalization, models from one grid to those from another. For example, the probability of some model X in our grid divided by the probability of some other model Y in our grid gives a measure of how much more likely model X is compared to model Y. There is also an aesthetic benefit that the probability space around a best matched parameter tends to be magnified (because of the exponentiation) when compared to the same region in χ^2 space. Although a χ^2 measure or a probability measure will arrive at the same best matched model within a grid, the probability approach shows the location of the matched parameter more readily (Kallinger et al., 2008a).

We match our models to the *MOST* observations listed in Tab. 3.1 using the 3σ bootstrap uncertainties as the σ_ν^2 input in Eq. 5.1. This is done for reasons discussed in § 3.3. Basically, we are being conservative by using the 3σ bootstrap uncertainties because they tend to be on the same order of magnitude as the lowest estimate of the frequency resolution given by Kallinger et al. (2008b); namely $0.25/\Delta$T. The oblique pulsator model described in § 1.2.2 tells us that the observed oscillations in roAp stars consist of the "main" or "true" oscillation mode and a group of surrounding frequencies spaced by the rotation frequency of the star. The number of rotationally split frequencies depends on the degree of the mode and on the geometry of the system. This is observed in the *MOST* data on HR 1217, where a number of the observed periodicities are spaced by ~ 0.9 μHz (Tab. 3.2), corresponding to the rotation rate of the star. In the simplest matching case we allow a model frequency to match multiple observed frequencies. Put another way, a frequency and its rotationally spaced sidelobes may all be matched to one mode in a given model. An alternative approach will be discussed in §5.2. We should also note that a proper statistical error should include the model uncertainties as well as the observational uncertainties. For the Sun, deviations between the modelled and the observed frequencies can be a few μHz for the highest order modes. Unfortunately, there is no reliable way to estimate the uncertainties introduced by the addition of a magnetic field in our models. By only using the observed frequency uncertainties, we are (dramatically) underestimating the true uncertainty needed to realistically weight our computed probabilities. We will discuss the scale of the uncertainties in more detail below.

Before discussing the results of the matching procedure we will address the scale of the uncertainties and how that scale relates to the presentation of the probabilities of the model properties within our grid. Figure 5.2 shows the matching probabilities in the magnetic field strength B, model mass M, and composition (Z/X) planes for two uncertainty scaling cases: 1. (Left panels of Fig. 5.2) The 3σ bootstrap uncertainties are not scaled, and 2. (Right panels of Fig. 5.2) The 3σ bootstrap uncertainties are scaled by a factor of 1000. Note that the probabilities in Fig. 5.2 are normalized so that the most probable model has a value of one. (The unnormalized probabilities will be given later.) In the first case (with no scaling) the most probable model (to be identified later) is clearly defined, with the next largest probability being, apparently, near zero. Most of the calculated probabilities in this case are essentially zero. This is because the Gaussian probability distribution heavily penalizes frequencies that are not well matched. When the total probability is calculated as a product of small numbers, its value becomes increasingly small. This is mainly caused by the lack of knowledge of a realistic uncertainty associated with our magnetic models. At face value, this graph could mislead a reader into thinking that (B, $M/M_{\odot}$, Z/X) = (8.8 kG, 1.5, 0.02) is the only reasonable set of parameters that could be assigned to HR 1217 based on the *MOST* data. We will show later that the situation is more complicated. In the second case, with the uncertainties scaled equally by a factor of 1000, there appears to be no constraints in probability space and no conclusions can be given. If we look for the model with the highest probability in both of the scaling cases, we find that the same model is identified. The equal scaling of uncertainties tends to magnify

regions of lower probability, but the relative uncertainties between observed frequencies results in a clear separation in the quality of the model match. We can arrive at the same result if we scale the uncertainties in a uniform way. This behaviour is obvious from the functional form of Eq. 5.1. We highlight it because, for presentation purposes, we want to find an equal uncertainty scaling that allows us to see how the probability of the model matches behaves in various parameter planes. The behaviour of the probability distribution around a set of parameters gives an indication of how degenerate the stellar parameters are within our model grid. For example, we know from § 4.3 that the magnetic perturbations are cyclic so we might expect that there will be (multiple) groupings of probability in the magnetic field plane showing which field strengths result in a better match to the seismic observations. We also know (as another example) that Z/X causes degeneracies in the position of a star in the HR diagram. So the presentation of the probability spaces within a number of parameter planes is important to identifying where these degeneracies are and also where future modelling should be focused. There is no statistical trickery being used by equally scaling the parameter uncertainties. We are simply finding a set of numbers that are easy to deal with numerically and that, for presentation purposes, helps us get a feel for the matches in various parameter planes. We will clearly state the value of the equal uncertainty scaling being used so that future studies will easily be able to reproduce our results. Some experimentation shows that an uncertainty scaling factor of 50 lets us calculate and properly normalize the model match probabilities, while at the same time allowing enough of a constraint on the models so we can visualize the results. We will further justify the choice of

a scaling factor of 50 at the end of this section.

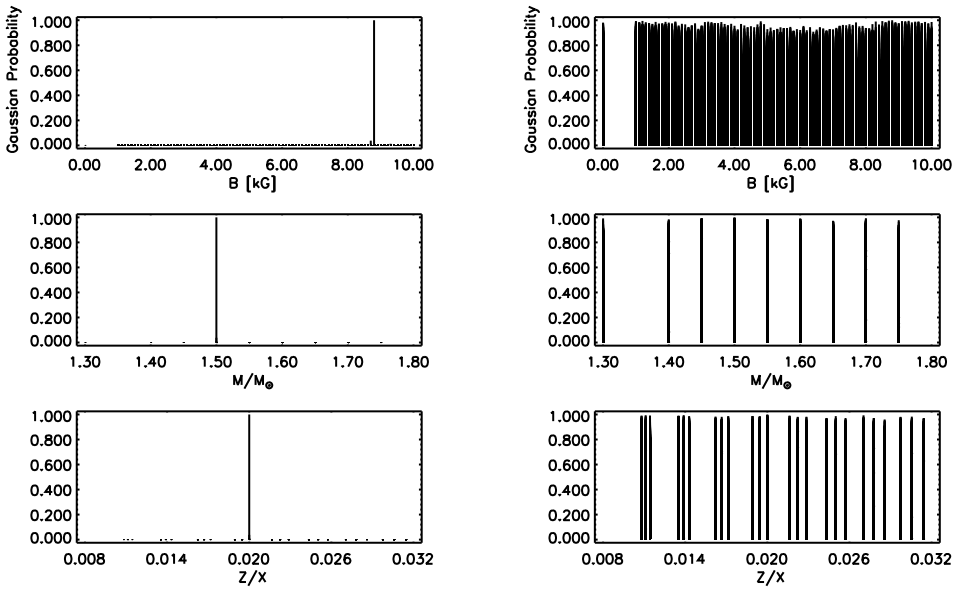

Figure 5.2: Probability distributions for models of HR 1217 using different error scales. All observed frequencies (those associated with both pulsation and rotational modulation) of Tab. 3.1 are used in the model search. Probabilities are assigned using Eq. 5.1. Model frequencies are matched to the observed frequencies with the 3σ bootstrap errors scaled. The left panels use a scale factor of 1 and the right panels scale the observed errors by a factor of 1000. The top panels shows the probability of all models as a function of magnetic field strength, the middle panels are probability as a function of model mass, and the bottom plots give probability as a function of composition (Z/X). Probabilities calculated with unscaled uncertainties show an extreme constraint on the models while those using the highly scaled (1000 $\times$) uncertainties show no constraint at all. However, because all observed errors are scaled in the same way, the most probable models are similarly ranked in both cases.

Figure 5.3 presents the matching results for a number of parameters in the model grid. The cumulative probability is given in each of the panels. The best matched model in our grid has a magnetic field strength of $B =$ 8.8 kG, a mass of 1.5 $M_\odot$, a composition of Z/X = 0.02, and has completed about half of its main sequence lifetime. Models with magnetic field strengths greater than about 8 kG are preferred. The scaling allows to see that probable models with values near 1 kG do exist. A mass near 1.5 $M_\odot$ is favoured, as is a sub-solar composition (Z/X $\simeq$ 0.0244 for the Sun). Once again, these results are also obtained without scaling the observed uncertainties; but, we see that other parameters combinations should be explored in more detail.

Even one poorly matched frequency can potentially drive the total probability of that model close to zero. We mitigated the effect that a poor match has on the graphical analysis of the probability space by uniformly scaling uncertainties. It is also possible to calculate the model probabilities under the assumption that the residuals between the model and observed frequencies follow another distribution function. In Eq. 5.1 we use a Gaussian probability function. We also calculate model match probabilities using a Laplace distribution of the form

$$P_i = f(\sigma_\nu) \exp\left(-\frac{|\nu_{\rm mod} - \nu_{\rm obs}|}{\sigma_\nu}\right) \tag{5.3}$$

where $f(\sigma_\nu) = 0.5/\sigma_\nu$. The Laplace distribution has fatter tails than a Gaussian distribution. As a result, outlying frequencies are given slightly larger weight when using a Laplace distribution instead of a Gaussian, or Normal, distribution. It is interesting to see how the "close" outliers affect the probability space around different parameter planes. If there is no in-

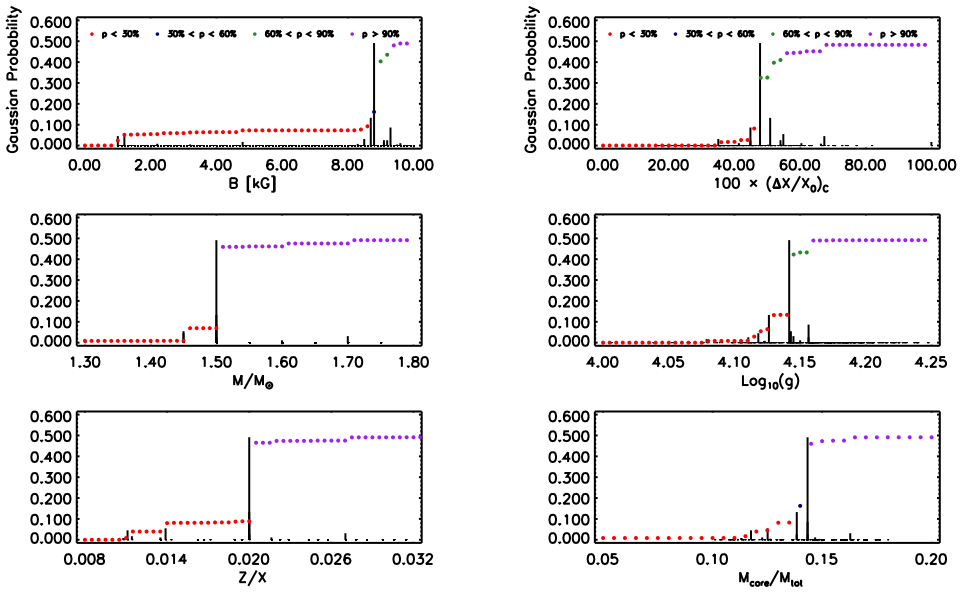

Figure 5.3: Probability distributions for models with uncertainties scaled by a factor of 50. All observed frequencies (those associated with both pulsation and rotational modulation) of Tab. 3.1 are used in the model search. Probabilities are assigned using Eq. 5.1. The left panels, from top to bottom, show the match probability as a function of magnetic field strength, the model mass, and the composition (Z/X) of the models. The right panels, again listed from top to bottom, show the match probabilities as a function of the percentage of the main sequence lifetime the model has completed, the surface gravity of the model, and the mass of the model's convective core in units of total stellar mass. Each panel has the cumulative probabilities plotted with circles and colours (labelled in the top panels) showing the percentage of the total probability. By using this scaling we see more details in the probability distributions than we would have if the uncertainties were not scaled. Magnetic models having $B \gtrsim 8$ kG are preferred.

formation about how the residuals between a model and observations are distributed, then a Gaussian distribution is the most conservative choice for the distributed errors (see, e.g., Gregory 2005).

Figure 5.4 shows the model match probabilities (labelled as Laplace probabilities, and using the same uncertainty scale factor) for the same parameters as in Fig. 5.3. Note that in both cases the same model is identified as the most probable model match. Because outliers are given some weight in the Laplace probabilities, we see a number of peaks in probability that are not seen when using a Gaussian probability model. Are the conclusions the same in both cases? Greater than 60% of the probability (of a model from our grid matching the observations) occurs after a magnetic field strength of 8.8 kG. Between 60 and 90% of the probability contribution occurs for masses between 1.5 and 1.6 $M_{\odot}$, and the largest contribution from the composition is less than $Z/X \sim 0.02$. So each of these (admittedly broad) conclusions remains the same if we use either of the Gaussian (Eq. 5.1) or Laplace (Eq. 5.3) probability distributions. A more detailed comparison between the probabilities obtained by using the different distributions shows how sensitive the probability space is to frequencies that, in a manner of speaking, do not make the Gaussian cut.

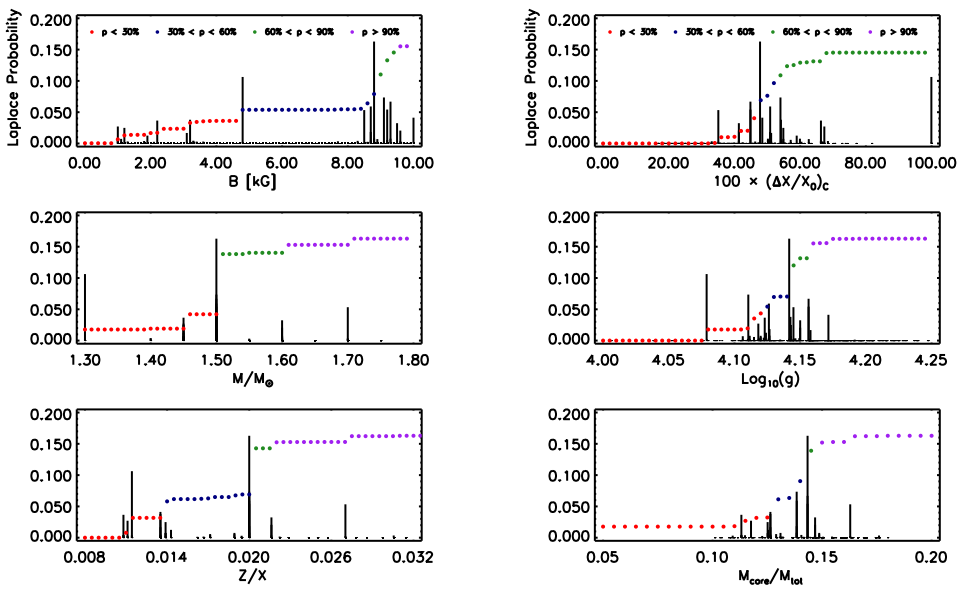

Figure 5.4: Probability distributions for models using a Laplace distribution. All observed frequencies (those associated with both pulsation and rotational modulation) are used in the model search and probabilities are assigned using the Eq. 5.3. Observed uncertainties are scaled by a factor of 50. The above plots have the same format as those in Fig. 5.3. Probability distributions are similar to those shown in Fig. 5.3. By using a Laplace probability distribution rather than a Normal (Gaussian) distribution we allow for a greater probability contribution from model frequency matches that fall in the distribution tails. In this way we can further explore the probability space.

At the beginning of this chapter we gave an example of model matches to the observations of the roAp star HD 101065 (Mkrtichian et al., 2008). Mkrtichian et al. (2008) used the mean as a statistic to discriminate between their models of HD 101065 and arrived at a closest matched model having a mean deviation from the observations of about 1.3 μHz. Those authors

used a weighted mean so that poorly fitted frequencies did not skew their mean calculation. In Fig. 5.5 we compare the median frequency differences between our models and the *MOST* observations of HR 1217 as a function of log probability using both the Gaussian and Laplace distributions. Instead of using a weighted mean like Mkrtichian et al. (2008), we use the median so that we do not bias our average differences toward poorly fitted frequencies. The purpose of Fig. 5.5 is to compare an average difference statistic to the probability method we have presented thus far. We also show in Fig. 5.5 how scaling the observed uncertainties affects the numerical values of our unnormalized probabilities.

For each value of probability in Fig. 5.5 there are a number of possible median matches. The Gaussian probability calculation drops off sharply for high probability matches, while the Laplace probability calculation gradually approaches the most probable model(s). The lowest median deviation and the highest probability models both show a small standard deviation between the differences in model and observations. Scaling the observed errors changes the scale and the width of the probability region, so that the models matched to observations with the largest uncertainty values show the smallest range in probabilities. The shape of the probability distribution does not change by (uniformly) scaling the observed errors. Using the mean or median as a discriminant between models and observations is not as effective as using a probability because the probability calculation takes into account the observed uncertainties. Poorly matched models are penalized much more within a probability framework than by using an average statistic. We have to be aware that even one extreme mismatch between an observed and calcu-

lated frequency can dramatically reduce the probability of that model being an acceptable match. In such a case the mean (or median) deviation of the model should be looked at in conjunction with the probability of that model to gauge the match quality.

We have introduced a number of relevant matching methodologies but have yet to discuss the quality of the matches or to formally list the physical parameters of the best matched models. In Tab. 5.1 we list a number of properties for the most probable model matches to the *MOST* observations. The models are listed as the 10 most probable, non-duplicate, models using both the Gaussian and Laplace probability matches.

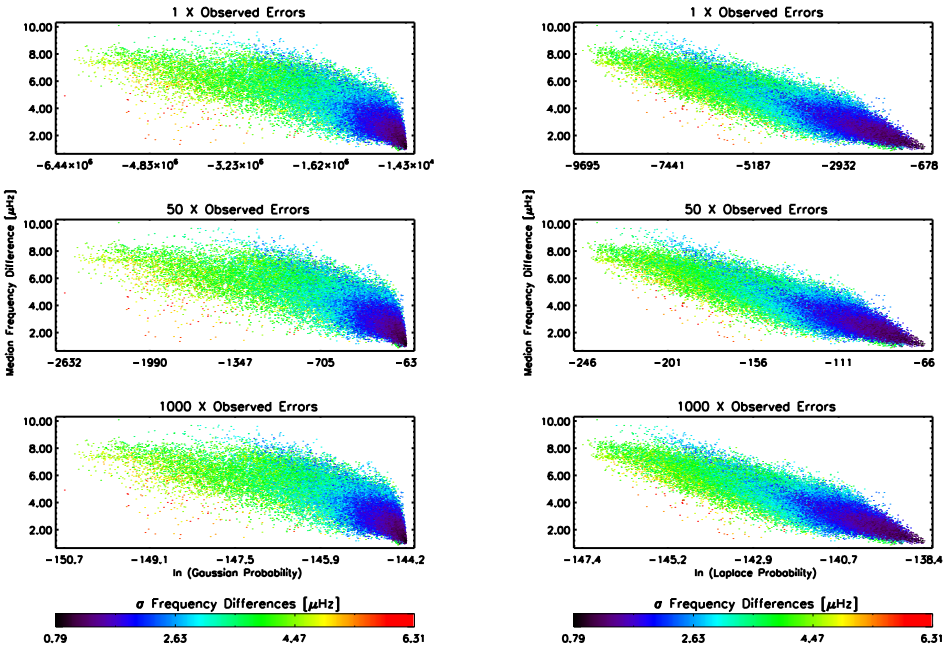

Figure 5.5: A comparison between the median model frequency matches and the model match probabilities. The left panels show the median of the difference between the observations and the best matched model frequencies for each model in the grid as a function of the natural logarithm of the Gaussian model probabilities. Best matches are located at the lower right in each plot. The top panel highlights the case with no frequency scaling while the middle and bottom panels show the cases with observational uncertainties scaled by a factor of 50 and 1000, respectively. Colour contours show the standard deviation of the matches between the model and the observed frequencies. The right panels are the same as the left except the model probabilities are calculated using the Laplace distribution. Note that scaling the observational uncertainties produces similar distributions but the value of the probabilities increases and the range in probabilities decreases with increasing scaling factor. For each probability there are a number of potential median matches. The Gaussian and Laplace probabilities give the same best matched models but the probabilities tend to increase more sharply when using a Gaussian distribution.

Table 5.1: Some properties of the most probable models of HR 1217. The top ten unique models from the Gaussian and Laplace probabilities are listed in decreasing probability order. Deviation refers to the absolute difference between a model frequency and the best matched observed frequency and σ is the standard deviation. The column labelled as probability label refers to the order of the probability from each of the Gaussian or Laplace probabilities. For example, 1 G is the most probable Gaussian probability and 10 L would be the 10th most probable Laplace probability. The probability ratio is defined as the Gaussian probability of the model divided by the Gaussian probability of the most probable model ($\ln P = -63.1$). The models in this table were matched to all frequencies listed in Tab. 3.1 using $50 \times 3\sigma$ errors.

Model ID	$M/M_\odot$ B (kG) cut-off (μHz)	X $M_{conv.env.}/M_\star$ median deviation (μHz)	Z Log_{10} (T_{eff}) mean deviation (μHz)	Age (Gyr) Log_{10} ($L/L_\odot$) σ deviation (μHz)	α Log_{10} ($R/R_\odot$) probability label	$M_{conv.core}/M_\star$ $\Delta\nu$ (μHz) probability ratio
M1	1.50	0.700	0.014	1.05	1.4	0.1434
	8.8	0.00	3.8645	0.8826	0.2361	69.25
	1866.36	1.18	1.53	1.16	1 G, 1 L	1.000
M2	1.50	0.700	0.014	1.10	1.4	0.1384
	8.7	0.00	3.8616	0.8866	0.2438	67.52
	1816.38	1.36	1.52	1.29	2 G, 5 L	0.273
M3	1.30	0.700	0.008	2.05	1.4	0.0000
	4.8	0.00	3.8680	0.8973	0.2364	64.61
	1597.02	1.08	1.31	0.99	2 L, 9 G	0.037
M4	1.50	0.700	0.014	1.00	1.6	0.1434
	9.3	0.00	3.8672	0.8787	0.2287	70.99
	1915.70	1.23	1.40	0.90	3 G, 4 L	0.183
M5	1.50	0.700	0.014	1.15	1.6	0.1384
	9.1	0.00	3.8587	0.8905	0.2517	65.90
	1767.56	1.01	1.49	1.35	3 L, 7G	0.055
M6	1.45	0.720	0.010	1.30	1.8	0.1251
	1.2	0.00	3.8637	0.8633	0.2281	70.16
	1857.29	1.40	1.45	0.95	4 G, 13 L	0.111
M7	1.45	0.720	0.008	1.35	1.6	0.1176
	1.0	0.00	3.8739	0.9289	0.2405	66.88

continued on next page

Table 5.1: *continued*

Model ID	$M/M_\odot$ B (kG) cut-off (μHz)	X $M_{conv.env.}/M_\star$ median deviation (μHz)	Z Log_{10} (T_{eff}) mean deviation (μHz)	Age (Gyr) Log_{10} ($L/L_\odot$) σ deviation (μHz)	α Log_{10} ($R/R_\odot$) probability label	$M_{conv.core}/M_\star$ $\Delta\nu$ (μHz) probability ratio
	1703.00	1.37	1.57	1.23	5 G, 12 L	0.091
M8	1.70	0.740	0.020	0.85	1.4	0.1628
	8.5	0.00	3.8577	0.9065	0.2617	67.64
	1883.37	1.10	1.32	0.89	6 G, 7 L	0.067
M9	1.50	0.700	0.014	1.00	1.6	0.1434
	9.2	0.00	3.8672	0.8787	0.2287	70.99
	1915.70	1.22	1.22	0.79	6 L, 8 G	0.050
M10	1.50	0.740	0.010	1.20	1.8	0.1264
	10.0	0.00	3.8695	0.8728	0.2212	72.78
	1931.66	1.05	1.25	0.92	8 L, 24 G	0.004

The most probable model match has a Gaussian probability of $\ln P =$ -63.1. That probability was calculated using the uniformly (50×) scaled 3σ frequency errors from Tab. 3.1. For completeness, the probability of that model calculated without scaling the *MOST* frequency uncertainties is $\ln P$ = -1.4 × 10^4. Clearly, with such low probability, the model match is not a statistically good match. Figure 5.6 shows the deviations between the model and observed frequencies as a function of the *MOST* frequencies. It is obvious that the *MOST* observations (Tab. 3.1) are determined to a level of precision that is much better than can be matched with our models. However, the mean absolute deviation between the observations and the theory of 1.53 μHz is similar to that obtained by (Mkrtichian et al., 2008) for the roAp star HD 101065. The median absolute deviation between model M1 and the *MOST* data is 1.18 μHz. An order 1 μHz deviation at frequencies of $\sim$ 2700 μHz constitutes a percentage agreement of 0.04% — A value that is about 10 times better than the current agreement between the high frequencies calculated and observed in the Sun (see Fig. 5.1)! The largest frequency deviation in model M1 is 4.307 μHz between an $\ell = 3$ mode having ν = 2792.107 μHz and the observed frequency of 2787.799 μHz (ν_{22} of Tab. 3.1). That frequency is most likely a rotational splitting and not a pulsation mode of HR 1217. Because we allow multiple matches between the model and the observed periodicities, that mode also matches frequencies between 2788.872 and 2792.249 μHz (ν_{23} through ν_{27} in Tab. 3.1). Those six frequencies correspond to the "missing modes" (§ 1.3) of Kurtz et al. (2005) and contain; within that frequency cluster, one of the suspected small spacings (see Tab. 3.2). The most closely matched frequency is at ν_{15} = 2720.914

μHz (Tab. 3.1). That is the observed frequency with the largest corresponding amplitude. The model mode from M1 that matches that frequency is an $\ell = 3$ mode with $\nu = 2720.844$ μHz. This represents a deviation of 0.070 μHz and is still more than a factor of 10 larger than the observed 3σ uncertainty of 0.005 μHz for that periodicity. Listed in Tab. 3.1 is the newly identified *MOST* frequency at $\nu_1 = 2603.832$ μHz that is spaced by ~ 15.7 μHz from the next closest mode. A spacing of about 15 μHz deviates from the regular asymptotic spacing of ~ 33.5 μHz and may represent a magnetically perturbed mode. The frequency from model M1 that most closely matches ν_1 is a mode with angular degree of $\ell = 1$ with $\nu = 2599.938$ μHz. That match deviates from the observed frequency by 3.895 μHz. On average[10], model M1 has a large spacing of 69.938 μHz. (This should be compared to the large spacing of 69.25 μHz listed for model M1 in Tab. 5.1 that was calculated using the integral definition of the large spacing given in Eq. 1.12.) The large spacing of model M1 ranges from a minimum of 69.086 μHz to a maximum of 70.449 μHz. The observed large spacing (Tab. 3.2) is, on average, 67.961 $\pm$ 0.053μHz. The small spacings ($\delta\nu^{2-0}$) for model M1 range from -4.755 μHz at 2619.780 μHz to -2.100 μHz at 2828.660 μHz. *MOST* identifies potential small spacings having values between ~ 1.5 and 2.6 μHz. Figure 5.6 shows that the closest matched modes would be alternating between $\ell = 0$ and $\ell = 3$ and the (potentially) magnetically perturbed frequencies at the smallest and largest observed frequencies have an angular degree of $\ell = 1$. Given that the frequencies show rotational splitting, a radial mode ($\ell = 0$) seems an

[10]The average is taken over all n and ℓ for frequencies in the range of 2618.600 to 2792.249 μHz.

unlikely candidate for a match.

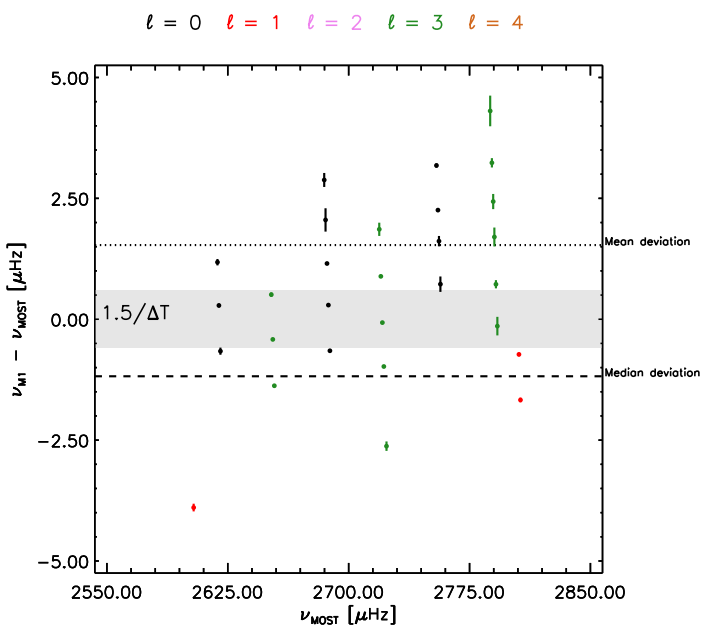

Figure 5.6: A comparison between model M1 (Tab. 5.1) pulsation modes and the *MOST* frequencies. The relative frequency deviation between theory and observation is plotted against the observed frequencies (Tab. 3.1). The shaded area ($\pm$ 1.5/ΔT) shows the most conservative frequency resolution discussed in § 2.2. The dotted line is the mean difference between the observations and theory. The dashed line shows the median difference between the model and data points. The matching procedure allows the same model frequency to match multiple observations.

The most probable models listed in Tab. 5.1 show mean deviations from the *MOST* observations ranging from 1.22 to 1.57 μHz, with a standard error of ~ 0.2 μHz. The median deviation ranges from 1.01 to 1.40 μHz. The model match with the lowest mean deviation is listed as model M9 of Tab. 5.1; however, the model with the lowest median deviation of 0.88 μHz is not one of the most probable models. The properties of the model with the smallest median are listed in Tab. 5.2 and the model is labelled as MM1. Interestingly, the model with the lowest median deviation is extremely improbable and has a mean deviation is about 2.4 μHz. The probability ratio of model MM1 to model M1 of Tab. 5.1 is $\sim 10^{-27}$. In Fig. 5.7 we compare the frequency deviations between the modelled modes and observations for models MM1 (Tab. 5.2) and M3 (Tab. 5.1). Model M3 is chosen for comparison because it shows a low mean frequency deviation (1.31 μHz) and because; of all the models listed in Tab. 5.1, its magnetic field strength (4.8 kG) is closest to the observed value of $\sim$ 2–4.4 kG (Bagnulo et al. 1995, Lüftinger et al. 2008). The frequency deviations of model M3 (left panel of Fig. 5.7) show an alternating pattern of $\ell = 2$ and $\ell = 1$ with the anomalously spaced modes at either end of the observed spectrum identified as $\ell = 4$ modes. There is no distinction between the pulsation, rotation, or small separated modes. That is, the same mode is used to match each frequency group that is separated by about $\Delta\nu/2$. Model MM1 has the smallest median deviation of all the models matched using this procedure. Its frequency deviations are shown in the right panel of Fig. 5.7. The modes shown alternate between $\ell = 3$ and $\ell = 0$ modes with some modes; located near those $\ell = 0$ modes, identified as $\ell = 2$ modes. This is what one would expect if a second order

(small) spacing was present in the data — Modes that are closely spaced by about a few μHz from each other that have angular degrees that differ by two. However, it is especially noteworthy that the potentially magnetically perturbed modes at the low and high end of the *MOST* frequencies are not identified in Fig. 5.7. That is because the modelled modes deviate from the observed modes by more than 10 μHz. The matching of modes from models MM1 and M3 illustrates the interesting result that we can come close to obtaining the magnetically perturbed modes (spaced by about 15 μHz in the *MOST* data) or the potential small spacings (spaced by about 3 μHz in the *MOST* data); but, we generally do not match both. None of the most probable models listed in Tab. 5.1 match a 0 kG model.

Table 5.2: Some properties of a selected model of HR 1217. The model with the lowest median deviation between observed and calculated frequencies is listed below. The column labelled as probability label refers to the order of the probability from each of the Gaussian or Laplace probabilities. For example, 1 G is the most probable Gaussian probability and 10 L would be the 10th most probable Laplace probability. The probability ratio is defined as the Gaussian probability of the model divided by the Gaussian probability of the most probable model (see Tab. 5.1). The models in this table were matched to all frequencies listed in Tab. 3.1 using $50 \times 3\sigma$ errors.

Model ID	$M/M_\odot$	X	Z	Age (Gyr)	α	$M_{conv.core}/M_\star$
	B (kG)	$M_{conv.env.}/M_\star$	Log_{10} (T_{eff})	Log_{10} ($L/L_\odot$)	Log_{10} ($R/R_\odot$)	$\Delta\nu$ (μHz)
	cut-off (μHz)	median deviation (μHz)	mean deviation (μHz)	σ deviation (μHz)	probability label	probability ratio
MM1	1.60	0.700	0.018	0.900	1.6	0.1634
	8.8	0.00	3.8645	0.9243	0.2569	66.68
	1809.45	0.88	2.39	4.14	3227 G, 1349 L	1.729×10^{-27}

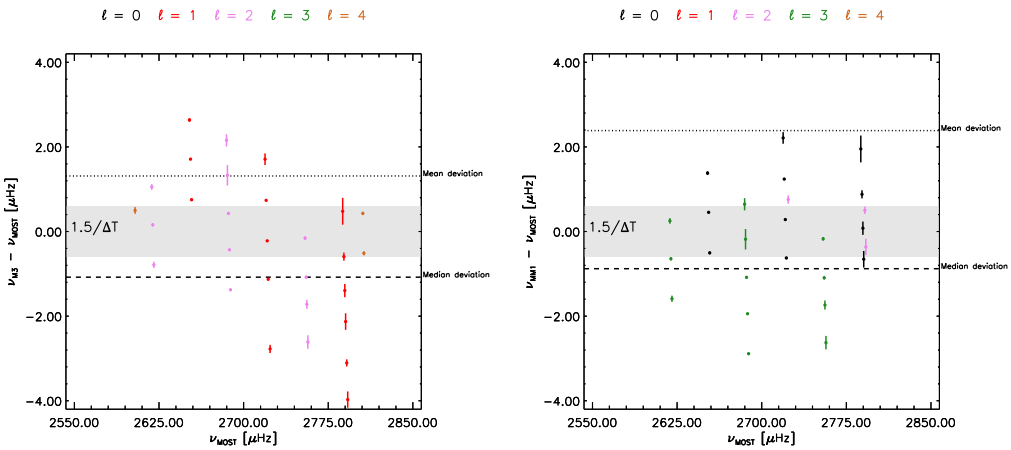

Figure 5.7: A comparison between the model M3 pulsation modes and the *MOST* observations (Tab. 3.1) in the left panel. Model MM1 pulsation frequencies (Tab. 5.2) are compared to the *MOST* observations in the right panel. The labels are the same as those in Fig. 5.6. Model M3 is more probable than model MM1 but the model MM1 frequencies have the smallest median deviation from the *MOST* observations of all of the models explored.

Up to this point we have calculated the probabilities of model matches to all of the observed oscillations extracted from the *MOST* data. Next we compare the closest matched oscillation spectra to models with the same properties, but having different magnetic field values. These diagrams; that we will refer to as Saio plots (see, e.g., Saio 2005), illustrate how changes in the magnetic field strength can greatly impact the matching of models

to observations. Figure 5.8 shows the magnetically perturbed modes as a function of magnetic field for the two most probable models; M1 (left panel) and M2 (right panel), of Tab. 5.1. The *MOST* observations are shown as horizontal, dotted, lines and the location of the best fitted magnetic field value is drawn as a solid, vertical line. It is clear that in both cases the magnetic perturbations cause cyclic matches to the observations. In some cases, the magnetic field causes the eigenspectrum to completely miss the observed modes. A small change in magnetic field strength of about 0.1 kG can result in a frequency shift (much) greater than 1 μHz. Frequency jumps are clearly visible and modes tend to cluster in groups of alternating even and odd parity. This is consistent with the *MOST* observations (chapter 3). A close inspection of the M1 model match shows that this even and odd alternating ℓ pattern is broken for the two highest frequency groups. Near those frequencies, the alternating pattern switches to an odd-odd ℓ pattern. The anomalous spacings of $\sim$ 15 μHz at each end of the observed spectrum are most closely matched by $\ell = 1$ modes (in this case), although the match is not perfect, or even statistically meaningful. There is also evidence that frequency spacings of a few μHz can exist, so that the observed spacings of $\sim$ 1.5–3 μHz may be explained as magnetic perturbations and not as the traditional asymptotic small spacings. In Fig. 5.9 we show the same type of diagram but for the lowest mean (left panel) and median (right panel) deviation models (Tab. 5.2). Those models show similar characteristics; but, in the case of the model with the lowest median deviation from the observations, the anomalous modes at the ends of the spectrum are completely missed. Not all of the models listed in Tab. 5.1 (e.g., model M3, Fig. D.2) match the

lowest and highest of the observed frequencies as odd modes. We also note that there are cases where the modes with ℓ values having similar parity tend to overlap or even cross each other. This phenomena was discussed at the end of chapter 4 and is the reason that the small spacing (when calculated from $\nu_{n,\ell} - \nu_{n-1,\ell+2}$) can become 0 or negative in the presence of a magnetic field. Appendix D provides Saio plots for all of the models presented in the tables in this chapter.

The model match probabilities; better described as model plausibilities within our grid, were computed with Eq. 5.1 by scaling our observed uncertainties by a factor of 50. At the beginning of this section we stated that this scaling factor, after some experimentation, was chosen because it allowed us to properly visualize and conveniently normalize our probabilities. The lack of a realistic model uncertainty causes most of the models in our grid to get too little weight given our stringent observational uncertainties. We now have enough information, based on the quality of our model matches, to show that a error scaling factor of 50 is reasonable. The average 1σ uncertainty of our observations (Tab. 3.1) is 0.032 μHz and the average 3σ uncertainty is 0.092 μHz. The most precise oscillation frequency identified in the *MOST* data is $\nu_{15} = 2720.914 \pm {}^{0.002(1\sigma)}_{0.005(3\sigma)}$ μHz. Traditional measures of the frequency resolution when applied to the *MOST* data range from $0.25/\Delta T \sim$ 0.1 μHz to $1.5/\Delta T \sim 0.6$ μHz. On average, our 1σ uncertainties would have to multiplied by 18.75 (= 0.6/0.032) to reach the $1.5/\Delta T \sim$ of 0.6 μHz. Our 3σ uncertainties (again on average) would have to be multiplied by 6.52 to reach the same upper resolution limit of 0.6 μHz. Our most precise frequency

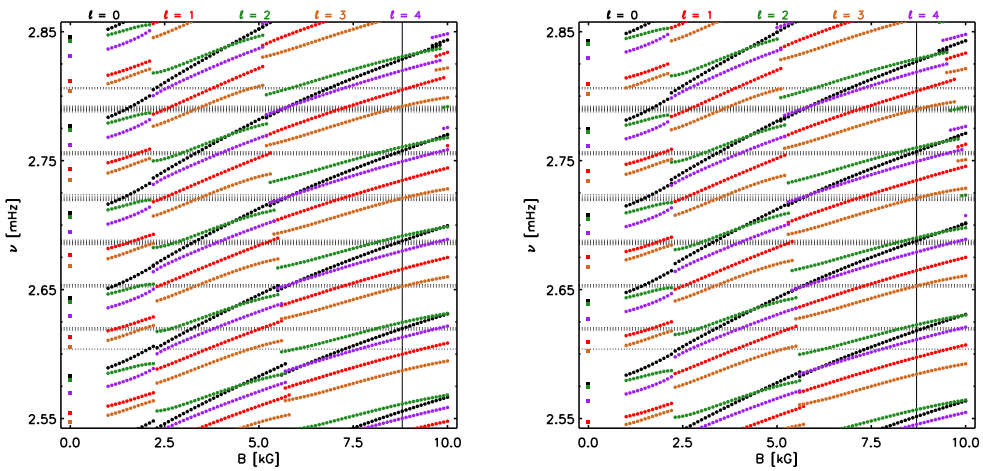

Figure 5.8: Magnetically perturbed oscillation frequencies as a function of magnetic field strength for selected models of HR 1217. The panels show the unperturbed frequencies as squares at the far left while magnetically perturbed values are plotted as coloured circles. The angular degrees ℓ of each mode are coloured according to the labels at the top of each panel. The *MOST* observations from Tab. 3.1 are plotted as horizontal dotted lines. The left panel shows model M1 of Tab. 5.1 identified as a solid vertical line while the right panel illustrates the match using model M2 of the same table. The best matched models for M1 and M2 have similar properties. Note that the magnetic perturbations produce a cyclic variation with magnetic field strength so that models with a lower magnetic field can also exist for models with physical characteristics like those of M1 and M2; but, these models would not be as statistically significant.

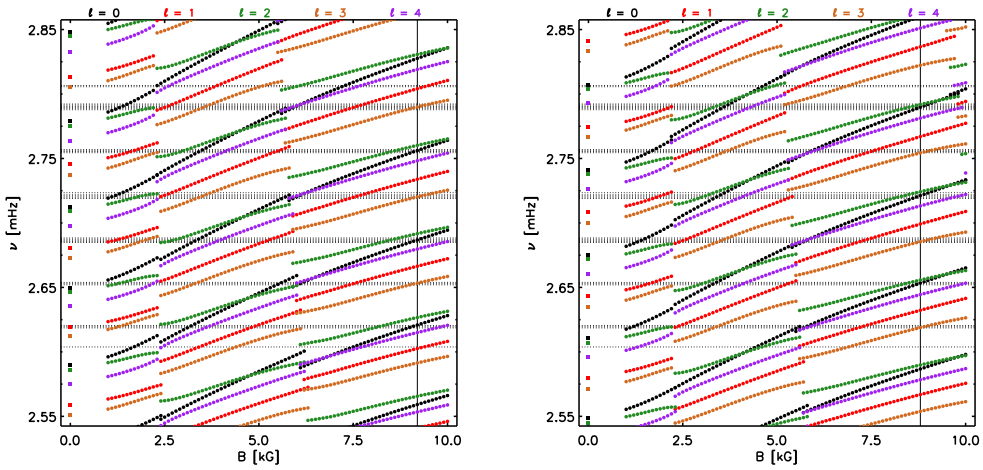

Figure 5.9: Magnetically perturbed oscillation frequencies as a function of magnetic field strength for selected models of HR 1217. Panel labels are the same as those in Fig. 5.8. The solid vertical line in the left panel shows the position of model M9 of Tab. 5.1. This model is selected because it has the smallest mean difference between model and observed frequencies of 1.22 μHz. The right panel identifies the model with the smallest median difference between model and observed frequencies of 0.88 μHz. That properties of that model (labelled MM1) are listed in Tab. 5.2. Although these models have low mean and median values, they are not the most probable matches. Note that the cyclic nature of the magnetic perturbation gives the closest matched modes at both low and high B values.

would have to have its 1σ uncertainty multiplied by 300 (or by 120 for the 3σ uncertainty) to arrive at 0.6 μHz. So, if we were to use the most conservative estimate of frequency resolution ($1.5/\Delta T$) to scale our frequency precision upward, we would have to use a factor that is some where between about 10 to 100. In Fig. 5.5 we showed that the model match probability correlates well with the median frequency deviation between the model frequencies and the observed periodicities. The median deviation of our most probable models (Tab. 5.1) is about 1 μHz. If we were to assume that our bootstrap uncertainties should be scaled to match the smallest median deviation ($\sim$ 1 μHz) between our calculated eigenmodes and our observations, our average 1σ uncertainties would have to be multiplied by 31.25 and our average 3σ uncertainties by 10.87. Our smallest frequency uncertainty would have to be multiplied by a few hundred ($\sim$ 200 using the 3σ uncertainties). This would again suggest an uncertainty scale that falls somewhere in the range of a few tens to a few hundreds. When there is some unknown systematic uncertainty, the observed uncertainties can be scaled so that the best matched model has a reduced $\chi^2 = 1$. If we do this for model M1 of Tab. 5.1, the observational uncertainties would have to be scaled by 41.06. The frequency scaling of 50 is reasonable given the above scaling scenarios. This is especially true because we are more concerned with the relative probabilities between models within our grid and not the value of the individual probabilities themselves.

5.2 Matching the true modes of HR 1217

In the preceding section models were matched to all of the observed periodicities in the *MOST* data (Tab. 3.1). Different probability distributions and average deviation statistics were used to highlight the differences between the computed magneto-acoustic models and the observed oscillation frequencies of HR 1217. In this section we isolate what we believe are the pulsation modes (as opposed to rotation splittings) in the HR 1217 data and illustrate what effect using this selection of frequencies has on the most plausible matches.

Consider frequencies ν_{28} and ν_{29} of Tab. 3.1. They are split by the rotation frequency of HR 1217 (~ 0.9 μHz) but they have the same amplitude to within their 1σ uncertainties. How can we decide which frequency is the rotational component and which frequency is the main oscillation mode? This dilemma was also discussed in § 3.3 for frequencies ν_8 through ν_{12} and near ν_{19} and ν_{20} (Tab. 3.1). Evidence suggests that there are potential small spacings of ~ 1.5 or 2.5 μHz near these frequency groups, along with rotational splittings, and it is difficult to decide which periodicity is the true oscillation frequency. For the purposes of matching models we select a subset of frequencies that we believe to be the main frequency within their respective frequency groupings. These are usually the largest amplitude components within their groupings. In the cases where we are not certain as to which mode should be considered as the main frequency, we select a frequency and adopt an uncertainty that reflects the range in frequency space that is spanned by its closest, approximately rotationally split, neighbours. For example, if we chose ν_9 as a main frequency, we adopt a value of $[\nu_{10} + \sigma_{10} - (\nu_8 - \sigma_8)]/2.0$

as its uncertainty. Table 5.3 lists the frequencies that we believe could be the main oscillation modes in the HR 1217 data. With the pulsation modes of HR 1217 identified, we can now assign a unique frequency match to each of the observed frequencies. By assigning a unique frequency match instead of allowing a model frequency to identify itself with multiple observations (as was done in the previous section), we can immediately ignore close model matches to rotational splittings. This is important because a close match to a rotational splitting could easily skew our matching statistics. The unique assignment of a modelled frequency to an observed frequency will also immediately give us an indication of how closely individual modes are spaced from each other.

Table 5.3: Selected frequencies identified using the *MOST* data. Both 1 and 3σ uncertainties on the fitted parameters are estimated from 100,000 bootstrap realizations. Frequency uncertainties marked by $*$ are average uncertainties based on the separation from the marked frequency to the nearest ($\sim$ rotationally split) frequency plus its uncertainty (see the text for details). The phases are referenced to the time of the first observations of HR 1217 (= HJD 2451545.00 + 1769.42 days). This table is reproduced in appendix B with frequencies in units of cycles day^{-1}.

#	ν [μHz]	A [μmag]	ϕ [rad]	$\sim$ S/N	σ_ν	$3\sigma_\nu$	σ_A	$3\sigma_A$	σ_ϕ	$3\sigma_\phi$
1	2603.832	39	2.22	3.8	$\pm$ 0.028	0.080	6	15	0.34	0.93
3	2619.495	125	5.70	9.2	$\pm$ 0.015	0.039	6	16	0.11	0.29
6	2652.924	365	5.56	24.2	$\pm$ 0.004	0.011	6	16	0.04	0.10
9	2685.659	31	2.83	3.1	$\pm$ 0.897$*$	0.951$*$	9	26	0.55	2.18
11	2687.420	467	4.46	29.7	$\pm$ 0.004	0.009	6	16	0.03	0.08
15	2720.914	764	1.83	41.6	$\pm$ 0.002	0.005	6	16	0.02	0.05
17	2723.469	41	2.08	3.1	$\pm$ 0.034	0.097	6	16	0.39	1.10
19	2755.393	118	3.45	8.9	$\pm$ 0.015	0.039	6	16	0.17	0.45
21	2756.925	39	5.14	3.1	$\pm$ 0.487$*$	0.578$*$	6	17	0.53	1.67
23	2788.872	37	0.24	3.6	$\pm$ 0.034	0.096	6	16	0.29	0.80
26	2791.384	82	5.00	6.8	$\pm$ 0.033	0.085	7	17	0.29	0.74

continued on next page

Table 5.3: *continued*

#	ν [μHz]	A [μmag]	ϕ [rad]	$\sim$ S/N	σ_ν	$3\sigma_\nu$	σ_A	$3\sigma_A$	σ_ϕ	$3\sigma_\phi$
28	2805.650	84	1.10	6.9	$\pm$ 0.488$*$	0.514$*$	6	15	0.15	0.37

As in the last section we show match probabilities assuming both Gaussian and Laplace probability distributions. The probabilities calculated using data from Tab. 5.3 are shown in Fig. 5.10. We immediately see that when we compare the probability distribution for the magnetic field strength in Fig. 5.10 to the multiple-match case shown in Figs. 5.3 and 5.4, that the probability peaks for the magnetic field near 8 kG has significantly dropped in comparison to probability peaks near 4 kG. This is an immediate indication that by allowing a single model frequency to match multiple observed periodicities; and, by including the rotational splittings in our data set, we were dramatically altering the weight of the matches. The use of the Gaussian or the Laplace distribution once again illustrates how outlying matches near the tails influences the shape of the probability curves. We can draw the same broad conclusions by using either of the Laplace or Gaussian distributions but some details of the probability space are exaggerated by choosing to match models using the Laplace distribution. The probability space around the mass parameter is broader in Fig. 5.10 than it is in Figs. 5.3 and 5.4. The composition (Z/X) seems to loosely favour values less than 0.02 in Fig. 5.10 but was strongly peaked at about Z/X = 0.02 in Figs. 5.3 and 5.4. In Fig. 5.11 we show the probability space for the percentage of the main sequence lifetime that the models have completed, $\log_{10} g$, and the models' convective core mass. In selecting only the pulsation modes in the HR 1217 data, we see that the probability distributions for these parameters are less affected than were the distributions for the magnetic field strength, mass, and composition (see Figs. 5.3 and 5.4). This may not be particularly surprising because $\log_{10} g$ varies slowly with position on the HR diagram and

the percentage of the main sequence lifetime that a model has traversed is selected by limiting our choice of luminosity and effective temperature (see § 4.1.1). The constraint on which stellar model masses fall in that luminosity and effective temperature range also limits the values of the convective core mass of our models.

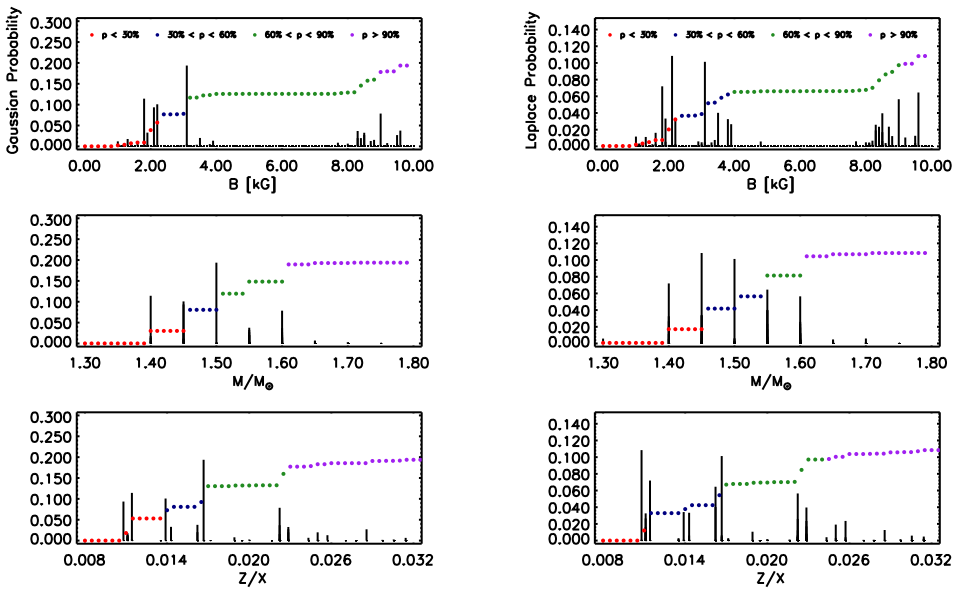

Figure 5.10: The observed frequencies of Tab. 5.3 are used in the model search with 3σ errors scaled by 50. Probabilities in the left panel are assigned using a Gaussian probability distribution (Eq. 5.1) and the panels on the right show probabilities calculated from a Laplace probability distribution (Eq. 5.3). The top panels show the probability of all models as a function of magnetic field strength, the middle panels are probability as a function of model mass, and the bottom plots give probability as a function of composition (Z/X). The distribution of probabilities for the magnetic field strengths; favouring magnetic fields less than about 5 kG, is a clear contrast from that presented in Fig. 5.3, where larger magnetic fields ($\sim$ 8 kG) are favoured. As in the previous examples, the Laplace distribution tends to highlight more models in probability space.

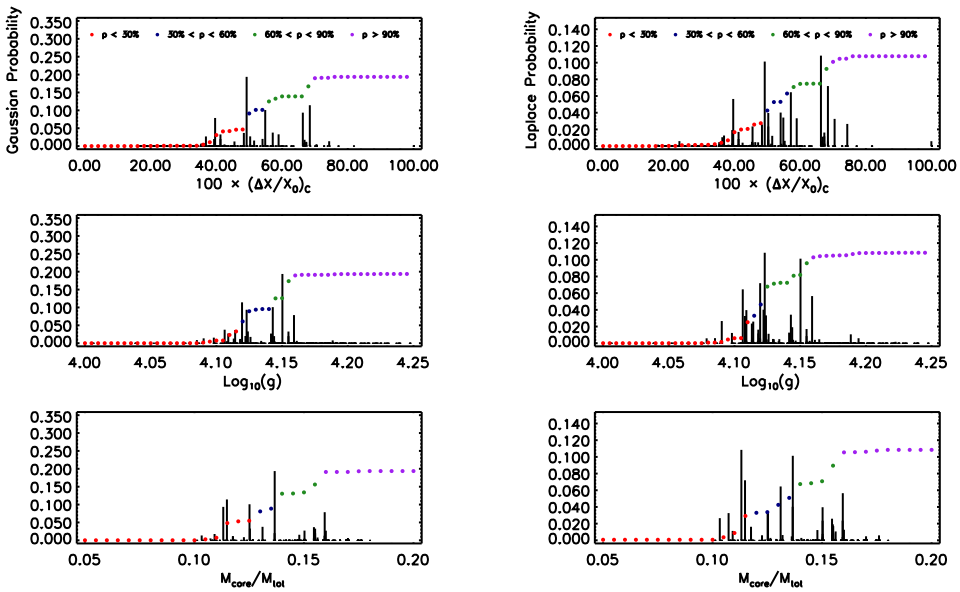

Figure 5.11: Model match probabilities using a subset of the *MOST* frequency values. The observations are matched in the same way as in Fig. 5.10. The left panels show Gaussian probabilities and the right panels show Laplace probabilities. Listed from top to bottom, the panels show the match probabilities as a function of the percentage of the main sequence lifetime the model has completed, the surface gravity of the model, and the mass of the model's convective core in units of total stellar mass. These are similar to the probability distributions shown in Figs. 5.3 and 5.4.

Table 5.4: Some properties of the most probable models of HR 1217. The top ten unique models from the Gaussian and Laplace probabilities are listed in decreasing probability order. Deviation refers to the absolute difference between a model frequency and the best matched observed frequency and σ is the standard deviation. The column labelled as probability label refers to the order of the probability from each of the Gaussian or Laplace probabilities. For example, 1 G is the most probable Gaussian probability and 10 L would be the 10th most probable Laplace probability. The probability ratio is defined as the Gaussian probability of the model divided by the Gaussian probability of the most probable model ($\ln P = -31.1$). The models in this table were matched to all frequencies listed in Tab. 5.3 using $50 \times 3\sigma$ errors.

Model ID	$M/M_\odot$ B (kG) cut-off (μHz)	X $M_{conv.env.}/M_\star$ median deviation (μHz)	Z Log_{10} (T_{eff}) mean deviation (μHz)	Age (Gyr) Log_{10} ($L/L_\odot$) σ deviation (μHz)	α Log_{10} ($R/R_\odot$) probability label	$M_{conv.core}/M_\star$ $\Delta\nu$ (μHz) probability ratio
U1	1.50	0.720	0.012	1.15	1.6	0.1366
	3.1	0.00	3.8657	0.8789	0.2318	70.26
	1877.92	2.84	4.51	4.76	1 G, 2 L	1.000
U2	1.45	0.740	0.008	1.50	1.6	0.1132
	2.1	0.00	3.8651	0.8888	0.2381	67.60
	1749.34	1.88	3.27	3.27	1 L, 4 G	0.483
U3	1.40	0.700	0.008	1.35	1.6	0.1148
	1.8	0.00	3.8730	0.9089	0.2322	67.66
	1729.36	2.35	3.39	3.15	2 G, 3 L	0.590
U4	1.45	0.720	0.010	1.30	1.8	0.1251
	2.2	0.00	3.8637	0.8633	0.2281	70.16
	1857.29	1.39	2.92	2.77	3 G, 8 L	0.521
U5	1.60	0.720	0.016	0.90	1.8	0.1595
	9.0	0.00	3.8690	0.9114	0.2414	70.20
	1899.10	3.07	4.87	5.22	5 G, 5 L	0.406
U6	1.55	0.740	0.012	1.30	1.8	0.1311
	9.6	0.00	3.8581	0.9067	0.2609	65.06
	1719.39	1.42	4.87	6.27	6 G, 4 L	0.195
U7	1.60	0.720	0.0160	1.05	1.6	0.1545
	8.3	0.00	3.8608	0.9232	0.2638	65.20

continued on next page

Table 5.4: *continued*

Model ID	$M/M_\odot$ B (kG) cut-off (μHz)	X $M_{conv.env.}/M_\star$ median deviation (μHz)	Z Log_{10} (T_{eff}) mean deviation (μHz)	Age (Gyr) Log_{10} ($L/L_\odot$) σ deviation (μHz)	α Log_{10} ($R/R_\odot$) probability label	$M_{conv.core}/M_\star$ $\Delta\nu$ (μHz) probability ratio
	1754.73	1.89	5.20	6.35	7 G, 12 L	0.190
U8	1.45	0.700	0.0100	1.20	1.4	0.1253
	1.9	0.00	3.8670	0.9069	0.2376	67.66
	1763.55	2.33	2.99	2.87	8 G, 9 L	0.170
U9	1.55	0.740	0.012	1.25	1.8	0.1366
	3.5	0.00	3.8612	0.9030	0.2530	66.69
	1766.91	1.09	4.52	5.90	6 L, 12 G	0.104
U10	1.55	0.700	0.016	1.05	1.6	0.1502
	8.5	0.00	3.8596	0.9100	0.2595	65.19
	1756.98	1.56	5.13	6.38	7 L, 10 G	0.140

Table 5.4 lists the properties of the most probable model matches to the *MOST* frequencies identified in Tab. 5.3. About half of the models listed in Tab. 5.4 have magnetic field strengths between 2 and 5 kG. This is in line with the magnetic field strengths measured in HR 1217 that range from about 2 to 4.5 kG (Bagnulo et al. 1995, Lüftinger et al. 2008). This is in contrast to the most probable model matches given in Tab. 5.1. Those models were matched to all of the frequencies (including rotational splittings) extracted from the HR 1217 data (Tab. 3.1) and gave magnetic field strengths near 1 kG or greater than about 8 kG.

The most probable model (U1 of Tab. 5.4) matched using only the "true" pulsation frequencies has a magnetic field strength of $B = 3.1$ kG. Its probability (unnormalized and calculated using a uniform uncertainty scaling of 50 $\times$) is $\ln P =$ -31.1. As discussed previously, this match probability is low. The *MOST* observations are measured to a precision that is much better than our modelled frequencies can be matched. Figure 5.12 shows the modelled mode deviations from the *MOST* frequencies and the Saio plot (magnetically perturbed eigenmodes as a function of magnetic field) for the same model. The mean deviation between the observed frequencies and the model U1 modes is 4.51 μHz with a standard deviation of 4.76 μHz. The median of the frequency deviations is 2.84 μHz. Note again that the matching procedure used in this section is different from the matching procedure used in the previous section. In this section we force a unique mode identification on each of the "true" frequencies measured in the *MOST* data (Tab. 5.4). Because of this, the mean differences between the theory and observations will tend to be larger than they would have been if we allowed one modelled eigenmode

to match multiple observed frequencies. The eigenmodes from model U1 that are the poorest matches are an $\ell = 2$, $\nu = 2796.694$ μHz (matched to $\nu_{28} = 2805.650$ μHz of Tab. 3.1) mode, an $\ell = 4$, $\nu = 2783.533$ μHz (matched to $\nu_{26} = 2791.384$ μHz) mode, and a mode having $\ell = 2$ and $\nu = 2727.779$ μHz (matched to $\nu_{17} = 2723.469$ μHz). All other matches deviate by less than about 1.4 μHz. The best matching mode is at 2720.908 μHz. That mode is an $\ell = 0$ mode and is matched to the most precise of the *MOST* frequencies ($\nu_{15} = 2720.914\mu$Hz). The perturbed small spacings ($\delta\nu^{2-0}$) of model U1 are all negative over the range in frequencies observed in HR 1217. The small spacing has its lowest absolute value of -5.614 μHz at $\nu = 2653.190$ μHz and increases in absolute value to -6.473 μHz at $\nu = 2859.900$ μHz. An average over n and ℓ; between frequencies 2618.600 and 2792.249 μHz, yields a large spacing of 68.792 μHz for model U1.

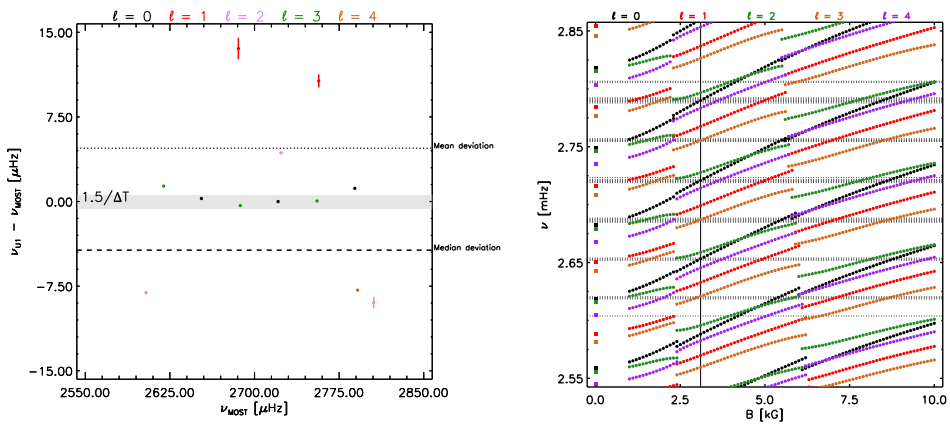

Figure 5.12: (Left) The modelled frequency deviations from the *MOST* frequencies (Tab. 5.3). The labels are the same as those in Fig. 5.6. Model U1 is the most probable model listed in Tab. 5.4. The average frequency deviation is 4.51 μHz. (Right) Magnetically perturbed frequencies as a function of magnetic field strength for the same model. The labels are the same as those in Fig. 5.8. Model U1 has a high probability because it does a reasonable job of matching the most precise frequencies from the *MOST* data set. The model cannot match frequencies to the high level of frequency precision measured by *MOST*.

The properties of the models having the smallest mean (= 2.32 μHz) and median (= 0.64 μHz) absolute deviation between the theoretical modes and the observed periodicities are listing in Tab. 5.5. The model with the lowest mean deviation (labelled UU1) and the model having the lowest median deviation (UU2) have magnetic field strengths of 1 and 8.4 kG, respectively.

Figure 5.13 shows the frequency deviation plot of model UU1. We see that the small spacings (modes spaced by $\lesssim 3$ μHz) are better reproduced than the potentially magnetically perturbed modes (at the highest and lowest frequencies) are matched. That being said, the model itself does not constitute a statistically sound match. Saio diagrams shown in Fig. 5.14 for the models (UU1 and UU2) of Tab. 5.5 show that the anomalous, non-asymptotic, frequencies located at either end of the observed oscillation spectrum are not well matched. The closest match to those magnetically perturbed modes in model UU1 are matched to $\ell = 4$ modes, and have deviations of about 3.5 μHz at ~ 2600 μHz and 6.5 μHz at ~ 2800 μHz. The frequencies of model UU1 tend to cluster in alternating even and odd parity groups, with one notable exception: Near ~ 2600 μHz, the $\ell = 4$ mode is separated in frequency from the $\ell = 0$, 2 couple (matched to the next closest mode) by about 11 μHz. On the opposite end of the spectrum (near ~ 2800 μHz) the last two measured frequencies have associated with them modes with opposite parity. This is interesting because the *MOST* frequencies at the low end of the spectrum could be interpreted as potential small spacings while the high end of the spectrum would not be interpreted as such. Of course, the magnetic perturbations between modes separated in degree by two can be so large that labelling spacings as "small" or second order separations; as calculated in the non-magnetic case, may simply not be appropriate. This behaviour is not apparent in the Saio plot of the model (UU2) with the lowest median frequency deviation (right panel of Fig. 5.14). Saio diagrams for all models listed in the tables of this chapter are given in appendix D.

Table 5.5: Some properties of selected models of HR 1217. The models with the lowest mean and median deviations between observed and calculated frequencies are listed (respectively) below. The column labelled as probability label refers to the order of the probability from each of the Gaussian or Laplace probabilities. For example, 1 G is the most probable Gaussian probability and 10 L would be the 10th most probable Laplace probability. The probability ratio is defined as the Gaussian probability of the model divided by the Gaussian probability of the most probable model (see Tab. 5.4). The models in this table were matched to all frequencies listed in Tab. 5.3 using $50 \times 3\sigma$ errors.

Model ID	$M/M_\odot$	X	Z	Age (Gyr)	α	$M_{conv.core}/M_\star$
	B (kG)	$M_{conv.env.}/M_\star$	Log_{10} (T_{eff})	Log_{10} ($L/L_\odot$)	Log_{10} ($R/R_\odot$)	$\Delta\nu$ (μHz)
	cut-off (μHz)	median deviation (μHz)	mean deviation (μHz)	σ deviation (μHz)	probability label	probability ratio
UU1	1.40	0.720	0.008	1.50	1.6	0.1092
	1.0	0.00	3.8645	0.8679	0.2287	68.61
	1782.97	1.92	2.32	1.96	13194 G, 6948 L	3.692×10^{-89}
UU2	1.55	0.700	0.016	1.05	1.4	0.1502361
	8.4	0.00	3.8595	0.9100	0.2598	65.06
	1755.53	0.64	4.79	6.31	38 G, 22 L	0.024

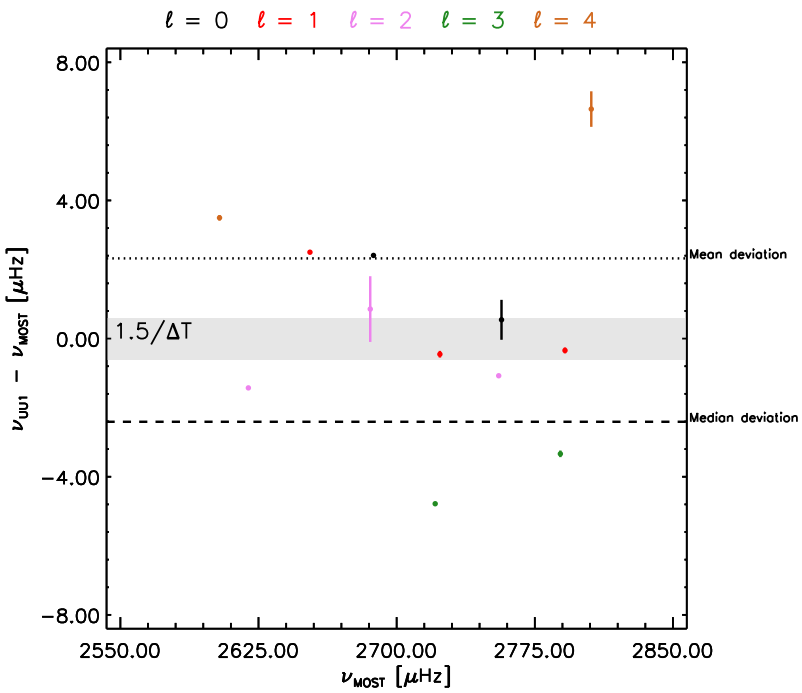

Figure 5.13: Model UU1 pulsation frequencies (Tab. 5.5) are compared to the *MOST* observations. The labels are the same as those in Fig. 5.6. Model UU1 is the model with the smallest mean frequency deviation (2.32 μHz) from the *MOST* frequencies.

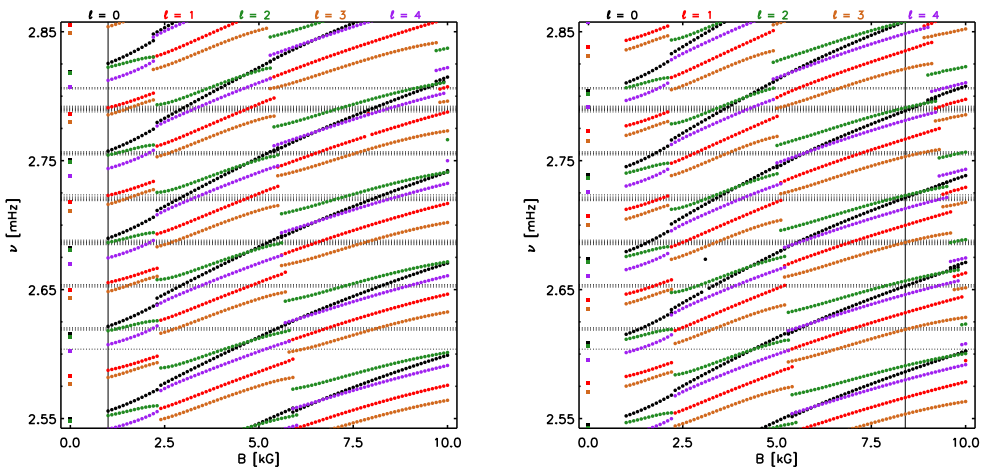

Figure 5.14: Magnetically perturbed frequencies as a function of magnetic field strength for the models with the lowest mean(model UU1 of Tab. 5.5, left) and median (model UU2 of Tab. 5.5, right) deviation matches. Panel labels are the same as those in Fig. 5.8. Comparing the closest models using the mean or the median as a statistic describing the match to observations can lead to dramatically different "best-fit" models.

5.2.1 Matches to a sub-set of the *MOST* frequencies

In the previous sections (§ 5.1.2 and 5.2) we matched our model grid to the frequencies observed by *MOST* using all of the frequencies identified in the data (Tab. 3.1) and by using only those modes that we believed to be the pulsation modes of HR 1217 (Tab. 5.4). We were not able to find a model that matched the observations to the level of precision obtained by

the *MOST* mission. That is, we can find models that match the observed frequencies with a mean deviation of a few μHz but the periodicities identified in the *MOST* time-series have frequency uncertainties that are, on average, hundredths of a μHz. Interestingly, it seems that in the majority of the cases presented thus far, we come closest to matching the frequencies spaced from their neighbours by ~ 15 μHz (usually referred to as the magnetically perturbed modes) or the frequencies spaced by $\sim$ 1–3 μHz (usually referred to as the small or second-order-spaced modes); but, we cannot seem to come close to matching both in a given model. In this section we explore this observation further by matching models to two sub-sets of the frequencies listed in Tab. 5.4.

In the first sub-set of frequencies we only attempt to match the two anomalous (magnetically perturbed) frequencies and the most precisely determined observational frequency. These are located at 2603.832, 2720.914 and 2805.650 μHz. The properties of the models leading to the most probable model match and the model match with the smallest mean deviation from the observations; labelled GS and MS, respectively, are listed in Tab. 5.6. The models have very similar physical characteristics but their matches show very different character (Fig. 5.16). The most probable model match shows the highest and lowest of observed frequencies being matched by either an $\ell =$ 0 or 4 mode. Figure 5.15 shows the frequency deviation plot for this model. The model with the smallest mean deviation (from the 3 observed frequencies being considered here) shows the best match to those anomalous, magnetically perturbed modes to be an $\ell = 2$ mode. The most probable model in this case matches the lowest two frequency groups with an even-even ℓ pattern,

and then continues with an odd-even alternating pattern. The best mean match, on the other hand, shows an even-odd alternating ℓ pattern for most of the modes, except near the highest two frequency groups. There, the pattern switches to an even-even ℓ match. This behaviour is illustrated in the Saio plots of models GS and MS (Fig. 5.16). The models GS and MS match well (with averages deviation of 0.23 and 0.09 μHz, respectively) the selected frequencies at 2603.832, 2720.914 and 2805.650 μHz; but, this comes at the expense of poorly matching the other frequencies. Model GS has modes that deviate at most by $\sim$ 18 μHz while model MS — having a slightly smaller deviation range — has its largest deviation between observations and theory of about 10 μHz.

Table 5.6: Some properties of the most probable models of HR 1217. The most probable (using either of the Gaussian or Laplace probability distributions) model (GS) is obtained by matching frequencies at 2603.832, 2720.914 and 2805.650 μHz (see Tab. 5.3). The lowest mean deviation model (MS) is also listed. Deviation refers to the absolute difference between a model frequency and the best matched observed frequency and σ is the standard deviation. Columns with probability labels 1 and 2 refer to the order of the probability from each of the Gaussian or Laplace probabilities. For example, 1 G is the most probable Gaussian probability and 10 L would be the 10th most probable Laplace probability.

Model ID	$M/M_\odot$	X	Z	Age (Gyr)	α	$M_{conv.core}/M_\star$
	B (kG)	$M_{conv.env.}/M_\star$	Log_{10} (T_{eff})	Log_{10} ($L/L_\odot$)	Log_{10} ($R/R_\odot$)	$\Delta\nu$ (μHz)
	cut-off (μHz)	median deviation (μHz)	mean deviation (μHz)	σ deviation (μHz)	probability label 1	probability label 2
GS	1.50	0.740	0.010	1.40	1.8	0.1211
	6.3	0.00	3.8587	0.8886	0.2507	66.24
	1740.21	0.29	0.23	0.19	1 G	1 L
MS	1.50	0.740	0.010	1.20	1.6	0.1264
	6.8	0.00	3.8694	0.8728	0.2214	72.65
	1930.08	0.11	0.09	0.04	138 G	64 L

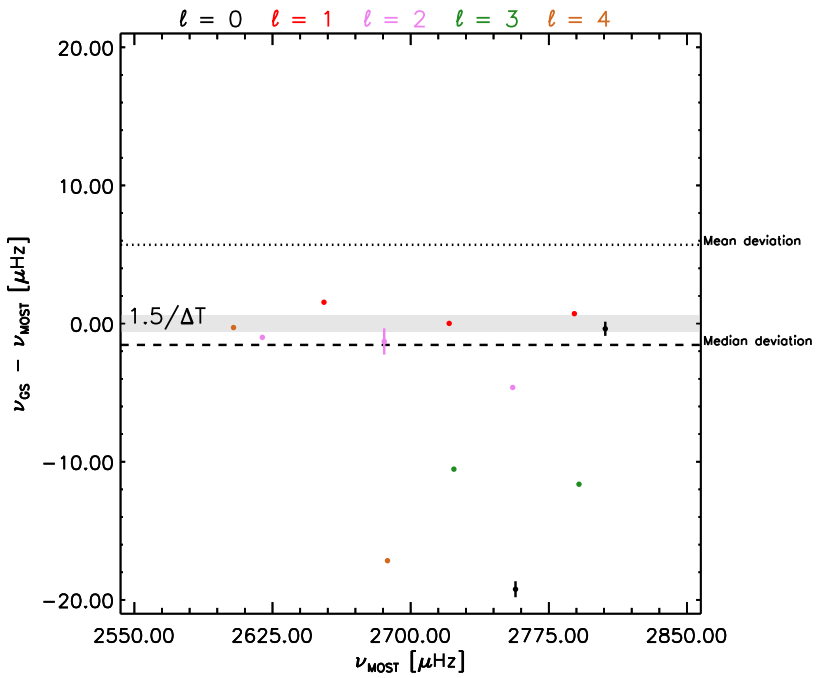

Figure 5.15: Frequency deviations for the most probable model matched to *MOST* frequencies at 2603.832, 2720.914 and 2805.650 μHz only. The model does a reasonable job of matching frequencies to within about $\pm$ 2 μHz. The obvious exception is for the potentially small-spaced frequencies that are spaced by between 1.5–3 μHz from their nearest frequency neighbours. Those frequencies deviate from the observations by between $\sim$ 4 and 20 μHz.

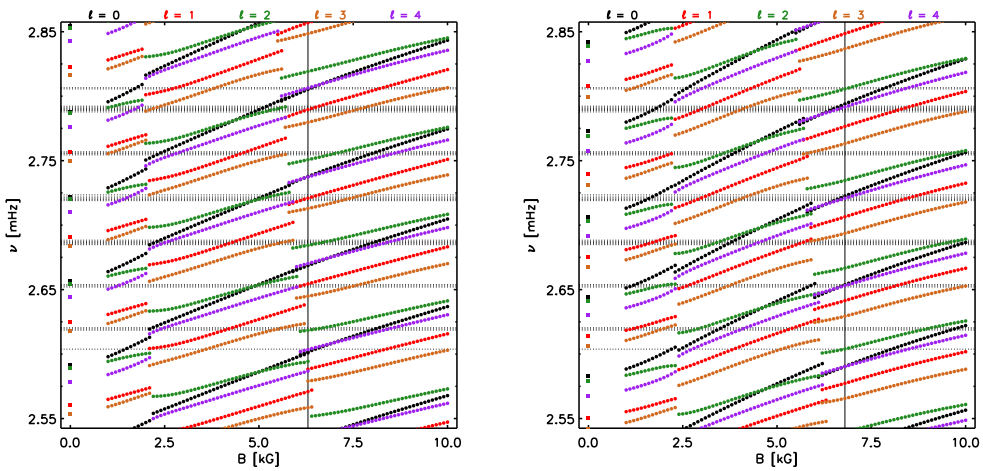

Figure 5.16: The best matched models using a forced match to the magnetically perturbed observations. Panel labels are the same as those in Fig. 5.8. The left panel shows the most probable (using either of the Gaussian or Laplace probability distributions) model obtained by matching frequencies at 2603.832, 2720.914 and 2805.650 μHz only. The right panel shows the model with the lowest mean difference between the theory and observations using only the three frequencies listed above. Model properties are listed in Tab. 5.6. Both models have similar properties.

In selecting another sub-set of frequencies from Tab. 5.3 to be matched to our models, we start by choosing only the frequencies identified in both the *MOST* data and the data of Kurtz et al. (2005). We exclude frequency ν_{26} = 2791.384 μHz (Tab. 3.1) from our new list. That frequency was common to the *MOST* observations and to those of Kurtz et al. (2005). It is also one

of the so-called "missing modes" of Kurtz et al. (2005). With its elimination, there are no second order (small) spacings present in the data. We add frequency $\nu_1 = 2603.832$ μHz to the new listing of frequencies because it is potentially a magnetically perturbed mode. Table 5.7 lists the new frequency sub-set to which our models will be matched.

Table 5.7: Selected frequencies identified using the *MOST* and Kurtz et al. (2005) data. This table gives frequencies found by both *MOST* and Kurtz et al. (2005) with the omission of all closely ($\lesssim 3$ μHz) spaced frequencies and with the addition of ν_1 of Tab. 3.1. A comparison should be made with entries in Tab. 5.3. Both 1 and 3σ uncertainties on the fitted parameters are estimated from 100,000 bootstrap realizations. Frequency uncertainties marked by $*$ are average uncertainties based on the separation from the marked frequency to the nearest ($\sim$ rotationally split) frequency plus its uncertainty (see the text for details). The phases are referenced to the time of the first observations of HR 1217 (= HJD 2451545.00 + 1769.42 days).

#	ν [μHz]	A [μmag]	ϕ [rad]	$\sim$ S/N	σ_ν	$3\sigma_\nu$	σ_A	$3\sigma_A$	σ_ϕ	$3\sigma_\phi$
1	2603.832	39	2.22	3.8	$\pm$ 0.028	0.080	6	15	0.34	0.93
3	2619.495	125	5.70	9.2	$\pm$ 0.015	0.039	6	16	0.11	0.29
6	2652.924	365	5.56	24.2	$\pm$ 0.004	0.011	6	16	0.04	0.10
11	2687.420	467	4.46	29.7	$\pm$ 0.004	0.009	6	16	0.03	0.08
15	2720.914	764	1.83	41.6	$\pm$ 0.002	0.005	6	16	0.02	0.05
19	2755.393	118	3.45	8.9	$\pm$ 0.015	0.039	6	16	0.17	0.45
23	2788.872	37	0.24	3.6	$\pm$ 0.034	0.096	6	16	0.29	0.80
28	2805.650	84	1.10	6.9	$\pm$ 0.488$*$	0.514$*$	6	15	0.15	0.37

Figure 5.17 plots the Gaussian probabilities of the most plausible model matches to the observations of Tab. 5.7. We can compare the probability distributions in each parameter plane to those using different super/sub-sets of the identified *MOST* frequencies. Figures 5.3, 5.4, and 5.10 show probabilities for the magnetic field strengths that are broadly distributed around ~ 4 kG and ~ 8 kG. This is also true of the probability distribution around the magnetic field strength shown in Fig. 5.17. Of all the frequency combinations explored in this chapter, the most probable magnetic field strengths tend to cluster in groups ranging from 1–5 kG and 8–10 kG. There are no preferred models that have a magnetic field strength of $B = 0$ kG. Of course, such conclusions come with the caveat that we cannot match the observations to within their measured precision. The magnetic field strength ranges should only be taken as a rough guide and not as statistical confidence limits. The probability space around the mass parameter favours models with masses less than about 1.5 $M_\odot$ and the composition (Z/X) seems to loosely favour values less than 0.02. This is true for each of the frequency matches explored. The other parameters common to each of the probability plots; e.g., $\log g$, show little variation when matches are made to different combinations of the frequencies listed in Tab. 3.1.

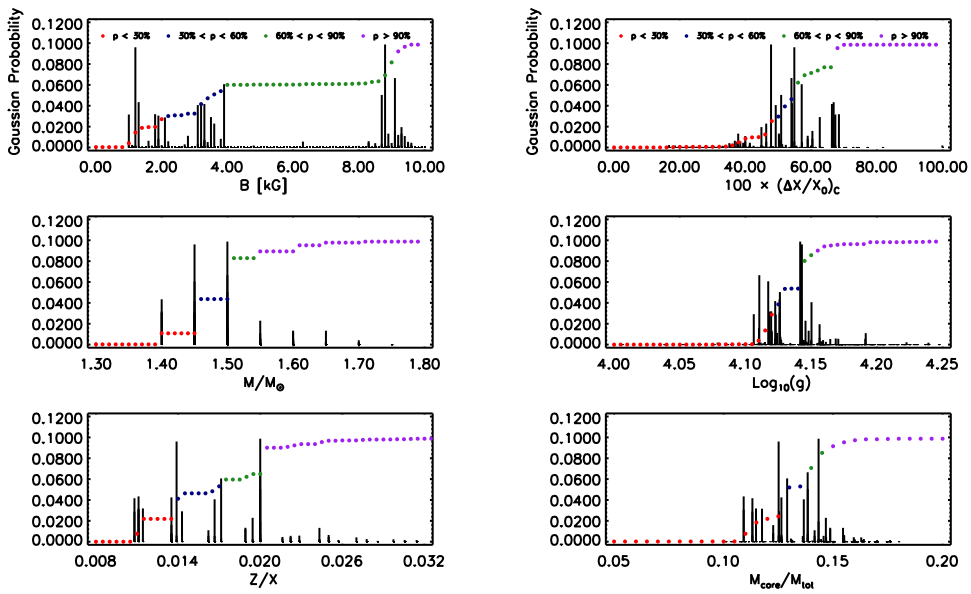

Figure 5.17: Probability distributions for models matched to frequencies in Tab. 5.7. Labels are the same as in Fig. 5.4. Favoured models have magnetic fields that fall within two broad groups. The first probability grouping is between $\sim$ 1–5 kG and the second range is between about 8–10 kG. This feature is common in all probability plots presented in this chapter. Likewise, the probability distributions for the percentage of main sequence lifetime completed, $\log_{10} g$, and for the models' convective core mass are similar in all of the probability plots in this chapter.

We label the model with the most probable ($\ln P$ = -14.02) match to the observed frequencies of Tab. 5.7 PGS, and list its properties in Tab. 5.8. A plot of its frequency deviations is given in Fig. 5.18 and a Saio plot; showing how the frequencies of model PGS change with magnetic field strength, is given in appendix D (Fig. D.14). The model has a magnetic field strength

that falls in the high range of 8.8 kG. The mean deviation between the modelled modes and the observed periodicities is 1.40 μHz. The modes deviate from the observations by less than 4 μHz. The magnetically perturbed (anomalously-spaced) pulsation modes located at either end of the observed frequency range are best identified as $\ell = 1$ modes (for model PGS). Other modes alternate between $\ell = 0$ and 3.

Table 5.8: Some properties of a selected model of HR 1217. This model has the highest Gaussian probability ($\ln P$ = -14.02) of the models matched to the frequencies listed in Tab. 5.7 (using $50 \times 3\sigma$ errors).

Model ID	$M/M_\odot$	X	Z	Age (Gyr)	α	$M_{conv.core}/M_\star$
	B (kG)	$M_{conv.env.}/M_\star$	Log_{10} (T_{eff})	Log_{10} ($L/L_\odot$)	Log_{10} ($R/R_\odot$)	$\Delta\nu$ (μHz)
	cut-off (μHz)	median deviation (μHz)	mean deviation (μHz)	σ deviation (μHz)		
PGS	1.50	0.700	0.014	1.05	1.4	0.1434
	8.8	0.00	3.8645	0.8826	0.2361	69.25
	1866.36	0.57	1.40	1.51		

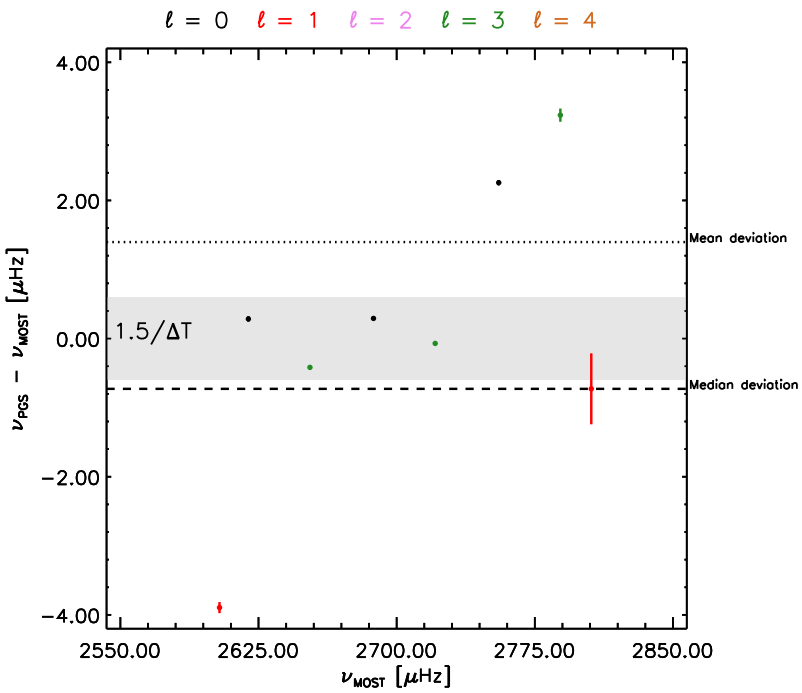

Figure 5.18: Deviations between the frequencies of model PGS (Tab. 5.8) and the *MOST* frequencies. Plot symbols are the same as those in Fig. 5.6. The model PGS has the largest probability ($\ln P$ = -14.02) of the models matched to the frequencies listed in Tab. 5.8. The mean deviation between the model frequencies and the *MOST* observations (as listed in Tab. 5.8) is 1.40 μHz. The model diverges from the observations by 3.89 μHz in the worst case.

Two of the best matched model spectra to the frequencies of Tab. 5.7 have already been identified in the multiple-matching section 5.1.2. Model M3 (see Tab. 5.1 for the physical parameters of this model) has the smallest mean deviation between the calculated and observed frequencies. Its mean frequency deviation is 0.640 μHz and the deviations of all modes from the observations are shown in Fig. 5.19. This model matches the anomalously spaced modes at $\sim$ 2600 and 2800 μHz as $\ell = 4$ modes and associates the other most closely matched modes with an alternating $\ell = 2$ and $\ell = 1$ pattern. Model M3 has the lowest mass (1.3 $M_\odot$) and metallicity (Z = 0.008, Z/X = 0.0114) of all models in our grid. The model has evolved to near the end of its main sequence life and has burned 99.93% of the Hydrogen in its core. The magnetic field matched from this model (= 4.8 kG) is in reasonable agreement with the measured values of $\sim$ 2–4.5 kG. For comparison we also show the deviations for the second most probable model match to the observed pulsation frequencies listed in Tab. 5.7 in Fig. 5.19. That model, (M6 of Tab. 5.1) matches all of the observed modes to less than 4 μHz and has a mean deviation of 1.29 μHz. M6 has a mass and metallicity that are higher (1.45 $M_\odot$, Z = 0.010, Z/X = 0.0139) than those of model M3 and has a magnetic field strength (B = 1.2 kG) that is smaller than that identified in model M3. As in model M3, the anomalous, non-asymptotically spaced modes are identified as $\ell = 4$ modes. The other most closely matched modes of model M6 alternate with angular degree values of $\ell = 0$ and 1.

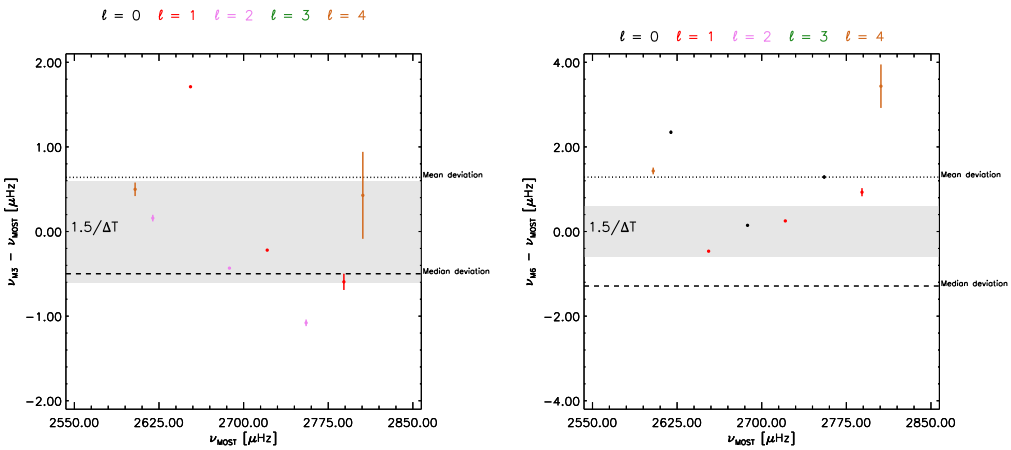

Figure 5.19: The frequency deviations for models M3 and M6 of Tab. 5.1. Plot symbols are the same as those in Fig. 5.6. Model M3 is the model with the smallest mean deviation (= 0.640 μHz) between the theoretical eigenfrequencies and the frequencies listed in Tab. 5.8. Model M6 is the second most probable model ($\ln P$ = -14.05) when matched to the frequencies in Tab. 5.8. Note that both models were already identified in § 5.1.2. In that section, we allowed a single model frequency to match multiple observations. The exclusion of the potential small spacings (frequencies spaced by $\sim$ 3 μHz) results in a better (smaller) mean deviation than those obtained earlier this chapter.

5.3 On discriminating between models

In chapter 4 we calculated a large grid of pulsation models that included magnetic perturbations. We adopted a large range in metallicity (Z = 0.008–

0.022) because the peculiar abundance patterns on the surface of the Ap stars limits a direct inference of their global metallicity. The allowed mass range ($M \sim 1.3$–$1.8\ M_\odot$) was limited by the external constraints on the luminosity and effective temperature of HR 1217 (see § 4.1.1). A thorough exploration of the range of magnetic field strengths that provided asteroseismically relevant results for HR 1217 had never been performed, so we adopted a wide range in B for our model calculations. We calculated 51,795 models that, as a whole, contain millions of modes to be matched to the frequencies determined from the time-series of *MOST* photometry. In the preceding sections of this chapter we showed that we were able to match models that have a mean deviation between the theoretically calculated modes and observations of less than a few μHz. Matching models to a fractional accuracy of about 0.05% is an amazing accomplishment considering the complexity of the models and the sensitivity of the pulsation modes to the magnetic perturbations. (The high frequency oscillations in the Sun are matched to a fractional accuracy of about 0.3%). Those models are; however, a poor statistical match because the *MOST* frequencies are determined to such a high precision. The current state of the observations of roAp star oscillations is so highly precise that the model calculations are being stretched to the limits of their applicability. How well can we distinguish between reasonable models of HR 1217 given the small match probabilities with our current grid?

The short answer is that matching modelled frequencies to (ultra-)precise observations (like those from *MOST*) is an extremely sensitive tool to discriminate between models. In Fig. 5.20 we plot the minimum frequency deviation required to match 50 and 75% (left and right panels of that figure,

respectively) of the observed frequencies of Tab. 5.3 as a function of magnetic field strength. (The model mass and composition Z/X are also identified in that figure.) Immediately we can see that there are only 142 of 51,795 models that match 50% of the observed frequencies below a 1 μHz threshold. We can rule out 99.7% of the models in our grid by adopting that match criteria. In order to match 75% of observations we have to raise our matching threshold to between $\sim$ 2–3 μHz. In that frequency range, 75% of the most observations are matched by 69 of the 51,795 models. Put another way, 136 models within our grid match between 6 and 8 of the *MOST* observations ($\sim$ 50–66%) to an accuracy that is less than 1 μHz. Figure 5.21 shows the same type of plot but we require matching 100% of the *MOST* observations listed in Tab. 5.3. There are 58 models that can match 100% of the observed periodicities with frequency deviations that are not greater than 6 μHz.

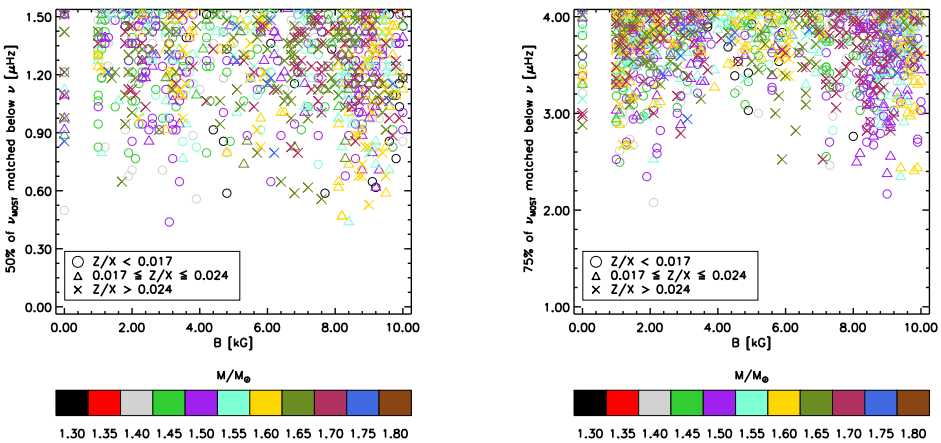

Figure 5.20: Minimum frequency deviations required to match 50 and 75% of the *MOST* observations as a function of magnetic field strength. The left panel plots the minimum frequency deviation required to match 50% of the *MOST* observations. The colour bar on the bottom identifies the mass of the model. Symbols shown in the legend identify the composition (Z/X) ranges ($\sim$ sub-solar Z/X, $\sim$ solar Z/X, $\sim$ super-solar Z/X) of the models. The right panel shows the minimum frequency deviation required to match 75% of the most frequencies. A total of 142 models (= 0.3% of the 51,795 models) match 50% of the *MOST* frequencies below 1 μHz and 69 models (= 0.1% of the models in the grid) match 75% of the *MOST* periodicities with deviations between 2–3 μHz.

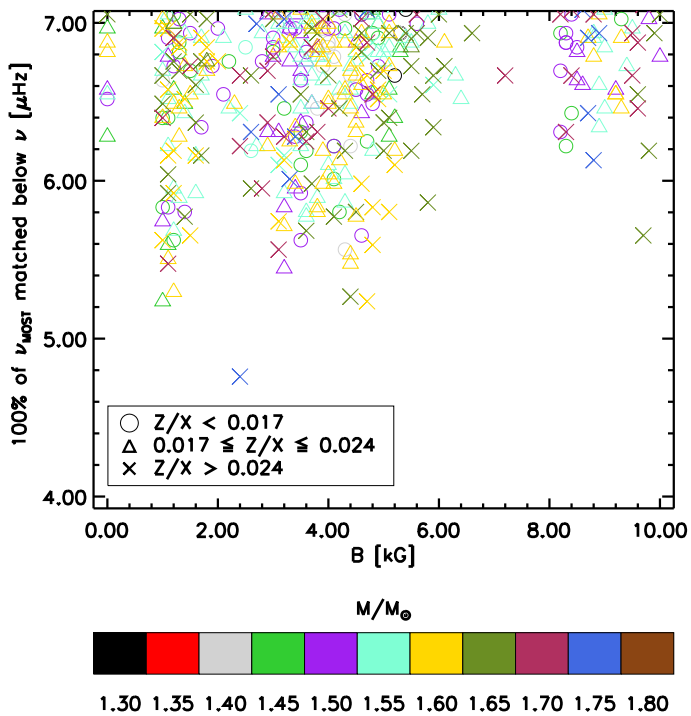

Figure 5.21: Minimum frequency deviations required to match 100% of the *MOST* observations. The labels are the same as those of Fig. 5.20. There are a total of 58 models (= 0.1% of the 51,795 models) that match all of the *MOST* observations with frequency deviations between 4.7–6 μHz.

The model (labelled LPC) with the smallest frequency deviation required

to match 100% of the *MOST* observations (Tab. 5.3) has properties that are listed in Tab. 5.9. The frequency deviations for model LPC are shown in Fig. 5.22 and a Saio plot for that same model is given in appendix D (Fig. D.14). In this model, the closest matches to the anomalous frequencies at about 2600 and 2800 μHz are $\ell = 0$ and 2 modes, respectively. The modes alternate in a pattern that would suggest that the closely (small or second order) spaced modes are in $\ell = 1$, 3 and $\ell = 0$, 4 pairs. Of course, the match in model LPC gives a small spacing that is between 2–3 times what is observed ($\lesssim 3$ μHz). The magnetic field of model LPC is 2.4 kG and is consistent with the lower end of the Lüftinger et al. (2008) measurement (B between 2–4.4 kG).

Table 5.9: Some properties of a selected model of HR 1217. This model has the smallest frequency deviation (= 4.759 μHz) required to match all of the *MOST* frequencies. The column labelled as probability label refers to the order of the probability from each of the Gaussian or Laplace probabilities. For example, 1 G is the most probable Gaussian probability and 10 L would be the 10th most probable Laplace probability. The probability ratio is defined as the Gaussian probability of the model divided by the Gaussian probability of the most probable model (see Tab. 5.4). The models in this table were matched to all frequencies listed in Tab. 5.3 using $50 \times 3\sigma$ errors.

Model ID	$M/M_\odot$	X	Z	Age (Gyr)	α	$M_{conv.core}/M_\star$
	B (kG)	$M_{conv.env.}/M_\star$	Log_{10} (T_{eff})	Log_{10} ($L/L_\odot$)	Log_{10} ($R/R_\odot$)	$\Delta\nu$ (μHz)
	cut-off (μHz)	median deviation (μHz)	mean deviation (μHz)	σ deviation (μHz)	probability label	probability ratio
LPC	1.75	0.740	0.022	0.65	1.8	0.1746
	2.4	0.00	3.866	0.9222	0.2535	70.50
	1966.12	2.55	2.43	1.60	3460 G, 1740 L	7.476×10^{-35}

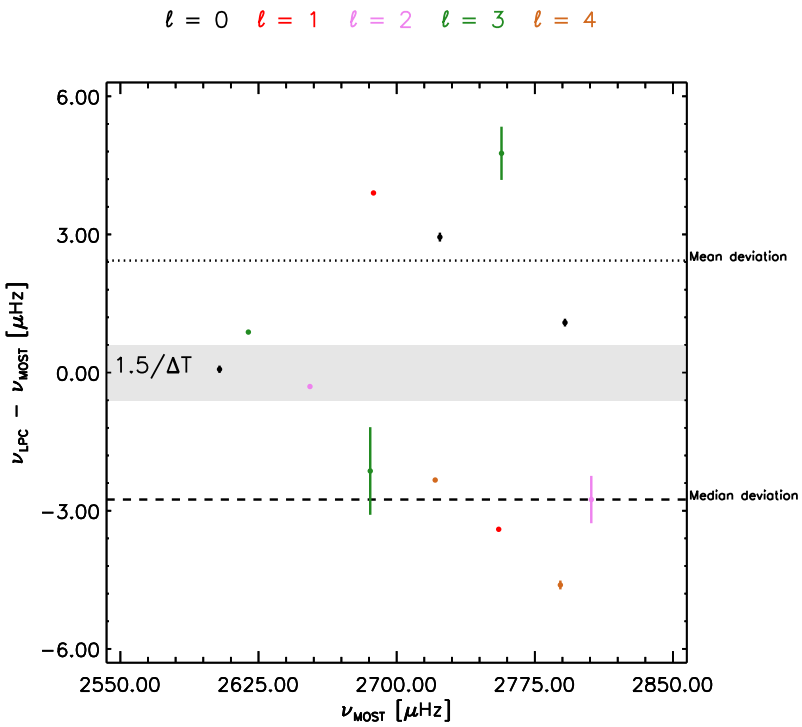

Figure 5.22: Deviations between the frequencies of model LPC (Tab. 5.9) and the *MOST* frequencies. The model LPC has the smallest frequency deviation (~ 4.7 μHz) of all the models that is needed to match 100% of the *MOST* observations. This model is still highly improbable and is 10^{-35} times less likely than model U1 (Tab. 5.4).

Given the range in frequency that is required to match all of the *MOST*

observations, we next see if our observed variations are matched more often to a mode with one particular angular degree over another. Figures 5.23, 5.24, and 5.25 show histograms of the number of matched modes for each of the angular degrees ($\ell = 0$–4). A match occurs if the best fit model frequencies fall within the 3σ uncertainties for the periodicities listed in Tab. 5.3. The histograms showing the matched ℓ values for each of the observed frequencies are presented in the left panels of Fig. 5.23 for all of the magnetic models. The right panels show only $B = 0$ kG models. There appears to be no statistically preferred ℓ value for any of the observed frequencies. This is also true for magnetic models with $B = 2$ and 4 kG (Fig. 5.24) and $B = 6$ and 8 kG (Fig. 5.25). The modelled frequency matches tend to alternate between even and odd modes. If we assume that for a particular frequency an odd or even mode match is equally likely, we could immediately eliminate half of the models in our grid by applying an external constraint on the mode parity for that match.

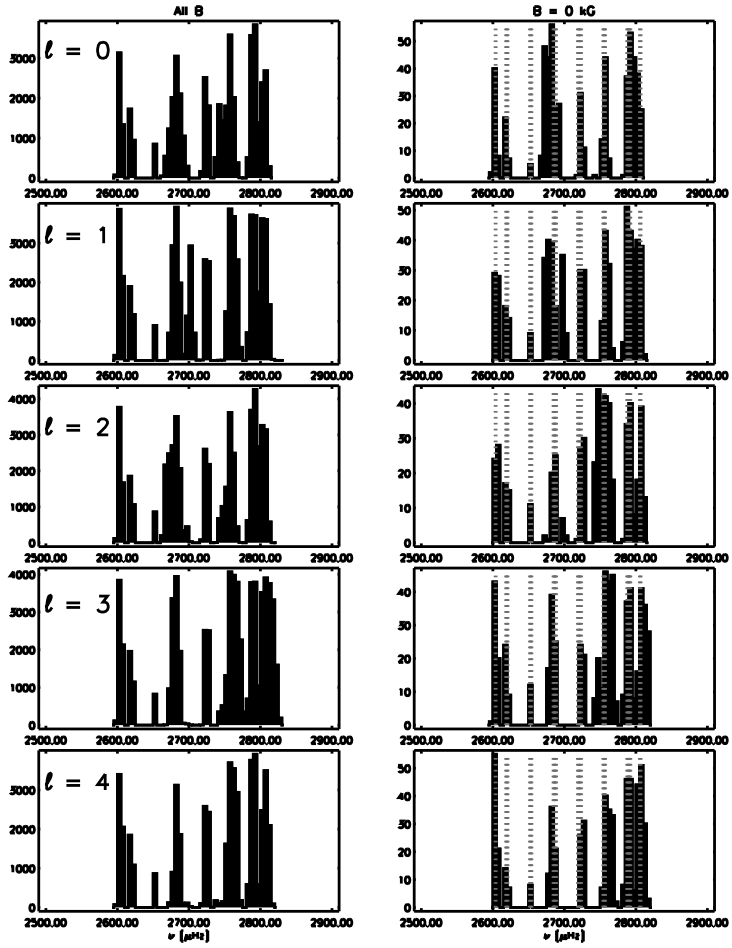

Figure 5.23: Histograms of matched model frequencies. A match occurs if the best fit model frequencies fall within the 3σ uncertainties for the periodicities listed in Tab. 5.3. The left panels present histograms of the matched frequencies in all of the magnetic and non-magnetic models. The right panels show matches in cases where $B = 0$ kG. Each column shows modes with different angular degrees, increasing from $\ell = 0$ at the top to $\ell = 4$ at the bottom. There are no preferred matches for ℓ values. Matches near 2650 μHz seem to be matched less often for all ℓ values when compared to the other frequencies.

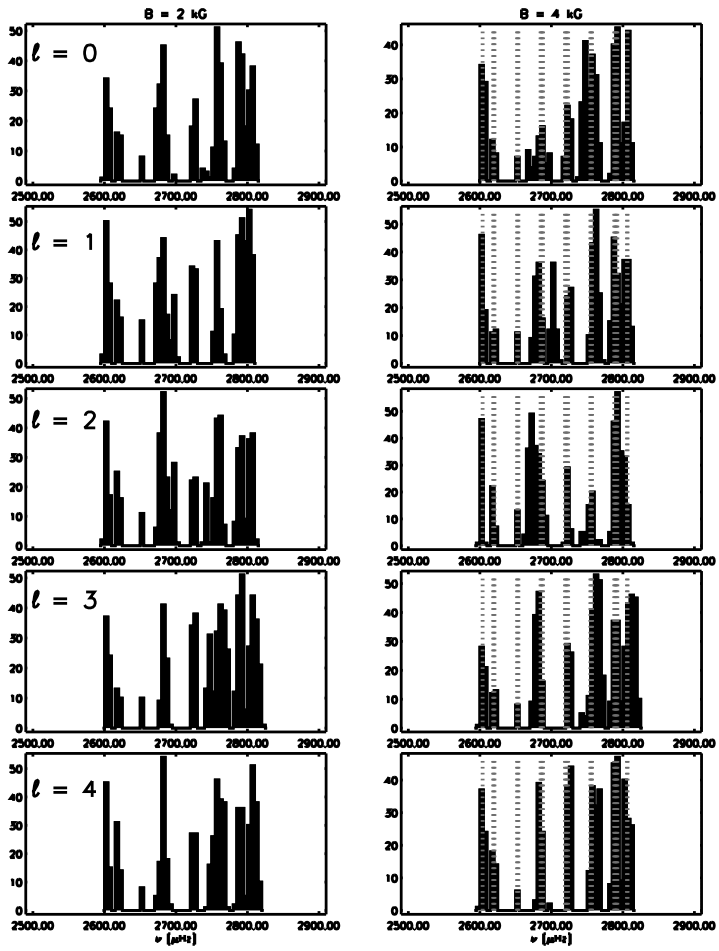

Figure 5.24: Histograms of matched model frequencies. The format is the same as that in Fig. 5.23. The left panels now show only models with $B = 2$ kG, and the right panels only those models with $B = 4$ kG. Model frequencies near 2650 μHz are again under-matched, especially for the $\ell = 0$, $B = 4$ kG case.

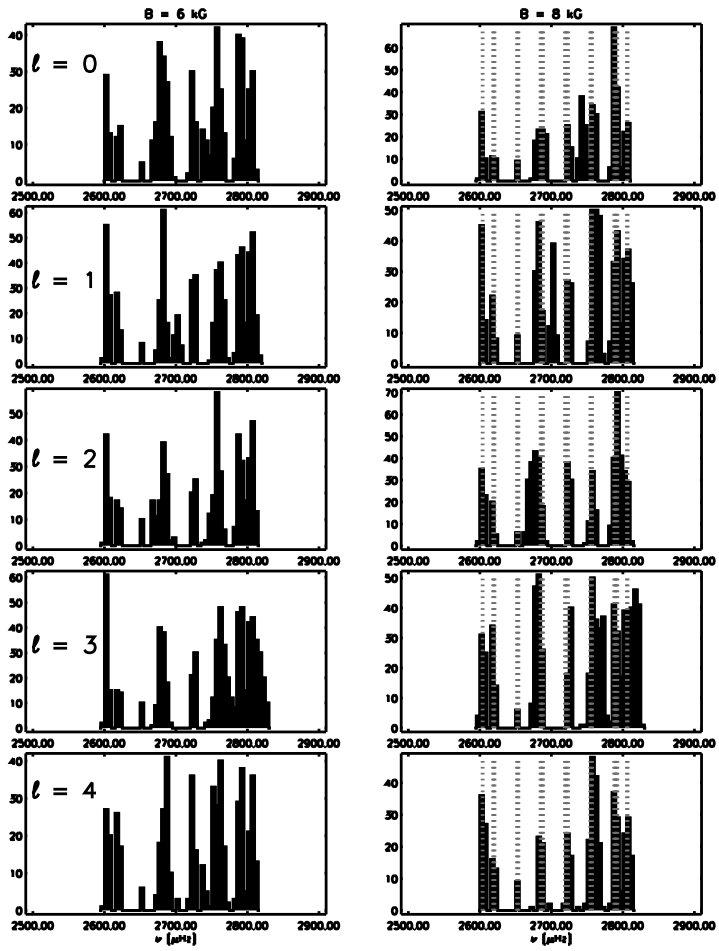

Figure 5.25: Histograms of matched model frequencies. The format is the same as that in Fig. 5.23. The left panels now show only models with $B = 6$ kG, and the right panels only those models with $B = 8$ kG. The $\ell = 0$ and 2 modes tend to be matched more often near 2800 μHz in the 8 kG models. As in the cases with different magnetic fields, models matched to the observed frequencies near 2650 μHz are less common.

We have used the largest grid of magneto-acoustic modes to date to search for a match to the most precise photometric data ever measured on the roAp star HR 1217. We are able to match models to within (on average) a few μHz. This represents an impressive accomplishment and gives hope that future advancements in theoretical modelling of roAp stars will yield accurate and meaningful constraint on the physics of these unique stellar structures. The matches explored are not perfect and local variations in the probability space of our modelled parameters occur for each of the matching scenarios discussed in this chapter. The magnetic field perturbations are cyclic in nature, and as such, leads to parameter degeneracies when matching models to observations. It is important to note that by using a small grid of models, one could, conceivably, find a reasonable match (with say a mean deviation of 1–2 μHz) to the observations. Such a match may not be (and is most likely not) the best global match to the data. Likewise, the large span of Z used in our model grid introduces degeneracies that allow a large range in model mass and evolutionary state to enter the luminosity-effective temperature error box into which HR 1217 falls (§ 4.1.1). In terms of probabilities, Figs. 5.3, 5.4, 5.10, and 5.17 show probabilities for the magnetic field strengths that are broadly distributed in groups ranging from 1–5 kG and 8–10 kG. There are no preferred models in our grid that have a magnetic field strength of B = 0 kG. The probability space around the mass parameter favours models with masses less than about 1.5 $M_\odot$ and the composition (Z/X) seems to loosely favour values less than 0.02. If the mean is used as a discriminant between models, there are no preferred parameter combinations. The mean or median frequency deviation; when used as the only matching statistic,

does not provide enough of a constraint on the models to draw even broad conclusions. The ranges in parameters we give based on our probability distributions should be used as guidelines for future modelling efforts and should not be taken as strict statistical limits on the physical parameters of HR 1217. We do not place confidence limits on any of the physical parameters of HR 1217 from our modelling efforts. The lack of a statistically meaningful match, and complications arising from the degeneracies in some of the model parameters, makes claims of precise parameter limits dubious at best. A model independent measure of the parity of the observed oscillations would greatly constrain the matched model properties. We will discuss the quality of the matches and suggest alternate modelling avenues that should be explored in the (following) concluding chapter.

Chapter 6

Summary, conclusions, & future work

The roAp star HR 1217 exhibits a rich eigenspectrum that obeys the regular asymptotic (§ 1.1.1) spacing between its oscillation modes. The observed frequencies are spaced by an alternating pattern of $\sim$ 33.5 and 34.5 μHz — values that are interpreted as half of the large spacing $\Delta\nu$ — with an important deviation. A global, multisite, photometric campaign (Kurtz et al., 1989) revealed an anomalous frequency spacing of $\sim$ 50 μHz that could not be explained by asymptotic theory. Much later, Cunha (2001) theorized that the strong magnetic field ($\sim$ 2–5 kG) of HR 1217 could significantly perturb its normal oscillation modes. She predicted the existence of a "missing mode" that would explain the anomalous increase in the regular spacings. At nearly the same time as Cunha's prediction there was another (global) photometric campaign organized by the Whole Earth Telescope (WET). Those new data (having a duty cycle of 36%, see Kurtz et al. 2002 and 2005) found a number of new periodicities that agreed well with the predictions of Cunha. A non-asymptotic, potentially magnetically perturbed, frequency spacing of $\sim$ 15 μHz was found at about 2785 μHz along with a frequency group that showed a spacing of 2.5 μHz. This was cautiously interpreted as a potential second

order separation, or small spacing (§ 1.1.1), that could possibly constrain the age of HR 1217. It was shown for the first time that the magnetic field plays a direct role in the pulsation spacings of a roAp star. The photometric variations identified in these earlier ground-based campaigns are shown schematically in Fig. 1.7.

Motivated by these earlier results, *MOST* observed HR 1217 near continuously as a Fabry target (§ 2.1) for about 30 days in late 2004. The satellite collected more than 68,000 photometric data points with a duty cycle of 95%. These data represent the ultimate photometric measurements on HR 1217. We used CAPER (Cameron et al., 2006, 2008); a tool developed specifically for time-series analysis of *MOST* data (§ 2.2), to determine the oscillation frequencies of HR 1217. The Fourier parameters extracted from the *MOST* light curve are summarized in Tab. 3.1. The uncertainties in our fitted parameters were determined using 100,000 bootstrap samples. In total there were 29 frequencies identified, each having a S/N ≥ 3.5 ($\gtrsim 2.5\sigma$ detection) to within uncertainties. (The reduction is described in full detail in chapter 3.) The most precise amplitude determined from the *MOST* data is 6 μmag, making this the most precise data set ever collected on HR 1217. We now address each of the observational objectives put forth in chapter 1 (§ 1.4) below:

1. It has been known since the early 1980s that HR 1217 is a multiperiodic variable star with near equally spaced modes, alternately spaced by ~ 33.5 and 34.5 μHz. The most recent confirmation of this was the analysis of the Whole Earth Telescope data by Kurtz et al. (2005), that achieved a duty cycle of 36% and reached an unprecedented precision

of 14 μmag for a ground-based photometric study. We will be able to unambiguously identify the spacings in the *MOST* data because of its near continuous coverage and ultra-high precision. Are the already identified periodicities constant over time for all observations on HR 1217, or do they vary over time, pointing to a selective mode damping mechanism or some nonlinear interaction?

2. The strange, apparently non-asymptotic, spacing that was observed between the highest two frequencies in HR 1217 remained a mystery until the recent results of Kurtz et al. (2005, 2002). Those authors identified a previously unidentified frequency near 2790 μHz that could only be explained as a magnetic perturbation Cunha (2001). Explaining that frequency (or lack of that frequency) has driven the theory of roAp star oscillations for more than two decades. Is this frequency identified in the *MOST* data on HR 1217 and is it stable since the last observations of Kurtz et al. (2005)?

The average difference between the frequencies extracted from the data of Kurtz et al. (2005) and those from the *MOST* data (§ 3.3) is 0.08 ± 0.09 μHz (3σ uncertainty), indicating that all frequencies identified by both the ground-based and space-based campaigns are consistent with each other. Those periods common to each of the data sets are stable since the initial ground-based collaboration of Kurtz et al. (1989), even though there are some differences in the amplitudes of the dominant peaks (e.g., § 3.3). Frequencies near the "missing mode" at $\sim$ 2790 μHz (present in the WET data of Kurtz et al. 2005, but were not found in the Kurtz et al. 1989 data) are identified in the *MOST* photometry. This suggests that those frequencies are stable over a

baseline of at least 4 years. It should be noted that these frequencies show the largest deviations ($\sim$ 0.2 μHz) from those determined by Kurtz et al. (2005) because they are located near a harmonic of the orbital period of the *MOST* satellite (16 $\times$ 165 μHz = 2640 μHz and 17 $\times$165 μHz = 2805 μHz) and are potentially influenced by the stray light (§ 2.1). That being said, the deviations between the *MOST* frequencies near 2790 μHz and the corresponding Kurtz et al. (2005) frequencies are near their 3σ uncertainties. Any deviations between the *MOST* and Kurtz et al. (2005) frequencies are well below the resolution of $1/T = 0.4$ μHz. Because the *MOST* and WET data show common frequencies, the alternating values of $\sim$ 33.5 and $\sim$ 34.5 μHz remain the same. Those values are consistent with acoustic modes that are alternating between even and odd angular degree ℓ and provide an asteroseismic parallax that is consistent with the Hipparcos parallax for HR 1217 (Matthews et al. 1999, see also § 1.3).

3. We expect to observe a number of new periodicities in the data because of the high level of photometric precision and the near contiguous data sampling of the *MOST* satellite. Can new periodicities be identified and, if so, can they be used to constrain the physics of this magnetic pulsator?

4. A recent spectroscopic study on HR 1217 by Mkrtichian & Hatzes (2005) identified new frequencies at $\sim$ 2553 and 2585 μHz. These frequencies are interesting because they approximately match the alternating $\sim$ 33.5 and 34.5 μHz pattern previously observed in HR 1217, but were not identified in the photometry of Kurtz et al. (2005). Does the *MOST* data uncover those potentially new periodicities?

There were 7 new frequencies identified in the *MOST* data (§ 3.3). Recurring frequency spacings of ~ 1.5 and ~ 2.5 μHz are evident in the *MOST* data. Main sequence models of A-type stars (e.g., § 4.2) have small spacings (§ 1.1.1) that are about 3 μHz and higher. This small spacing can potentially constrain the age of the star because its value is most sensitive to changes in the composition of the stellar core as the star evolves. The magnetic perturbations to the frequencies may be of the same order, or larger than, the small spacing (e.g., Dziembowski & Goode 1996). This was also illustrated in § 4.3. We must be cautious in interpreting these spacings as small separations. Some frequencies in the *MOST* data are spaced in such a way that it is not immediately obvious whether or not the frequencies are rotational splittings or "small spacings". A repeating pattern of ~ 1.5 and ~ 2.5 μHz is evident if ν_9 is chosen as the main (not a rotational splitting) frequency in the grouping. However, the uncertainties suggest that the difference between ν_{10} and ν_{11} is not a rotational splitting. One would expect the frequency set ν_{10}, ν_{11}, and ν_{12} to be a rotational triplet based on the alternating $\sim \Delta\nu/2$. It is possible that magnetic effects are causing a non-repeating pattern of ~ 1.5 and ~ 2.5 μHz, or that the closely spaced modes are convolved in such a way that a stable least squares frequency solution exists where ν_{10} and ν_{11} are spaced close to, but not at (within the 3σ errors) the rotation frequency of the star. Because a spacing of ~ 2.5 μHz had been observed by Kurtz et al. (2005), and there is more than one example of this spacing in the *MOST* data, we believe that these spacings are not related to unresolved rotational splittings. It should be noted here that the rotation frequency observed in the *MOST* data (0.924 ± 0.047 μHz, see § 3.2 and 3.3) is de-

termined to a level of precision that allows us to compare it to the observed "small separations", but it is not determined to a high enough level of precision to allow us to favour one of the previously measured rotation frequency measurements (§ 3.2).

A new *MOST* frequency at $\nu_1 = 2603.832$ μHz is inconsistent with the new frequencies at ~ 2553 and 2585 μHz found in radial velocity measurements of Mkrtichian & Hatzes (2005). Recent results by Kurtz et al. (2006) suggest that there can be pulsations detected in radial velocity data that are not present in photometric data. This was illustrated for the case of the roAp star HD 134214 (Cameron et al. 2006, § 2.3.1) where *MOST* photometry identified a single periodicity during a short observing run while Kurtz et al. (2006) identified up to 6 periodicities in their radial velocity data (not observed synchronously with *MOST*). It is possible that there is some unknown selection effect in the atmospheres of roAp stars that reflects certain modes at different depths, causing results from spectroscopy to sometimes be discrepant with photometric measurements.

5. In order to determine the reliability and uniqueness of the periodicities in a multiperiodic variable, we need to develop tools that can test the precision and resolution of our data set. Techniques we have developed for other *MOST* targets will be applied to the HR 1217 data. The resolution of our data set and the assertion that closely spaced frequencies are spaced by the rotation rate of the star will be tested.

The bootstrap technique described in § 2.2 provides a means to test if we are extracting resolved (or unresolved) frequencies in the data. In § 3.3

we were able to show that the addition of a number of closely space frequencies (spaced by approximately half of the rotation frequency of HR 1217) causes the fit to become unstable and the new frequencies (Tab. 3.3) clearly interact with the previously identified, resolved, parameters of Tab. 3.1 (see Fig. 3.8). Because of this, we are confident that we have extracted only resolved frequencies.

The ultra-precise photometric measurements of the *MOST* satellite reveal a number of new periodicities that are spaced close to what is expected for an asymptotic small spacing ($\lesssim 3$ μHz) and one new frequency that is spaced by an amount (~ 15 μHz) that is reminiscent of the magnetically perturbed modes identified by Kurtz et al. (2005). We next summarize the modelling efforts we used to describe the observed oscillations in HR 1217.

In recent years there have been a number of studies that have attempted to model specific roAp stars. Cunha et al. (2003) examined a small number of stellar models for HR 1217 in hopes of determining its evolutionary status. They did not include the effects of a magnetic field and were not able to reproduce the anomalous spacings. Gruberbauer et al. (2008) and Huber et al. (2008) attempted to constrain the properties of the roAp stars γ Equ and 10 Aql using ~ 10 A-star models (including magnetic perturbations using the method of Saio & Gautschy 2004) and data collected by *MOST*. HD101065; a.k.a. Przybylski's star, was studied by Mkrtichian et al. (2008), who also use only a few stellar models (again using the method of Saio & Gautschy 2004) to explore the physics of that star. Their results were discussed in more detail in chapter 5. Brandao et al. (2008) also use only a few (non-magnetic) models to study the spectrum of α Cir that was obtained from photometry

collected with the *WIRE* (NASA's Wide Field Infrared Explorer) satellite (Bruntt et al., 2009; Buzasi, 2002). Each of the above studies places some limits on the properties of the star they were studying, even without a thorough parameter space search. Interestingly, the modelling efforts referenced above that included magnetic effects arrived at "best matched" magnetic field strengths that were about a factor of 2 larger than what was measured from spectropolarimetric observations.

Our study explores the magnetic effects on the pulsation frequencies for models of HR 1217 for the first time and significantly extends the number of models and the breadth of the parameter space explored when compared to earlier asteroseismic studies on HR 1217, or any other roAp star. The high quality *MOST* data and this extensive grid of state-of-the-art models of magneto-acoustic modes for HR 1217 is a first, and is unlikely to be surpassed in the near future. Our grid covers the observable characteristics of HR 1217 ($T_{\rm eff} = 7400^{+100}_{-200}$ K, $L = 7.8 \pm 0.7$ L$_\odot$, $B \sim 2$–5 kG), and includes magnetic perturbations to the calculated normal modes of the models. These models are outlined in detail in chapter 4. This grid extensively covered the parameter space (§ 4.1.1) in stellar mass (1.3 to 1.8 M$_\odot$ in 0.05 M$_\odot$ steps), composition (Z = 0.008 to 0.022 in steps of 0.002 and X = 0.700 to 0.740 in steps of 0.020) and frequency range (ℓ = 0–4 over the range 1900–3100 μHz.) appropriate for HR 1217. Mixing length parameters of $\alpha = 1.4,\ 1.6$, and 1.8 are adopted and the models in the grid have a large spacing ($\Delta\nu \sim (\mathrm{M/R^3})^{1/2}$) that ranges from $\sim$ 57–81 μHz. The pulsation mode calculation was tested using a new method developed by Kobayashi (2007, § 4.2.1) for terrestrial seismology. The modes calculated using the JIG

code were confirmed by comparison to modes calculated using Kobayashi's method. (Showing the consistency between the modes calculated using the two different pulsation codes was the last of the modelling goals outlined in § 1.3) Our model grid, composed of 569 A-star models that fall in the HR 1217 luminosity–effective temperature error bounds, is the most extensive grid of models used to study the magnetic effects on the pulsation modes of roAp star to date. The magnetic perturbations to the eigenfrequencies of the models were estimated using the variational method of Cunha & Gough (2000); see § 4.3, assuming a dipolar magnetic field, with polar strengths ranging from 1 to 10 kG in steps of 0.1 kG. This brings the total number of magneto-acoutic pulsation models to 51,795.

The modelling goals outlined in § 1.3 have a common thread: Namely, how closely can we match the frequencies (and or spacings) observed by *MOST*, and what constraints can we place on the physical parameters of the star?

In chapter 5 we showed that we are able to match models to within (on average) a few μHz. A mean match of a few μHz represents a fractional accuracy of about ($\sim$ 1.5 μHz / 2700 μHz =) 0.05%. For comparison, the high frequency oscillations in the Sun are matched to a fractional accuracy of about 0.3%. This is an extraordinary accomplishment considering the complexity of our models and the large perturbations introduced by the inclusion of a magnetic field. The matches obtained are not perfect; but, matching modelled frequencies to the *MOST* frequencies has proven to be an extremely sensitive tool to discriminate between models. For example, 136 models within our grid match between 6 and 8 ($\sim$ 50–66%) of the *MOST* observations to an

accuracy that is less than 1 μHz. That represents only (100 $\times$ 136/51,795 =) 0.3% of the models in our grid. We were able to show that there are 58 models that can match 100% of the observed periodicities with frequency deviations that are not greater than 6 μHz (§ 5.3). There are about (100 $\times$ 17579/51796 =) 33% of the models in our grid that match the observed large spacing of HR 1217 ($\sim$ 68 μHz) to within about 1.25 μHz. (To arrive at a value for the large spacing we calculated an average over all n and ℓ for frequencies in the range of 2618.600 to 2792.249 μHz.) Using the large spacing as a discriminant between models is less effective than matching individual frequencies. The matching of the observed frequencies to our modelled modes eliminates a large percentage of parameter space that is allowed within the luminosity-effective temperature error bounds for HR 1217. We cannot find a model that matches both the magnetically perturbed modes (spaced by $\sim$ 15 μHz) and the oscillations spaced by the small spacing ($\lesssim$ 3 μHz) simultaneously. This presents a significant challenge to the modelling of roAp stars and remains an outstanding problem.

The probability of our models matching the *MOST* frequencies was thoroughly explored in chapter 5. In general, the probability of a match is very low. While we achieve average deviations of a few μHz between our measured periodicities and the modelled eigenmodes, the measured precision on the *MOST* frequencies is on the order of 0.01 μHz. The magnetic field perturbations are cyclic in nature, and as such, there are parameter degeneracies when matching models to observations. The large span of Z used in our model grid introduces an indeterminacy that allow a large range in model mass and evolutionary state to enter the luminosity-effective temperature error box into

which HR 1217 falls (§ 4.1.1). The magnetic field of HR 1217 was estimated by Bagnulo et al. (1995) to be 3.9 kG. More recently, Lüftinger et al. (2008) measured a field variation over the rotation period of HR 1217 of 2.2 to 4.4 kG. We have illustrated in chapter 5 that probabilities of a model match for the magnetic field strengths broadly distributed in groups ranging from 1–5 kG and 8–10 kG. In previous studies on roAp stars (e.g., Gruberbauer et al. 2008, and the others mentioned above), the modelled magnetic field strengths were about a factor of 2 larger than the spectroscopically measured values. The range in probability for a match to the magnetic field strength of HR 1217 in our models are consistent with both the spectroscopically determined values and twice those values. We conclude that there are probably magnetic field matches for those other roAp stars that are consistent with external measures, provided the model parameter space is explored in more detail. There are no preferred models in our grid that have a magnetic field strength of $B =$ 0 kG. The probability space around the mass parameter favours models with masses less than about 1.5 $M_\odot$ and the composition (Z/X) seems to loosely favour values less than 0.02. There is no meaningful constraint on the mixing length parameter α. If the mean is used as a discriminant between models, there are no preferred parameter combinations because there is a wide range of models that have low mean deviation matches. The ranges in parameters we give based on our probability distributions should be used as guidelines for future modelling efforts and should not be taken a strict statistical limits on the physical parameters of HR 1217. We do not place confidence limits on any of the physical parameters of HR 1217 from our models. The lack of a statistically meaningful match, and complications arising from the degenera-

cies in some of the model parameters, makes claims of precise limits dubious at best. The current state of the observations of roAp star oscillations is so highly precise that the model calculations are being stretched to the limits of their applicability.

In stellar seismology we usually look for the closest matched model and then explore different physics to see how the models can be improved. Stellar models do not generally correspond to simple analytical models where one parameter can be tweaked to match an observation without having to change other parameters as well. That is simply why we have explored a large coverage in the parameter space relevant for models of HR 1217. As an aside, most of the modes observed in the Sun could not be matched in the 80s and early 90s. The best helioseismic agreement at high frequencies still show a discrepancy that is many standard deviations from the observations. Our grid of magnetically perturbed oscillation models represents a unique first step to try to constrain the properties of a roAp star. The models we calculate use standard physics and focus on the addition of a magnetic perturbation to the oscillation modes as an important (first) non-standard addition. Calculating our models came at a significant computational cost so we focused on as wide of a parameter space as we possibly could. This comes at the expense of fine grid resolution. We found that our current grid resolution in age and mass is not sufficient to be able to properly constrain the properties of HR 1217. Take, for example, model E of Tab. 4.1. Over its corresponding evolutionary sequence the large spacing changes from 80 to 68 μHz. There were 11 models with detailed seismic information output. The change in $\Delta\nu$ is not equally spaced along an evolutionary track and ranges

by about 0.2 μHz near 68 μHz to about 1 μHz near 80 μHz. We expect a percentage change in $\Delta\nu$ to roughly correspond to the same percentage change for a given mode along an evolving set of models. That means the frequencies between the models in our grid (that are adjacent in age) change from about 5 to 40 μHz near 2700 μHz. A model that matches frequencies to within about 5 μHz can potentially be changed in age slightly to get a better match — at least in the non-magnetic case. The behaviour of the modes in the magnetic models is more difficult to predict because of the non-linear coupling between frequencies, magnetic field strength and the structure of the outer layers of the model.

So where should future modelling efforts be focused? Recent, non-standard, models were used to explore the excitation physics of the roAp stars (Gautschy et al. 1998,Balmforth et al. 2001,Saio 2005, and Théado et al. 2005,2009). Although some of those models excited oscillations in a very specific frequency range, or over specific temperature and luminosity ranges, none were successful in calculating a globally applicable excitation model. This leaves us with a number of unsolved problems in our understanding of the roAp star pulsations that should also be addressed. These include: 1) the understanding of what excites the observed periodicities in these stars, 2) how the pulsation modes interact with the chemical gradients in the upper stellar atmosphere, 3) why some roAp stars show frequencies above the theoretical acoustic cut-off frequency, and 4) what the effects of alternate magnetic geometries are on the pulsation modes. We point to recent reviews by Kurtz & Martinez (2000), Cunha (2007), Saio (2008) and Shibahashi (2008) to highlight the current efforts within the asteroseismic community to address these issues.

Because previous studies using non-standard model physics focused on the excitation of the calculated modes, they did not highlight what affect their model alterations had on the individually calculated model frequencies and spacings. This is necessary to define which non-standard additions should be added to future model grids to improve the matches to observations. A fiducial model sequence should be defined so that modellers within the roAp community can easily compare and contrast the addition of new physics to a standard set of models. To increase the efficiency of grid calculations, we suggest that a study be undertaken that defines the minimum spacing in the basic stellar parameters (M, Z/X, $\Delta\nu$, B) that is needed to interpolate modelled frequencies to within a sub-μHz accuracy. Interpolation within a small grid of models having a relatively large spread in parameters is generally untrustworthy. We suspect that the sharp jumps in frequency caused by the introduction of a magnetic field could significantly complicate the interpolation of modelled frequencies. Finally, we found that there is no apparent constraint on ℓ from our model grid. We need a model independent constraint on ℓ (or at least the parity of ℓ) to get firm asterosesimic constraints.

The relatively small deviations between our theoretical models and the *MOST* observations give us hope that future advancements in theoretical modelling of roAp stars will yield accurate and meaningful constraint on the physics of the unique Ap stellar structures. There is the potential to thoroughly test the role a magnetic field plays on the structure of these stars and to infer the properties of that field in the hidden stellar interior. When *MOST* observed HR 1217 in late 2004, it set the standard for photometric

observations of roAp stars. The oscillation spectrum of HR 1217 extracted from the *MOST* data is the most precise and complete spectrum ever observed for this star, and other roAp stars. This data represents the ultimate photometric data set on this magnetic pulsator and has uncovered a number of new frequencies that will be a challenge to model without additional observational constraints. At this time, the quality of the observational data is far superior to our theoretical understanding of roAp star oscillations.

Bibliography

Aerts, C., Christensen-Dalsgaard, J., Cunha, M., & Kurtz, D. W. 2008, Sol. Phys., 251, 3

Alexander, D. R. & Ferguson, J. W. 1994, ApJ, 437, 879

Böhm-Vitense, E. 1958, Zeitschrift fur Astrophysics, 46, 108

Babel, J. & Michaud, G. 1991, A&A, 241, 493

Bagnulo, S., Landi degl'Innocenti, E., Landolfi, M., & Leroy, J. L. 1995, A&A, 295, 459

Bahcall, J. N., Pinsonneault, M. H., & Wasserburg, G. J. 1995, Reviews of Modern Physics, 67, 781

Balmforth, N. J., Cunha, M. S., Dolez, N., Gough, D. O., & Vauclair, S. 2001, MNRAS, 323, 362

Basu, S. & Antia, H. M. 2008, Phys. Rep., 457, 217

Bigot, L. & Dziembowski, W. 2002, A&A, 391, 235

Binney, J. & Merrifield, M. 1998, Galactic Astronomy, Princeton University Press

Brandao, I. M., Bruntt, H., Cunha, M., & Kurtz, W. D. 2008, Communications in Asteroseismology, 157, 234

Breger, M. 2007, Communications in Asteroseismology, 150, 25

Breger, M., Stich, J., Garrido, R., Martin, B., Jiang, S. Y., Li, Z. P., Hube, D. P., Ostermann, W., Paparo, M., & Scheck, M. 1993, A&A, 271, 482

Bruntt, H., Kurtz, D. W., Cunha, M. S., Brandão, I. M., Handler, G., Bedding, T. R., Medupe, T., Buzasi, D. L., Mashigo, D., Zhang, I., & van Wyk, F. 2009, MNRAS, 396, 1189

Buzasi, D. 2002, in Astronomical Society of the Pacific Conference Series, Vol. 259, IAU Colloq. 185: Radial and Nonradial Pulsationsn as Probes of Stellar Physics, ed. C. Aerts, T. R. Bedding, & J. Christensen-Dalsgaard, 616–+

Cameron, C., Matthews, J. M., Rowe, J. F., Kuschnig, R., Guenther, D. B., Moffat, A. F. J., Rucinski, S. M., Sasselov, D., Walker, G. A. H., & Weiss, W. W. 2006, Communications in Asteroseismology, 148, 57

Cameron, C., Saio, H., Kuschnig, R., Walker, G. A. H., Matthews, J. M., Guenther, D. B., Moffat, A. F. J., Rucinski, S. M., Sasselov, D., & Weiss, W. W. 2008, ApJ, 685, 489

Campbell, C. G. & Papaloizou, J. C. B. 1986, MNRAS, 220, 577

Chaplin, W. J., Elsworth, Y., Isaak, G. R., Miller, B. A., & New, R. 1999, MNRAS, 308, 424

Christensen-Dalsgaard, J. 1988, in IAU Symposium, Vol. 123, Advances in Helio- and Asteroseismology, ed. J. Christensen-Dalsgaard & S. Frandsen, 295–+

Christensen-Dalsgaard, J. 2002, Reviews of Modern Physics, 74, 1073

Christensen-Dalsgaard, J. 2003, Lecture Notes on Stellar Oscillations. Fifth Edition (University of Aarhus)

Clement, C. M., Jankulak, M., & Simon, N. R. 1992, ApJ, 395, 192

Cox, J. P. 1980, Theory of stellar pulsation (Research supported by the National Science Foundation Princeton, NJ, Princeton University Press, 1980. 393 p.)

Cunha, M. S. 2001, MNRAS, 325, 373

—. 2005, Journal of Astrophysics and Astronomy, 26, 213

—. 2006, MNRAS, 365, 153

—. 2007, Communications in Asteroseismology, 150, 48

Cunha, M. S., Aerts, C., Christensen-Dalsgaard, J., Baglin, A., Bigot, L., Brown, T. M., Catala, C., Creevey, O. L., Domiciano de Souza, A., Eggenberger, P., Garcia, P. J. V., Grundahl, F., Kervella, P., Kurtz, D. W., Mathias, P., Miglio, A., Monteiro, M. J. P. F. G., Perrin, G., Pijpers, F. P., Pourbaix, D., Quirrenbach, A., Rousselet-Perraut, K., Teixeira, T. C., Thévenin, F., & Thompson, M. J. 2007, A&A Rev., 14, 217

Cunha, M. S., Fernandes, J. M. M. B., & Monteiro, M. J. P. F. G. 2003, MNRAS, 343, 831

Cunha, M. S. & Gough, D. 2000, MNRAS, 319, 1020

Deeming, T. J. 1975, Ap&SS, 36, 137

Demarque, P., Guenther, D. B., Li, L. H., Mazumdar, A., & Straka, C. W. 2008, Ap&SS, 316, 31

Dziembowski, W. A. 1971, Acta Astronomica, 21, 289

Dziembowski, W. A. & Goode, P. R. 1996, ApJ, 458, 338

Everett, M. E. & Howell, S. B. 2001, PASP, 113, 1428

Gabriel, K., Noels, A., Scuflaire, R., & Mathys, G. 1985, A&A, 143, 206

Gautschy, A. & Saio, H. 1995, ARA&A, 33, 75

—. 1996, ARA&A, 34, 551

Gautschy, A., Saio, H., & Harzenmoser, H. 1998, MNRAS, 301, 31

Gough, D. 1987, Nature, 326, 257

Gough, D. O. 2007, Astronomische Nachrichten, 328, 273

Gough, D. O. & Tayler, R. J. 1966, MNRAS, 133, 85

Gregory, P. C. 2005, Bayesian Logical Data Analysis for the Physical Sciences: A Comparative Approach with 'Mathematica' Support, ed. Gregory, P. C. (Cambridge University Press)

Grevesse, N. & Noels, A. 1993, in Origin and Evolution of the Elements, ed. M. Pratzo, E. Vangioni-Flam, & M. Casse, Cambridge Univ. Press

Gruberbauer, M., Kolenberg, K., Rowe, J. F., Huber, D., Matthews, J. M., Reegen, P., Kuschnig, R., Cameron, C., Kallinger, T., Weiss, W. W., Guenther, D. B., Moffat, A. F. J., Rucinski, S., Sasselov, D., & Walker, G. A. H. 2007, MNRAS, 379, 1498

Gruberbauer, M., Saio, H., Huber, D., Kallinger, T., Weiss, W. W., Guenther, D. B., Kuschnig, R., Matthews, J. M., Moffat, A. F. J., Rucinski, S., Sasselov, D., & Walker, G. A. H. 2008, A&A, 480, 223

Guenther, D. B. 1994, ApJ, 422, 400

—. 2002, ApJ, 569, 911

Guenther, D. B. & Brown, K. I. T. 2004, ApJ, 600, 419

Guenther, D. B. & Demarque, P. 1997, ApJ, 484, 937

Guenther, D. B., Demarque, P., Kim, Y.-C., & Pinsonneault, M. H. 1992, ApJ, 387, 372

Guenther, D. B., Pinsonneault, M. H., & Bahcall, J. N. 1993, ApJ, 418, 469

Guzik, J. A. & Swenson, F. J. 1997, ApJ, 491, 967

Hansen, C. J. & Kawaler, S. D. 1994, Stellar Interiors. Physical Principles, Structure, and Evolution, Springer-Verlag Berlin Heidelberg New York. Also Astronomy and Astrophysics Library

Henyey, L. G., Forbes, J. E., & Gould, N. L. 1964, ApJ, 139, 306

Henyey, L. G., Wilets, L., Böhm, K. H., Lelevier, R., & Levee, R. D. 1959, ApJ, 129, 628

Huber, D., Saio, H., Gruberbauer, M., Weiss, W. W., Rowe, J. F., Hareter, M., Kallinger, T., Reegen, P., Matthews, J. M., Kuschnig, R., Guenther, D. B., Moffat, A. F. J., Rucinski, S., Sasselov, D., & Walker, G. A. H. 2008, A&A, 483, 239

Iglesias, C. A. & Rogers, F. J. 1996, ApJ, 464, 943

Johnson, H. L. & Morgan, W. W. 1953, ApJ, 117, 313

Kallinger, T., Gruberbauer, M., Guenther, D. B., Fossati, L., & Weiss, W. W. 2008a, ArXiv e-prints

Kallinger, T., Reegen, P., & Weiss, W. W. 2008b, A&A, 481, 571

King, H., Matthews, J. M., Row, J. F., Cameron, C., Kuschnig, R., Guenther, D. B., Moffat, A. F. J., Rucinski, S. M., Sasselov, D., Walker, G. A. H., & Weiss, W. W. 2006, Communications in Asteroseismology, 148, 28

Kippenhahn, R. & Weigert, A. 1994, Stellar Structure and Evolution (Stellar Structure and Evolution, XVI, 468 pp. 192 figs.. Springer-Verlag Berlin Heidelberg New York. Also Astronomy and Astrophysics Library)

Kleinman, S. J., Nather, R. E., & Phillips, T. 1996, PASP, 108, 356

Kobayashi, N. 2007, Geophysical Journal International, 168, 315

Kochukhov, O. 2008, Communications in Asteroseismology, 157, 228

Kochukhov, O. & Bagnulo, S. 2006, A&A, 450, 763

Kochukhov, O. & Wade, G. A. 2007, A&A, 467, 679

Kreidl, T. J., Kurtz, D. W., Schneider, H., van Wyk, F., Roberts, G., Marang, F., & Birch, P. V. 1994, MNRAS, 270, 115

Krishna Swamy, K. S. 1966, ApJ, 145, 174

Kurtz, D. W. 1978, Informational Bulletin on Variable Stars, 1436, 1

—. 1981, MNRAS, 194, 747

—. 1982, MNRAS, 200, 807

—. 1985, MNRAS, 213, 773

—. 1990, ARA&A, 28, 607

Kurtz, D. W., Cameron, C., Cunha, M. S., Dolez, N., Vauclair, G., Pallier, E., Ulla, A., Kepler, S. O., da Costa, A., Kanaan, A., Fraga, L., Giovannini, O., Wood, M. A., Silvestri, N., Kawaler, S. D., Riddle, R. L., Reed, M. D., Watson, T. K., Metcalfe, T. S., Mukadam, A., Nather, R. E., Winget, D. E., Nitta, A., Kleinman, S. J., Guzik, J. A., Bradley, P. A., Matthews, J. M., Sekiguchi, K., Sullivan, D. J., Sullivan, T., Shobbrook, R., Jiang, X., Birch, P. V., Ashoka, B. N., Seetha, S., Girish, V., Joshi, S., Moskalik, P., Zola, S., O'Donoghue, D., Handler, G., Mueller, M., Perez, J. M. G., Solheim, J.-E., Johannessen, F., & Bigot, L. 2005, MNRAS, 358, 651

Kurtz, D. W., Elkin, V. G., & Mathys, G. 2006, MNRAS, 370, 1274

Kurtz, D. W., Elkin, V. G., Mathys, G., & van Wyk, F. 2007, MNRAS, 381, 1301

Kurtz, D. W., Kawaler, S. D., Riddle, R. L., Reed, M. D., Cunha, M. S., Wood, M., Silvestri, N., Watson, T. K., Dolez, N., Moskalik, P., Zola, S., Pallier, E., Guzik, J. A., Metcalfe, T. S., Mukadam, A. S., Nather, R. E., Winget, D. E., Sullivan, D. J., Sullivan, T., Sekiguchi, K., Jiang, X., Shobbrook, R., Ashoka, B. N., Seetha, S., Joshi, S., O'Donoghue, D., Handler, G., Mueller, M., Gonzalez Perez, J. M., Solheim, J.-E., Johannessen, F., Ulla, A., Kepler, S. O., Kanaan, A., da Costa, A., Fraga, L., Giovannini, O., & Matthews, J. M. 2002, MNRAS, 330, L57

Kurtz, D. W. & Marang, F. 1987, MNRAS, 229, 285

Kurtz, D. W. & Martinez, P. 2000, Baltic Astronomy, 9, 253

Kurtz, D. W., Matthews, J. M., Martinez, P., Seeman, J., Cropper, M., Clemens, J. C., Kreidl, T. J., Sterken, C., Schneider, H., Weiss, W. W., Kawaler, S. D., & Kepler, S. O. 1989, MNRAS, 240, 881

Kuschnig, R., Weiss, W. W., Gruber, R., Bely, P. Y., & Jenkner, H. 1997, A&A, 328, 544

Landstreet, J. D. 1992a, A&AR, 4, 35

—. 1992b, Reviews of Modern Astronomy, 5, 105

Landstreet, J. D. 1993, in ASP Conf. Ser. 44: IAU Colloq. 138: Peculiar versus Normal Phenomena in A-type and Related Stars, 218

Larson, R. B. & Demarque, P. R. 1964, ApJ, 140, 524

Leibacher, J. W. & Stein, R. F. 1971, Astrophys. Lett., 7, 191

Leighton, R. B., Noyes, R. W., & Simon, G. W. 1962, ApJ, 135, 474

Lenz, P. & Breger, M. 2005, Communications in Asteroseismology, 146, 53

Leone, F. & Catanzaro, G. 2004, A&A, 425, 271

Leroy, J. L., Landstreet, J. D., Deglinnocenti, E. L., & Landolfi, M. 1993, in ASP Conf. Ser. 44: IAU Colloq. 138: Peculiar versus Normal Phenomena in A-type and Related Stars, 274

Loumos, G. L. & Deeming, T. J. 1978, Astrophys. and Space Science, 56, 285

Lüftinger, T., Kochukhov, O., Ryabchikova, T., Piskunov, N., Weiss, W. W., & Ilyin, I. 2008, Contributions of the Astronomical Observatory Skalnate Pleso, 38, 335

Mathys, G. 1989, Fundamentals of Cosmic Physics, 13, 143

—. 1991, A&AS, 89, 121

Mathys, G., Hubrig, S., Landstreet, J. D., Lanz, T., & Manfroid, J. 1997, A&AS, 123, 353

Matthews, J. M. 1991, PASP, 103, 5

—. 2007, Communications in Asteroseismology, 150, 333

Matthews, J. M., Kurtz, D. W., & Martinez, P. 1999, ApJ, 511, 422

Matthews, J. M., Kusching, R., Guenther, D. B., Walker, G. A. H., Moffat, A. F. J., Rucinski, S. M., Sasselov, D., & Weiss, W. W. 2004, Nature, 430, 51

Matthews, J. M., Kuschnig, R., Walker, G. A. H., Pazder, J., Johnson, R., Skaret, K., Shkolnik, E., Lanting, T., Morgan, J. P., & Sidhu, S. 2000, in ASP Conf. Ser. 203: IAU Colloq. 176: The Impact of Large-Scale Surveys on Pulsating Star Research, 74–75

Matthews, J. M. & Wehlau, W. H. 1985, PASP, 97, 841

Metcalfe, T. S., Creevey, O. L., & Christensen-Dalsgaard, J. 2009, ApJ, 699, 373

Michaud, G. 1970, ApJ, 160, 641

Michaud, G. 1976, in IAU Colloq. 32: Physics of Ap Stars, 81

Michaud, G. 1996, in IAU Symp. 176: Stellar Surface Structure, 321

Michaud, G., Charland, Y., & Megessier, C. 1981, A&A, 103, 244

Michaud, G. J. & Proffitt, C. R. 1993, in ASP Conf. Ser. 44: IAU Colloq. 138: Peculiar versus Normal Phenomena in A-type and Related Stars, 439

Mkrtichian, D. E. & Hatzes, A. P. 2005, A&A, 430, 263

Mkrtichian, D. E., Hatzes, A. P., Saio, H., & Shobbrook, R. R. 2008, A&A, 490, 1109

Montgomery, M.-H. & O'Donoghue, D. 1999, DSSN (Vienna), 13

Moon, T. T. & Dworetsky, M. M. 1985, MNRAS, 217, 305

Moya, A., Christensen-Dalsgaard, J., Charpinet, S., Lebreton, Y., Miglio, A., Montalbán, J., Monteiro, M. J. P. F. G., Provost, J., Roxburgh, I. W., Scuflaire, R., Suárez, J. C., & Suran, M. 2008, Ap&SS, 316, 231

North, P. L., Babel, J., & Erspamer, D. 2008, Contributions of the Astronomical Observatory Skalnate Pleso, 38, 375

Perryman, M. A. C., Lindegren, L., Kovalevsky, J., Hoeg, E., Bastian, U., Bernacca, P. L., Crézé, M., Donati, F., Grenon, M., van Leeuwen, F., van der Marel, H., Mignard, F., Murray, C. A., Le Poole, R. S., Schrijver, H., Turon, C., Arenou, F., Froeschlé, M., & Petersen, C. S. 1997, A&A, 323, L49

Press, W. H., Teukolsky, S. A., Vetterling, W. T., & Flannery, B. P. 1992, Numerical recipes in FORTRAN. The art of scientific computing (Cambridge: University Press, —c1992, 2nd ed.)

Preston, G. W. 1972, ApJ, 175, 465

—. 1974, ARA&A, 12, 257

Provost, J. 1984, in IAU Symp. 105: Observational Tests of the Stellar Evolution Theory, 47

Reegen, P., Kallinger, T., Frast, D., Gruberbauer, M., Huber, D., Matthews, J. M., Punz, D., Schraml, S., Weiss, W. W., Kuschnig, R., Moffat, A. F. J., Walker, G. A. H., Guenther, D. B., Rucinski, S. M., & Sasselov, D. 2006, MNRAS, 367, 1417

Roberts, P. H. & Soward, A. M. 1983, MNRAS, 205, 1171

Rogers, F. J. 1986, ApJ, 310, 723

Rogers, F. J., Swenson, F. J., & Iglesias, C. A. 1996, ApJ, 456, 902

Rowe, J. F. 2008, PhD thesis, University of British Columbia (Canada)

Rowe, J. F., Matthews, J. M., Cameron, C., Bohlender, D. A., King, H., Kuschnig, R., Guenther, D. B., Moffat, A. F. J., Rucinski, S. M., Sasselov, D., Walker, G. A. H., & Weiss, W. W. 2006a, Communications in Asteroseismology, 148, 34

Rowe, J. F., Matthews, J. M., Kuschnig, R., Guenther, D. B., Moffat, A. F. J., Rucinski, S. M. R., Sasselov, D., Walker, G. A. H., & Weiss, W. W. 2006b, Memorie della Societa Astronomica Italiana, 77, 282

Rowe, J. F., Matthews, J. M., Seager, S., Kuschnig, R., Guenther, D. B., Moffat, A. F. J., Rucinski, S. M., Sasselov, D., Walker, G. A. H., & Weiss, W. W. 2006c, ApJ, 646, 1241

Rowe, J. F., Matthews, J. M., Seager, S., Miller-Ricci, E., Sasselov, D., Kuschnig, R., Guenther, D. B., Moffat, A. F. J., Rucinski, S. M., Walker, G. A. H., & Weiss, W. W. 2008a, ApJ, 689, 1345

Rowe, J. F., Matthews, J. M., Seager, S., Sasselov, D., Kuschnig, R., Guenther, D. B., Moffat, A. F. J., Rucinski, S. M., Walker, G. A. H., & Weiss, W. W. 2008b, ArXiv e-prints

Roxburgh, I. W. 2008, Ap&SS, 316, 141

Rucinski, S. M., Walker, G. A. H., Matthews, J. M., Kuschnig, R., Shkolnik, E., Marchenko, S., Bohlender, D. A., Guenther, D. B., Moffat, A. F. J., Sasselov, D., & Weiss, W. W. 2004, PASP, 116, 1093

Ryabchikova, T. A. 2008, Contributions of the Astronomical Observatory Skalnate Pleso, 38, 257

Ryabchikova, T. A., Landstreet, J. D., Gelbmann, M. J., Bolgova, G. T., Tsymbal, V. V., & Weiss, W. W. 1997, A&A, 327, 1137

Ryabchikova, T. A., Wade, G. A., Aurière, M., Bagnulo, S., Donati, J.-F., Jeffers, S. V., Johnson, N., Landstreet, J. D., Lignières, F., Lueftinger, T., Marsden, S., Mouillet, D., Paletou, F., Petit, P., Reegen, P., Silvester, J., Strasser, S., & Toque, N. 2005, A&A, 429, L55

Saio, H. 2005, MNRAS, 360, 1022

—. 2008, Journal of Physics Conference Series, 118, 012018

Saio, H., Cameron, C., Kuschnig, R., Walker, G. A. H., Matthews, J. M., Rowe, J. F., Lee, U., Huber, D., Weiss, W. W., Guenther, D. B., Moffat, A. F. J., Rucinski, S. M., & Sasselov, D. 2007, ApJ, 654, 544

Saio, H. & Cox, J. P. 1980, ApJ, 236, 549

Saio, H. & Gautschy, A. 2004, MNRAS, 350, 485

Saio, H., Kuschnig, R., Gautschy, A., Cameron, C., Walker, G. A. H., Matthews, J. M., Guenther, D. B., Moffat, A. F. J., Rucinski, S. M., Sasselov, D., & Weiss, W. W. 2006, ApJ, 650, 1111

Shibahashi, H. 2005, Journal of Astrophysics and Astronomy, 26, 139

—. 2008, Communications in Asteroseismology, 157, 222

Shibahashi, H. & Saio, H. 1985, PASJ, 37, 245

Sperl, M. 1998, Communications in Asteroseismology, 112, 1

Stibbs, D. W. N. 1950, MNRAS, 110, 395

Tassoul, M. 1980, ApJS, 43, 469

—. 1990, ApJ, 358, 313

Théado, S., Dupret, M., Noels, A., & Ferguson, J. W. 2009, A&A, 493, 159

Théado, S., Vauclair, S., & Cunha, M. S. 2005, A&A, 443, 627

Turcotte, S. 2003, in Astronomical Society of the Pacific Conference Series, Vol. 305, Astronomical Society of the Pacific Conference Series, ed. L. A. Balona, H. F. Henrichs, & R. Medupe, 199

Turcotte, S. 2005, Journal of Astrophysics and Astronomy, 26, 231

Ulrich, R. K. 1970, ApJ, 162, 993

Unno, W., Osaki, Y., Ando, H., Saio, H., & Shibahashi, H. 1989, Nonradial oscillations of stars (Nonradial oscillations of stars, Tokyo: University of Tokyo Press, 1989, 2nd ed.)

Vauclair, S. & Vauclair, G. 1982, ARA&A, 20, 37

Wade, G. A. 1997, A&A, 325, 1063

—. 2006, ArXiv Astrophysics e-prints

Walker, G., Matthews, J., Kuschnig, R., Johnson, R., Rucinski, S., Pazder, J., Burley, G., Walker, A., Skaret, K., Zee, R., Grocott, S., Carroll, K., Sinclair, P., Sturgeon, D., & Harron, J. 2003, PASP, 115, 1023

Walker, G. A. H. 2008, Journal of Physics Conference Series, 118, 012013

Walker, G. A. H., Kuschnig, R., Matthews, J. M., Cameron, C., Saio, H., Lee, U., Kambe, E., Masuda, S., Guenther, D. B., Moffat, A. F. J., Rucinski, S. M., Sasselov, D., & Weiss, W. W. 2005, ApJ, 635, L77

Wall, J. V. & Jenkins, C. R. 2003, Practical Statistics for Astronomers (Princeton Series in Astrophysics)

Wolff, S. C. 1983, The A-stars: Problems and perspectives. Monograph series on nonthermal phenomena in stellar atmospheres

Appendix A

HD 127756 and HD 217543 parameter tables

Tables of fit parameters identified in the slowly pulsating Be (SPBe) stars HD 127756 and HD 217543 by the *MOST* team (Cameron et al., 2008).

Table A.1: Frequencies identified in the star HD 127756 by the *MOST* team (Cameron et al., 2008)

#	ν [cycles day^{-1}]	A [μmag]	ϕ [rad]	$\sim$ S/N	σ_ν	$3\sigma_\nu$	σ_A	$3\sigma_A$	σ_ϕ	$3\sigma_\phi$
1	0.0335	7.2	3.60	8.68	$\pm$ 0.0009	0.0023	0.2	0.6	0.11	0.30
2	0.0739	2.2	0.59	6.97	$\pm$ 0.0020	0.0055	0.1	0.4	0.22	0.58
3	0.1300	8.8	3.65	9.50	$\pm$ 0.0007	0.0017	0.1	0.4	0.07	0.19
4	0.1664	7.3	1.27	8.31	$\pm$ 0.0004	0.0010	0.2	0.4	0.06	0.16
5	0.1957	5.0	2.64	8.71	$\pm$ 0.0007	0.0018	0.2	0.5	0.10	0.24
6	0.2530	1.8	4.11	5.12	$\pm$ 0.0031	0.0078	0.2	0.4	0.32	0.81
7	0.2827	1.4	4.27	3.89	$\pm$ 0.0032	0.0079	0.2	0.4	0.34	0.88
8	0.7108	2.3	3.31	5.74	$\pm$ 0.0015	0.0038	0.2	0.6	0.15	0.37
9	0.7393	1.7	5.22	4.80	$\pm$ 0.0016	0.0040	0.2	0.5	0.19	0.52
10	0.7740	5.1	4.80	9.04	$\pm$ 0.0005	0.0013	0.2	0.5	0.06	0.17
11	0.8035	6.7	4.24	8.16	$\pm$ 0.0005	0.0013	0.3	0.7	0.03	0.08
12	0.8280	7.2	4.13	8.22	$\pm$ 0.0005	0.0015	0.3	0.7	0.03	0.09
13	0.8702	2.4	2.57	5.17	$\pm$ 0.0015	0.0048	0.2	0.4	0.15	0.45
14	0.9149	10.2	4.18	11.12	$\pm$ 0.0004	0.0011	0.1	0.4	0.04	0.10
15	0.9595	6.5	2.67	9.80	+ 0.0006	0.0015	0.1	0.4	0.06	0.17

continued on next page

Table A.1: *continued*

#	ν [cycles day^{-1}]	A [μmag]	ϕ [rad]	$\sim$ S/N	σ_ν	$3\sigma_\nu$	σ_A	$3\sigma_A$	σ_ϕ	$3\sigma_\phi$
.....	0.9595	6.5	2.67	9.80	− 0.0006	0.0015	0.1	0.4	0.06	0.16
16	1.0236	4.2	0.31	8.74	± 0.0007	0.0021	0.1	0.4	0.08	0.22
17	1.0595	2.3	0.06	5.00	± 0.0015	0.0042	0.1	0.4	0.15	0.41
18	1.1297	1.9	4.55	4.00	± 0.0024	0.0064	0.2	0.5	0.28	0.72
19	1.1418	6.2	1.65	8.24	± 0.0007	0.0016	0.2	0.5	0.08	0.21
20	1.5301	1.2	4.16	4.04	± 0.0021	0.0051	0.1	0.3	0.22	0.56
21	1.7761	1.8	5.56	5.65	± 0.0017	0.0047	0.1	0.4	0.19	0.46
22	1.8208	4.8	4.63	8.97	+ 0.0009	0.0024	0.2	0.5	0.10	0.35
.....	1.8208	4.8	4.63	8.97	− 0.0009	0.0024	0.2	0.5	0.10	0.30
23	1.8441	5.1	4.67	9.11	± 0.0010	0.0027	0.2	0.7	0.09	0.24
24	1.8685	2.1	4.81	5.08	± 0.0019	0.0054	0.2	0.5	0.18	0.49
25	1.9066	4.3	3.26	8.53	+ 0.0007	0.0019	0.2	0.4	0.08	0.23
.....	1.9066	4.3	3.26	8.53	− 0.0007	0.0019	0.2	0.4	0.08	0.19
26	2.0171	1.1	3.44	3.87	± 0.0028	0.0076	0.1	0.4	0.32	0.79
27	2.0512	6.1	1.91	9.38	+ 0.0006	0.0015	0.1	0.4	0.08	0.29
.....	2.0512	6.1	1.91	9.38	− 0.0006	0.0015	0.1	0.4	0.08	0.19

continued on next page

Table A.1: *continued*

#	ν [cycles day^{-1}]	A [μmag]	ϕ [rad]	$\sim$ S/N	σ_ν	$3\sigma_\nu$	σ_A	$3\sigma_A$	σ_ϕ	$3\sigma_\phi$
28	2.1160	1.8	0.11	5.10	$\pm$ 0.0014	0.0036	0.1	0.4	0.15	0.40
29	2.7814	1.5	2.77	5.22	$\pm$ 0.0018	0.0049	0.1	0.4	0.21	0.54
30	2.8771	1.0	6.18	3.55	+ 0.0029	0.0072	0.1	0.3	0.34	1.01
.....	2.8771	1.0	6.18	3.55	− 0.0029	0.0086	0.1	0.3	0.34	1.01

Table A.2: Frequencies identified in the star HD 217543 by the *MOST* team (Cameron et al., 2008)

#	ν [cycles day^{-1}]	A [μmag]	ϕ [rad]	$\sim$ S/N	σ_ν	$3\sigma_\nu$	σ_A	$3\sigma_A$	σ_ϕ	$3\sigma_\phi$
1	0.0269	12.9	1.01	10.80	+ 0.0003	0.0035	0.2	1.2	0.07	0.58
.....	0.0269	12.9	1.01	10.80	− 0.0003	0.0066	0.2	0.7	0.07	0.30
2	0.0806	7.1	0.09	5.48	+ 0.0013	0.0058	0.3	0.7	0.14	0.43
.....	0.0806	7.1	0.09	5.48	− 0.0013	0.0031	0.3	0.7	0.14	0.43
3	0.1201	13.3	1.76	8.28	± 0.0012	0.0043	0.2	0.7	0.10	0.36
4	0.1806	5.7	3.03	4.59	± 0.0016	0.0071	0.3	0.8	0.12	0.57
5	0.2454	4.6	3.97	5.10	± 0.0017	0.0074	0.3	0.9	0.12	0.62
6	0.2904	1.9	2.03	3.15	± 0.0042	0.0121	0.2	1.7	0.27	1.01
7	0.3133	3.1	4.67	4.40	± 0.0024	0.0099	0.3	2.2	0.19	0.75
8	0.3987	2.0	5.78	3.97	± 0.0022	0.0053	0.2	0.6	0.19	0.59
9	0.5147	1.6	2.80	3.32	± 0.0034	0.0091	0.2	0.6	0.31	0.82
10	0.5668	1.7	4.37	3.17	± 0.0034	0.0091	0.2	0.6	0.32	0.79
11	0.6154	2.0	5.61	3.09	± 0.0026	0.0062	0.2	0.5	0.23	0.56
12	0.7772	1.3	1.87	3.11	± 0.0026	0.0068	0.2	0.5	0.23	0.61
13	1.0006	2.1	2.68	3.67	± 0.0019	0.0051	0.2	0.5	0.16	0.42

continued on next page

Table A.2: *continued*

#	ν [cycles day^{-1}]	A [μmag]	ϕ [rad]	$\sim$ S/N	σ_ν	$3\sigma_\nu$	σ_A	$3\sigma_A$	σ_ϕ	$3\sigma_\phi$
14	1.5826	2.4	0.72	4.36	$\pm$ 0.0016	0.0048	0.2	0.5	0.16	0.44
15	1.7164	2.2	1.85	4.21	$\pm$ 0.0020	0.0053	0.2	0.5	0.19	0.52
16	1.7948	2.6	0.45	4.16	+ 0.0019	0.0054	0.2	0.5	0.17	0.69
.....	1.7948	2.6	0.45	4.16	− 0.0019	0.0074	0.2	0.5	0.17	0.46
17	1.8881	6.0	1.81	5.66	+ 0.0011	0.0038	0.3	1.6	0.10	0.55
.....	1.8881	6.0	1.81	5.66	− 0.0011	0.0038	0.3	0.8	0.10	0.44
18	1.9237	12.7	3.51	8.17	+ 0.0006	0.0014	0.2	0.7	0.05	0.48
.....	1.9237	12.7	3.51	8.17	− 0.0006	0.0056	0.2	0.7	0.05	0.18
19	1.9643	4.9	4.44	5.07	+ 0.0009	0.0209	0.4	3.6	0.08	0.19
.....	1.9643	4.9	4.44	5.07	− 0.0009	0.0027	0.4	1.8	0.08	1.28
20	1.9971	7.6	6.22	6.80	+ 0.0008	0.0029	0.3	4.7	0.05	0.17
.....	1.9971	7.6	6.22	6.80	− 0.0008	0.0029	0.3	0.8	0.05	0.41
21	2.0335	23.8	2.25	14.25	+ 0.0002	0.0007	0.3	0.9	0.02	0.39
.....	2.0335	23.8	2.25	14.25	− 0.0002	0.0036	0.3	5.3	0.02	0.02
22	2.0704	7.1	5.30	6.26	+ 0.0010	0.0031	0.3	3.9	0.07	1.18
.....	2.0704	7.1	5.30	6.26	− 0.0010	0.0102	0.3	0.7	0.07	0.28

continued on next page

Table A.2: *continued*

#	ν [cycles day^{-1}]	A [μmag]	ϕ [rad]	$\sim$ S/N	σ_ν	$3\sigma_\nu$	σ_A	$3\sigma_A$	σ_ϕ	$3\sigma_\phi$
23	2.1237	9.9	2.50	7.28	+ 0.0006	0.0066	0.2	1.1	0.05	0.13
.....	2.1237	9.9	2.50	7.28	− 0.0006	0.0012	0.2	0.7	0.05	0.52
24	2.1766	9.4	4.20	6.80	+ 0.0006	0.0081	0.3	0.7	0.06	0.38
.....	2.1766	9.4	4.20	6.80	− 0.0006	0.0038	0.3	0.9	0.06	0.53
25	2.2288	6.5	6.03	5.68	+ 0.0010	0.0037	0.2	0.6	0.08	0.39
.....	2.2288	6.5	6.03	5.68	− 0.0010	0.0037	0.2	1.0	0.08	0.39
26	2.2985	2.8	1.60	4.06	+ 0.0018	0.0047	0.2	0.5	0.18	0.48
.....	2.2985	2.8	1.60	4.06	− 0.0018	0.0047	0.2	0.5	0.18	0.42
27	2.3674	3.0	1.59	4.27	± 0.0016	0.0046	0.2	0.6	0.15	0.40
28	3.7755	2.0	4.00	4.00	± 0.0019	0.0049	0.2	0.5	0.18	0.51
29	3.8947	2.3	0.17	4.33	+ 0.0019	0.0045	0.2	0.5	0.18	0.56
.....	3.8947	2.3	0.17	4.33	− 0.0019	0.0045	0.2	0.5	0.18	0.42
30	4.0017	3.4	2.13	4.52	± 0.0014	0.0037	0.2	0.5	0.13	0.35
31	4.0646	4.2	1.18	5.20	+ 0.0015	0.0045	0.2	0.6	0.15	0.56
.....	4.0646	4.2	1.18	5.20	− 0.0015	0.0048	0.2	0.6	0.15	0.37
32	4.1079	2.6	1.03	4.08	± 0.0025	0.0068	0.2	0.6	0.20	0.52

continued on next page

Table A.2: *continued*

#	ν [cycles day^{-1}]	A [μmag]	ϕ [rad]	$\sim$ S/N	σ_ν	$3\sigma_\nu$	σ_A	$3\sigma_A$	σ_ϕ	$3\sigma_\phi$
33	4.1886	5.9	4.84	6.01	+ 0.0011	0.0031	0.2	0.6	0.12	0.73
.....	4.1886	5.9	4.84	6.01	− 0.0011	0.0060	0.2	0.7	0.12	0.24
34	4.2350	4.9	0.84	5.83	+ 0.0017	0.0044	0.2	0.7	0.16	1.00
.....	4.2350	4.9	0.84	5.83	− 0.0017	0.0080	0.2	0.6	0.16	0.35
35	4.2665	2.3	3.05	4.15	+ 0.0027	0.0081	0.2	0.6	0.27	1.16
.....	4.2665	2.3	3.05	4.15	− 0.0027	0.0085	0.2	0.6	0.27	0.73
36	4.4017	3.6	2.01	4.91	+ 0.0012	0.0033	0.2	0.5	0.14	0.51
.....	4.4017	3.6	2.01	4.91	− 0.0012	0.0033	0.2	0.5	0.14	0.36
37	4.4695	2.1	4.02	4.20	+ 0.0019	0.0055	0.2	0.5	0.20	0.57
.....	4.4695	2.1	4.02	4.20	− 0.0019	0.0055	0.2	0.5	0.20	0.41
38	4.5406	2.4	5.24	4.26	+ 0.0020	0.0056	0.2	0.5	0.18	0.55
.....	4.5406	2.4	5.24	4.26	− 0.0020	0.0056	0.2	0.5	0.18	0.52
39	4.6210	1.6	5.40	3.38	± 0.0029	0.0072	0.2	0.5	0.27	0.73
40	4.7226	2.6	4.63	4.47	+ 0.0016	0.0042	0.2	0.5	0.17	0.47
.....	4.7226	2.6	4.63	4.47	− 0.0016	0.0042	0.2	0.5	0.17	0.46

Appendix B

Frequency lists in cycles day^{-1}

It is more common to use units of μHz when presenting both theoretical and observational results on roAp stars. However, there are still cases when units of cycles day^{-1} are used. The latter units are particularly useful when describing the fine (rotational) spacings observed in roAp stars. In this appendix we reproduce the tables in the main text with frequencies in units of cycles day^{-1}.

Table B.1: Table 3.1 with frequencies in units of cycles day^{-1}

#	ν [cycles day^{-1}]	A [μmag]	ϕ [rad]	$\sim$ S/N	σ_ν	$3\sigma_\nu$	σ_A	$3\sigma_A$	σ_ϕ	$3\sigma_\phi$
1	224.9711	39	2.22	3.8	$\pm$ 0.0025	0.0069	6	15	0.34	0.93
2	226.2470	50	3.29	4.2	$\pm$ 0.0021	0.0057	6	16	0.27	0.72
3	226.3244	125	5.70	9.2	$\pm$ 0.0013	0.0034	6	16	0.11	0.29
4	226.4061	68	1.68	6.3	$\pm$ 0.0024	0.0064	6	16	0.28	0.74
5	229.1326	96	3.36	7.5	$\pm$ 0.0015	0.0039	6	16	0.14	0.35
6	229.2127	365	5.56	24.2	$\pm$ 0.0004	0.0010	6	16	0.04	0.10
7	229.2955	92	2.07	7.8	$\pm$ 0.0011	0.0028	6	16	0.10	0.27
8	231.9695	43	2.02	3.7	$\pm$ 0.0047	0.0125	6	16	0.38	1.10
9	232.0409	31	2.83	3.1	$\pm$ 0.0078	0.0209	9	26	0.55	2.18
10	232.1187	123	1.26	8.9	$\pm$ 0.0010	0.0025	7	17	0.10	0.26
11	232.1931	467	4.46	29.7	$\pm$ 0.0003	0.0008	6	16	0.03	0.08
12	232.2747	139	1.13	10.9	$\pm$ 0.0008	0.0020	6	16	0.07	0.18
13	234.9202	51	4.50	5.8	$\pm$ 0.0044	0.0118	6	16	0.25	0.68
14	235.0043	319	6.04	23.3	$\pm$ 0.0005	0.0012	6	16	0.05	0.13
15	235.0870	764	1.83	41.6	$\pm$ 0.0002	0.0005	6	16	0.02	0.05

continued on next page

Table B.1: *continued*

#	ν [cycles day^{-1}]	A [μmag]	ϕ [rad]	$\sim$ S/N	σ_ν	$3\sigma_\nu$	σ_A	$3\sigma_A$	σ_ϕ	$3\sigma_\phi$
16	235.1654	177	4.59	12.4	$\pm$ 0.0009	0.0023	6	16	0.10	0.26
17	235.3077	41	2.08	3.1	$\pm$ 0.0029	0.0084	6	16	0.39	1.10
18	237.9862	110	1.81	8.5	$\pm$ 0.0014	0.0037	6	16	0.17	0.45
19	238.0660	118	3.45	8.9	$\pm$ 0.0013	0.0034	6	16	0.17	0.45
20	238.1214	67	2.75	6.2	$\pm$ 0.0033	0.0093	6	16	0.36	1.05
21	238.1983	39	5.14	3.1	$\pm$ 0.0039	0.0138	6	17	0.53	1.67
22	240.8659	24	4.72	2.7	$\pm$ 0.0110	0.0274	6	16	0.90	2.59
23	240.9585	37	0.24	3.6	$\pm$ 0.0030	0.0083	6	16	0.29	0.80
24	241.0277	33	5.56	3.3	$\pm$ 0.0041	0.0136	7	16	0.38	1.16
25	241.0911	37	2.85	4.4	$\pm$ 0.0063	0.0169	7	18	0.45	1.24
26	241.1755	82	5.00	6.8	$\pm$ 0.0028	0.0073	7	17	0.29	0.74
27	241.2503	57	1.47	5.6	+ 0.0047	0.0178	9	24	0.35	1.06
.....	241.2503	57	1.47	5.6	− 0.0047	0.0154	9	25	0.35	1.06
28	242.4082	84	1.10	6.9	$\pm$ 0.0013	0.0033	6	15	0.15	0.37
29	242.4896	81	2.09	7.1	$\pm$ 0.0016	0.0041	6	16	0.16	0.44

Table B.2: Table 3.2 with frequencies in units of cycles day^{-1}. Columns with headers ν_i - ν_j use i and j to denote the frequency number from Table B.1. The average rotation separation (spacings 9 ... 18 & 27 ... 35) is 0.0798 ± 0.0041 μHz ($3\sigma = 0.0112$ μHz).

#	ν_i - ν_j	$\delta^\dagger$ [μHz]	$\sigma_{\delta^\dagger}$	$3\sigma_{\delta^\dagger}$	#	ν_i - ν_j	$\delta^\dagger$ [μHz]	$\sigma_{\delta^\dagger}$	$3\sigma_{\delta^\dagger}$
1	6 - 3	2.8883	0.0013	0.0035	19	11 - 8	0.2236	0.0047	0.0125
2	11 - 6	2.9804	0.0005	0.0012	20	11 - 9	0.1522	0.0079	0.0209
3	15 - 11	2.8939	0.0003	0.0009	21	17 - 15	0.2208	0.0029	0.0084
4	19 - 15	2.9790	0.0013	0.0035	22	21 - 19	0.1324	0.0041	0.0142
5	23 - 19	2.8926	0.0032	0.0090	23	26 - 23	0.2170	0.0041	0.0111
6	3 - 1	1.3533	0.0028	0.0077	24	28 - 26	1.2326	0.0031	0.0080
7	17 - 8	3.3382	0.0055	0.0150	25	17 - 9	3.2669	0.0084	0.0225
8	21 - 17	2.8906	0.0048	0.0162	26	26 - 21	2.9773	0.0048	0.0156
9	3 - 2	0.0773	0.0026	0.0069	27	16 - 15	0.0785	0.0009	0.0026
10	4 - 3	0.0816	0.0026	0.0069	28	19 - 18	0.0797	0.0017	0.0052
11	6 - 5	0.0800	0.0017	0.0043	29	20 - 19	0.0555	0.0035	0.0095
12	7 - 6	0.0828	0.0009	0.0026	30	21 - 20	0.0769	0.0052	0.0164
13	9 - 8	0.0715	0.0095	0.0242	31	23 - 22	0.0926	0.0112	0.0285

continued on next page

Table B.2: *continued*

#	ν_i - ν_j	$\delta^\dagger$ [μHz]	$\sigma_{\delta^\dagger}$	$3\sigma_{\delta^\dagger}$	#	ν_i - ν_j	$\delta^\dagger$ [μHz]	$\sigma_{\delta^\dagger}$	$3\sigma_{\delta^\dagger}$
14	10 - 9	0.0778	0.0078	0.0207	32	24 - 23	0.0693	0.0052	0.0156
15	11 - 10	0.0743	0.0009	0.0026	33	26 - 25	0.0845	0.0069	0.0181
16	12 - 11	0.0816	0.0009	0.0017	34	27 - 26	0.0748	0.0052	0.0173
17	14 - 13	0.0841	0.0043	0.0121	35	29 - 28	0.0814	0.0017	0.0052
18	15 - 14	0.0827	0.0009	0.0017					

Table B.3: Table 3.3 with frequencies in units of cycles day^{-1}. Frequencies numbered 30 and higher are the unresolved components.

#	ν [cycles day^{-1}]	A [μmag]	ϕ [rad]	σ_ν	σ_A	σ_ϕ	$3\sigma_\nu$	$3\sigma_A$	$3\sigma_\phi$
1	224.9710	38	2.22	± 0.0023	5	0.26	0.0067	16	0.11
2	226.2480	45	3.25	± 0.0020	5	0.21	0.0060	17	0.50
3	226.3196	106	5.96	± 0.0021	12	0.20	0.0047	15	0.75
4	226.4012	64	2.07	± 0.0037	5	0.34	0.0072	24	1.42
5	229.1339	95	3.20	± 0.0012	5	0.16	0.0042	17	0.36
6	229.2125	364	5.59	± 0.0003	5	0.04	0.0011	16	0.08
7	229.2938	81	2.13	± 0.0017	9	0.14	0.0052	17	0.31
8	231.9733	43	1.67	± 0.0038	5	0.35	0.0073	30	0.95
9	232.0429	40	3.02	± 0.0042	10	0.44	0.0133	16	0.11
10	232.1167	111	1.37	± 0.0018	10	0.10	0.0037	36	0.12
11	232.1927	475	4.50	± 0.0003	9	0.05	0.0007	16	0.23
12	232.2726	131	1.30	± 0.0015	8	0.17	0.0031	16	0.88
13	234.9166	54	5.18	± 0.0036	8	0.52	0.0099	16	0.50
14	235.0042	320	6.11	± 0.0003	5	0.06	0.0010	28	0.58
15	235.0875	761	1.81	+ 0.0004	8	0.02	0.0012	36	0.12

continued on next page

Table B.3: *continued*

#	ν [cycles day^{-1}]	A [μmag]	ϕ [rad]	σ_ν	σ_A	σ_ϕ	$3\sigma_\nu$	$3\sigma_A$	$3\sigma_\phi$
.....	235.0875	761	1.81	− 0.0004	8	0.02	0.0012	36	0.12
16	235.1680	184	4.45	± 0.0012	6	0.13	0.0026	16	0.23
17	235.3059	31	2.33	± 0.0024	9	0.27	0.0073	16	0.88
18	237.9839	108	1.99	+ 0.0019	5	0.18	0.0042	16	0.50
.....	237.9839	108	1.99	− 0.0019	5	0.18	0.0043	16	0.45
19	238.0632	112	4.02	± 0.0024	6	0.22	0.0057	28	0.58
20	238.1313	53	1.75	+ 0.0038	12	0.40	0.0356	25	1.29
.....	238.1313	53	1.75	− 0.0038	12	0.40	0.0098	25	1.29
21	238.1960	33	5.35	± 0.0027	6	0.29	0.0099	16	1.24
22	240.8660	24	4.73	± 0.0041	5	0.44	0.0123	15	1.37
23	240.9585	36	0.19	± 0.0026	5	0.28	0.0077	15	0.84
24	241.0280	34	5.48	± 0.0031	5	0.31	0.0093	15	0.95
25	241.0901	35	3.02	± 0.0029	5	0.30	0.0086	16	0.87
26	241.1750	82	5.04	± 0.0013	5	0.14	0.0039	16	0.41
27	241.2498	58	1.50	± 0.0022	5	0.22	0.0067	16	0.69
28	242.4082	84	1.10	± 0.0011	5	0.12	0.0032	15	0.36

continued on next page

Table B.3: *continued*

#	ν [cycles day^{-1}]	A [μmag]	ϕ [rad]	σ_ν	σ_A	σ_ϕ	$3\sigma_\nu$	$3\sigma_A$	$3\sigma_\phi$
29	242.4896	82	2.09	± 0.0011	5	0.13	0.0034	15	0.37
30	226.3359	36	4.63	+ 0.0135	12	0.72	0.0247	24	1.65
.....	226.3359	36	4.63	− 0.0135	12	0.72	0.0247	24	4.38
31	226.4391	31	5.19	± 0.0085	6	0.54	0.0164	17	1.50
32	229.2147	10	2.08	+ 0.0927	8	2.00	0.1700	15	4.13
.....	229.2147	10	2.08	− 0.0927	8	2.00	0.1700	10	2.08
33	229.2515	51	3.47	± 0.0029	5	0.31	0.0098	17	0.99
34	232.0707	57	2.84	± 0.0029	8	0.27	0.0120	24	1.20
35	232.2356	55	2.10	± 0.0037	7	0.47	0.0086	18	0.92
36	234.9088	25	3.63	+ 0.0096	8	1.22	0.0289	27	2.63
.....	234.9088	25	3.63	− 0.0096	8	1.22	0.0289	25	2.73
37	235.0711	47	2.06	+ 0.0056	16	0.51	0.0168	47	1.68
.....	235.0711	47	2.06	− 0.0056	16	0.51	0.0168	44	1.68
38	235.1226	77	3.06	± 0.0030	10	0.20	0.0073	21	0.76
39	238.0214	48	3.48	± 0.0051	6	0.49	0.0119	18	1.28
40	238.0867	55	6.07	+ 0.0074	17	0.49	0.0251	42	1.76

continued on next page

Table B.3: *continued*

#	ν [cycles day^{-1}]	A [μmag]	ϕ [rad]	σ_ν	σ_A	σ_ϕ	$3\sigma_\nu$	$3\sigma_A$	$3\sigma_\phi$
.....	238.0867	55	6.07	− 0.0074	17	0.49	0.0251	42	2.57
41	241.2817	28	0.19	± 0.0042	5	0.46	0.0128	15	1.39

Table B.4: Table 5.3 with frequencies in units of cycles day^{-1}. Frequency uncertainties marked by $*$ are average uncertainties based on the separation from the marked frequency to the nearest ($\sim$ rotationally split) frequency plus its uncertainty.

#	ν [cycles day^{-1}]	A [μmag]	ϕ [rad]	$\sim$ S/N	σ_ν	$3\sigma_\nu$	σ_A	$3\sigma_A$	σ_ϕ	$3\sigma_\phi$
1	224.9711	39	2.22	3.8	$\pm$ 0.0024	0.0069	6	15	0.34	0.93
3	226.3244	125	5.7	9.2	$\pm$ 0.0013	0.0034	6	16	0.11	0.29
6	229.2126	365	5.56	24.2	$\pm$ 0.0003	0.0010	6	16	0.04	0.1
9	232.0409	31	2.83	3.1	$\pm$ 0.0775 $*$	0.0822$*$	9	26	0.55	2.18
11	232.1931	467	4.46	29.7	$\pm$ 0.0003	0.0008	6	16	0.03	0.08
15	235.0870	764	1.83	41.6	$\pm$ 0.0002	0.0004	6	16	0.02	0.05
17	235.3077	41	2.08	3.1	$\pm$ 0.0029	0.0084	6	16	0.39	1.1
19	238.0660	118	3.45	8.9	$\pm$ 0.0013	0.0034	6	16	0.17	0.45
21	238.1983	39	5.14	3.1	$\pm$ 0.0421$*$	0.0499$*$	6	17	0.53	1.67
23	240.9585	37	0.24	3.6	$\pm$ 0.0029	0.0083	6	16	0.29	0.8
26	241.1756	82	5	6.8	$\pm$ 0.0029	0.0073	7	17	0.29	0.74
28	242.4082	84	1.1	6.9	$\pm$ 0.0422$*$	0.0444$*$	6	15	0.15	0.37

Appendix C

Bootstrap distributions

All bootstrap distributions for the fit parameters given in Tab. 3.1 are presented below. In each figure the top panels show the phase (ϕ) in radians, the middle panels are the amplitudes (A) in mmag, and lower panels are frequencies (ν) in μHz. Increasing parameter numbers from Tab. 3.1 are read left to right for each figure. Thus, distributions for parameter set (ν_1, A_1, ϕ_1) are shown in the left panels while distributions for the set (ν_2, A_2, ϕ_2) are shown on the right. In each plot the green and red lines show the 1 and 2 σ uncertainties calculated by counting 68% and 95% of the realizations, centred on the best fit parameter, respectively. The pink lines show the best fit parameter with the standard deviation calculated from the analytic formula and the blue dots are the mean of the distribution with the standard error on that mean. (Note: The phases are calculated by referencing to the time of the first *MOST* observation, HJD 2451545.00 + 1769.42 days.)

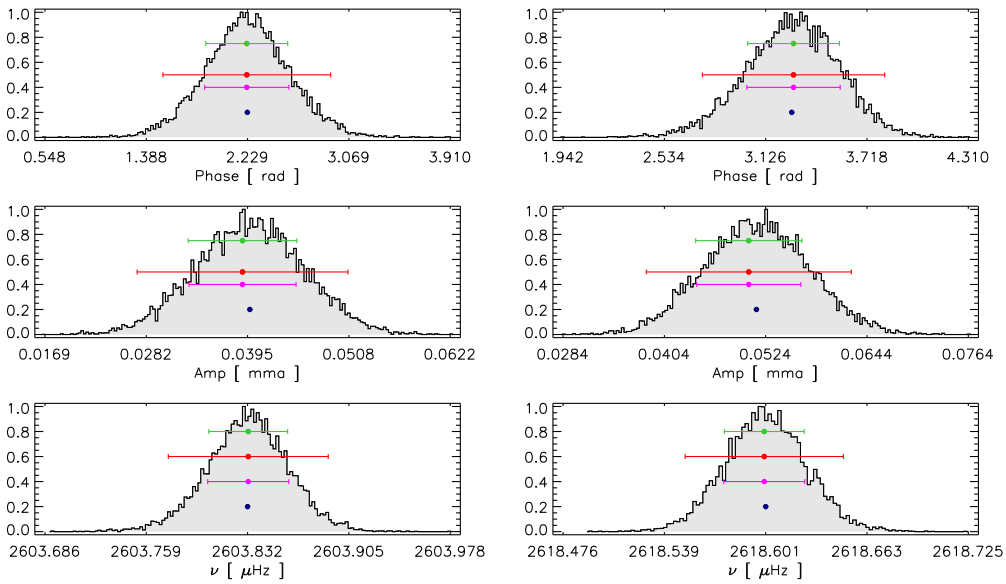

Figure C.1: Bootstrap distributions for fit parameters 1 and 2 in Tab. 3.1.

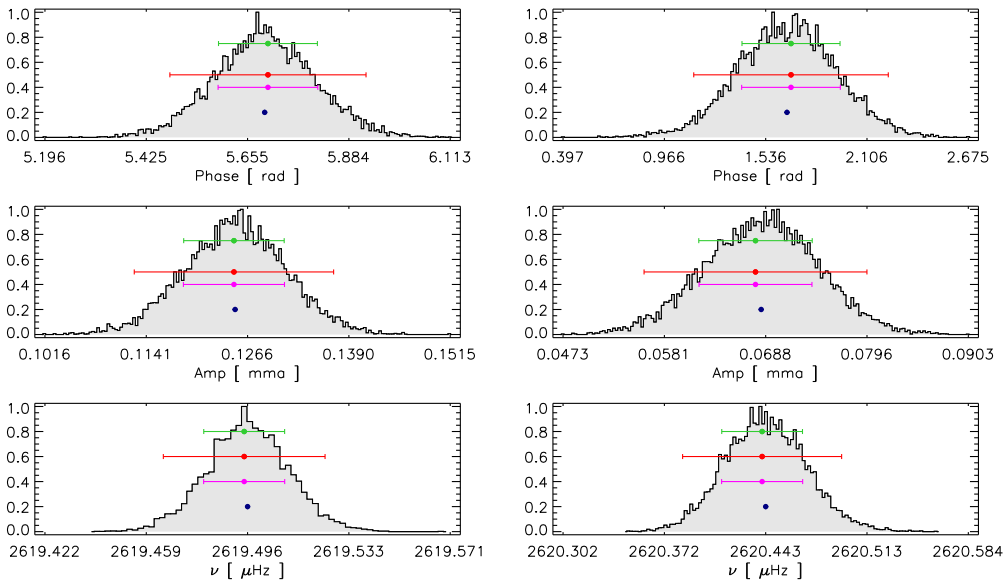

Figure C.2: Bootstrap distributions for fit parameters 3 and 4 in Tab. 3.1.

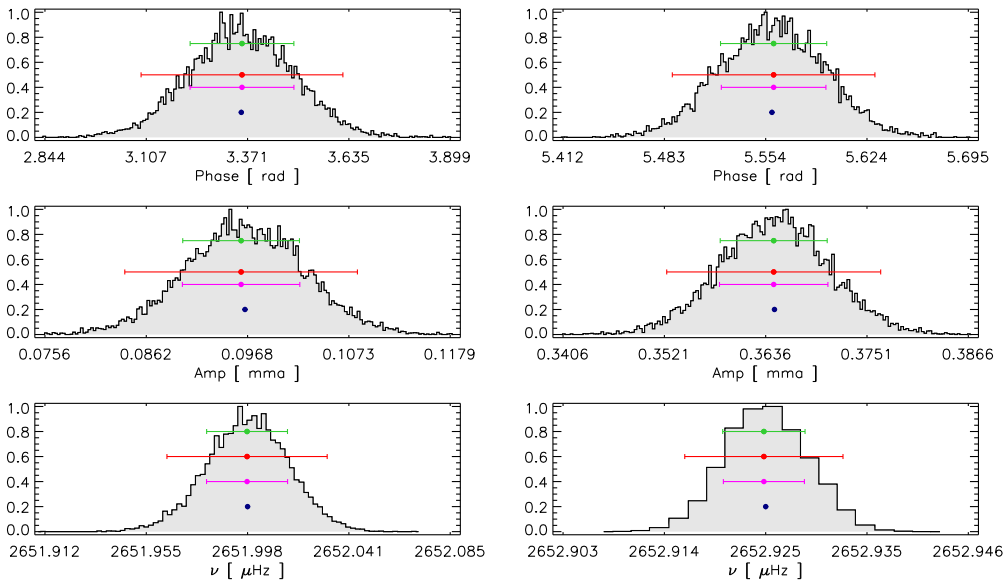

Figure C.3: Bootstrap distributions for fit parameters 5 and 6 in Tab. 3.1.

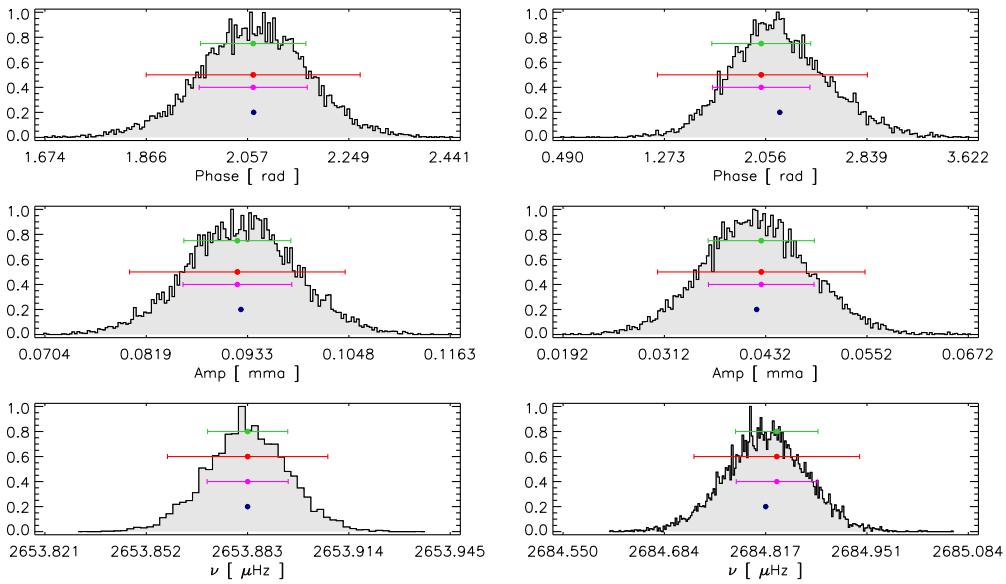

Figure C.4: Bootstrap distributions for fit parameters 7 and 8 in Tab. 3.1.

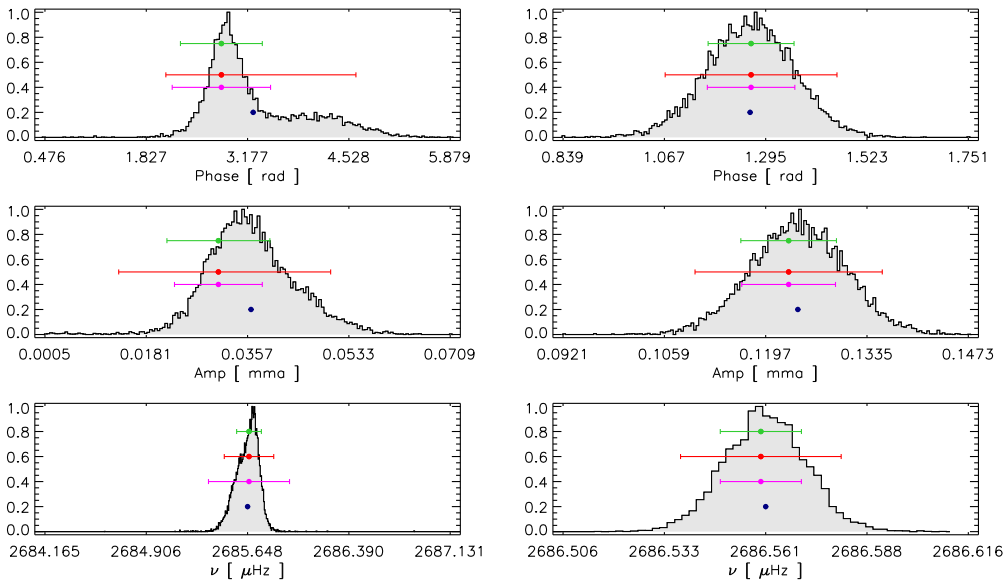

Figure C.5: Bootstrap distributions for fit parameters 9 and 10 in Tab. 3.1.

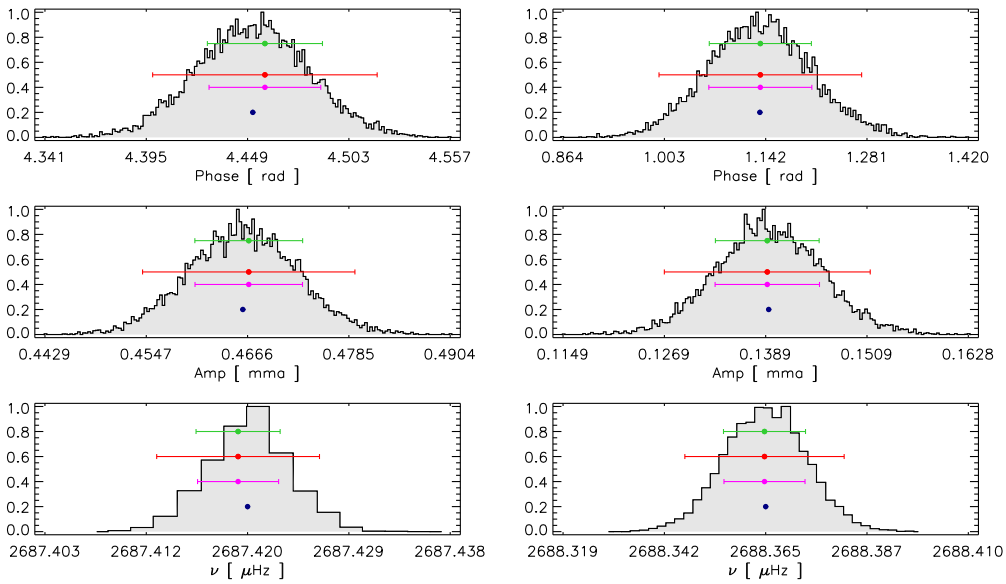

Figure C.6: Bootstrap distributions for fit parameters 11 and 12 in Tab. 3.1.

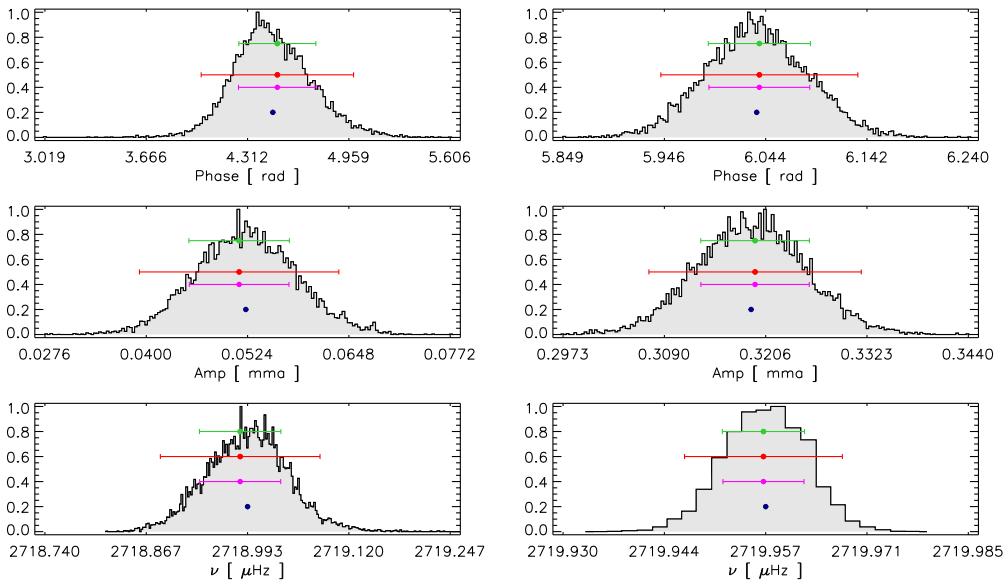

Figure C.7: Bootstrap distributions for fit parameters 13 and 14 in Tab. 3.1.

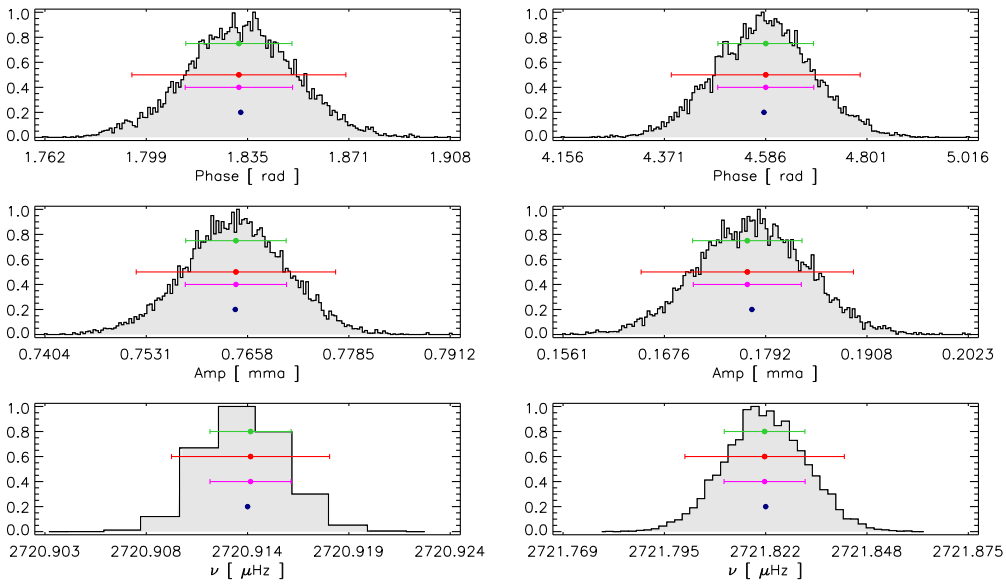

Figure C.8: Bootstrap distributions for fit parameters 15 and 16 in Tab. 3.1.

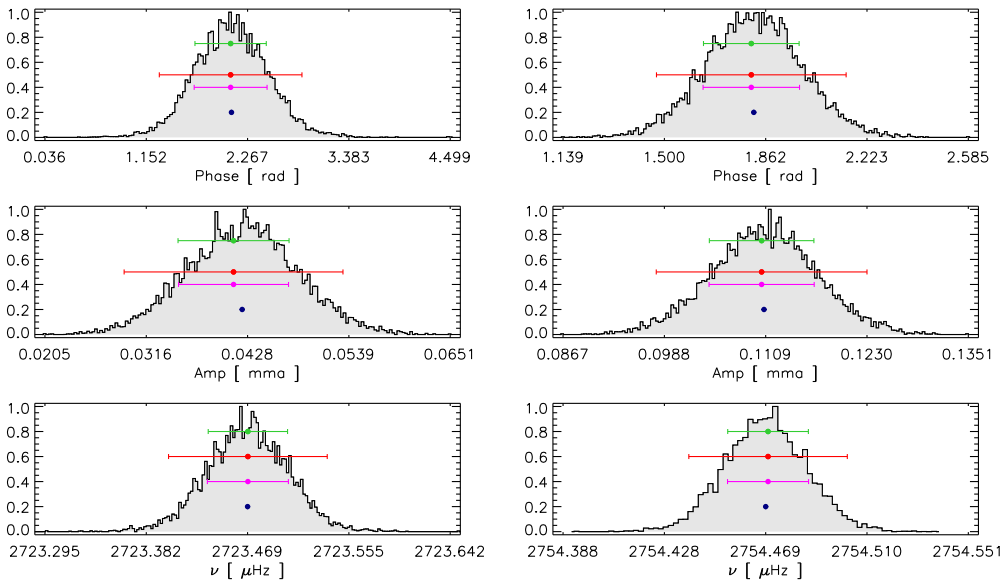

Figure C.9: Bootstrap distributions for fit parameters 17 and 18 in Tab. 3.1.

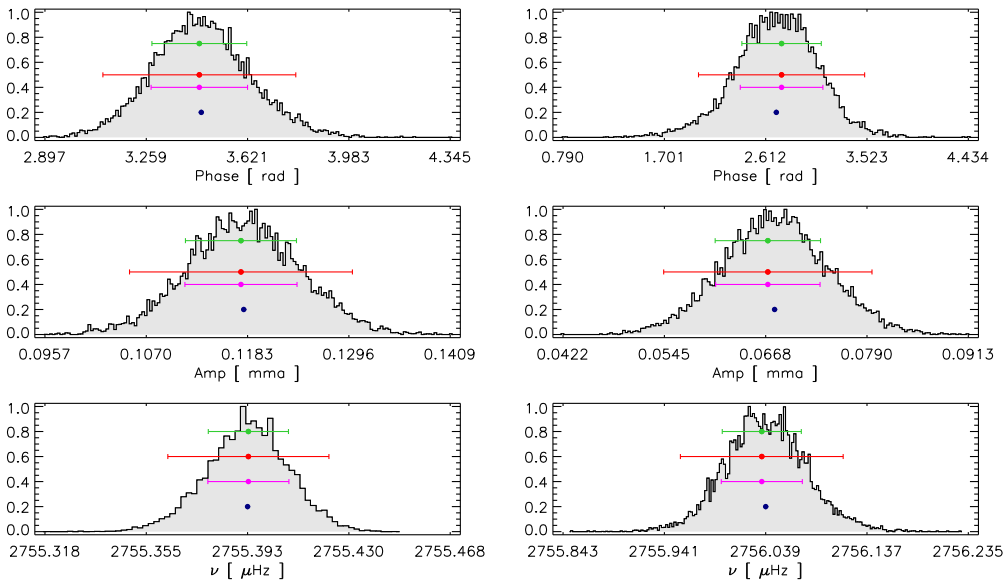

Figure C.10: Bootstrap distributions for fit parameters 19 and 20 in Tab. 3.1.

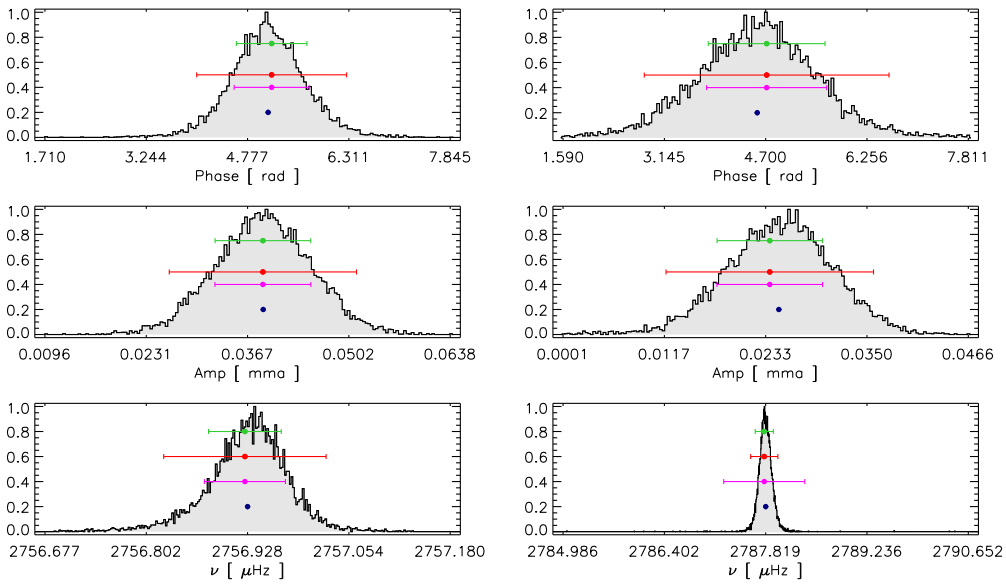

Figure C.11: Bootstrap distributions for fit parameters 21 and 22 in Tab. 3.1.

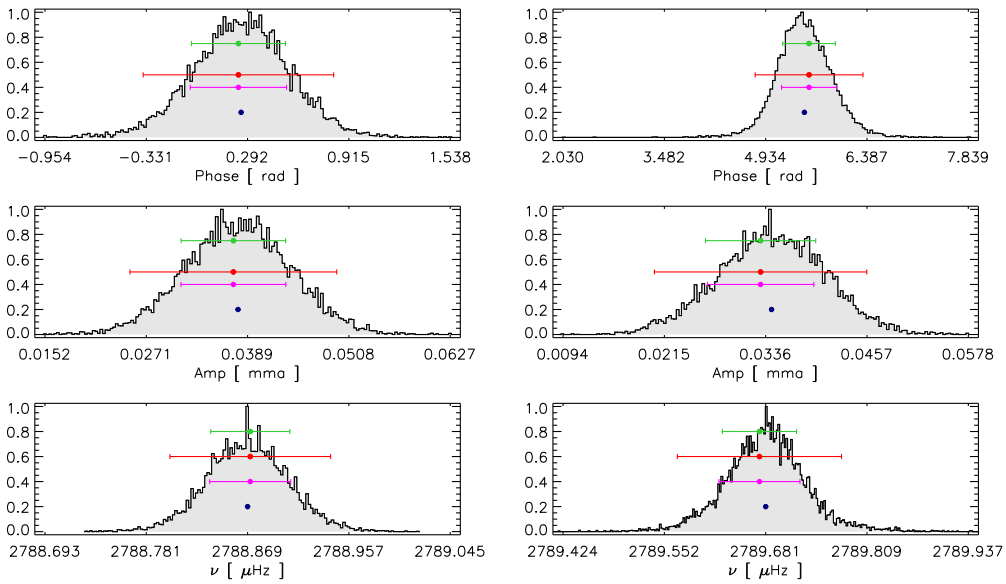

Figure C.12: Bootstrap distributions for fit parameters 23 and 24 in Tab. 3.1.

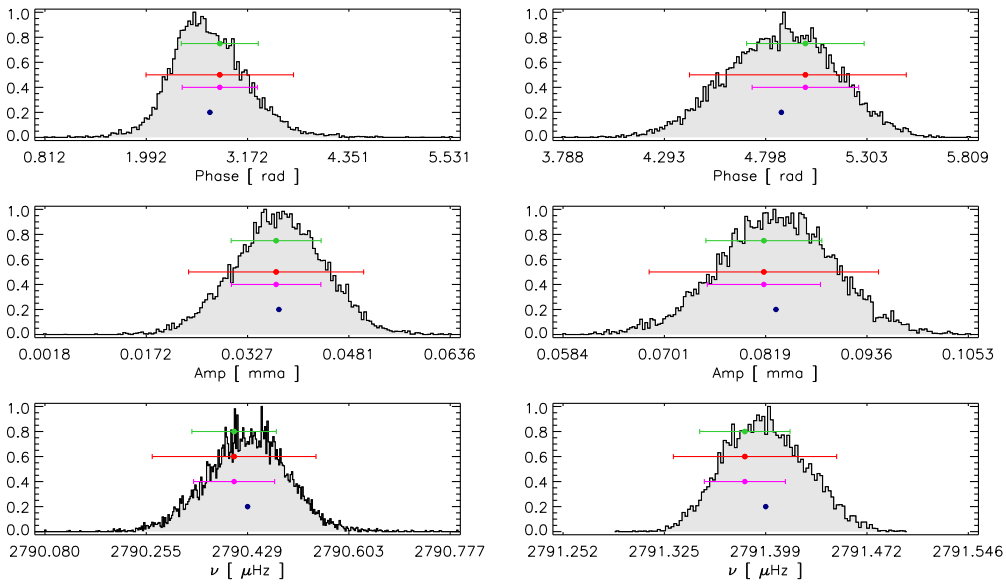

Figure C.13: Bootstrap distributions for fit parameters 25 and 26 in Tab. 3.1.

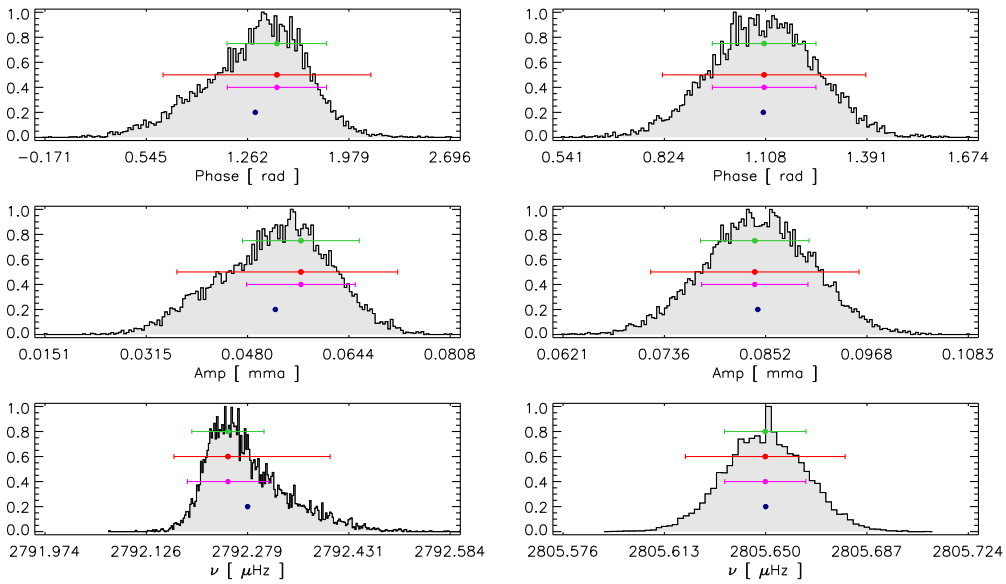

Figure C.14: Bootstrap distributions for fit parameters 27 and 28 in Tab. 3.1.

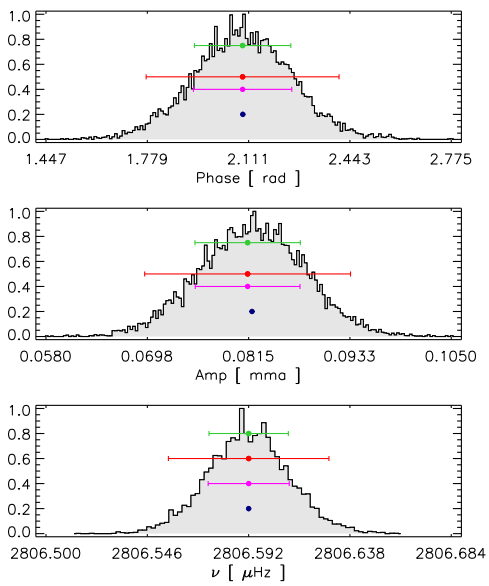

Figure C.15: Bootstrap distributions for fit parameters 29 in Tab. 3.1.

Appendix D

Magnetic perturbation (Saio) plots

Plots of magnetically perturbed pulsation modes are presented below. The plots give perturbed frequencies as a function of magnetic field (Saio plots) for degrees of ℓ ranging from 0 to 4. (See the legend at the top of each plot for degree identifications.) The caption below each plot identifies the model using the same labelling system used in Tables 5.1, 5.2, 5.4, 5.5, 5.9, 5.6, and 5.8. Each plot identifies (with a solid vertical line) the closest matched model listed in the aforementioned tables found in chapter 5. The observed frequencies from the HR 1217 data (Tab. 3.1) are shown as horizontal black dots in each plot.

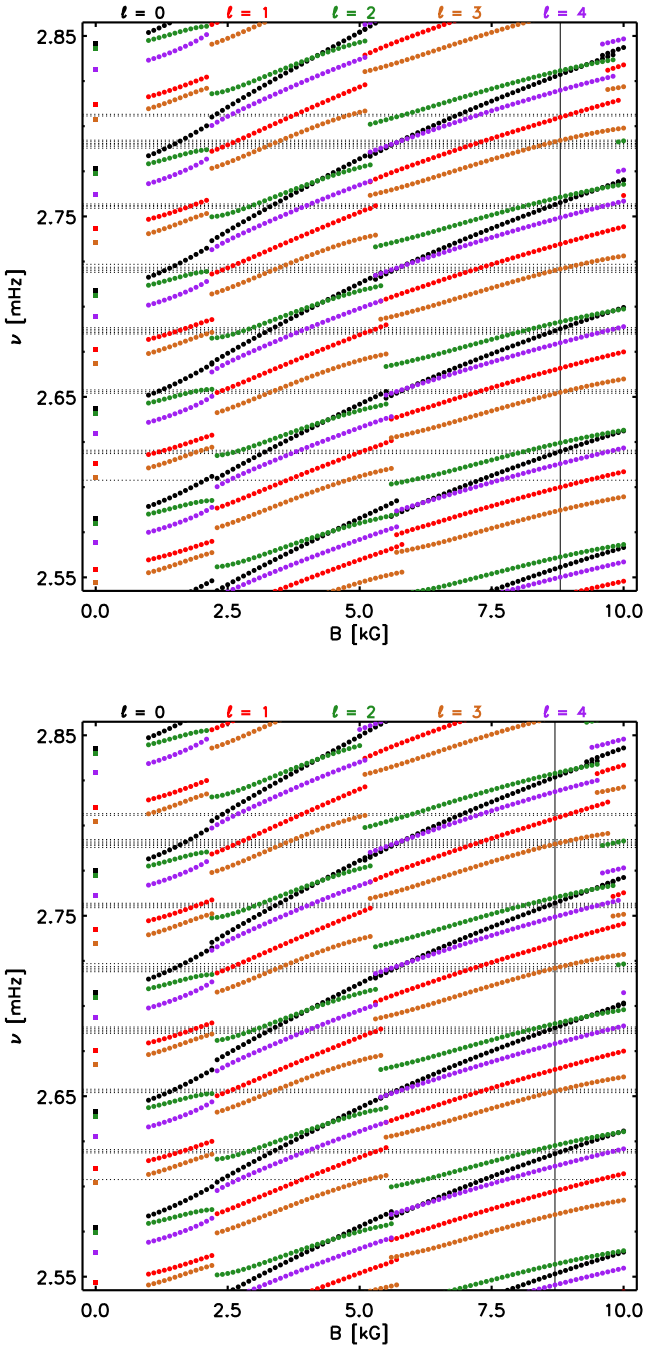

Figure D.1: Saio plots showing the best fit models M1 (top) and M2 (bottom) in Tab. 5.1.

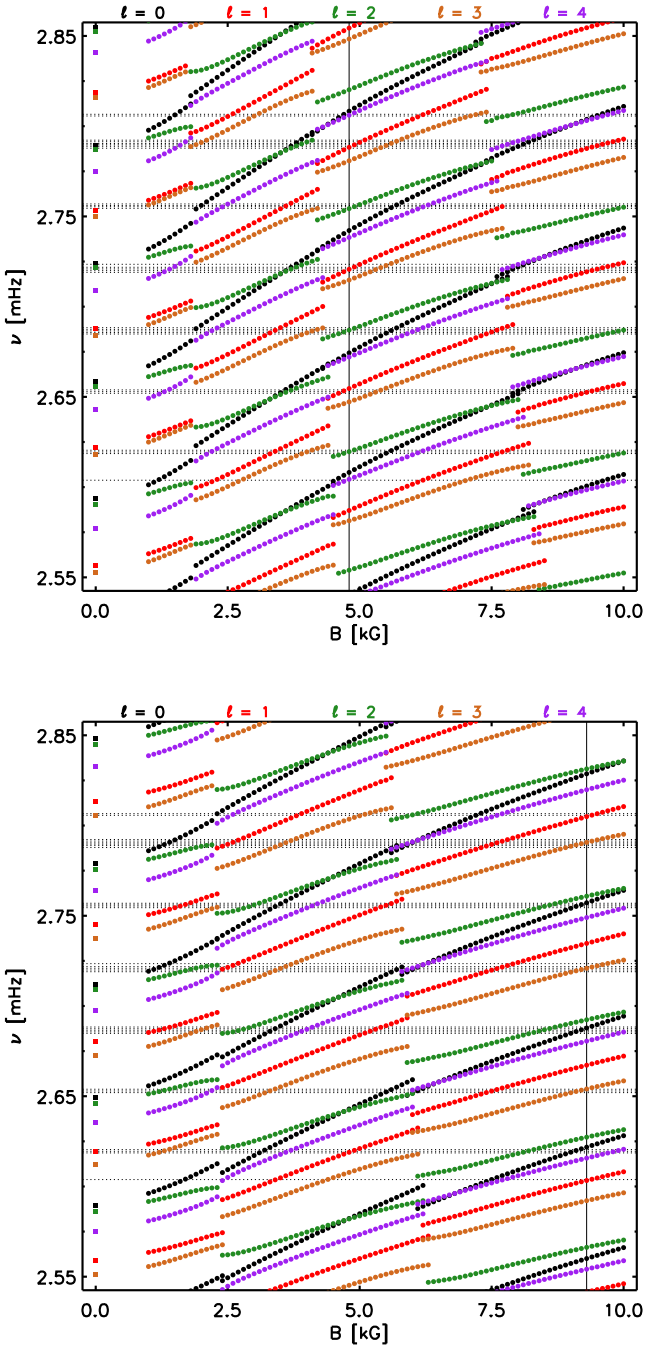

Figure D.2: Saio plots showing the best fit models M3 (top) and M4 (bottom) in Tab. 5.1.

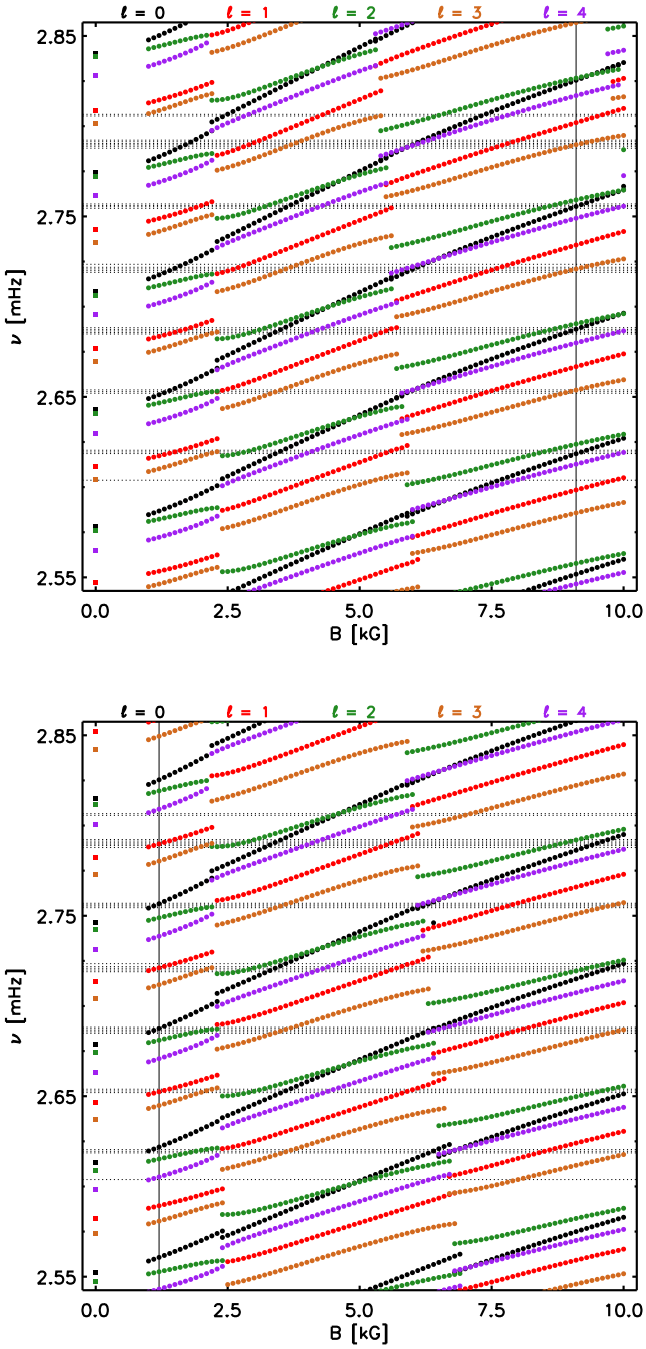

Figure D.3: Saio plots showing the best fit models M5 (top) and M6 (bottom) in Tab. 5.1.

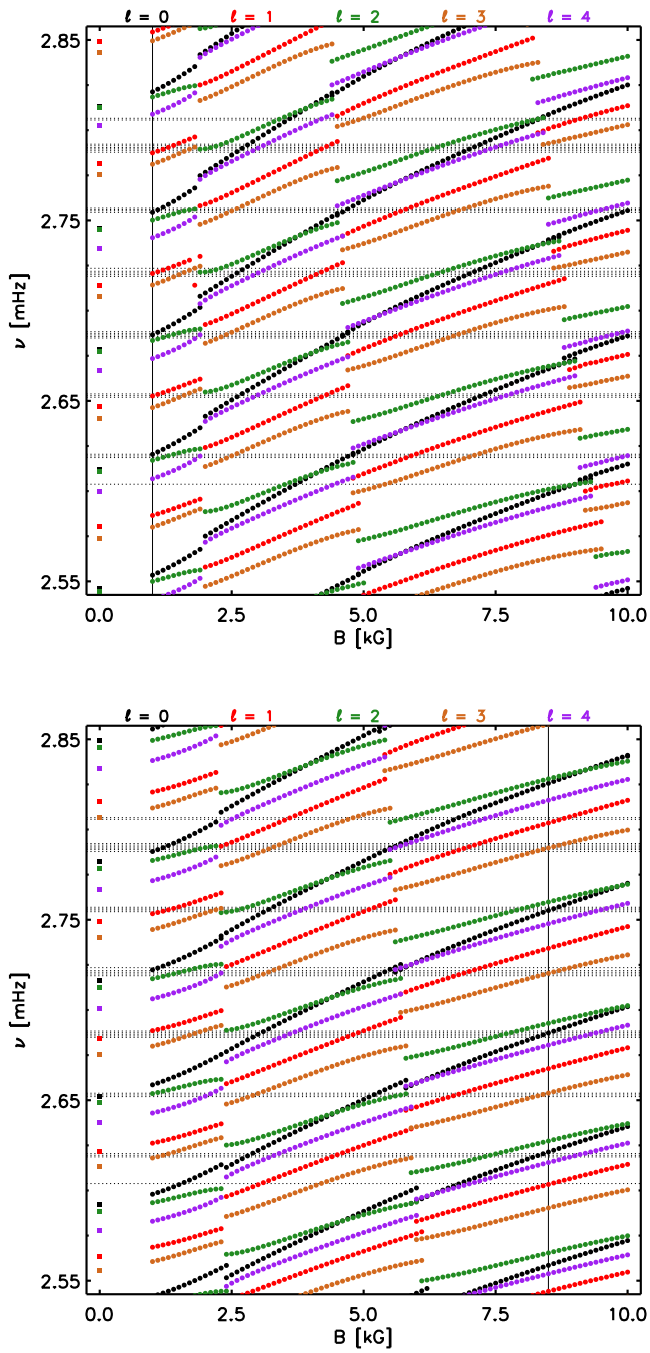

Figure D.4: Saio plots showing the best fit models M7 (top) and M8 (bottom) in Tab. 5.1.

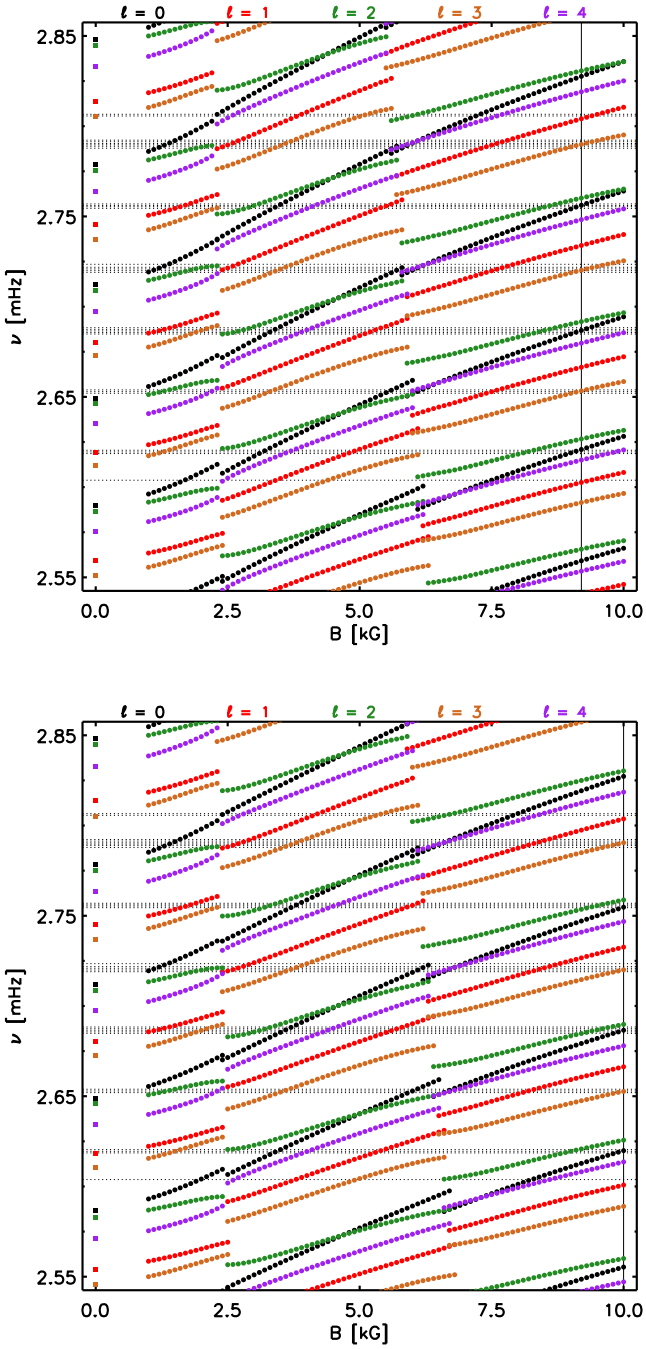

Figure D.5: Saio plots showing the best fit models M9 (top) and M10 (bottom) in Tab. 5.1.

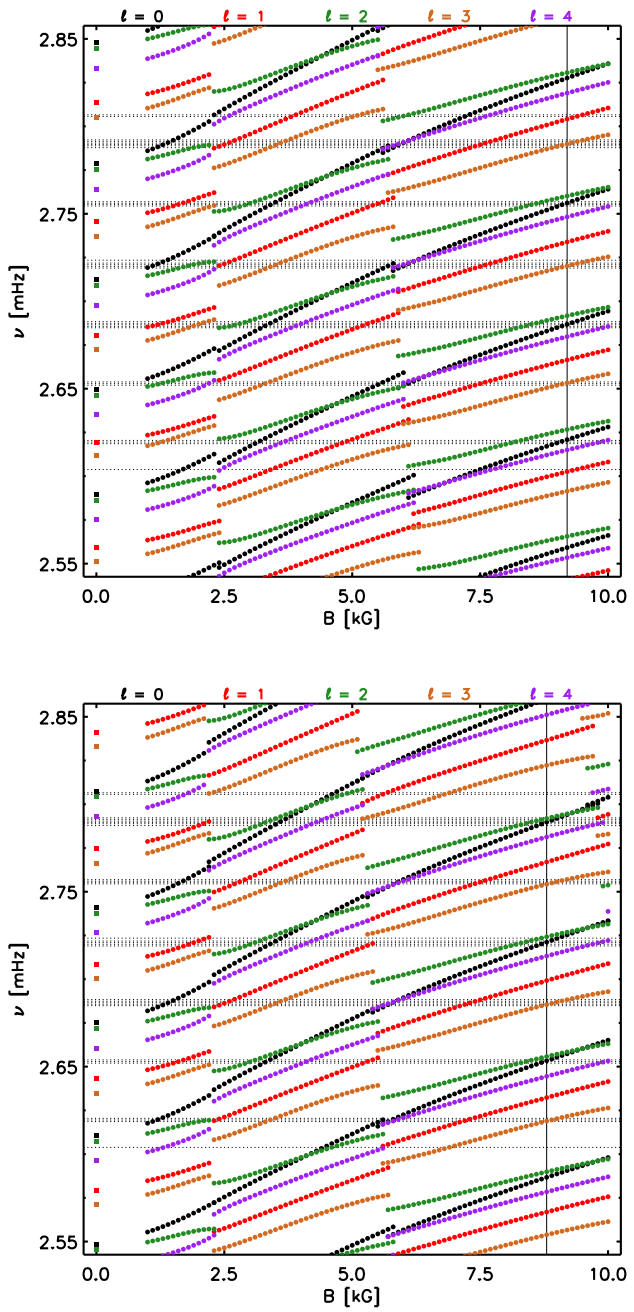

Figure D.6: Saio plots showing the best fit models M9 (top) and MM1 (bottom) in Tables 5.1 and 5.2.

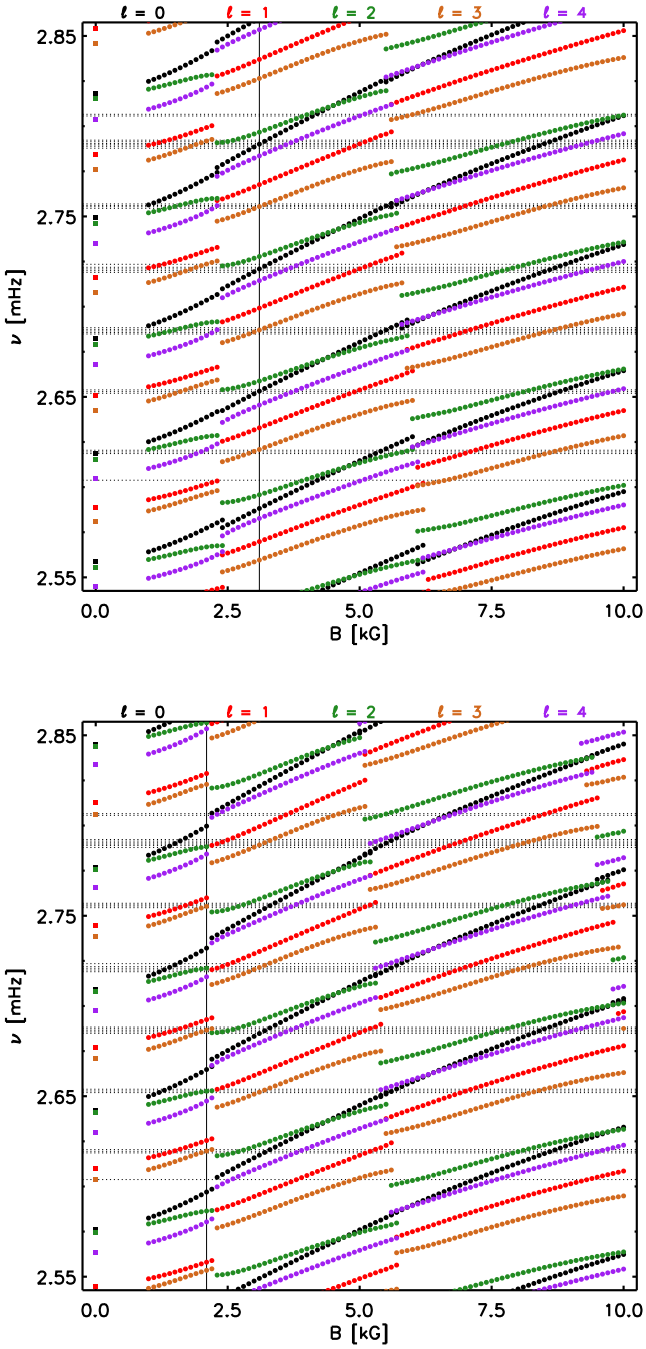

Figure D.7: Saio plots showing the best fit models U1 (top) and U2 (bottom) in Tab. 5.4.

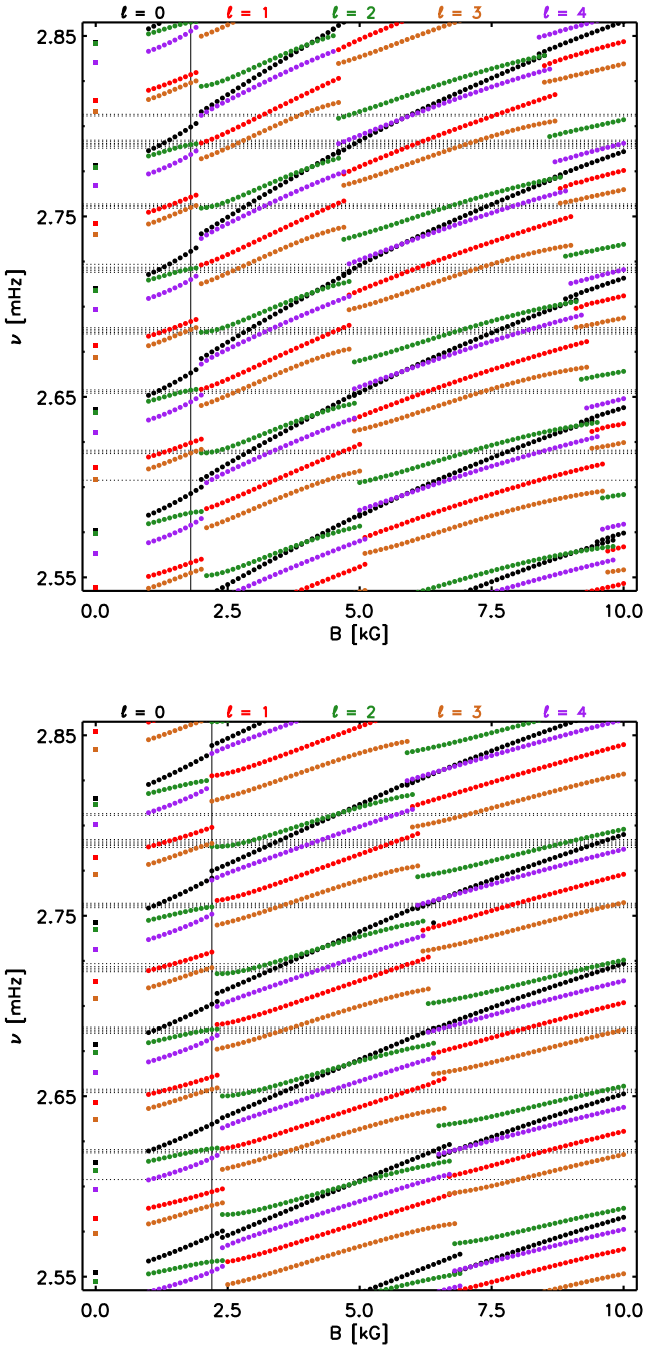

Figure D.8: Saio plots showing the best fit models U3 (top) and U4 (bottom) in Tab. 5.4.

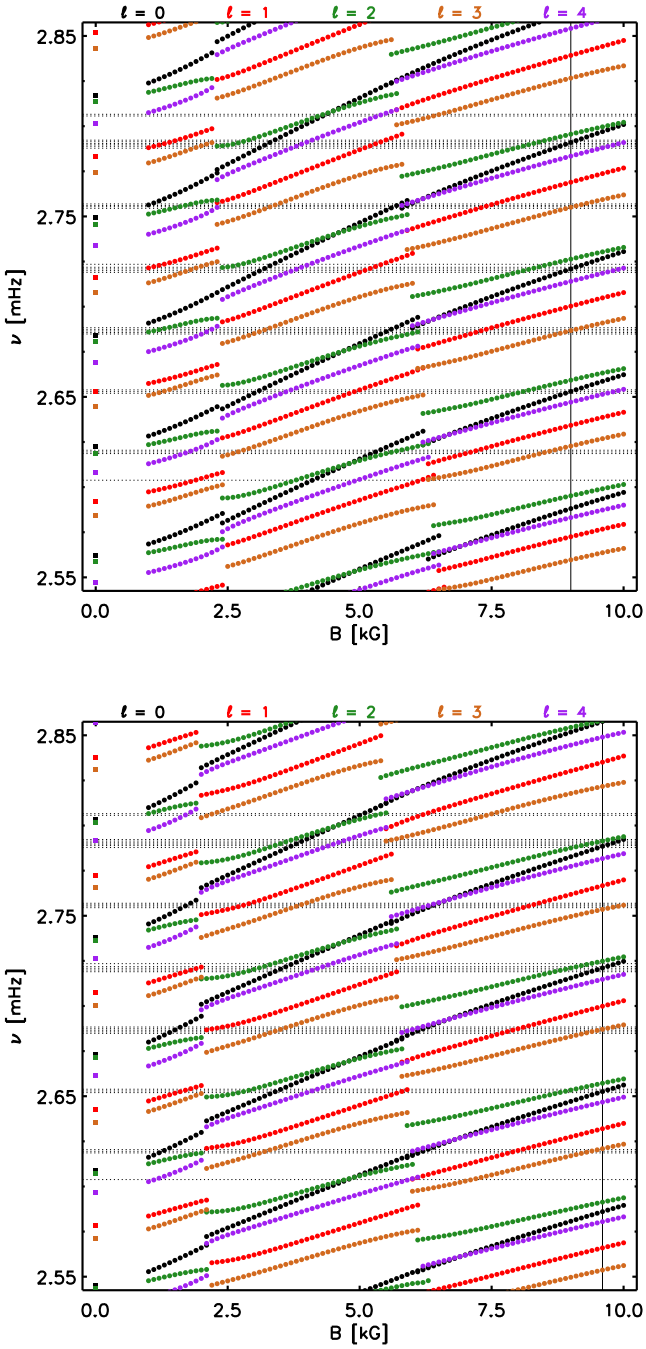

Figure D.9: Saio plots showing the best fit models U5 (top) and U6 (bottom) in Tab. 5.4.

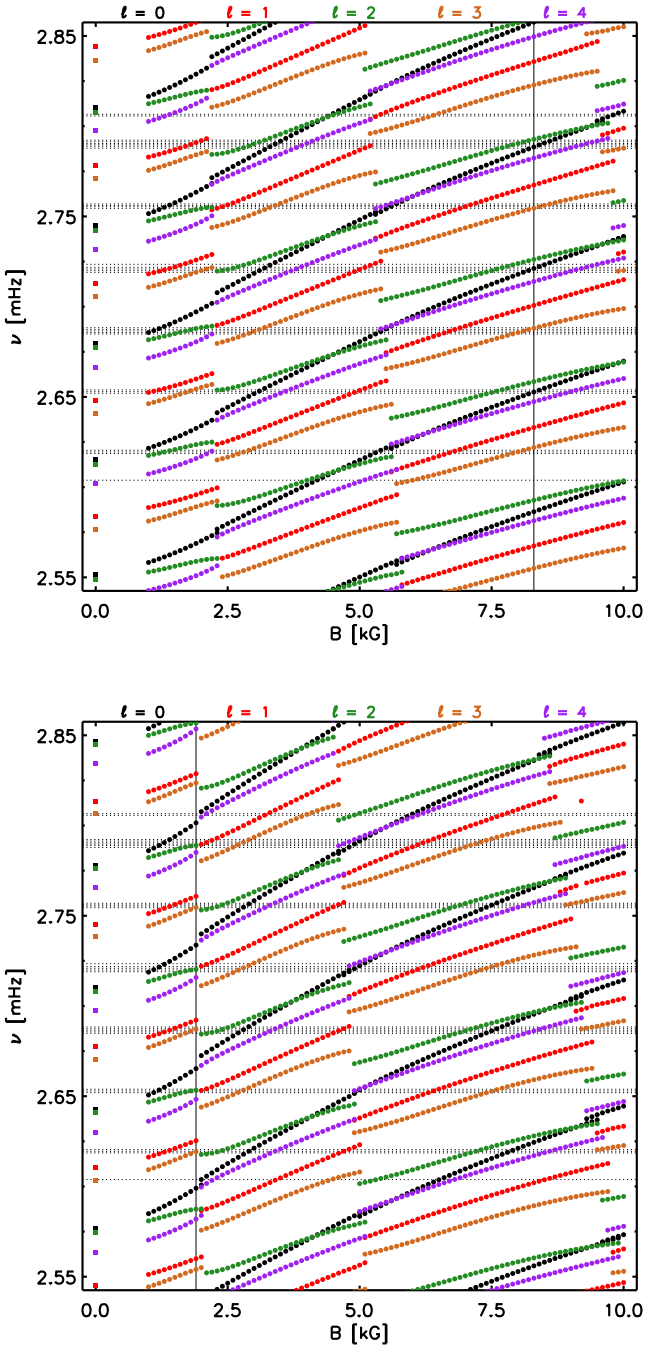

Figure D.10: Saio plots showing the best fit models U7 (top) and U8 (bottom) in Tab. 5.4.

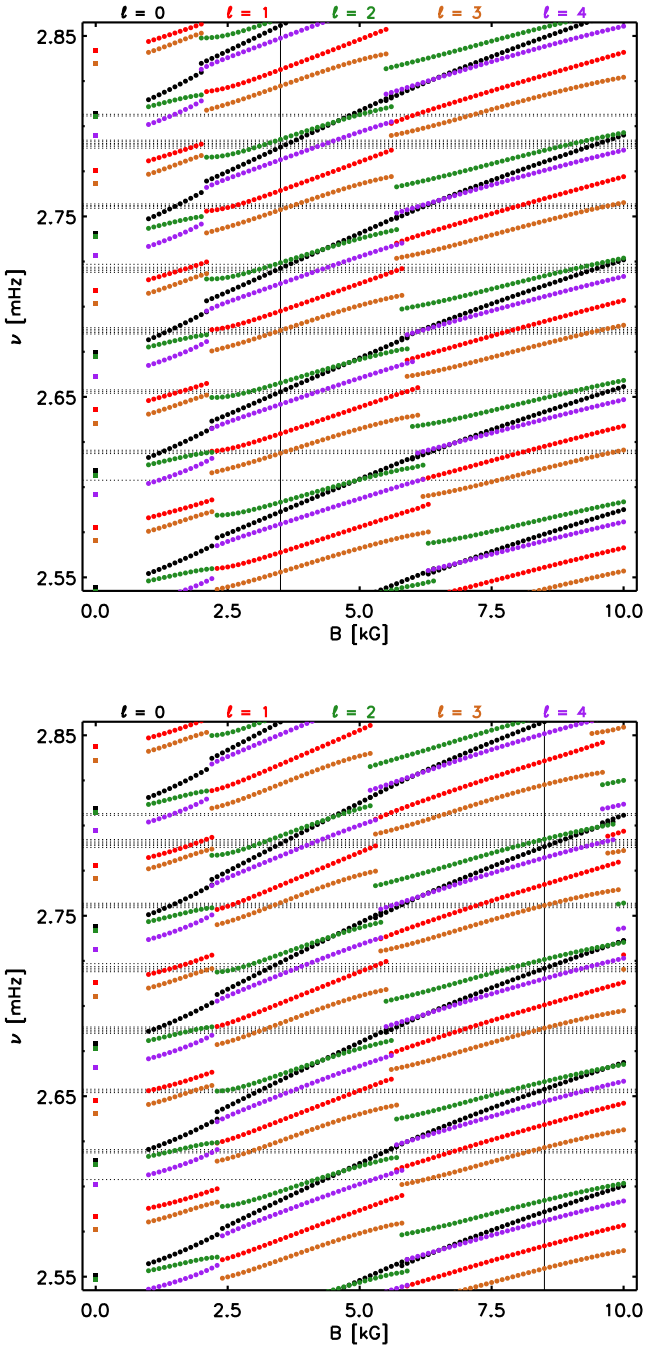

Figure D.11: Saio plots showing the best fit models U9 (top) and U10 (bottom) in Tab. 5.4.

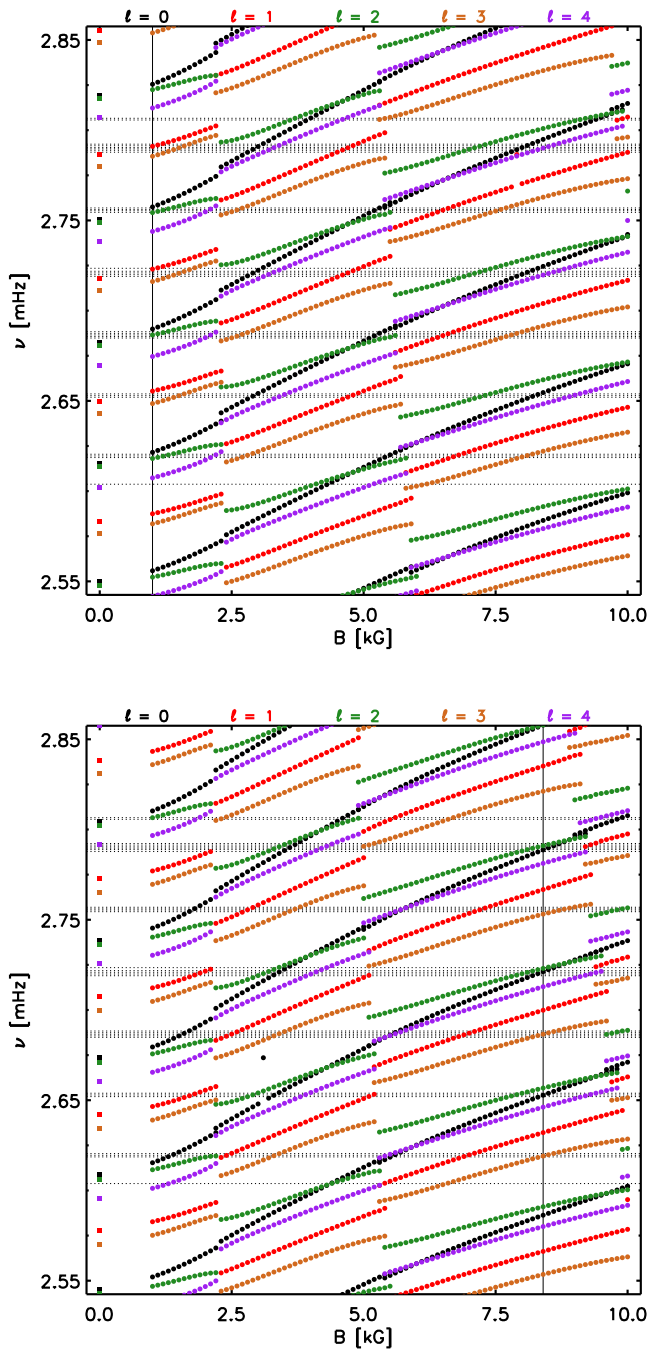

Figure D.12: Saio plots showing the best fit models UU1 (top) and UU2 (bottom) in Tab. 5.5.

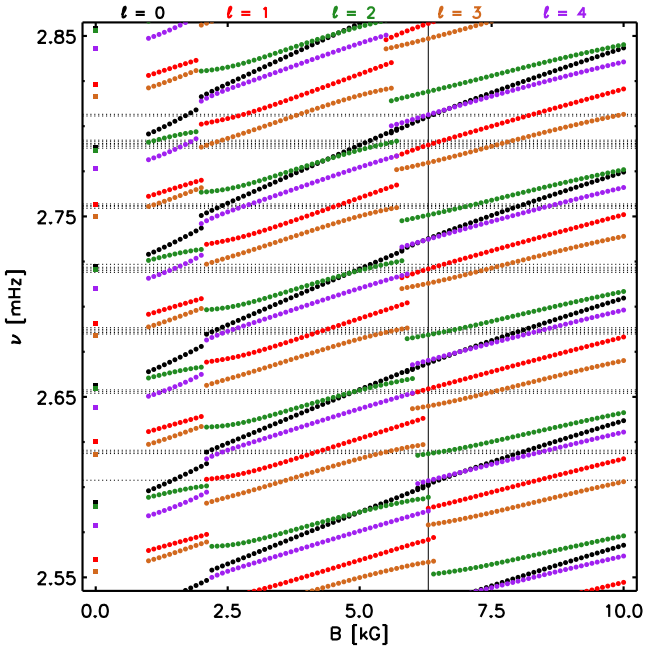

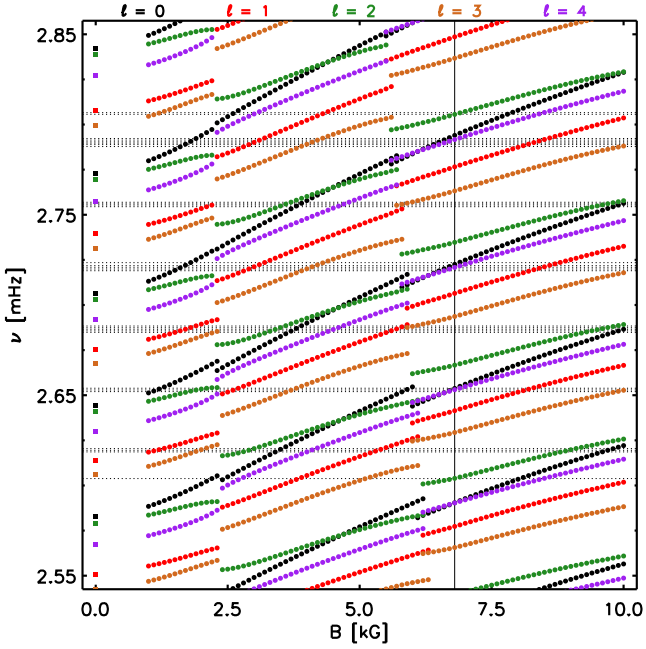

Figure D.13: Saio plots showing the best fit models GS (top) and MS (bottom) in Tab. 5.6.

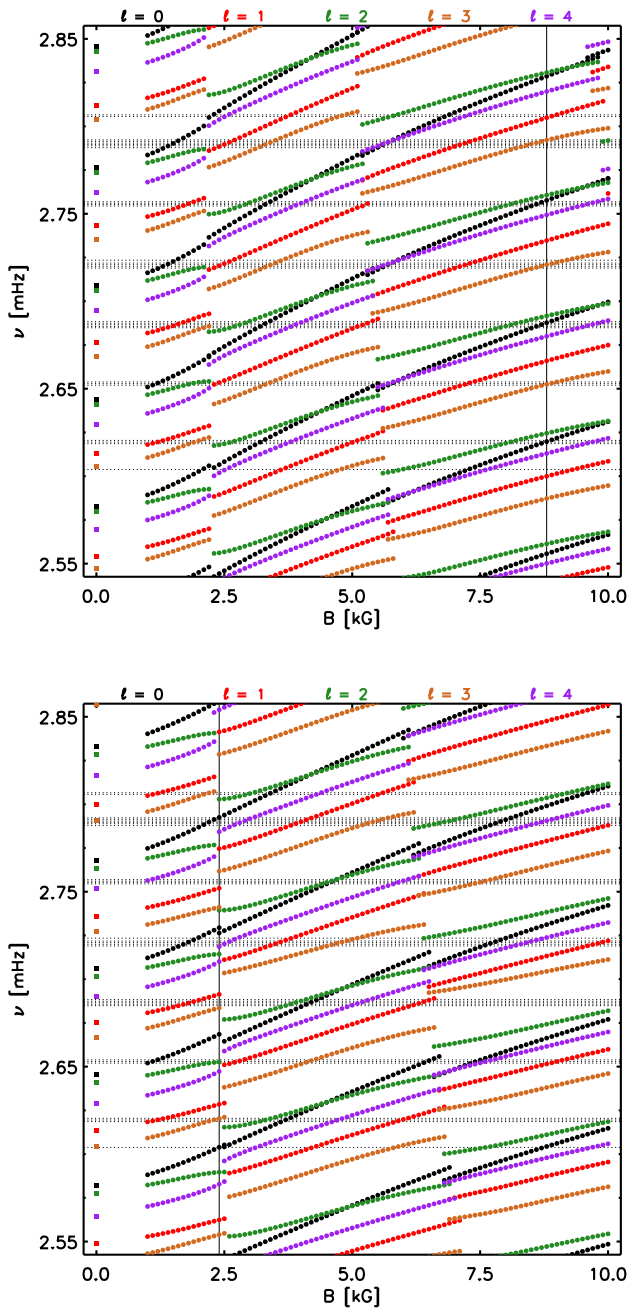

Figure D.14: Saio plots showing the best fit models PGS (top) and LPC (bottom). Model properties are given in Tabs. 5.8 and Tab. 5.9, respectively.